Femtosecond Photoelectron Imaging of Anions

Daniel Alfred Horke

Department of Chemistry
University of Durham

2012

A thesis submitted in partial fulfilment of the requirements for the degree of *Doctor of Philosophy*.

Declaration

The material contained within this thesis has not previously been submitted for a degree at the University of Durham or any other university. The research reported within this thesis has been conducted by the author unless indicated otherwise.

Abstract

Several recent results of a time-resolved photoelectron imaging experiment are presented. Following a broad introduction into the area of femtochemistry and time-resolved photoelectron spectroscopy, a detailed description of the spectrometer is given. This utilises an electrospray ionisation source, coupled to an electrostatic ion trap. Ions are mass selected using time-of-flight methods and investigated using photoelectron imaging in a velocity-mapping geometry. Ultrafast dynamics are investigated by pump-probe spectroscopy with femtosecond laser pulses.

Recent results are separated into three distinct projects:
(i) The investigation of electron acceptor radical anions based on the quinone backbone. These commonly exhibit electron transfer rates exceeding those predicted by Marcus theory by orders of magnitude. We show that an alternative pathway to electron transfer could involve the participation of electronic excited states, as these couple strongly to the anion ground state. Specifically, for *p*-Benzoquinone we show that electronic resonances located in the detachment continuum primarily undergo internal conversion via a number of conical intersections.
(ii) Several polyanions have been investigated in the gas-phase. These systems exhibit unusual electronic properties, due to the presence of multiple excess charges, leading to the formation of a repulsive Coulomb barrier to photodetachment. We investigate the effect of excess internal energy on this barrier and how it affects outgoing photoelectrons. We show that the trajectories of electrons are strongly influenced by this potential and demonstrate its use as a probe for large amplitude structural dynamics in polyanions.
(iii) The isolated chromophore of the green fluorescent protein (GFP) has been studied, and the vertical and adiabatic detachment energies determined for the first time. Using time-resolved spectroscopy the excited state dynamics are investigated. We show that the first singlet excited state of the anion primarily decays through internal conversion, explaining the absence of fluorescence in the gas-phase. Using high level quantum chemistry calculations we show the specific motion involved and hence confirm the function of the protein backbone in GFP.

This thesis is concluded with a few suggested experimental improvements and ideas for future studies of anions using the presented spectrometer.

Acknowledgements

This thesis is the outcome of three years of work and it would not have been possible (and would have been significantly less fun) were it not for the following people:

Most importantly, I would like to thank my supervisor Jan Verlet. Your patience, guidance and motivation have made all this possible, and I learned a great deal from you. Thank you for kicking me when I needed it, without it this thesis would be significantly shorter (or non-existent)!

I am also truly thankful to all those people that contributed to the photoelectron imaging experiment, Gareth Roberts and Julien Lecointre in the early days, and Adam Chatterley afterwards. Thank you also to our project students over the years.

Some results described in this thesis would not have been possible without the help of others, and I would like to thank the groups of Paul Low and Steven Cobb for synthesising samples; and Vas Stavros, Andy Beeby, Eckart Wrede and the EPSRC laser loan pool for loan of equipment.

The SDG group in Durham is an extremely fun and stimulating environment to work in, and I would like to especially thank Oliver Willis, Scott Sanders and Adrian Rowland, as well as Hendrik Nahler, Eckart Wrede and David Carty for all the scientific (and non-scientific) discussions, entertaining lunch breaks and the occasional pint in the Vic. I will miss this dearly!

I would also like the express my gratitude towards Durham University and especially Hatfield College and my many friends here (sorry for not naming you all!). The many opportunities for personal and professional development (and the chance of earning some cash as a student!) have helped me be the person I want to be.

On a personal level, I must thank my good friends Robin Cooper, Julia Blower, John Corcoran, Andy Burn, Dan Busbridge and James Radcliffe. You were there for me when I needed you most, made sure I see this thing through and kept me sane(*ish*). I am truly indebted to all of you.

Finally, I must thank my family for all their support. Papa and Gisela, you made all of this possible and ensured I received the best education available, thank you. I would also like to thank all the rest of my family for their support, but especially my brother Kristof and his wife Christina (and of course Jan and Clara!) and my sister Eva, you were always there for me, listened to me and encouraged me. Thank you!

Contents

Chapter 1

Introduction: Femtosecond Dynamics of Anions

It's not what you're looking at that matters, it's what you see...

Henry David Thoreau

1.1 Femtochemistry

Chemists have long strived to understand their discipline on the most fundamental of levels; how does a chemical reaction happen? What is the pathway by which electrons and nuclei rearrange and move during a chemical reaction, forming products? This formed the branch of chemistry now called *Reaction Dynamics* and its study was fundamentally limited by the timescale at which scientists were able to observe the world around them. Until the 19th century the best time resolution available was from the human senses - the blink of an eye ($\sim$ 0.1 s) or the response of the ear ($\sim$ 1 ms). The first advance towards understanding nature at faster timescales was the invention of snapshot photography by Eadweard Muybridge in 1878, answering the question if a horse has all four legs off the ground while galloping. However, there was still a crucial element missing for the application to chemical reactions: How does one start a chemical reaction at a well defined moment in time? In other words, how does one define "time zero"? It was not until the 1920s that chemical dynamics could be studied with sub-second resolution, with the invention of the flowtube technique by Hartridge and Roughton.[1] This was pushed into the millisecond regime by Chance with the stopped-flow technique.[2] However these techniques relied on rapidly mixing reagents together to define the starting point of a reaction.

A breakthrough in the study of reaction dynamics was made by Eigen, Norrish and Porter in the 1950s through the invention of flash-photolysis.[3,4] The idea of initiating and subsequently probing a chemical reaction with light was ingenious, it meant time resolution was now limited by how short a pulse of light one can produce! It immediately extended available time resolution into the microsecond regime (through the use of flash lamps) and the basic principle of this technique is used to this day, as it forms the basis of *pump-probe spectroscopy*. In this scheme a reaction is initiated by a burst of light (the "pump") defining the zero of time and investigated some time later by a second burst of light (the "probe"). This enables one to start the reaction many times over, each time changing the delay between the pump and the probe, thus building up a picture of the dynamical evolution of the process studied. The second major breakthrough for the study of chemical reaction dynamics happened some 10 years later - the invention of the laser. This provided well defined, controllable and highly intense pulses of light, ideally suited for pump-probe spectroscopy. The speed of technological advances in the decades following the first demonstration of lasing was immense: Maiman demonstrated the first laser (producing microsecond pulses) in 1960,[5] by 1962 nanosecond lasers were realised,[6] the picosecond regime was reached in 1964,[7,8] femtosecond pulses were first made in 1974[9] and by 1987 a 6 fs laser pulse was produced,[10] close to the optical cycle limit of visible light (a single optical cycle in the visible part of the spectrum is

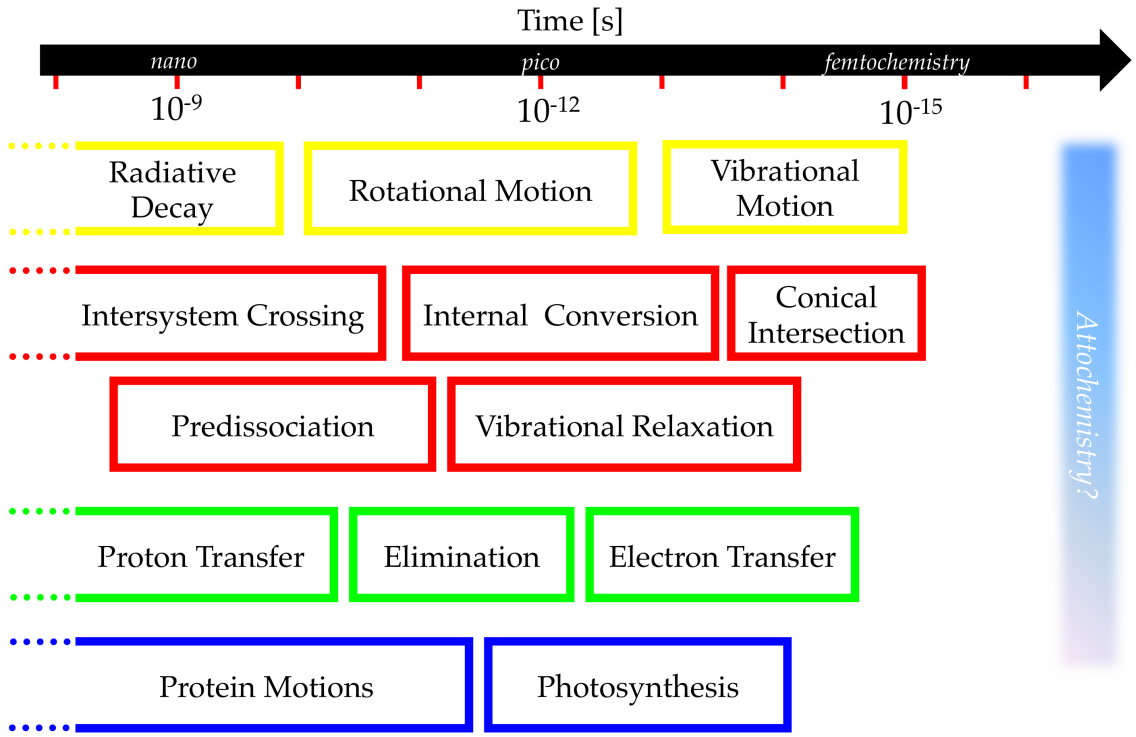

Figure 1.1: The *Arrow of Time*, relating various physical, chemical and biological processes to their associated timescales.

$\sim$ 2 fs)! A further advantage of using laser based light sources is their coherence, allowing the well-defined initiation of a molecular state at a point in time was crucial for experiments in the picosecond regime and beyond. This coherent localisation allows observation of the motion of nuclei as classical particles, through so-called wavepackets.[11,12]

The fundamental timescale of chemistry and chemical reactions can be easily approximated; considering typical atomic distances are on the order of ångströms (1 Å $= 10^{-10}$ m) and atoms typically move (at room temperature) at about 1 km s^{-1}, yields reaction times on the order of 100s of femtosecond (1 fs = 10^{-15} s).[12] An overview of the timescales involved in fundamental molecular processes is shown in Figure 1.1, relating some physical, chemical and biological processes to their natural timescales. With these technological advances it was therefore possible to study chemistry at its most basic level and begin to answer some of the fundamental questions of reaction dynamics: How do nuclei rearrange during chemical reactions and can one observe transition states, so far treated as a "mythical entity" between reactants and products, as a molecular entity?[11] How do reactions happen from a quantum mechanical point of view, how do the quantum states in isolated reactants combine to form a single quantum mechanical system? How do isolated molecules react to excess energy ("activation"), do they redistribute or dissipate the energy, or do they dissociate? These are the fundamental questions femtochemistry tries to address.[12] Of course technologi-

cal advance has not stood still and we now have the ability of producing isolated attosecond (10^{-18} s) pulses in the extreme ultraviolet part of the electromagnetic spectrum, that should allow the study of core electron dynamics (orbital period of an electron in Hydrogen is ~ 100 as).[13,14] The development of high-harmonic generation[15] and Free-Electron Lasers,[16] providing femtosecond pulses of unprecedented brilliance in the X-ray part of the spectrum, and ultrafast electron diffraction techniques should enable fully structure resolving methods to break into the femtosecond domain.[17]

The ideas of femtochemistry have been applied to numerous systems, from gas-phase isolated molecules, to solutions, interfaces, solids, nano particles and clusters. A wide range of spectroscopic techniques have been adapted for femtosecond time-resolved experiments, including (but not limited to) mass spectroscopy, Raman spectroscopy, transient absorption, X-ray absorption and Coloumb explosion imaging.[12] One of the most important tools for investigating the electronic structure of gas-phase species that has evolved over the past decade or so is time-resolved photoelectron spectroscopy, probing the electronic structure and dynamics in isolated molecules. Our work here in Durham, and the rest of this thesis, focusses on time-resolved photoelectron spectroscopy of molecular anions. Working in a gas-phase environment allows one to study the underlying fundamental properties of molecules and reactions, free from interactions with the environment around them, such as solvents. This helps to develop a greater understanding, aided by electronic structure and dynamics calculations. The choice of studying anionic systems seem a natural one; they have a huge importance in nature and technology, yet their ultrafast dynamics are not very well studied or understood (primarily due to experimental limitations).

The remainder of this thesis is organised as follows. The first chapter introduces the basic theoretical concepts needed for the processes involved in and studied by time-resolved photoelectron spectroscopy. This is followed by an overview of the current literature on time-resolved photoelectron spectroscopy, with a focus on studies of anionic systems. Chapter 2 gives a detailed description of our experimental setup and the advantages of our new design. The next three chapters present recent results from our laboratory; Chapter 3 focusses on relaxation dynamics in the radical anions of common electron acceptors, primarily based on the *p*-Benzoquinone backbone; Chapter 4 deals with electronic dynamics in multiply-charged anions, specifically dianions and how the excess charges effect outgoing photoelectrons and chapter 5 contains recent results on the electronic structure and dynamics in the isolated chromophore of the green fluorescent protein. Chapter 6 presents an overall summary and conclusion to the presented material, as well as providing an outlook into the near future and some suggestions for further study.

1.2 Excited State Dynamics

This section aims to provide an overview of electronic excitation and relaxation processes, their underlying physical principles and how to study their dynamics. Starting from basic molecular quantum mechanics, a theoretical framework is build up to describe molecular systems in terms of wavefunctions and different states of a system in terms of potential energy surfaces. The theory of molecular electronic excitations is introduced and the associated cross-sections and selection rules described. Electronic relaxation processes are discussed in detail and a quantum mechanical treatment of these processes, both radiative and non-radiative, given. In later sections this theoretical background will be applied to understand experimental techniques and results, focussing on photoelectron spectroscopy.

1.2.1 Molecular quantum mechanics

The Schrödinger Equation

The basic premise of quantum mechanics is to express a system (be it a single electron, an atom or a molecule) as a wavefunction that describes the amplitude of the wave in space and time, commonly denoted $\Psi(\boldsymbol{r}, t)$ where $\boldsymbol{r}$ denotes all space. For the basic example of an electron wave, the wavefunction will associate an amplitude of the electron wave to every point in space and time. The probability of finding the electron at any one point is then given by the product of the wavefunction with its own complex conjugate at that point, $P(e^-) = \Psi^*\Psi$. The probability of finding the electron at any point in space must be equal to 1, leading to[18]

$$\int \Psi^*\Psi d\boldsymbol{r} = \langle\Psi|\Psi\rangle = 1 \tag{1.1}$$

where we have introduced the Dirac bra-ket notation as a shorthand for integrals over all space. The quantum mechanical Hamiltonian (H) is, much like its classical counterpart, given by the sum of all kinetic (T) and potential (V) energy, however with the corresponding quantum mechanical operators replacing the classical ones. The Hamiltonian can furthermore be thought of as the rate of change of action (A) as a function of time. We obtain[19]

$$H = T + V = -\frac{\hbar^2}{2m}\nabla^2 + V = -\frac{\partial A}{\partial t}, \tag{1.2}$$

where ∇^2 is the Laplacian. The form postulated for the wavefunction is that of a complex exponential of the Action, with a proportionality constant b; $\Psi = b\exp\left(\frac{iA}{\hbar}\right)$. Combing this with equation 1.2 yields

$$H\Psi = i\hbar\frac{\partial\Psi}{\partial t} \tag{1.3}$$

$$-\frac{\hbar^2}{2m}\nabla^2\Psi + V\Psi = i\hbar\frac{\partial\Psi}{\partial t}, \tag{1.4}$$

the time-dependent Schrödinger equation (SE).[20] A description of the simplest atomic system, the Hydrogen atom, in which a single electron orbits a single proton, can thus be obtained by substituting the correct potential energy:[19]

$$-\frac{\hbar^2}{2m}\nabla^2\Psi - \frac{e^2}{4\pi\epsilon_0 r}\Psi = i\hbar\frac{\partial\Psi}{\partial t}. \tag{1.5}$$

The full time-dependent SE can be significantly simplified when considering stationary, non time-dependent systems. Assuming the SE is factorisable into a spatial part $\psi(\boldsymbol{r})$ and a temporal part $\theta(t)$ such that $\Psi(\boldsymbol{r},t) = \psi(\boldsymbol{r})\theta(t)$, we substitute this into equation 1.4 to obtain

$$-\frac{\hbar^2}{2m}\theta\nabla^2\psi + V(\boldsymbol{r})\psi\theta = i\hbar\psi\frac{d\theta}{dt} \tag{1.6}$$

By dividing both sides of equation 1.6 by $\psi\theta$ we obtain expression 1.7, where the left-hand side is dependent only on the spatial coordinate $\boldsymbol{r}$ and the right-hand side is dependent only on time, t.

$$-\frac{\hbar^2}{2m}\frac{1}{\psi}\nabla^2\psi + V(\boldsymbol{r}) = i\hbar\frac{1}{\theta}\frac{d\theta}{dt} \tag{1.7}$$

This allows the separation into two equations, one describing the spatial evolution of the system, 1.8, and one describing the temporal evolution of the system, 1.9.[19,21]

$$-\frac{\hbar^2}{2m}\nabla^2\psi + V(\boldsymbol{r})\psi = E\psi \tag{1.8}$$

$$i\hbar\frac{d\theta}{dt} = E\theta \tag{1.9}$$

Equation 1.8 is the time-independent SE, which takes the form of a stationary wave equation. The temporal evolution of a stationary system is given by equation 1.9, which is a first order differential equation with solutions $\theta \propto \exp\left(-\frac{iEt}{\hbar}\right)$. The time-independent SE satisfies the eigenvalue equation

$$H\psi = E\psi. \tag{1.10}$$

The time-dependence for a stationary SE can be constructed by multiplication with $\theta(t) = \exp\left(-\frac{iEt}{\hbar}\right)$. This modulates the phase of the wavefunction but leaves the probability of finding the system at a given spatial coordinate unaf-

fected.[21]

$$\Psi^*\Psi = \left(\psi^* \mathrm{e}^{\frac{iET}{\hbar}}\right)\left(\psi \mathrm{e}^{-\frac{iET}{\hbar}}\right) = \psi^*\psi \tag{1.11}$$

Uncertainty principle

An important consequence of quantum mechanics and the wave-particle duality is the uncertainty principle, first postulated by Werner Heisenberg in 1927.[22] In its most common form it states that the position of a particle, x, and its associated momentum, p_x, cannot be know to arbitrary precision at the same time, but rather the uncertainties in the two quantities are related by

$$\Delta x \Delta p_x \geq \frac{1}{2}\hbar. \tag{1.12}$$

The uncertainty principle holds for all non-commutating quantum mechanical operators. In its most general form, the uncertainty between two operators, A and B, can be related to their commutator $[A, B]$;[21,23]

$$\Delta A \Delta B \geq \frac{1}{2}\left\langle [A, B] \right\rangle. \tag{1.13}$$

Commuting operators, that is $[A, B] = 0$, comprise independent observables and are not related by any uncertainty. For a set of two dependent variables their operators will not commute and their measurement uncertainties are related by equation 1.13. A common uncertainty relation is that between Energy, E, and time, t:

$$\Delta E \Delta t \geq \hbar. \tag{1.14}$$

While this is not strictly speaking an uncertainty relationship of the type presented in equation 1.13, as time is not a quantum mechanical operator but a parameter, it nevertheless has important consequences.[21] The equivalent of the time-energy uncertainty can be derived from first principles using pulses of light. Consider a monochromatic plane wave, defined here as the real part of a complex exponential for mathematical ease:[24]

$$E_x = \Re[E_0 \exp(i\omega_0 t)]. \tag{1.15}$$

To describe a finite duration laser pulse, this is multiplied by a shape function describing the temporal envelope. For a Gaussian shaped laser pulse,

$$E = \Re[E_0 \exp\left(-\Gamma t^2 + i\omega_0 t\right)] \tag{1.16}$$

where the temporal width is described by the shape factor $\Gamma \propto t_0^{-2}$. As time and frequency are Fourier related quantities, one can evaluate the frequency envelope from the temporal pulse profile. For a plane continuous wave (equation

1.15) a delta function is obtained containing only a single frequency. The Fourier transform of a Gaussian function however is another Gaussian function and we obtain for the width of a Gaussian temporal profile[24]

$$E(\omega) = \exp\left[-\frac{(\omega-\omega_0)^2}{4\Gamma}\right] \tag{1.17}$$

An equivalent version of equation 1.14 can be derived by considering the standard definitions of time and frequency Fourier transforms;

$$\epsilon(t) = \frac{1}{2\pi}\int E(\omega)\exp(i\omega t)d\omega \tag{1.18}$$

$$E(\omega) = \int \epsilon(t)\exp(i\omega t)dt \tag{1.19}$$

Calculating the spectral width and temporal profile from the standard definitions,

$$\langle\Delta t\rangle = \frac{\int t|\epsilon(t)|^2dt}{\int|\epsilon(t)|^2dt} \tag{1.20}$$

$$\langle\Delta\omega^2\rangle = \frac{\int \omega^2|E(\omega)|^2d\omega}{\int|E(\omega)|^2d\omega} \tag{1.21}$$

it can be shown that pulse duration and spectral width are related by[24]

$$\Delta t\Delta\omega \geq \frac{1}{2} \tag{1.22}$$

This relationship between the duration and spectrum of a laser pulse has important consequences in ultrafast spectroscopy. For example, a laser pulse centered at a wavelength of 800 nm with a Gaussian temporal pulse profile of 100 fs duration will have a spectral width of $\sim$ 10 nm.

Born-Oppenheimer approximation

Solving the SE for any system with more than 3 particles exactly is impossible, and the introduction of numerical methods and approximations becomes inevitable. The complexity of the task at hand becomes clear when considering the overall Hamiltonian for a molecular system, H_{mol}.[19,25]

$$H_{\text{mol}} = T_{\text{el}} + V_{\text{el-nuc}} + V_{\text{el-el}} + T_{\text{nuc}} + V_{\text{nuc-nuc}}, \tag{1.23}$$

where we consider separately the kinetic energies of electrons (T_{el}) and nuclei (T_{nuc}), given by the respective quantum mechanical kinetic energy operators; and the potential energy interactions given by the respective Coulomb forces, namely electron-electron ($V_{\text{el-el}}$), electron-nuclei ($V_{\text{el-nuc}}$) and nuclei-nuclei interactions ($V_{\text{nuc-nuc}}$). These terms comprise the overall molecular Hamiltonian which is a

function of electronic ($\boldsymbol{r}$) and nuclear ($\boldsymbol{R}$) coordinates.[25] We can therefore write the time-independent SE as

$$H_{\mathrm{mol}}\Psi(\boldsymbol{r},\boldsymbol{R}) = E\Psi(\boldsymbol{r},\boldsymbol{R}). \tag{1.24}$$

This situation can be simplified by separating nuclear and electronic motion, based on the justification that electronic motion occurs significantly faster due the much lower mass of the electrons compared to the nuclei. This means that electrons respond to any change in nuclear geometry essentially instantaneously and the electronic wavefunction always responds to a stationary nuclear state. The electron-nuclear repulsion ($V_{\mathrm{el-nuc}}$) is thus modified by the nuclear motion only in an adiabatic fashion. The validity and limits of this approach will be discussed later. The overall electronic Hamiltonian (H_{el}) then depends parametrically on the nuclear coordinates, $\boldsymbol{R}$, and the overall molecular wavefunction $\Psi(\boldsymbol{r},\boldsymbol{R})$ can be separated into an electronic and nuclear part.

$$\Psi(\boldsymbol{r},\boldsymbol{R}) = \psi_{\mathrm{el}}(\boldsymbol{r};\boldsymbol{R}) + \psi_{\mathrm{nuc}}(\boldsymbol{R}) \tag{1.25}$$

The motion of electrons in the static field of the nuclei still depends parametrically on the nuclear coordinates and the SE for electrons becomes[25]

$$H_{\mathrm{el}}(\boldsymbol{R})\psi_a(\boldsymbol{r};\boldsymbol{R}) = \epsilon_a(\boldsymbol{R})\psi_a(\boldsymbol{r};\boldsymbol{R}), \tag{1.26}$$

where the index a denotes a specific electronic state. The set of eigenfunctions $\psi_a(\boldsymbol{r};\boldsymbol{R})$ of the electronic Hamiltonian then forms a complete basis in the electronic space at every value of $\boldsymbol{R}$ and fulfils the orthonormality condition:[26]

$$\int \psi_a^*(\boldsymbol{r};\boldsymbol{R})\psi_b(\boldsymbol{r};\boldsymbol{R})d\boldsymbol{r} = \langle\psi_a(\boldsymbol{r};\boldsymbol{R})|\psi_b(\boldsymbol{r};\boldsymbol{R})\rangle = \delta_{ab} \tag{1.27}$$

where δ_{ab} represents the Kronecker delta. This allows the expansion of the total molecular wavefunction in the basis of adiabatic electronic states, the Born-Oppenheimer expansion:[26]

$$\Psi(\boldsymbol{r},\boldsymbol{R}) = \sum_a \psi_a(\boldsymbol{r};\boldsymbol{R})\chi_a(\boldsymbol{R}). \tag{1.28}$$

Here the expansion coefficients $\chi_a(\boldsymbol{R})$ are a function of the nuclear coordinates. Inserting the expansion 1.28 into the molecular SE 1.24, followed by multiplication from the left with $\psi_b^*(\boldsymbol{r};\boldsymbol{R})$ and integration over the electronic coordinates yields expression 1.29 for the expansion coefficients,[25]

$$[T_{\mathrm{nuc}} + \epsilon_b(\boldsymbol{R})]\chi_a(\boldsymbol{R}) - \sum_a \Theta_{ab}\chi_a(\boldsymbol{R}) = E\chi_b(\boldsymbol{R}) \tag{1.29}$$

where Θ_{ab} describes the non-adiabatic couplings, the interaction between electronic and nuclear motion, and is an operator within the nuclear coordinates $\boldsymbol{R}$.

It is given by[25]

$$\Theta_{ab} = \delta_{ab} T_{\text{nuc}} - \langle \psi_b(\boldsymbol{r};\boldsymbol{R}) | T_{\text{nuc}} | \psi_a(\boldsymbol{r};\boldsymbol{R}) \rangle \,. \tag{1.30}$$

Equation 1.29 can be considered the stationary SE for the motion of the nuclei with the respective nuclear wavefunctions represented by $\chi(\boldsymbol{R})$.[25] Using the non-adiabatic coupling term, we can define an effective nuclear potential, $U_a(\boldsymbol{R})$, for a given adiabatic state a.[25] This leads to the familiar potential energy surfaces, solving the electronic Schrödinger equation at a given frozen nuclear configuration, and repeating this calculation over all geometries of interest.[27]

$$U_a(\boldsymbol{R}) = \epsilon_a(\boldsymbol{R}) + V_{\text{nuc-nuc}} + \Theta_{aa} \tag{1.31}$$

The central assumption of the Born-Oppenheimer approximation is to set any non-adiabatic coupling to zero, such that $\Theta_{ab} = 0$. Equation 1.29 then yields the Born-Oppenheimer adiabatic approximation:[26,28]

$$[T_{\text{nuc}} + \epsilon(\boldsymbol{R})]\chi(\boldsymbol{R}) = E\chi(\boldsymbol{R}) \tag{1.32}$$

The limits of validity of this approximation can be assessed by considering the corrections to the adiabatic energies, $\epsilon_a^{(\text{adia})}$, using perturbation theory. The second order energy correction takes the form[25]

$$\epsilon_a^{(2)} = \epsilon_a^{(adia)} + \sum_b \frac{|\langle \chi_a | \Theta_{ab} | \chi_b \rangle|^2}{\epsilon_a^{(\text{adia})} - \epsilon_b^{(\text{adia})}} \tag{1.33}$$

where χ_a represents the Born-Oppenheimer nuclear wavefunction in the adiabatic electronic state a. The denominator of equation 1.33 immediately highlights the dependence on the energy separation between states. The Born-Oppenheimer approximation is valid when the non-adiabatic coupling between two states, Θ_{ab}, is small compared to their energy separation. However, the non-adiabatic effect becomes non-negligible when two adiabatic electronic states converge in energy. In general this approach is well suited to electronic ground states, where the non-adiabatic coupling to higher lying excited states tends to be small due to large energy separations, but there are notable exceptions and non-Born-Oppenheimer dynamics can occur even in ground state reactions.[27] Processes involving the breakdown of the Born-Oppenheimer approximation[29,30] are known as electronically non-adiabatic.[31] These can be classified into cases involving the breakdown of the entire Born-Oppenheimer framework, requiring the equal treatment of electronic and nuclear degrees of freedom;[32] and cases in which the notion of nuclear potential energy surfaces is valid, but electronic dynamics cannot be restricted to a single surface. The later case can be treated within the electronic state approximation (Born-Huang approximation), describing non-adiabatic processes as radiationless transitions between

electronic states.[31] These are of particular importance around intersections of potential energy surfaces. An important case of non-adiabatic process occurring at or near potential energy surface degeneracies is that of conical intersections, leading to ultrafast radiationless transitions between electronic states, which will be discussed in more detail in section 1.2.3.[31,33]

Wavepackets

So far we have primarily considered stationary eigenstates of a system. Experimental reality however differs from this description, particularly in the ultrafast domain where, due to the uncertainty principle, a large spread in energies is observed and systems are prepared in non-stationary superpositions of eigenstates termed wavepackets. Consider the time-dependent form of one such wavepacket, $|\Psi(t)\rangle$. The stationary eigenstates of the system, $|\psi_a\rangle$ with energies E_a, will satisfy the eigenvalue equation

$$H\,|\psi_a\rangle = E_a\,|\psi_a\rangle \tag{1.34}$$

and form a complete basis set. Expanding the time-dependent wavepacket in this basis we obtain;

$$|\Psi(t)\rangle = \sum_a c_a(t)\,|\psi_a\rangle\,. \tag{1.35}$$

The expansion coefficients $c_a(t)$ are now time-dependent and we describe the non-stationary system $|\Psi(t)\rangle$ in terms of stationary eigenstates $|\psi_a\rangle$ with time-dependent coefficients $c_a(t)$.[34] Recalling the time-dependent SE, equation 1.9, and substituting the eigenvalue equation 1.34, we derive an expression for the expansion coefficients $c_a(t)$ based on the state of the system at $t = 0$;[25]

$$c_a(t) = \langle\psi_a|\exp\left(-\frac{iE_a(t-t_0)}{\hbar}\right)|\Psi_0\rangle = c_a(t_0)\exp\left(-\frac{-iE_a(t-t_0)}{\hbar}\right) \tag{1.36}$$

Substituting the expression for $c_a(t)$ into the basis set expansion of the time-dependent state given in equation 1.35 yields a description of the time-dependent wavepacket based on the expansion coefficients at the moment of creation of the wavepacket ($t = t_0$) and the stationary eigenstates of the system, multiplied by a time-dependent phase factor:[25]

$$|\Psi(t)\rangle = \sum_a c_a(t_0)\exp\left(-\frac{iE_a(t-t_0)}{\hbar}\right)|\psi_a\rangle \tag{1.37}$$

Equation 1.37 describes a coherent superposition of oscillatory terms. The oscillation frequencies depend on the energies of the involved eigenstates (E_a), leading to motion of the wavepacket as the areas of constructive and destruc-

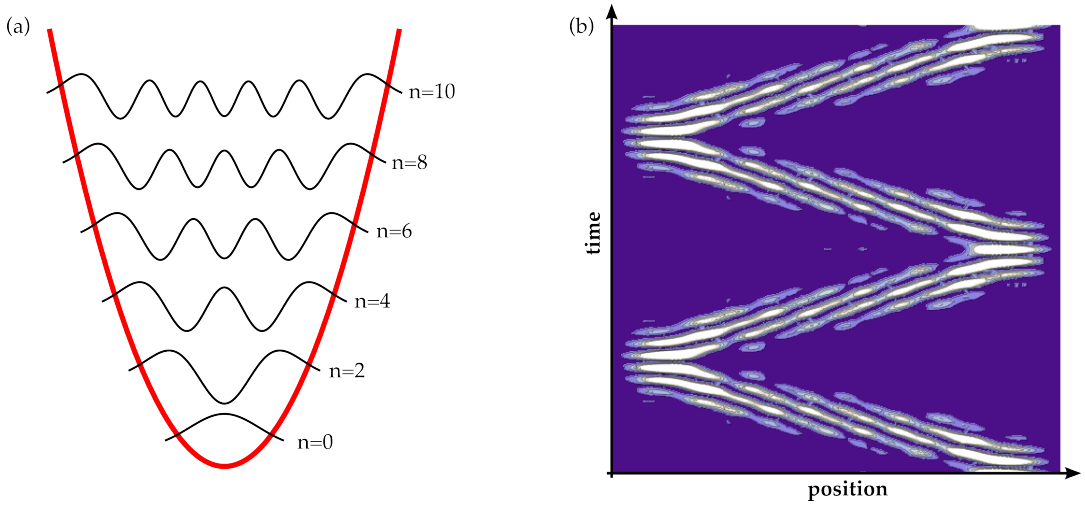

Figure 1.2: (a) Potential of the one dimensional harmonic oscillator (red) showing the even eigenstates (wavefunctions) with principal quantum numbers $n \leq 10$ (b) A wavepacket formed by superposition of the $n = 5 - 10$ eigenstates of the harmonic oscillator will oscillate in space between the inner and outer turning points of the potential. If undisturbed this wavepacket motion will continue indefinitely.

tive interference move in space.[35] Figure 1.2(a) shows the even eigenstates for the one dimensional harmonic oscillator with $n \leq 10$, and shown in 1.2(b) is a wavepacket comprising a superposition of the $n = 5-10$ eigenstates. Plotted is the probability distribution for different points in time, showing the motion of the formed wavepacket between the inner and outer turning points. In an ideal harmonic oscillator this wave packet motion will continue indefinitely, as shown in figure 1.2(b). In real systems dephasing is observed, as the eigenstates comprising the superposition have different phase factors and run out of phase with each other.[21,25] However, the coherence is not lost and rephasing occurs, leading to phenomena such as quantum beats, and this forms the basis of rotational coherence spectroscopy.[36–38]

In systems with high densities of states, such as large polyatomics, it is often appropriate to replace the discrete superposition of equation 1.35 with a continuous superposition, where the initial shape of the wavepacket is given by a function $g(k)$.[21]

$$\Psi(x,t) = \int g(k)\psi_k(x,t)dk \tag{1.38}$$

The shape function $g(k)$ peaks around a value k_0 and describes the width of the superposition by a width factor Γ, such that $g(k)$ goes to zero in the limit of $|k - k_0| \gg \Gamma$. In the case of a Gaussian shaped wavepacket, the shape function takes the form of equation 1.39, where N ensures normalisation.

$$g(k) = N \exp\left(-\frac{(k-k_0)^2}{2\Gamma^2}\right) \tag{1.39}$$

The spatial extend of the wavepacket at time t_0 is then given by[21]

$$G(x) = N \int \exp\left(-\frac{(k-k_0)^2}{2\Gamma^2} + i(k-k_0)x\right) = \exp\left(-\frac{x^2\Gamma^2}{2}\right), \tag{1.40}$$

describing a Gaussian shaped wavepacket centred at $x = 0$ with a width $\sim \frac{1}{\Gamma}$.

1.2.2 Formation of electronic excited states

Electronic excited states of molecules can be formed by absorption of an incident photon, through the interaction between the molecular electronic dipole moment and the incident electric field. Selection rules for allowed electronic transitions in molecules are related to the total angular momentum (Λ) and total spin (S) quantum numbers;[39]

$$\begin{aligned} \Delta\Lambda &= 0, \pm 1 \\ \Delta S &= 0 \end{aligned} \tag{1.41}$$

For a qualitative understanding of this interaction and the resulting excitation, we again consider the large mass difference between nuclei and electrons, analogous to arguments made within the Born-Oppenheimer (BO) approximation. In the context of electronic and associated vibrational transitions this is termed the Franck-Condon (FC) approximation and states that, during an electronic transition, the nuclear framework can be treated as static, such that any electronic transition can be considered vertical.[40–42] This necessitates that the excited state is initially formed in the ground state geometry, potentially with significant vibrational excitation. In a quantum mechanical sense, the transition will occur onto the excited state whose wavefunction most closely resembles the ground state wavefunction, as indicated in Figure 1.3. This requires least change of the wavefunction during a vertical transition and retains the dynamic state of the nuclei introduced by the FC approximation.[19,21,39]

For a quantitative treatment, we consider the transition leading from an inital state ψ_i to a final state ψ_f, caused by the interaction between an incident electric field, $\vec{E}$, and the electric dipole moment of the system, $\vec{\mu}$. The transition dipole moment, denoted $\boldsymbol{d}_\mathbf{if}$, is then given by

$$\boldsymbol{d}_\mathbf{if} = \langle \psi_\mathrm{f}(\boldsymbol{r}, \boldsymbol{R}) | \vec{\mu} \cdot \vec{E} | \psi_\mathrm{i}(\boldsymbol{r}, \boldsymbol{R}) \rangle \,. \tag{1.42}$$

Here the electric dipole moment operator $\vec{\mu}$ contains electronic and nuclear degrees of freedom and the integration is over the entire $\boldsymbol{r}, \boldsymbol{R}$ space. Utilising the Born-Oppenheimer approximation to separate the respective degrees of freedom, the transition dipole moment in electronic coordinates, $\boldsymbol{r}$, becomes a con-

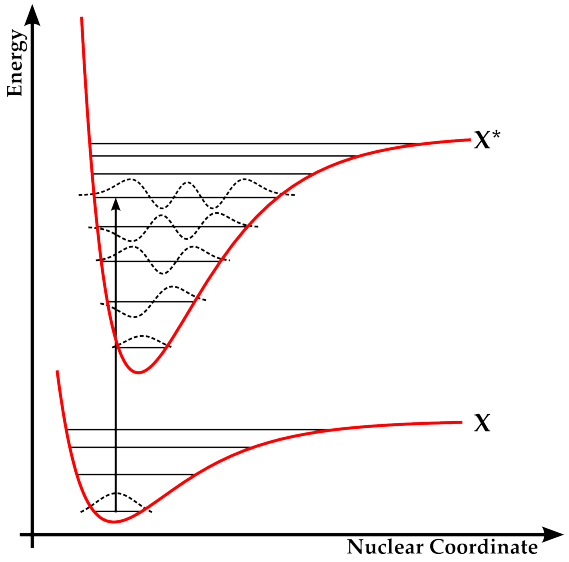

Figure 1.3: Electronic transitions from a ground state, X, to an electronic excited state, X*, can be considered vertical, implying that the nuclear geometry does not change during the excitation. The population transferred into each vibrational level of X* depends on the wavefunction overlap between the initial and final state, the Franck-Condon factor.

stant at a given nuclear configuration and will be denoted $\boldsymbol{d}^e_{\mathbf{if}}$.[19]

$$\boldsymbol{d}^e_{\mathbf{if}} = \langle \psi_\mathrm{f}(\boldsymbol{r}) | \vec{\mu}_\mathrm{e} \cdot \vec{E} | \psi_\mathrm{i}(\boldsymbol{r}) \rangle \tag{1.43}$$

One can now express the overall transition dipole moment as a function of $\boldsymbol{d}^e_{if}$ and the wavefunction overlap between the initial and final states in nuclear coordinates, which is commonly denoted as an overlap integral $S_\mathrm{fi}(\boldsymbol{R})$.[21]

$$\boldsymbol{d}_{\mathbf{if}} = \boldsymbol{d}^e_{\mathbf{if}} \langle \psi_\mathrm{f}(\boldsymbol{R}) | \psi_\mathrm{i}(\boldsymbol{R}) \rangle = \boldsymbol{d}^e_{\mathbf{if}} S_\mathrm{fi}(\boldsymbol{R}) \tag{1.44}$$

The transition probability between an initial state ψ_i and final state ψ_f is then dependent upon the square of the overlap integral, $|S_\mathrm{fi}(\boldsymbol{R})|^2$, this quantity is also termed the Franck-Condon (FC) factor. A non-negligible overlap can exist between an initial state and multiple final states in the electronic excited product, especially for short-pulse, large bandwidth excitation sources. The frequency dependence of the excitation pulse can be included through multiplication of the transition dipole moment with an appropriate shape function describing the frequency envelope of the excitation pulse (as discussed in section 1.2.1).

The rate equation for an electronic excitation therefore depends on $|S_\mathrm{fi}|^2$, as well as on the number of available ground state reactants, N_i, and the incident photon flux, commonly described as a radiation density ρ_rad.

$$\frac{dN_\mathrm{f}}{dt} \propto N_\mathrm{i} \rho_\mathrm{rad} \boldsymbol{d}^e_{\mathbf{if}} |S_\mathrm{fi}|^2 \tag{1.45}$$

The required proportionality constant, along with the overlap intergral, is com-

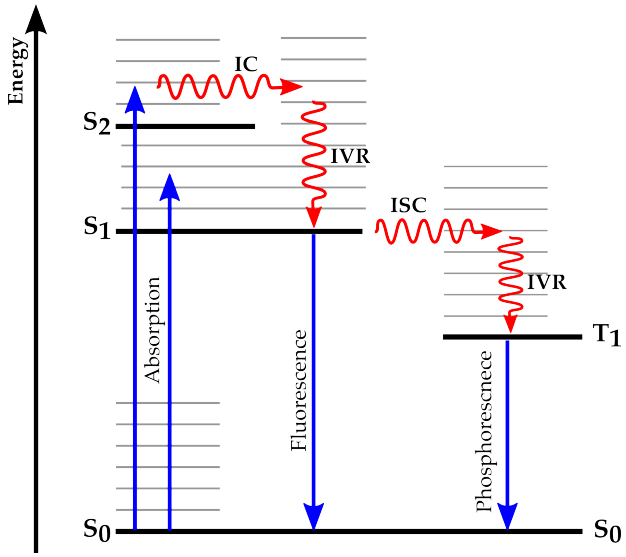

Figure 1.4: Jablonski diagram of radiative and non-radiative processes occuring in isolated molecules. Radiative process are indicated by straight arrows, with up-arrows indicating absorption and down-arrows indicating emission. Non-radiative processes are shown as wavy lines and include Internal Conversion (IC), Intramolecular Vibrational Redistribution (IVR) and Intersystem Crossing (ISC). S denotes singlet electronic states and T denotes triplet electronic configurations.

monly expressed as the Einstein B_{if} coefficient;[19,21,43]

$$\frac{dN_{\mathrm{f}}}{dt} = N_{\mathrm{i}}\rho_{\mathrm{rad}}\frac{\boldsymbol{d}_{\mathbf{if}}^{e}|S_{\mathrm{fi}}|^2}{6\epsilon_0\hbar^2} = N_{\mathrm{i}}\rho_{\mathrm{rad}}B_{\mathrm{if}} \tag{1.46}$$

1.2.3 Excited state relaxation pathways

While all electronic excited states throughout this work are created by optical excitation, as discussed in the previous section, there are numerous pathways through which electronic excited states can relax. These are broadly classed into radiative and non-radiative processes and summarised in a Jablonski diagram, figure 1.4.[44] Radiative processes involve the relaxation from an excited electronic state to a lower lying electronic state (typically the ground state) through the emission of a photon. These are represented by straight arrows in figure 1.4. Non-radiative processes describe the redistribution of energy within the different degrees of freedom of a molecule and are classed as Intramolecular Vibrational Relaxation (IVR), Internal Conversion (IC) and Intersystem Crossing (ISC). These are indicated by zigzag arrows in figure 1.4. Further relaxation pathways not indicated in figure 1.4 are electron loss, either through autodetachment or thermionic emission, and dissociation, the breaking of chemical bonds, leading to two (or more) distinct products.

Radiative relaxation

Both fluorescence and phosphorescence are luminescent transitions that differ only in the total spin conservation during the transitions. A fluorescent transition conserves the total spin, $\Delta S = 0$, whereas during phosphorescence the system undergoes a change in total spin quantum number ($\Delta S \neq 0$).[19] Fluorescence typically occurs from the first singlet excited state, labelled as S_1 in figure 1.4, to the singlet electronic ground state, S_0 (*Kasha's Rule*).[25,45] It is an allowed electronic transition and typical lifetimes are on the order of a few nanoseconds. In contrast, phosphorescence commonly occurs between the T_1 triplet ground state and the singlet ground state and is formally forbidden as it involves a change in total spin quantum number. However, if the electronic selection rules are relaxed, for example in the case of strong spin-orbit interactions, this process can occur. This leads to typical phosphorescence lifetimes being significantly longer than fluorescence lifetimes and can be on the order of microseconds to seconds. Both fluorescence and phosphorescence usually occur from the vibrational ground state of the electronic excited state, as the IVR process (see section 1.2.3) occurs significantly faster than emission of a photon and dissipates vibrational energy into the available bath modes of the surroundings (in a condensed phase environment).[21,46] However, the ground electronic state formed after emission of a photon can have significant vibrational excitation, depending on FC overlaps between the excited and ground state wavefunctions. Fluorescence spectra appear red-shift in comparison with excitation spectra, due to the energy dissipated in the IVR process prior to photon emission, as shown in figure 1.5 for the absorption and emission bands of a Ti:Sapphire laser crystal. While an excitation spectrum probes the vibrational structure of the excited state, a fluorescence spectrum probes the available vibrational states in the ground electronic state and can yield complementary information.

The fraction of excited state molecules that undergo fluorescence, rather than a non-radiative decay, is typically expressed as a quantum yield, Φ_F, defined as the ratio of molecules that fluoresce to the number of photons absorbed. It is related to the relative rates of radiative (k_r) and non-radiative (k_{nr}) decay by[19]

$$\Phi_F = \frac{k_r}{k_r + k_{nr}}. \tag{1.47}$$

Physically, both fluorescence and phosphorescence are types of spontaneous emission. The rate of emission for a spontanous process depends only on the number of emitters in the upper state, N_f, with the proportionality constant for a transition from a "final" upper state f to a lower state i given by the Einstein A

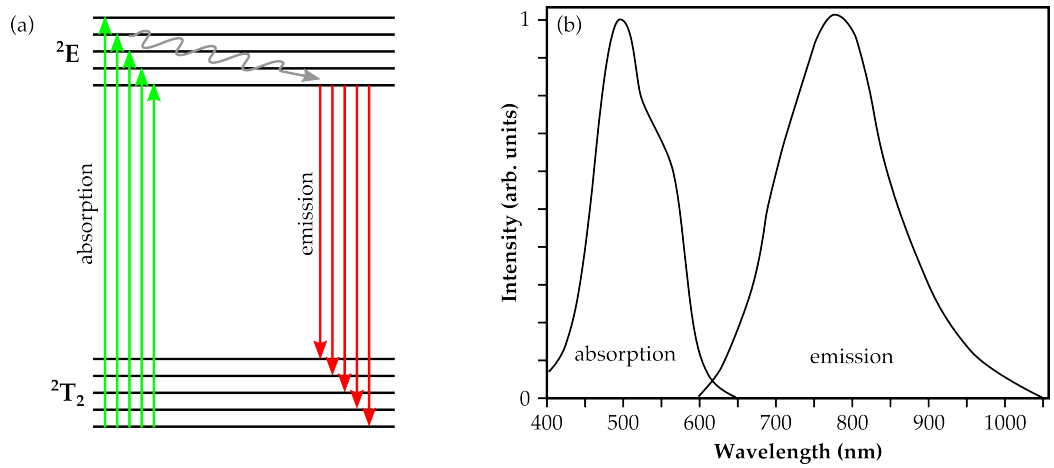

Figure 1.5: (a) Schematic electronic (and vibrational) state diagram for a Ti:Sapphire crystal. Absorption occurs primarily from the vibrational ground state and can terminate into multiple vibrational levels of the upper state. In the upper state fast IVR occurs, such that emission happens from the ground vibrational level into multiple vibrational states of the ground electronic state, followed by IVR to the vibrational ground state. This leads to a typical red-shift of the emission spectrum compared with the absorption spectrum, as shown in (b). Reproduced from [47].

coefficient, A_{fi};[19,21]

$$\frac{dN_{\mathrm{f}}}{dt} = -N_{\mathrm{f}} A_{\mathrm{fi}}. \tag{1.48}$$

A further radiative de-excitation pathway not indicated in figure 1.4 is that of stimulated emission. In this case an incident photon drives a resonant electronic transition in the system, resulting in the emission of a second photon of equal energy and in phase with the incident photon. This process is analogous to the absorption process and its rate depends on the incident photon flux and the number density of excited states and can be described by the Einstein B_{fi} coefficient for a transition from a final upper electronic state f to a lower state i;

$$\frac{dN_{\mathrm{f}}}{dt} = -N_{\mathrm{f}} B_{\mathrm{fi}} \rho_{\mathrm{rad}} \tag{1.49}$$

This is the basis for the operation of a laser, which requires stimulated emission to dominate over spontaneous emission. This can only be achieved through the creation of a non-equilibrium population inversion, that is $N_{\mathrm{f}} > N_{\mathrm{i}}$. The Einstein A and B coefficients are related to each other by[19,21]

$$A_{\mathrm{fi}} = \frac{8\pi h \nu_{\mathrm{fi}}^3}{c^3} B_{\mathrm{fi}} \tag{1.50}$$

Equation 1.50 shows the dominance of spontaneous emission over stimulated emission at higher transition energies, due to the cubic dependence on the transition frequency ν_{fi}, therefore making it increasingly difficult to build laser systems with very high photon energies.

Intramolecular vibrational redistribution

Intramolecular Vibrational Redistribution (IVR) is a non-radiative relaxation process that relocates vibrational energy from a few (or a single) initially excited vibrational modes into other available vibrational modes, with no overall loss of energy.[48] If only a limited number of states are coupled, for example through narrowband excitation in small molecules, IVR is a reversible process and quantum mechanical phenomena, such as quantum beats, can be observed between the coupled states.[34,48] However, in the case of broadband ultrafast excitation of large molecular species, as is the case in our work, IVR can be considered a statistical and irreversible flow of energy from initially excited bright states into bath states of the molecule. For this statistical regime of IVR to be accessible, the density of states needs to be sufficiently high and systems with at least 5 - 10 atoms are needed.[46,49,50] Such a statistical process can then be described by a *Fermi's Golden Rule* approach.[21,25,51,52]

If we consider IVR from a single initially excited state $|0\rangle$ to a large manifold of final states $|\alpha\rangle$, then the rate of IVR, k_{IVR}, will depend on the strength of the inter-state coupling between the initial state and a specific final state. This coupling is given by the anharmonic matrix coupling element, written as $V_{0\alpha}$ and the IVR rate is given to a first approximation by[21,25]

$$k_{\mathrm{IVR}} = \frac{2\pi}{\hbar} \sum_{\alpha} |V_{0\alpha}|^2 \delta(E_0 - E_\alpha), \tag{1.51}$$

where multiplication by the delta function of the individual mode energies ensures overall conservation of energy. Expression 1.51 contains several approximations; (i) as the *golden rule* approach is based on second-order perturbation theory, the coupling strength has to be sufficiently small. This is a reasonable approximation given the large number of bath states the coupling is distributed over, however the coupling has to be much larger than the average level spacing of the bath states. (ii) the quantity E_α is treated as a continuum of states and only those transition are allowed where the initial energy E_0 matches some energy of the final states E_α.[25] This *golden rule* description can easily be extended to IVR from a manifold of initially excited states into a manifold of final states. If the rate of IVR is significantly faster than thermalisation of the initial states takes place, which in the systems considered in our laboratory certainly is the case, then the overall IVR rate is simply given by the sum of all individual rates from every initially excited state.[25]

Equation 1.51 can be further simplified by assuming that the coupling between the initial state and all final states within the manifold $|\alpha\rangle$ is identical, and replace the individual coupling strengths by the root mean square coupling, V_{RMS}. Furthermore, the δ-function can be replaced by the global density of states in

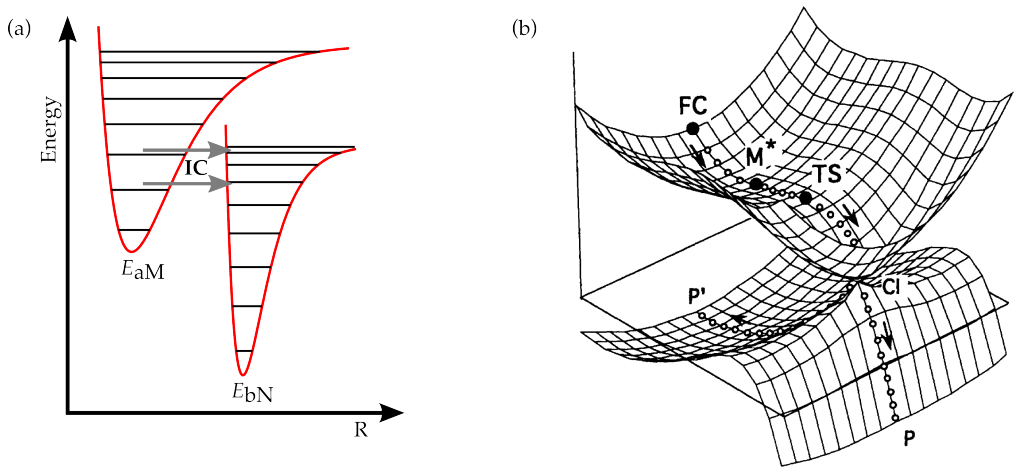

Figure 1.6: (a) Internal Conversion (IC). Population is transferred from a higher lying electronic state to vibrationally excited levels of a lower lying electronic state, conserving overall energy. (b) A conical intersection between potential energy surfaces. Following excitation into the Franck-Condon (FC) region, motion on the excited state leads through a transition state (TS) to the conical intersection (CI) from where two products can be reached. Reproduced by permission of The Royal Society of Chemistry from [53].

the system, $N(E_0)$.[25,46,49] This description has the advantage that both V_{RMS} and $N(E_0)$ are experimentally observable. This basic statistical model predicts a single exponential decay for the population in $|0\rangle$ and is valid for describing the fast initial decay of vibrational energy from $|0\rangle$.[46] However, after some characteristic time the IVR process will become dominated by the local density of states and specific local anharmonic couplings.[25] It should furthermore be noted that resonances in the IVR process, most importantly Fermi resonances between near degenerate vibrational states, can lead to strong mixing of states and therefore influence the observed relaxation pattern.[48,52]

Internal conversion

Internal conversion (IC) is an intramolecular relaxation process that transfers population from an excited electronic state to high vibrational levels of a lower lying electronic state, thereby transforming electronic into vibrational excitation with no overall loss of energy, as shown schematically in Figure 1.6(a). The mechanism facilitating IC is similar to IVR, in so far as a few (or a single) initial state couples to a vibrational manifold of final states. However in IC this is mediated through the electronic-vibrational coupling elements. It is thus an inherently non-adiabatic (non BO) process involving at least two potential energy surfaces.[34,52]

To a first approximation the rate of IC can be evaluated by a *golden rule* approach. For a transition from the vibrational states M of the electronic state a (χ_{aM}), into the vibrational states N of electronic state b (χ_{bN}) we obtain, in analogy to

equation 1.51:[25,34,49]

$$k_{\mathrm{IC}} = \frac{2\pi}{\hbar} \sum_{\mathrm{MN}} |\, \langle \chi_{\mathrm{aM}} | \Theta_{\mathrm{ab}} | \chi_{\mathrm{bN}} \rangle \,|^2 \delta(E_{\mathrm{aM}} - E_{\mathrm{bN}}); \tag{1.52}$$

where Θ_{ab} describes the non-adiabatic coupling between the states. If we consider a constant coupling strength over the range of final vibrational states in b, the expression for the coupling interaction becomes simply the product of a constant with the Franck-Condon overlap for the involved states.[53] IC is often dominated by certain modes with strong couplings, so called *promoting modes*, and is essentially an irreversible process. The coupling strengths between two states, and therefore the IC rate, is inversely proportional to the energy gap between the states,[34,54]

$$k_{\mathrm{IC}} \propto \exp\left(-\frac{\Delta E}{\hbar\omega}\right), \tag{1.53}$$

where ω is the mode frequency. Similar to the IVR process, the density of states in the accepting electronic state is of crucial importance for the rate, and IC is most effective in large (10+ atoms) molecules.[49,52]

A special case arises when the energy gap between the involved states approaches zero and the potential energy surfaces cross, as indicated in Figure 1.6(b). This leads to a complete breakdown of the BO approximation, as is evident from the energy correction introduced by the BO approximation, given in equation 1.33. Therefore a strong coupling between electronic and nuclear modes is observed in the vicinity of surface crossings, which can lead to ultrafast internal conversion. These surface crossings were first considered shortly after the introduction of the BO approximation,[55–57] but long considered unimportant to chemical reactivity. It is only recently that the importance of these crossings, now termed conical intersections, has become apparent.[58–61]

The intersection between two multidimensional energy surfaces does not take the form of a single point, but rather an intersection seam is observed, extending in $N-2$ dimensions, where N is the degrees of freedom in the molecular system. The symmetry point group of the involved electronic states plays a crucial role for the observation of conical intersections. Indeed, intersections are required by symmetry when two electronic states form the components of a single irreducible point group representation.[26] Conical intersections not required by symmetry arguments are termed *accidental* intersections. Two cases are differentiated; for two electronic states of the same symmetry a strict non-crossing rule exists for diatomics, and the surfaces do not intersect, but exhibit an avoided crossing.[55–57,59] While this non-crossing rule was long believed to be valid for polyatomic systems too,[62,63] we now know that no strict non-crossing rule exists

for triatomic or larger systems,[33,64,65] and conical intersections between electronic states of the same symmetry are commonly observed in polyatomic systems.[26,59,66] The second case concerns electronic states of different symmetry, for these no non-crossing rules exists, and the potential energy surfaces can intersect even in the diatomic case.[26] Accidental (non-symmetry required) concial intersections are more likely to be present in large polyatomic molecules, due to the large number of electronic states in close proximity and the many degrees of freedom in these systems.[60]

The presence of a conical intersection between two electronic states can act as a *chemical funnel*, facilitating ultrafast internal conversion from the upper to the lower electronic state.[26,30,34,60] During this transition the excess electronic energy is transferred into vibrational energy of the lower lying electronic state, analogous to internal conversion in a non-crossing situation. Once a system has reached a conical intersection, passage through it can be extremely fast, often within a single vibrational period, and lifetimes of 2 fs have been suggested.[53,67] Motion through a conical intersection always leads to 2 or more product valleys on the lower state, the yield between the different pathways depends on the exact geometry of the potential energy surfaces around the intersections (Figure 1.6(b)).[53] The lifetime of internal conversion processes through conical intersections is often limited by the time the wavepacket takes to reach the intersection seam, and possible barriers on the potential energy surfaces en-route to the intersection. Typical timescales for internal conversion through conical intersections are 10s of femtoseconds,[34,60,66] and we now understand that this mechanism is crucial in many biological processes, such as vision, photosynthesis and biostability.[61]

Intersystem crossing

Intersystem crossing (ISC) is a process analogous to IC, however during ISC the overall spin is not conserved. ISC typically occurs from an excited singlet state to the triplet ground state, as indicated in figure 1.4. ISC is a formally forbidden process, breaking the selection rules for electronic transitions (equation 1.41). In order for ISC to occur, some coupling needs to exist between the singlet and triplet state. This is most commonly provided through the spin-orbit interaction, and therefore particularly pertinent to heavy atoms.

The rate of ISC can again be expressed in a *golden rule* formulation, in analogy with IVR and IC. In this case the coupling interaction hamiltonian is denoted H_{SO} and we label the involved singlet and triplet state as S and T respectively.

$$k_{\mathrm{ISC}} = \frac{2\pi}{\hbar} \sum_{\mathrm{T}} |\, \langle \mathrm{T}|H_{\mathrm{SO}}|\mathrm{S}\rangle \,|^2 \delta(E_{\mathrm{S}} - E_{\mathrm{T}}) \tag{1.54}$$

Once again to a good approximation the coupling H_{SO} between states can be assumed to be independent of nuclear geometry and we can perform a BO separation of variables for equation 1.54. This leads to a rate expression for ISC that depends on the singlet-triplet coupling strength and the square of the vibrational overlap between the states, the Franck-Condon factor.[52] Due to the small spin-orbit coupling, typical lifetimes for ISC processes are on the order of 10 ps to several μs, however there are some notable exceptions to this where ISC occurs on a femtosecond timescale, for example in dye-sensitised solar cells.[68–71]

Autodetachment and thermionic emission

Both autodetachment (AD) and thermionic emission (TE) are processes that dissipate energy through the loss of an electron from the system. This can occur if the energy of the initial excited state is higher than the energy of an available electronic state of the product following electron loss. For example in the case of anions this requires the anion excited state to be higher in energy than a corresponding neutral state, such that electron loss is energetically allowed. Both processes are non-BO and occur through the coupling between the initially excited vibrational levels and the vibrational levels in the final product state.

Autodetachment is the process of electron loss from an excited state in the electronic continuum (i.e. unbound with respect to electron loss) to a final electronic state in the system with one fewer electron (e.g. anion $\rightarrow$ neutral or neutral $\rightarrow$ cation). As the initial state is located in the unbound continuum this process can be extremely fast, depending on the electronic configuration of the involved states. If the final state's electronic configuration is identical to that of the initial state with a single electron removed (the states are Koopmans' correlated, as outlined in the following section), lifetimes as short as 10s of femtosecond are not uncommon. If, on the other hand, a rearrangement of the remaining electrons following the loss of an electron is required, lifetimes can be considerable longer and on the order of picoseconds.[72,73]

Thermionic emission is similar to AD, however the loss of an electron occurs not from an electronic excited state, but rather from highly vibrationally excited levels of the ground electronic state. Such high vibrational levels are typically populated via internal conversion from an excited electronic state, following optical excitation. If the total energy in the initial system is above that of the corresponding system with one electron removed, the very high density of states in the vibrationally excited initial states can couple to vibrational levels of the final state. This is a statistical, Boltzmann-type process and depends strongly on the initially populated vibrational levels (i.e. the temperature) of the system. The ejected electron is lost with a statistical distribution of kinetic energies (*eKE*s),

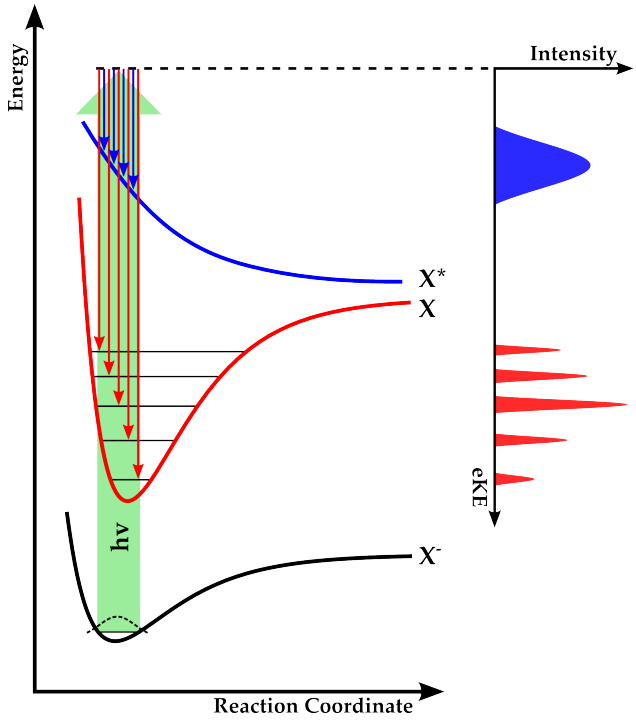

Figure 1.7: Schematic of anion photoelectron spectroscopy (PES). An electronic ground state (denoted X^-) absorbs an incident photon of energy $h\nu$, which promotes an electron to a virtual energy level (dashed line). If this is above the electronic binding energy, a photoelectron is ejected and the system left in one of the accessible neutral states (denoted X and X^*). The intensity of the observed photoelectron bands, indicated on the right, depends on the Franck-Condon overlap between the initial and final state.

which can be described by[74,75]

$$I(eKE) \propto \exp\left(-\frac{eKE}{k_B T}\right). \tag{1.55}$$

This leads to an exponentially falling feature in photoelectron spectra, peaking at threshold ($eKE = 0$ eV) and quickly decaying towards higher energies.[76–78]

1.3 Photoelectron Spectroscopy

Photoelectron spectroscopy (PES) has emerged as one of the most valuable tools for studying electronic spectroscopy and dynamics.[35,48,66,79–85] It is fundamentally based on the photoelectric effect; if light of sufficient energy is incident on a material, electrons will be released from the material.[86] Due to the conservation of energy, if one knows the energy of the incident light ($h\nu$) and measures the kinetic energy of the ejected electrons (eKE), one can infer the internal binding energy of the electrons in the material (BE);

$$BE = h\nu - eKE \tag{1.56}$$

This was developed into a spectroscopic technique in the 1950s and 60s by Siegbahn,[87] Turner[88] and Vilesov[89] and their co-workers, and Kai Siegbahn was

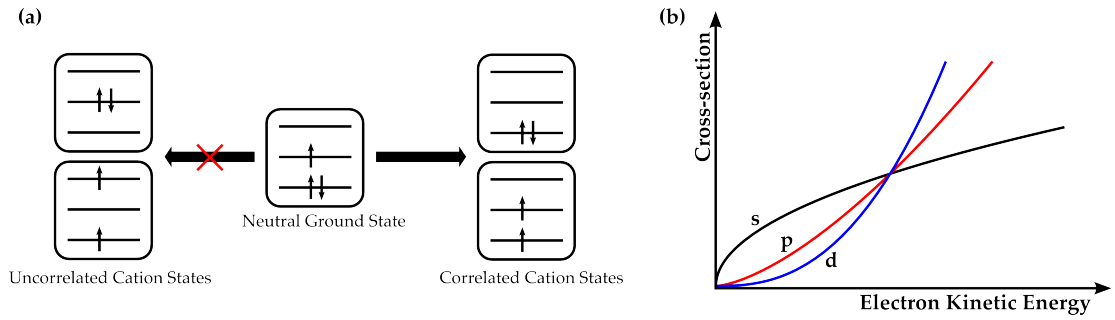

Figure 1.8: (a) Illustration of Koopmans' correlations between energy levels. Only those levels are correlated that can be reached by detachment of a single electron from the inital electronic configuration. (b) Wigner photodetachment cross-section for outgoing photoelectron waves of s,p and d symmetry from an anion. The cross-section below threshold is zero.

awarded the 1981 Nobel Prize in physics for the development of high-resolution electronic spectroscopy. On a molecular level, PES involves the absorption of a photon by a molecule or ion (typically) in the ground state, as shown in figure 1.7. If the absorbed photon is energetic enough to promote an electron into the unbound continuum, the electron leaves the system with a characteristic kinetic energy, and the system is left in the electronic state of a cation (for neutral molecules) or neutral (for anionic parent systems). The observed photoelectron signal depends on the photodetachment cross-section of the parent species. As one is mapping the initial ground state wavefunction onto the available final states, the envelope of observed eKEs depends on the Franck-Condon (FC) overlap between the initial and final vibrational wavefunctions (c.f. section 1.2.2), as indicated in figure 1.7.[80,83]

The use of photoionisation (or photodetachment) as a probe in electronic spectroscopy has several important advantages:[79,80,83,90–94] (i) the detection of charged particles is extremely sensitive and can in most cases be achieved with near-unit efficiency; (ii) ionic species involved (either in parents, products or both) can be detected separately and allow for mass-selected experiments and coincidence experiments and (iii) in general the detachment of an electron is a universally allowed process, as there are no symmetry restrictions on the outgoing photoelectron wave and any neutral, ion or radical can be ionised, such that there are no "dark" states.[92]

While an electron can be detached from any parent state, given sufficient energy, not all electronic final states are equally likely to be populated. One has to take into account the electronic structure of the involved states. Koopmans' theorem[79,95,96] states that the electronic structure formed upon photodetachment is identical to the electronic structure of the parent with a single electron removed, in other words, no electronic reorganisation processes are allowed during the detachment. This arises because electron detachment can be considered a ver-

tical transition (in analogy to the Condon principle, section 1.2.2). Therefore any final product state must be accessible from the initial electronic state via the detachment of a single electron only. This is illustrated in figure 1.8(a); given an initial electronic configuration, some electronic final states might be energetically accessible, but require a concerted 2-electron process to be reached. This is significantly less likely (but not unfeasible as many electronic states contain a certain degree of "mixed" character) and the two states are said to be not Koopmans correlated. Koopmans' correlations can be extremely useful in determining the nature of electronic excited states encountered in time-resolved PES, and an example is discussed in detail in the following section.[79,96–98]

A further consideration is the dependence of the photodetachment cross-section on the available energy above threshold, described in detail by the Wigner threshold laws.[82,99,100] Of particular importance to the current work is the cross-sectional behaviour of anions, which depends on the angular momentum of the outgoing photoelectron wave, l. If the threshold electron detachment energy is given by E_t, the detachment cross section σ within the Wigner laws scales as[100]

$$\sigma \propto (E - E_\mathrm{t})^{l+1/2} = (eKE)^{l+1/2} \tag{1.57}$$

and is zero for energies below threshold, $E \leq E_\mathrm{t}$. This is plotted in figure 1.8(b) for an outgoing electron wave of s,p and d symmetry, corresponding to $l = 0, 1, 2$ respectively. Therefore, the photodetachment cross-section goes to zero at threshold (i.e. at zero eKE); this implies that any intensity observed at zero eKE cannot (to a first approximation) arise from a direct detachment process, but must arise via an indirect pathway, such as thermionic emission.

1.3.1 Time-resolved photoelectron spectroscopy

In order to study the femtosecond electronic dynamics of molecular systems, we turn to Time-Resolved Photoelectron Spectroscopy (TRPES).[35,48,66,79–81,83] This advanced form of PES utilises a two pulse pump-probe scheme. A first laser pulse excites the system of interest into an electronic excited state, creating a non-stationary wavepacket on the excited state. A second laser pulse then probes the state of the system a delay Δt later through photodetachment, thereby projecting the evolving excited state intermediate onto a final state (figure 1.9(a)). By varying the delay Δt between the pump and probe pulses one can map out the temporal evolution of the excited state through changes in the photoelectron spectrum with time, as shown schematically in figure 1.9(b). The time varying signal, $I(\Delta t)$, can be evaluated by considering the projection of the time-dependent excited state wavepacket, $\Psi_\mathrm{Ex}(\Delta t)$, onto a final state ψ_f through the interaction of the electric dipole moment $\vec{\mu}_\mathrm{e}$ with the electric field of the detachment laser, $\vec{E}$;[79,80]

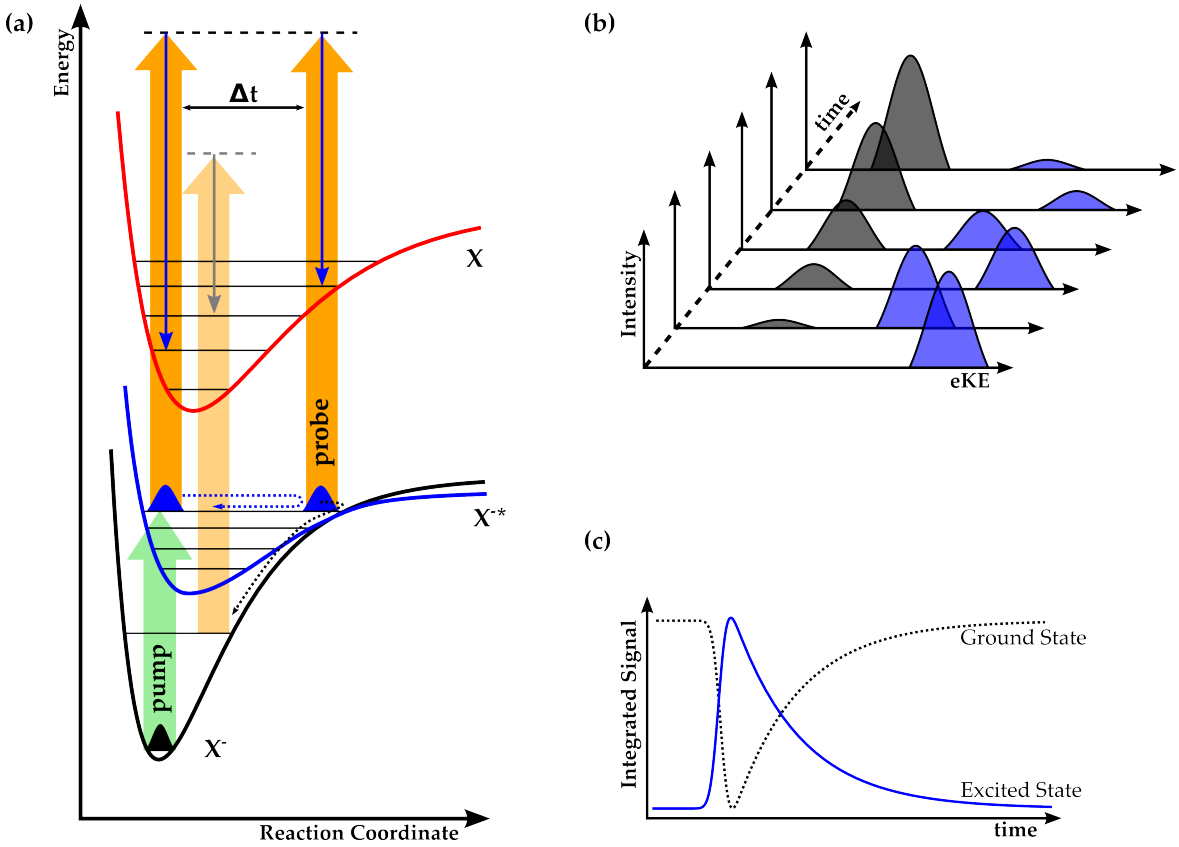

Figure 1.9: Schematic of time-resolved photoelectron spectroscopy. (a) a pump pulse excites a wavepacket on the excited state (blue) which can subsequently evolve on the excited state (blue dotted arrow) or return to the ground state via internal conversion (black dotted arrow). The state of the system is probed by a second laser pulse at varying delays, detaching an electron. Depending on the position of the wavepacket, different electron kinetic energies (downwards arrows) are observed due to different Franck-Condon overlaps. (b) Model photoelectron spectra as a function of time. Wavepacket motion can be observed as a spectral oscillation. The intensity of the excited state signal (blue) decreases in time as population returns to the ground state, which subsequently recovers (black). (c) Integrating the observed photoelectron signals over spectral regions corresponding to the signal from a specific state yields its lifetime.

$$I(\Delta t) = \langle \psi_f | \vec{\mu}_e \cdot \vec{E} | \Psi_{Ex}(\Delta t) \rangle \,, \tag{1.58}$$

where the excited state wavepacket evolves in time according to equation 1.37, introduced in section 1.2.1. For the investigation of isolated gas-phase species, the excess energy injected into the system by the pump laser pulse is not lost, due to the conservation of energy. Rather the FC factors encountered by an evolving wavepacket might shift with the position on the potential energy surfaces, as indicated in figure 1.9(a), leading to an observed spectral oscillation as the wavepacket evolves (1.9(b)). Changes in population in the ground or excited state manifest themselves as differences in the observed total intensity of the signal. This can be analysed by integration of the corresponding spectral slice in the photoelectron spectrum, yielding a measure of the population as a function of pump-probe delay, as shown in figure 1.9(c). From this excited state lifetimes can be extracted.

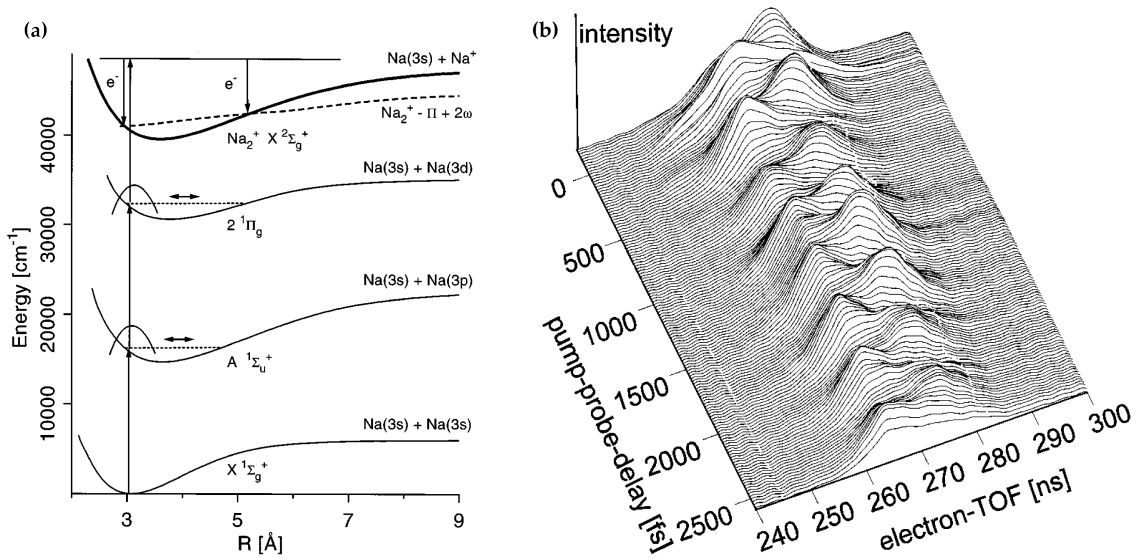

Figure 1.10: Wavepacket motion observed in the Na_2 molecule. (a) Energy level diagram showing the double electronic resonance excited at 618 nm leading to 3-photon ionisation. Wavepacket motion in both the Σ and Π states is observed and oscillations in the *eKE* are apparent due to the changing energy differences between the excited states and the final state along the wavepacket coordinate (indicated by the dashed line). (b) Photoelectron spectra as a function of pump-probe delay. Note that the electron time-of-flight (TOF) is proportional to the electron kinetic energy. Reproduced from [101]. Copyright 1996 by The American Physical Society.

An example for the observation of wavepacket motion in TRPES is provided by the time-resolved experiments on the sodium dimer, Na_2, conducted by Assion *et al.*[101] Here a double resonance leads to 3-photon ionisation at 618 nm, an energy level diagram for this system is shown in figure 1.10(a). The wavepacket motion in both excited states was investigated by introducing a second 618 nm laser pulse, temporally delayed with respect to the first pulse. Following excitation into both the lower lying Σ and the higher lying Π excited state lead to periodic shifts in the *eKE* observed following ionisation with the probe pulse, as shown in figure 1.10(b). This *eKE* shift is due to a difference in energy separation between the excited states and the ionised state between the two turning points of the wavepacket, as indicated by the dashed line in figure 1.10(a). The period of oscillation can be related to the vibrational frequencies of the involved excited states via a Fourier transform of the time integrated photoelectron signal. This example elegantly highlights the ability of TRPES to investigate vibrational dynamics at the femtosecond time scale.

In addition to the observation of wavepacket motion, TRPES is perfectly suited for the study of energy transfer between the different degrees of freedom available in a system, for example from electronic to vibrational energy in an internal conversion processes, or from an initially excited vibrational mode into several modes of the system during IVR. While naturally no energy is lost from the sys-

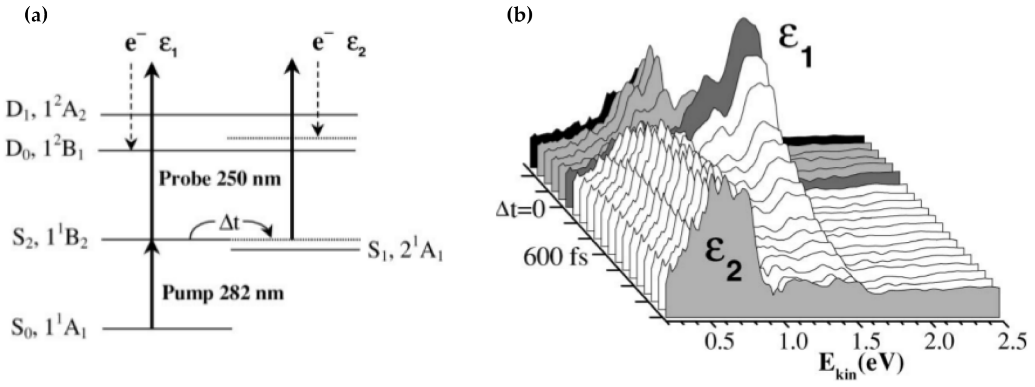

Figure 1.11: Excited state dynamics of phenanthrene. (a) Basic energy level diagram for the pump-probe process. The S_2 state is excited at 282 nm and subsequently undergoes internal conversion to the S_1 state. The two states can be clearly resolved in energy in the photoelectron spectrum in (b) due to the conservation of vibrational excitation (propensity rule), meaning the signature for S_1 population appears at lower electron kinetic energies (E_{kin}). Reproduced from [79] with permission of Annual Reviews.

tem overall, the modes populated in such a fashion might not be "accessible" any more, due to shifting FC factors, leading to observable shifts in the measured *eKE* as the system evolves. This is especially pertinent if the potential energy surfaces of the excited state and the final state are very similar, leading to a propensity rule of $\Delta v \sim 0$, such that vibrational energy is conserved during the photodetachment process and the final state is formed vibrationally excited.[34] An elegant example of this behaviour is observed for excited state dynamics of the phenanthrene S_2 state.[79,98] A basic energy level diagram for the involved processes is shown in figure 1.11(a). Following excitation at 282 nm the S_2 state can undergo IC to the S_1 state, located 0.75 eV lower in energy. The S_1 is thus created with 0.75 eV of vibrational energy. Probing this system at various delays Δt later with a 250 nm probe pulse however shows a clear energy separation between the signatures of the S_2 and S_1 states, as shown in figure 1.11(b). As the overall energy within the system must be identical before and after the IC event, this energetic shift arises from the formation of a vibrationally excited (or "hot") final state (in this case the D_0 cation state), allowing the clear identification of different electronic states in the photoelectron spectrum.

In certain cases favourable Koopmans' correlations will allow the clear identification of the involved electronic states. This is the case if different electronic states that are probed correlate with different final states, leading to clearly distinct features in the photoelectron spectrum. A classic example of this behaviour are the excited state dynamics in *all trans* 2,4,6,8-decatetraene.[79,96,97] Following optical excitation into the S_2 excited state at 287 nm, this system undergoes ultrafast IC to form vibrationally excited S_1 state population, similar to the dynamics observed in phenanthrene. This is shown schematically in figure 1.12(a). However in this case the S_2 and S_1 excited states are of different symmetry and Koopmans

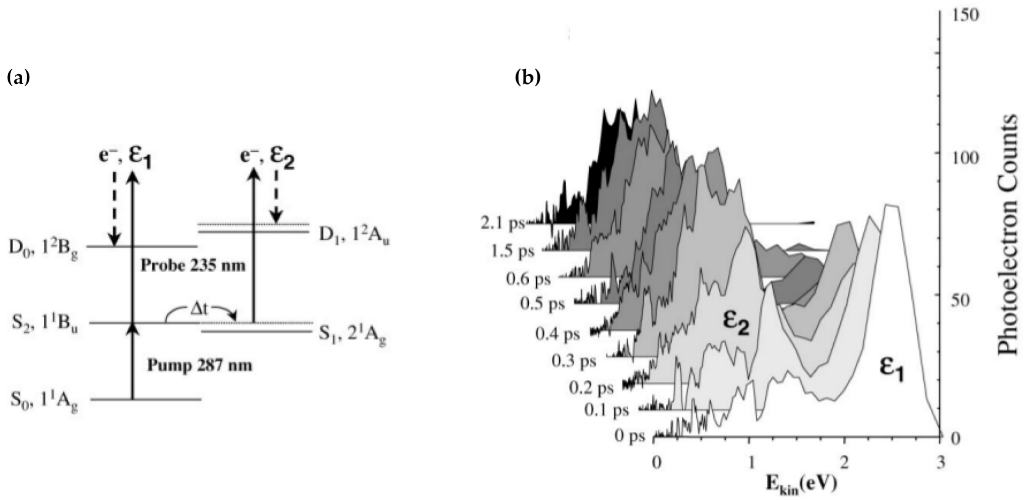

Figure 1.12: Excited state dynamics of *all trans* 2,4,6,8-decatetraene. (a) Basic energy level diagram for the pump-probe process. The S_2 state is excited at 287 nm and subsequently undergoes internal conversion to the S_1 state. Due to differing electronic configurations in the two excited states, they correlate with different final states in the cation, meaning the signature for S_1 population appears at lower electron kinetic energies (E_{kin}) in the photoelectron spectra in (b). Reproduced from [79] with permission of Annual Reviews.

correlate with different final cation states; the S_2 will primarily photodetach to form the D_0 state, while the S_1 will primarily form the D_1 cation state. As these states are separated in energy, the resulting features in the photoelectron spectrum will appear clearly spectrally separated (figure 1.12(b)), despite the total amount of internal energy within the system remaining unchanged throughout the dynamics. In this favourable "corresponding correlations" Koopmans case, one is essentially measuring differing binding energies for the two features, due to the different final states, leading to distinct *eKE*s.

1.3.2 Photoelectron angular distributions

A further dimension of information routinely extracted from photoelectron spectroscopic experiments are the Photoelectron Angular Distributions (PADs), that is the spatial dependence of the probability of electron ejection from the system relative to the direction of the electric field vector of the (linearly polarised) detachment laser. While the first studies of angular distributions of photoelectrons following ionisation from atomic systems were made over 80 years ago,[102] PADs have long been treated primarily as a source of confirmatory or complementary information.[103–105] This view has changed radically over the past decade, with the advent of ultrafast laser sources and the widespread availability of photoelectron imaging techniques (see chapter 2 for a detailed description of our photoelectron imaging setup), and PADs and time-resolved PADs are now a very active area of research.[35,81,82,84,105–109]

The nature of observed PADs is determined by the interference of outgoing pho-

toelectron waves, and the general expression for PADs is given by symmetry arguments and can be expressed in terms of spherical harmonics ($Y_{LM}(\theta,\phi)$.[105,110] We obtain the following expression for the angular dependence of the total photoelectron signal:

$$I(\theta,\phi) \propto \sum_{L=0}^{L_{\max}} \sum_{M=-L}^{L} B_{LM} Y_{LM}(\theta,\phi), \tag{1.59}$$

where L is related to the angular momentum quantum number and, in the case of an isotropically distributed sample in space, equal to $2n$, where n is the number of photons involved in the detachment process; and M, related to the angular momentum projection quantum number, runs from $-L_{\max} \leq M \leq L_{\max}$. In this expression the individual components B_{LM} contain information about the contribution of each individual photoelectron partial wave and its interference with each other partial wave, which depend upon the photoionisation dynamics, the geometry of the system, the orbital from which the photoelectron originated and the spatial distribution of the system.[105,109] This expression is significantly simplified within the dipole approximation, limiting the considered values of L to $l-1$ and $l+1$, where l is the angular momentum of the orbital from which the photoelectron is ejected.[84,105] The use of linearly polarised light, leading to cylindrical symmetry in the system, furthermore restricts to $\Delta M = 0$.[35] For polyatomic molecular systems, where l is no longer a good quantum number, the PAD depends on the symmetry of the ejecting orbital. This relationship can be expressed in terms of the molecular symmetry groups and, in the case of a molecular anion, requires that the symmetry product ($\otimes$) of the prepared excited state symmetry (Γ_{ex}), the dipole moment operator (Γ_{μ}), the remaining final state (Γ_{f}) and the outgoing photoelectron wave (Γ_{e^-}) must contain the totally symmetric irreducible representation of the molecular symmetry point group (Γ_{TS});[80,84]

$$\Gamma_{\mathrm{ex}} \otimes \Gamma_{\mu} \otimes \Gamma_{\mathrm{f}} \otimes \Gamma_{e^-} \supseteq \Gamma_{\mathrm{TS}}. \tag{1.60}$$

Therefore a dynamic process leading to a change in symmetry of the remaining neutral necessitates a change in the symmetry of the outgoing photoelectron wave and PADs can be used to probe non-adiabatic processes, yielding complimentary information to photoelectron spectra.[35,80]

For the case of photodetachment with a specified number of photons, n, of linearly polarised light from a sample distributed isotropically in space, the analytical description of the observed PADs can be substantially simplified, and is

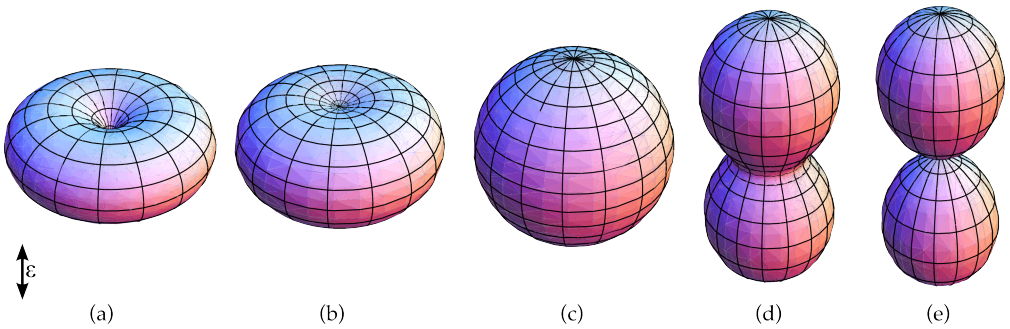

Figure 1.13: Calculated photoelectron angular distributions for a single photon detachment process, with the laser polarisation ϵ as indicated, defining the axis of cylindrical symmetry. β_2 parameters shown are $-1, -0.5, 0, 1, 2$ for (a)-(e), respectively.

given by the Cooper and Zare formalism;[35,111]

$$I(\theta) = \sum_{L=0}^{2n} \beta_L P_L(\cos\theta). \tag{1.61}$$

Here the number of photons absorbed is given by n and $P_L(\cos\theta)$ describes the L^{th}-order Legendre polynomial around $\cos\theta$. The constant β_0 corresponds to the total integrated photodetachment cross-section across the entire 4π solid angle, and subsequent β_L parameters are termed *anisotropy parameters* and describe the spatial distribution of photoelectrons with respect to the laser polarisation axis. For the simplest case of 1-photon direct detachment, only the β_2 anisotropy parameter is needed to describe the obtained distribution. This parameter takes values between $-1 \leq \beta_2 \leq 2$, with negative values describing primarily perpendicular emission of electrons and positive values a primarily parallel emission of electrons with respect to the polarisation of the detachment laser, as indicated in figure 1.13. An example of a photoelectron image showing a high degree of anisotropy is shown in figure 1.14, along with the photoelectron spectrum and angle resolved photoelectron signal extracted from the image. This was obtained for the one-photon detachment from iodide (I^-) at 4.66 eV (267 nm). Two distinct features are observed, corresponding to the formation of iodine in one of two spin-orbit split states.[112] The relative intensity of the peaks is determined by the total photodetachment cross-section, taking into account the degeneracy of the involved states. The observed anisotropies for this image are $\beta_2 = -0.46$ for the $^2P_{1/2}$ state and $\beta_2 = -0.49$ for the $^2P_{3/2}$, corresponding to photoelectrons being ejected primarily perpendicular to the laser polarisation, as is evident from the photoelectron image.

The theoretical calculation of PADs obtained from a molecular system is non-trivial in all but the simplest cases, where the molecular orbitals can be likened to atomic orbitals.[113–115] One needs to consider the spatial orientation of the molecule in the molecular frame, how outgoing photoelectron waves interfere,

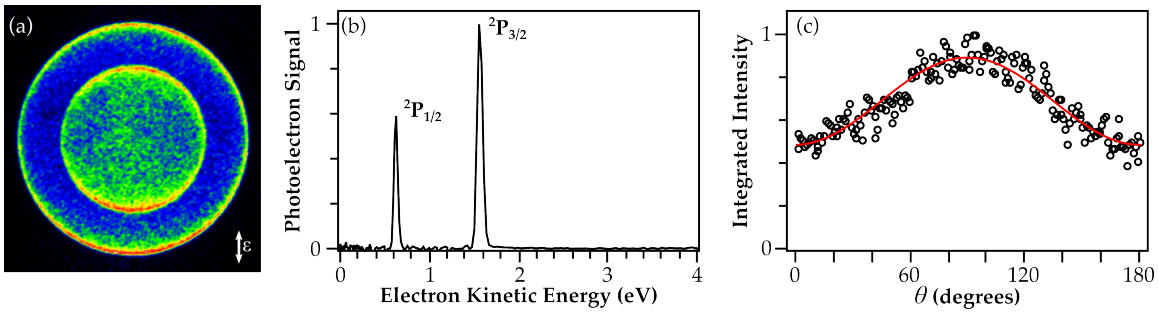

Figure 1.14: Electron detachment from I^- yields highly anisotropic photoelectron images, as shown in (a). The two observed rings correspond to two spectral features, due to the $^2P_{3/2}$ and $^2P_{1/2}$ spin orbit states of iodide, as indicated in the photoelectron spectrum in (b). Radial integration of the spectral peaks around the emission angle θ yields the angular distributions, as shown in (c) for the $^2P_{1/2}$ feature. Measured β_2 parameters for the shown image are $\beta_2 = -0.49$ for the $^2P_{1/2}$ and $\beta_2 = -0.46$ for the $^2P_{3/2}$ state.

and how this manifests itself in the observable distribution in the laboratory frame. A basic qualitative model has been developed in the group of Sanov, named the *s&p model*, which is applicable to polyatomics where electrons are emitted at low *eKE* (typically up to a few eV), and aims to give a qualitative prediction of the observable PADs by considering three principal orientations of the molecule in space and considering the allowed symmetries of the outgoing photoelectron in each of the principal orientations.[82,84,116] However the quantitative prediction of molecular PADs remains a formidable theoretical challenge and is beyond the scope of this introduction.[35,109,117–119] Recently a lot of work in the area of molecular frame PADs has been reported, aiming to directly record PADs from fixed-in-space molecules, thereby reducing the spatial averaging and obtaining direct spatial information about the involved molecular orbitals.[35,109,120–126]

1.4 Applications to Anionic Systems

This section aims to give a brief overview of current work done on photoelectron spectroscopy (PES) and time-resolved photoelectron spectroscopy (TRPES) of anions. It will focus exclusively on experimental studies of polyatomic anions or cluster anions, and the reader is referred to recent reviews for studies of atomic anions[100] or theoretical investigations.[127,128] Examples are broadly classed by type of anionic system investigated, starting with molecular anions, followed by studies of cluster systems and solvation and finally polyanions (multiply-charged anions). The overview given here will focus on recent studies in the areas of anion PES and TRPES, for older examples and investigations the reader is referred to earlier reviews.[66,79–85]

PES of anions was pioneered by Carl Lineberger and co-workers[129] and has

now been adopted in laboratories around the world for the study of atomic and molecular anions, polyanions and clusters. Until the late 1990s experimental setups used only molecular beam sources, with anionic samples produced via electron attachment with an electron gun or directly through laser ablation. While this is a very effective method of generating small molecular anions or anionic clusters, it does not allow for the production of large molecular anions, such as those of biological interest, or the production of polyanions. For these fragile systems a soft ionisation technique is needed to produce stable species in the gas-phase. The group of Lai-Shang Wang were the first to successfully couple a soft ionisation source, in this case electrospray ionisation (ESI), to a photoelectron spectrometer.[130] This allows for the detailed investigation of many systems of interest to biology, such as fluorescent proteins or oligonucleotides. Consequently, machines that couple ESI with PES or TRPES are now in use in several laboratories.[131–135]

1.4.1 Molecular systems

Photoelectron spectroscopy (PES) is a versatile tool to investigate the energetics and dynamics (in its time-resolved variant, TRPES) of anionic molecular systems. A brief overview of recent studies is given here, details of older studies, as well as experimental details, can be found in recent reviews of photoelectron spectroscopy[82,84,127,136] and time-resolved photoelectron spectroscopy[35,66,79–81] and references therein.

Non-time resolved PES studies on anions, offering higher spectral resolution than the time-resolved variant, are being undertaken in several groups. Numerous recent PES studies of molecular anions have focussed on investigating small organic anions, and in particular radical anions, important intermediates in organic and biological reactions. Sanov and co-workers have recently studied the tetracyanoethylene,[137] thiophenyl and furanyl,[138] dicyanocarbene[139] and oxyallyl[140,141] radical anions using their photoelectron imaging apparatus, while the Neumark group investigated phenoxide and thiophenoxide,[142] as well as several vinoxide anions[143–145] using slow-electron velocity map imaging (SEVI),[146,147] allowing for greater spectral resolution at the expense of spectral range that can be investigated in a single experiment. Radicals were also investigated in the Lineberger group, focussing on Carbene,[148] peroxyformate,[149] furanide,[150] anilidine[151] and azine species.[152] A joint study, utilising conventional PES and SEVI techniques, was conducted on propadienylidene.[153] Larger organic systems, such as carboranes,[154] hydroxyphenoxyl[155] and benzoquinone[156] radical anions were investigated in the groups of Xue-Bin Wang and Lai-Shang Wang, both utilising an ESI source for the production of anions. The former group furthermore has the ability to cool anion samples to 20 K in an ion trap, leading

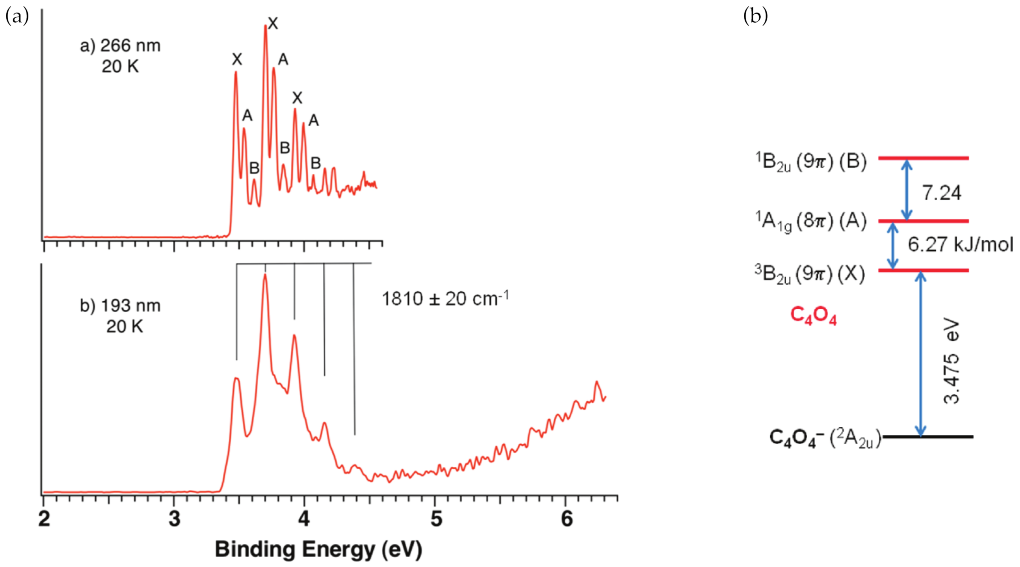

Figure 1.15: Low temperature photoelectron spectroscopy of the Cyclobutanetetraone radical anion. (a) Spectra collected at 266 nm (4.661 eV) and 193 nm (6.424 eV), the latter shows an equally spaced vibrational progression, which is further split into electronic states in the higher resolution spectrum at 266 nm. (b) Spectral assignment and summary of numerical results. Reprinted with permission from [157]. Copyright 2012 American Chemical Society.

to high-resolution PES.[131] An elegant example of this is their recent work on the radical anion of cyclobutanetetraone (C_4O_4), shown in figure 1.15.[157] Due to the increased resolution and supression of hot bands, the electronic ground state of the radical anion, as well as the ground and two low lying electronic excited states of the neutral (labelled X, A and B respectively) have been identified and assigned. The authors were able to determine the electron affinity as 3.475 ± 0.005 eV, as well as the energetic spacing between excited states, providing an excellent benchmark for electronic structure calculations.

Further studies of small molecular anions have concentrated on halogenated organic systems,[158–161] primarily investigating photodissociation and branching ratios between reaction channels, oxides and sulfites of Carbon[162,163] or rare gases[164–166] and compounds with a central heavy or transition metal.[167,168] The high resolution offered by PES furthermore allows the elucidation of structural isomers, based on comparison with high level theoretical calculations,[128] for example the investigations of carbon chains in the Neumark group, which can form linear, bend or cyclic isomers that can be seperated by energetics and vibrational frequencies.[163,169–172]

PES is increasingly used for the study of biologically relevant anions, especially with the utilisation of ESI sources allowing the study of larger species. The group of Kit Bowen have studied several DNA bases and pre-cursors,[173–175] and Dugourd and co-workers have recently reported an investigation of the tryptophan anion.[176] They observe a large bathochromic red-shift, explained by the

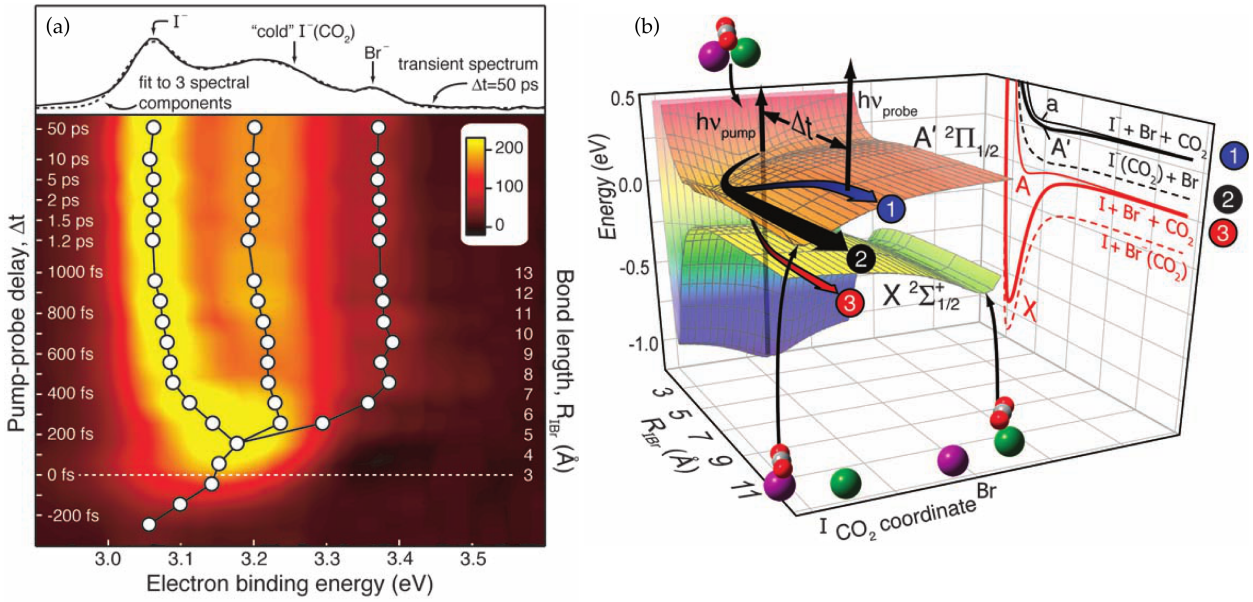

Figure 1.16: (a) Time-resolved photoelectron spectra of $IBr^-(CO_2)$. The top panel shows a transient spectrum at 50 ps pump-probe delay, and assigns the spectral components to their respective detachment channels. The false colour plot shows the measured electron binding energy as a function of pump-probe delay, with white circles indicating the centre of the spectral components. The appearance of Br^- is clearly observed 350 fs after excitation. (b) Overview of the potential energy surfaces involved in photodissociation of $IBr^-(CO_2)$, with product channels labelled 1,2 and 3. Solid curves represent calculated electronic states in isolated IBr^-, with dotted curves showing the minimum energy paths taken along the two dimensional X and A′ surfaces in the presence of carbon dioxide. From [179]. Reprinted with permission from AAAS.

energetic shift of the π and π^* levels due to the nearby negative charge. The study of biological anions in the gas-phase is becoming increasingly important, with the study of entire proteins in the gas-phase now a possibility.[177,178] The majority of large peptides or proteins contain multiple charges, and these will be reviewed in section 1.4.3.

TRPES of anionic systems was pioneered in the group of Dan Neumark and has in recent years primarily been applied to cluster systems, reviewed in the following sections, due to the ease of mass selection, allowing the detailed study of the dependence of molecular properties on cluster size.[83] Recent dynamics studies on molecular anions include the investigation of the 7,7,8,8-tetracyanoquinodimethane radical anion by the Verlet group,[132,180] who investigated the excited state relaxation pathways in this important electron acceptor. Lineberger and co-workers studied the dissociation dynamics and pathways in IBr^- and the $IBr^-(CO_2)$ complex.[179,181] They were able to show that isolated iodine monobromide yields exclusively $I^- + Br$ products, however the addition of a single carbon dioxide opens a new dissociation channel, leading to the production of Br^-, as shown in figure 1.16(a). They elucidate the responsible mechanism using molecular dynamics simulations and find that an electron transfer occurs 350 fs after the initial dissociation event, from I^- to the Br atom. This

charge transfer is mediated by the CO_2, whose interaction with the outgoing I^- minimises the energy separation between the potential energy surfaces corresponding to the two product channels and populates the otherwise inaccessible pathway leading to the formation of Br^-, figure 1.16(b).[179]

1.4.2 Anionic clusters

As in the previous section, only a brief overview of current areas of interest is given here, but several recent reviews are available for further reading.[83,136,182,183] The advantage of using charged clusters is the ease with which they can be separated by mass, allowing precise determination of the number of atoms or molecules that constitute the cluster. Studies have broadly centred on four areas of interest; the study of metal clusters, carbon clusters (fullerenes), transition metal oxide or hydrite clusters, and models of solvation, where a central moiety is surrounded by a well defined number of solvent molecules.

The study of metal clusters primarily investigates the geometric properties and isomers of limited size molecular aggregates, as well as their electronic structure and the intermediate region between individual quantised energy levels and the bulk like band structure of metals. Of interest is furthermore the coupling between electronic and vibrational (or phonon) modes, leading to vibrational autodetachment or thermionic emission from clusters. One of the most studied system is gold clusters, most notably in the group of Lai-Sheng Wang.[184–193] This is an interesting system as nanoparticles of gold are catalytically very active, whereas bulk gold surfaces are considered inert. Anion PES on gold clusters allows the study of the electronic properties as a function of cluster size, as well as elucidating the geometric structures of finite size gold clusters, such as the tetrahedral Au_{20}^-,[194] or the cage-like structure of Au_{16}^- and Au_{17}^-.[195] Other metal clusters of interest are Mercury,[196–198] Silver[199,200] and Lead,[201] the latter was investigated with a next generation light source, the free-electron laser FLASH in Hamburg.

The study of large carbon cluster (fullerene) anions was one of the first systems studied when ESI sources became available for use with PES.[202] TRPES followed shortly after, with the investigation of relaxation dynamics in C_{60}^- following excitation into the vibrationally hot $B(^2E_g)$ state. These were investigated in the group of Kappes and found to proceed on a 2.2 ps timescale via intramolecular radiationless transitions into the anionic ground state.[203] Subsequent studies have been conducted on larger fullerenes,[204] oxygen linked fullerene dimers[205] and fluoro-fullerenes.[206] Similar structures to carbon clusters were found to exist in anionic clusters of Boron (or metal borides), extensively studied by the group of Lai-Sheng Wang.[207–214] These systems are of interest not only due to their

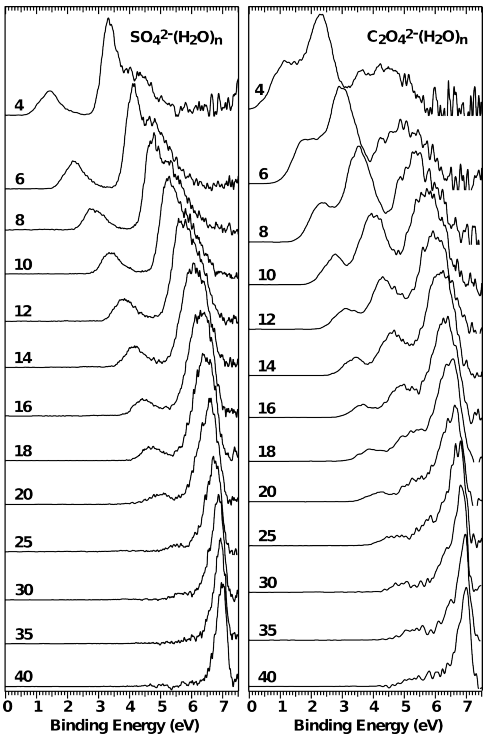

Figure 1.17: Photoelectron spectra for water clusters containing a single SO_4^{2-} (left) or $C_2O_4^{2-}$ (right) anion surrounded by n water molecules. The low binding energy peak, corresponding to detachment from the solute, decreases with increasing cluster size once the cluster is larger than $\sim$12 molecules. Concomitantly a peak due to electron detachment from the cluster appears on the high energy side, increasing in intensity as n increases. From [228]. Reprinted with permission from AAAS.

structural similarities to carbon clusters, but also due to the unusual and highly delocalised bonds formed by electron deficient boron.

A further area of active research in cluster science is the investigation of transition metal oxide clusters. These are model systems for catalytic surfaces widely used throughout chemistry and allow the detailed study of the energetics and geometry of the underlying systems. Gas-phase investigations furthermore allow one to control the stoichiometry of the clusters, systematically controlling the oxygen content.[215–226] An elegant example of the type of information that can be gained from transition metal clusters is the recent study of $AlMoO_y^-$ by Waller *et al*.[227] The authors find an ionic bonding character between Al^+ and singly or double charged molybdenum oxide subunits, explaining the relative strengths of the Mo=O bond compared to the Al=O bonds. This leads to the most accessible electrons in the system localised on the Mo, despite the formally higher oxidation state of the molybdenum compared to the aluminium.

One of the key motivations of cluster studies is to understand the effect of solvation by systematically introducing solvent molecules around a central species.[83] A model case here is the solvation around halogen anions, where recent studies have been undertaken by the groups of Mabbs[229–233] and Neumark.[234–237] The

use of a halogen anion not only allows one to study the arrangement of solvent molecules around a negative charge, but through a charge-transfer-to-solvent transition the electron can furthermore be transferred to the solvent cluster. Several recent reviews are available in this very active field of research,[238–240] and the development of liquid jet photoelectron spectroscopy[241] and surface sensitive probing techniques[242] now allows the direct comparison of bulk data with cluster data, and one can begin to understand how much solvent is required to establish bulk-like properties. These phenomena can also directly be studied through the formation of negatively charged solvent-only clusters, allowing the solvation of an excess electron to be investigated as a function of solvent properties and cluster size.[243–246]

Solvation studies in clusters have also concentrated on understanding the effect of a solvent cage around a central molecular anion, the geometry of the first solvation shell and the degree of solvation needed to establish bulk properties.[247–251] The introduction of a solvation shell can also lead to the observation of anions otherwise unstable in the gas-phase, such as SO_4^{2-}.[252] An excellent example of the transition from gas-phase properties to bulk properties is the work by the Wang group on solvated sulfate and oxalate anions, shown in figure 1.17.[228] For both systems the PES in small clusters resembles that of the lone solute. However, as the number of solvent molecules is increased, the detachment channel from the solute not only shifts towards higher binding energies (as predicted by theoretical calculations), but also decreases in intensity, most notable above $\sim$12 solvent molecules, and completely disappears in clusters with $n > 30$. Concomitantly, a new feature emerges in the PES on the high binding energy side as the cluster size is increased. This corresponds to electron detachment from the solvent only, increasing in detachment cross-section as the cluster size is increased. Therefore this study nicely shows the transition from gas-phase solute behaviour, to bulk-like solvent behaviour.

1.4.3 Polyanions

The study of polyanions, commonly also called multiply-charged anions, was made possible through the use of electrospray ionisation in combination with PES.[130] A number of unusual electronic properties arise in isolated polyanions, due to the close proximity of multiple charges. This introduces an inherent instability, and small highly charged anions, often ubiquitous in nature such as SO_4^{2-}, are not experimentally observed in the gas-phase.[253] At the same time, the balance between electron-electron repulsion and nuclear-electron attraction leads to a barrier to electron detachment from a polyanion, termed the Repulsive Coulomb Barrier (RCB).[254,255] This implies that in order to detach an elec-

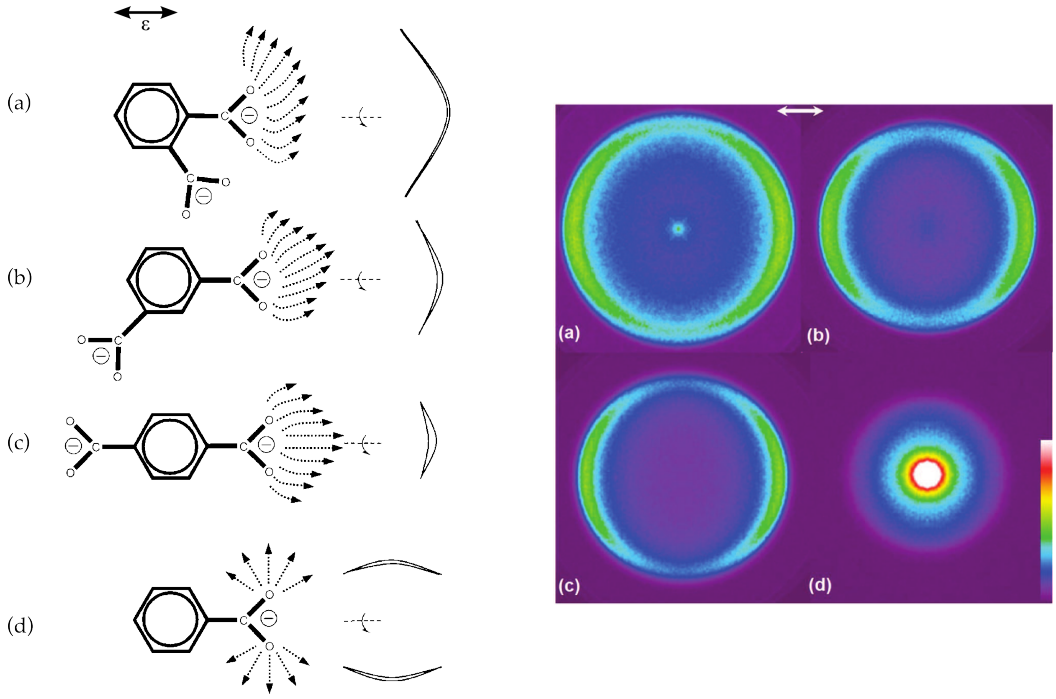

Figure 1.18: Effect of negative charges on observed photoelectron angular distributions (PADs). The repulsive force experienced by an outgoing electron depends on the conformer of $C_6H_4(CO_2)_2^{2-}$ studied (*o*, *m* or *p* as shown in (a)-(c) respectively), leading to different PADs that can be predicted qualitatively. The singly charged case is shown in (d) for comparison. The laser polarisation, defining the axis of cylindrical symmetry is indicated at the top. On the right are the experimentally observed photoelectron images, matching qualitative predictions. Reprinted with permission from [258]. Copyright 2009 American Chemical Society.

tron form a polyanion, sufficient energy must be available not just to overcome the inherent binding energy, but also to reach over the RCB. A more detailed description, and several of our own studies probing the inherent properties of the RCB, can be found in Chapter 4. There are also several recent reviews available.[85,256,257]

Early studies of polyanions primarily researched the RCB and the unusual properties that follow from it, such as the observation of negative electron binding energies[253,259,260] or the electronic stability it imparts on multiply-charged systems.[261] More recently, utilising photoelectron imaging methodologies, the effect of the RCB on the trajectories of outgoing photoelectrons has become an active field of research.[258,262–264] Our own contributions to this field to date are described in detail in Chapter 4.[265,266] When an electron is detached from a polyanion, the trajectory of the outgoing electron is dominated by the long-range Coulomb interaction with the remaining charge. This can lead to profound changes in the photoelectron angular distributions, which now depend on the location of excess charges on the molecular framework, and how these charges interact with a parting electron. An early demonstration of this effect were the proof-of-principle experiments by the Wang group on different struc-

tural isomers of benzene dicarboxylate dianions, and the observed PADs following photodetachment.[258] In these studies the relative location of the excess charge on the remaining anion, systematically varied through the use of *o*-, *m*- and *p*-isomers, was shown to influence the observed anisotropy (figure 1.18). This was interpreted qualitatively based on the repulsion between charges and their relative locations on the molecule. In order for this inherently molecular frame effect to be observable in the laboratory frame, the two need to be linked together. In these studies this link is provided by the non-isotropic photodetachment cross-section, which peaks along the benzene carboxylate bond. In order for this effect to be observable in all generality, alignment of the polyanions is necessary.[265] If this connection is established however, the measured PADs carry information about the relative location of excess charges on the molecular framework, and thus contain structural information that can, in principle, be probed with femtosecond resolution.

Use of electrospray ionisation furthermore allows the introduction of large anionic species, such as proteins or peptides, into the gas-phase[267] and the first studies have recently been reported.[268,269] By combining PES with ion mobility measurements the authors were able to distinguish and separate several protein conformers,[134] which were subsequently probed in different charge states. Positive electron affinities were observed even for high charge states ($n = -12$), which are rationalised by an unfolding of the peptide and therefore a distribution of the charges in space, minimising the Coulomb repulsion. This flexibility thus leads to an increased stability compared to rigid structures which fragment under the high repulsive forces.

Time-resolved PES has recently been applied to polyanions by Kappes and coworkers, studying the excited state dynamics in transition metal complexes.[270,271] In the case of phtalocyanine tetranions, the authors found that the presence of a central metal atom (Cu or Ni) dramatically increases the non-radiative relaxation via internal conversion following *Q* band excitation, compared to the "free-base" system, $[H_2Pc(SO_3)_4]^{4-}$. This is attributed to the stronger coupling to lower lying states within the spin manifold in the presence of heavy metal atoms and leads to a reduction in fluorescence quantum yield for metal containing systems in solution. Furthermore the authors found that in the "free-base" system a new, slower deactivation channel opens up. This was attributed to tunnelling through the RCB, with a characteristic lifetime of $\sim$70 ps. While this tunnelling has been observed before,[272,273] this is the first study of the dynamics of the tunnelling process,[270] and has prompted several other studies investigating the dynamics and energetics of tunnelling through repulsive barriers in polyanions.[265,266,274]

1.5 Summary

This chapter aimed to provide a general introduction of the theoretical background necessary for our research, as well as give an overview of the existing literature on photoelectron spectroscopy and time-resolved spectroscopy of anions. The first section is a general outline of the field of *Femtochemistry*, its history, its current state and general future directions. Section 1.2 gave a general outline of molecular quantum mechanics from first principles, required to understand the interpretation of work to follow. It introduced the Born-Oppenheimer approximation, frequently applied in molecular dynamics, but also frequently found to be an inadequate description of the fastest chemical reactions, involving conical intersections. The optical formation of electronic excited states was presented and the corresponding radiative de-excitation processes of fluorescence and phosphorescence. The relaxation processes studied in this work are all of a non-radiative nature, and several different pathways for energy dissipation from excited states were introduced, and a theoretical description of the expected rates given. The general principles of photoelectron spectroscopy, the primary tool employed in our laboratory, were outlined in section 1.3, with particular attention paid to its application to anionic systems. The general observables, the photoelectron spectrum and photoelectron angular distribution, were introduced and their information content explained and related back to the general ideas of molecular quantum mechanics presented earlier. It was shown how dynamic processes manifest themselves in time-resolved photoelectron spectra and how intrinsic information about the studied system can be gained from TRPES. Finally, section 1.4 gave a brief overview of recent investigations of anionic systems using PES and TRPES. Systems were categorised into molecular systems, were the intrinsic electronic relaxation dynamics are primarily studied, cluster systems, which can be used as model systems for solvation or nanoparticles, and polyanions, an emerging field of research due to the unusual properties arising from the repulsion of charges within a single molecule. Several examples were treated in detail, and numerous references to current work, as well as recent reviews, given for further reading.

The following chapters will build on the foundations laid in the first chapter. Chapter 2 will introduce our experimental setup and photoelectron imaging spectrometer. Following this are three chapters that explain in detail different research projects on anions undertaken in our group. Chapter 3 focusses on studies of electron acceptor radical anions, Chapter 4 deals with studies of polyanions and investigations of the properties of the Repulsive Coulomb Barrier in these systems and Chapter 5 discusses the photophysics and dynamics of the chromophore of the green fluorescent protein. The final chapter will conclude the findings of this thesis and give some ideas for experimental improvements

and areas of further study.

References

[1] H. Hartridge, F. J. W. Roughton, *Proc. R. Soc. London, Ser. A* **104**, 376 (1923).

[2] B. Chance, *J. Franklin Inst.* **229**, 455 (1940).

[3] R. Norrish, G. Porter, *Nature* **164**, 658 (1949).

[4] M. Eigen, *Discuss. Faraday Soc.* **17**, 194 (1954).

[5] T. H. Maiman, *Nature* **187**, 493 (1960).

[6] F. J. McClung, R. W. Hellwarth, *J. Appl. Phys.* **33**, 828 (1962).

[7] L. E. Hargrove, R. L. Fork, M. A. Pollack, *Appl. Phys. Lett.* **5**, 4 (1964).

[8] D. A. Stetser, A. J. DeMaria, *Appl. Phys. Lett.* **9**, 118 (1966).

[9] C. V. Shank, E. P. Ippen, *Appl. Phys. Lett.* **24**, 373 (1974).

[10] R. L. Fork, C. H. B. Cruz, P. C. Becker, C. V. Shank, *Opt. Lett.* **12**, 483 (1987).

[11] J. C. Polanyi, A. H. Zewail, *Acc. Chem. Res.* **28**, 119 (1995).

[12] A. H. Zewail, *J. Phys. Chem. A* **104**, 5660 (2000).

[13] M. Hentschel, *et al.*, *Nature* **414**, 509 (2001).

[14] E. Goulielmakis, *et al.*, *Science* **320**, 1614 (2008).

[15] J. Seres, *et al.*, *Nature* **433**, 596 (2005).

[16] E. Hand, *Nature* **461**, 708 (2009).

[17] H. Ihee, *et al.*, *Science* **291**, 458 (2001).

[18] M. Born, *Z. Phys. A* **37**, 863 (1926).

[19] J. M. Hollas, *Modern Spectroscopy* (John Wiley & Sons Ltd., Chichester, 2004), fourth edn.

[20] E. Schrödinger, *Ann. Phys.* **384**, 361 (1926).

[21] P. Atkins, R. Friedman, *Molecular Quantum Mechanics* (Oxford University Press, Oxford, 2005), fourth edn.

[22] W. Heisenberg, *Z. Phys. A* **43**, 172 (1927).

[23] H. P. Robertson, *Phys. Rev.* **34**, 163 (1929).

[24] C. Rulliere, *Femtosecond Laser Pulses* (Spinger, New York, 2005), second edn.

[25] V. May, O. Kühn, *Charge and Energy Transfer Dynamics in Molecular Systems* (Wiley-VCH, Weinheim, 2004).

[26] L. Cederbaum, *Born-Oppenheimer Approximation and Beyond* (World Scientific Publishing, Singapore, 2004).

[27] L. J. Butler, *Annu. Rev. Phys. Chem.* **49**, 125 (1998).

[28] M. Born, R. Oppenheimer, *Ann. Phys.* **389**, 457 (1927).

[29] F. London, *Z. Phys. A* **74**, 143 (1932).

[30] D. R. Yarkony, *Rev. Mod. Phys.* **68**, 985 (1996).

[31] D. R. Yarkony, *Conical Intersections: Their Description and Consequences* (World Scientific Publishing, Singapore, 2004).

[32] E. Deumens, A. Diz, R. Longo, Y. Ohrn, *Rev. Mod. Phys.* **66**, 917 (1994).

[33] D. R. Yarkony, *Acc. Chem. Res.* **31**, 511 (1998).

[34] I. V. Hertel, W. Radloff, *Rep. Prog. Phys.* **69**, 1897 (2006).

[35] G. Wu, P. Hockett, A. Stolow, *Phys. Chem. Chem. Phys.* **13**, 18447 (2011).

[36] P. M. Felker, J. S. Baskin, A. H. Zewail, *J. Phys. Chem.* **90**, 724 (1986).

[37] P. M. Felker, A. H. Zewail, *J. Chem. Phys* **86**, 2460 (1987).

[38] P. M. Felker, *J. Phys. Chem.* **96**, 7844 (1992).

[39] W. T. Silfvast, *Laser Fundamentals* (Cambridge University Press, Cambridge, 2004), second edn.

[40] J. Franck, *Trans. Faraday Soc.* **21**, 536 (1926).

[41] E. U. Condon, *Phys. Rev.* **28**, 1182 (1926).

[42] E. U. Condon, *Phys. Rev.* **32**, 858 (1928).

[43] A. Einstein, *Verh. d. Deut. Phys. Gesell.* **18**, 318 (1916).

[44] A. Jablonski, *Nature* **131**, 839 (1933).

[45] M. Kasha, *Discuss. Faraday Soc.* **9**, 14 (1950).

[46] M. Bixon, J. Jortner, *J. Chem. Phys.* **48**, 715 (1968).

[47] Spectra Physics, *Tsunami Mode-Locked Ti:sapphire Laser, User's Manual*.

[48] K. L. Reid, *Int. Rev. Phys. Chem.* **27**, 607 (2008).

[49] M. Bixon, J. Jortner, *J. Chem. Phys.* **50**, 4061 (1969).

[50] K. G. Kay, *J. Chem. Phys.* **61**, 5205 (1974).

[51] P. A. M. Dirac, *Proc. R. Soc. London, Ser. A* **114**, 243 (1927).

[52] J. T. Yardley, *Introduction to Molecular Energy Transfer* (Academic Press, New York, 1980).

[53] F. Bernardi, M. Olivucci, M. A. Robb, *Chem. Soc. Rev.* **25**, 321 (1996).

[54] R. Englman, J. Jortner, *Mol. Phys.* **18**, 145 (1970).

[55] J. von Neuman, E. Wigner, *Physik. Z.* **30**, 467 (1929).

[56] E. Teller, *J. Phys. Chem.* **41**, 109 (1937).

[57] H. A. Jahn, E. Teller, *Proc. R. Soc. London, Ser. A* **161**, 220 (1937).

[58] M. V. Berry, M. Wilkinson, *Proc. R. Soc. London, Ser. A* **392**, 15 (1984).

[59] D. R. Yarkony, *J. Phys. Chem. A* **105**, 6277 (2001).

[60] G. A. Worth, L. S. Cederbaum, *Annu. Rev. Phys. Chem.* **55**, 127 (2004).

[61] W. Domcke, D. R. Yarkony, *Annu. Rev. Phys. Chem.* **63**, 325 (2012).

[62] K. Razi Naqvi, *Chem. Phys. Lett.* **15**, 634 (1972).

[63] H. C. Longuet-Higgins, *Proc. R. Soc. London, Ser. A* **344**, 147 (1975).

[64] C. A. Mead, *J. Chem. Phys.* **70**, 2276 (1979).

[65] C. A. Mead, D. G. Truhlar, *J. Chem. Phys.* **84**, 1055 (1986).

[66] T. Suzuki, *Int. Rev. Phys. Chem.* **31**, 265 (2012).

[67] D. A. Farrow, W. Qian, E. R. Smith, A. A. Ferro, D. M. Jonas, *J. Chem. Phys.* **128**, 144510 (2008).

[68] N. H. Damrauer, *et al.*, *Science* **275**, 54 (1997).

[69] A. T. Yeh, C. V. Shank, J. K. McCusker, *Science* **289**, 935 (2000).

[70] G. Benkö, J. Kallioinen, J. E. I. Korppi-Tommola, A. P. Yartsev, V. Sundström, *J. Am. Chem. Soc.* **124**, 489 (2001).

[71] O. Bram, A. Cannizzo, M. Chergui, *Phys. Chem. Chem. Phys.* **14**, 7934 (2012).

[72] J. Simons, *Roles Played by Metastable States in Chemistry* (American Chemical Society, 1984), vol. 263 of *ACS Symposium Series*, chap. 1, pp. 3–16.

[73] J. Schiedt, R. Weinkauf, *J. Chem. Phys.* **110**, 304 (1999).

[74] C. E. Klots, *Z. Phys. D: At., Mol. Clusters* **20**, 105 (1991).

[75] M. Kjellberg, *et al.*, *Phys. Rev. A* **81**, 023202 (2010).

[76] B. Baguenard, J. C. Pinar, C. Bordas, M. Broyer, *Phys. Rev. A* **63**, 023204 (2001).

[77] B. Baguenard, J. C. Pinar, F. Lpine, C. Bordas, M. Broyer, *Chem. Phys. Lett.* **352**, 147 (2002).

[78] K. Hansen, K. Hoffmann, E. E. B. Campbell, *J. Chem. Phys.* **119**, 2513 (2003).

[79] A. Stolow, *Annu. Rev. Phys. Chem.* **54**, 89 (2003).

[80] A. Stolow, A. E. Bragg, D. M. Neumark, *Chem. Rev.* **104**, 1719 (2004).

[81] T. Suzuki, *Annu. Rev. Phys. Chem.* **57**, 555 (2006).

[82] A. Sanov, R. Mabbs, *Int. Rev. Phys. Chem.* **27**, 53 (2008).

[83] J. R. R. Verlet, *Chem. Soc. Rev.* **37**, 505 (2008).

[84] R. Mabbs, E. R. Grumbling, K. Pichugin, A. Sanov, *Chem. Soc. Rev.* **38**, 2169 (2009).

[85] X.-B. Wang, L.-S. Wang, *Annu. Rev. Phys. Chem.* **60**, 105 (2009).

[86] A. Einstein, *Ann. Phys.* **322**, 132 (1905).

[87] C. Nordling, E. Sokolowski, K. Siegbahn, *Phys. Rev.* **105**, 1676 (1957).

[88] D. W. Turner, M. I. A. Jobory, *J. Chem. Phys.* **37**, 3007 (1962).

[89] F. Vilesov, A. Terenin, B. Kurbatoy, *Dokl. Akad. Nauk SSSR* **138**, 1329 (1961).

[90] M. Seel, W. Domcke, *Chem. Phys.* **151**, 59 (1991).

[91] M. Seel, W. Domcke, *J. Chem. Phys.* **95**, 7806 (1991).

[92] I. Fischer, D. M. Villeneuve, M. J. J. Vrakking, A. Stolow, *J. Chem. Phys.* **102**, 5566 (1995).

[93] I. Fischer, M. J. J. Vrakking, D. M. Villeneuve, A. Stolow, *Chem. Phys.* **207**, 331 (1996).

[94] S. Lochbrunner, *et al.*, *J. Electron Spectrosc. Relat. Phenom.* **112**, 183 (2000).
[95] T. Koopmans, *Physica* **1**, 104 (1934).
[96] V. Blanchet, M. Z. Zgierski, T. Seideman, A. Stolow, *Nature* **401**, 52 (1999).
[97] V. Blanchet, M. Z. Zgierski, A. Stolow, *J. Chem. Phys.* **114**, 1194 (2001).
[98] M. Schmitt, *et al.*, *J. Chem. Phys.* **114**, 1206 (2001).
[99] E. P. Wigner, *Phys. Rev.* **73**, 1002 (1948).
[100] D. J. Pegg, *Rep. Prog. Phys.* **67**, 857 (2004).
[101] A. Assion, M. Geisler, J. Helbing, V. Seyfried, T. Baumert, *Phys. Rev. A* **54**, R4605 (1996).
[102] E. O. Lawrence, M. A. Chaffee, *Phys. Rev.* **36**, 1099 (1930).
[103] J. Berkowitz, H. Ehrhardt, T. Tekaat, *Z. Phys. A* **200**, 69 (1967).
[104] T. Carlson, R. White, *Faraday Discuss.* **54**, 285 (1972).
[105] K. L. Reid, *Annu. Rev. Phys. Chem.* **54**, 397 (2003).
[106] T. Suzuki, B. J. Whitaker, *Int. Rev. Phys. Chem.* **20**, 313 (2001).
[107] T. Seideman, *Annu. Rev. Phys. Chem.* **53**, 41 (2002).
[108] M. N. R. Ashfold, *et al.*, *Phys. Chem. Chem. Phys.* **8**, 26 (2006).
[109] K. L. Reid, *Mol. Phys.* **110**, 131 (2012).
[110] C. N. Yang, *Phys. Rev.* **74**, 764 (1948).
[111] J. Cooper, R. N. Zare, *J. Chem. Phys.* **48**, 942 (1968).
[112] R. Mabbs, E. Surber, A. Sanov, *J. Chem. Phys.* **122**, 054308 (2005).
[113] K. J. Reed, A. H. Zimmerman, H. C. Andersen, J. I. Brauman, *J. Chem. Phys.* **64**, 1368 (1976).
[114] M. K. Gilles, K. M. Ervin, J. Ho, W. C. Lineberger, *J. Phys. Chem.* **96**, 1130 (1992).
[115] H.-J. Deyerl, L. S. Alconcel, R. E. Continetti, *J. Phys. Chem. A* **105**, 552 (2000).
[116] E. Surber, R. Mabbs, A. Sanov, *J. Phys. Chem. A* **107**, 8215 (2003).
[117] D. Dill, J. L. Dehmer, *J. Chem. Phys.* **61**, 692 (1974).
[118] S. N. Dixit, V. McKoy, *J. Chem. Phys.* **82**, 3546 (1985).
[119] C. M. Oana, A. I. Krylov, *J. Chem. Phys.* **131**, 124114 (2009).
[120] O. Gessner, *et al.*, *Science* **311**, 219 (2006).
[121] D. Akoury, *et al.*, *Science* **318**, 949 (2007).
[122] M. Meckel, *et al.*, *Science* **320**, 1478 (2008).
[123] C. Z. Bisgaard, *et al.*, *Science* **323**, 1464 (2009).
[124] A. I. Chichinin, K. H. Gericke, S. Kauczok, C. Maul, *Int. Rev. Phys. Chem.* **28**, 607 (2009).
[125] L. Holmegaard, *et al.*, *Nat. Phys.* **6**, 428 (2010).
[126] J. L. Hansen, *et al.*, *Phys. Rev. Lett.* **106**, 073001 (2011).
[127] J. Simons, *J. Phys. Chem. A* **112**, 6401 (2008).
[128] J. Simons, *Annu. Rev. Phys. Chem.* **62**, 107 (2011).
[129] R. R. Corderman, W. C. Lineberger, *Annu. Rev. Phys. Chem.* **30**, 347 (1979).
[130] L.-S. Wang, C.-F. Ding, X.-B. Wang, S. E. Barlow, *Rev. Sci. Instrum.* **70**, 1957 (1999).
[131] X.-B. Wang, L.-S. Wang, *Rev. Sci. Instrum.* **79**, 073108 (2008).
[132] J. Lecointre, G. M. Roberts, D. A. Horke, J. R. R. Verlet, *J. Phys. Chem. A* **114**, 11216 (2010).
[133] A. R. McKay, *et al.*, *Rev. Sci. Instrum.* **81**, 123101 (2010).
[134] M. Vonderach, O. T. Ehrler, P. Weis, M. M. Kappes, *Anal. Chem.* **83**, 1108 (2011).
[135] E. Papalazarou, *et al.*, *Analyst* **137**, 3496 (2012).
[136] T. Waters, X.-B. Wang, L.-S. Wang, *Coord. Chem. Rev.* **251**, 474 (2007).
[137] D. Khuseynov, M. T. Fontana, A. Sanov, *Chem. Phys. Lett.* **550**, 15 (2012).
[138] L. M. Culberson, A. Sanov, *J. Chem. Phys.* **134**, 204306 (2011).
[139] D. J. Goebbert, K. Pichugin, D. Khuseynov, P. G. Wenthold, A. Sanov, *J. Chem. Phys.* **132**, 224301 (2010).
[140] T. Ichino, *et al.*, *Angew. Chem. Int. Ed.* **48**, 8509 (2009).
[141] T. Ichino, *et al.*, *J. Phys. Chem. A* **115**, 1634 (2011).
[142] J. B. Kim, T. I. Yacovitch, C. Hock, D. M. Neumark, *Phys. Chem. Chem. Phys.* **13**, 17378 (2011).
[143] T. I. Yacovitch, E. Garand, D. M. Neumark, *J. Chem. Phys.* **130**, 244309 (2009).

[144] T. I. Yacovitch, E. Garand, D. M. Neumark, *J. Phys. Chem. A* **114**, 11091 (2010).

[145] T. I. Yacovitch, J. B. Kim, E. Garand, D. G. van der Poll, D. M. Neumark, *J. Chem. Phys.* **134**, 134307 (2011).

[146] A. Osterwalder, M. J. Nee, J. Zhou, D. M. Neumark, *J. Chem. Phys.* **121**, 6317 (2004).

[147] D. M. Neumark, *J. Phys. Chem. A* **112**, 13287 (2008).

[148] S. M. Villano, N. Eyet, W. C. Lineberger, V. M. Bierbaum, *J. Am. Chem. Soc.* **130**, 7214 (2008).

[149] S. M. Villano, *et al.*, *J. Phys. Chem. A* **114**, 191 (2009).

[150] K. M. Vogelhuber, S. W. Wren, L. Sheps, W. C. Lineberger, *J. Chem. Phys.* **134**, 064302 (2011).

[151] S. W. Wren, K. M. Vogelhuber, T. Ichino, J. F. Stanton, W. C. Lineberger, *J. Phys. Chem. A* **116**, 3118 (2012).

[152] S. W. Wren, *et al.*, *J. Am. Chem. Soc.* **134**, 6584 (2012).

[153] J. F. Stanton, *et al.*, *J. Chem. Phys.* **136**, 134312 (2012).

[154] M. M. Meyer, X.-B. Wang, C. A. Reed, L.-S. Wang, S. R. Kass, *J. Am. Chem. Soc.* **131**, 18050 (2009).

[155] X.-B. Wang, Q. Fu, J. Yang, *J. Phys. Chem. A* **114**, 9083 (2010).

[156] Q. Fu, J. Yang, X.-B. Wang, *J. Phys. Chem. A* **115**, 3201 (2011).

[157] J.-C. Guo, G.-L. Hou, S.-D. Li, X.-B. Wang, *J. Phys. Chem. Lett.* **3**, 304 (2012).

[158] K. M. Vogelhuber, S. W. Wren, A. B. McCoy, K. M. Ervin, W. C. Lineberger, *J. Chem. Phys.* **134**, 184306 (2011).

[159] A. S. Case, *et al.*, *Angew. Chem. Int. Ed.* **51**, 2651 (2012).

[160] E. M. Miller, *et al.*, *J. Chem. Phys.* **136**, 044313 (2012).

[161] P. D. Dau, *et al.*, *J. Chem. Phys.* **136**, 194304 (2012).

[162] E. Garand, T. I. Yacovitch, D. M. Neumark, *J. Chem. Phys.* **129**, 074312 (2008).

[163] E. Garand, T. I. Yacovitch, D. M. Neumark, *J. Chem. Phys.* **130**, 064304 (2009).

[164] E. Garand, *et al.*, *J. Phys. Chem. A* **113**, 4631 (2009).

[165] E. Garand, *et al.*, *J. Phys. Chem. A* **113**, 14439 (2009).

[166] E. Garand, D. M. Neumark, *J. Chem. Phys.* **135**, 024302 (2011).

[167] Y.-L. Wang, *et al.*, *J. Phys. Chem. A* **114**, 11244 (2010).

[168] L.-S. Wang, *Phys. Chem. Chem. Phys.* **12**, 8694 (2010).

[169] S. M. Sheehan, *et al.*, *J. Chem. Phys.* **128**, 034301 (2008).

[170] S. M. Sheehan, B. F. Parsons, T. A. Yen, M. R. Furlanetto, D. M. Neumark, *J. Chem. Phys.* **128**, 174301 (2008).

[171] T. A. Yen, E. Garand, A. T. Shreve, D. M. Neumark, *J. Phys. Chem. A* **114**, 3215 (2009).

[172] E. Garand, T. I. Yacovitch, J. Zhou, S. M. Sheehan, D. M. Neumark, *Chem. Sci.* **1**, 192 (2010).

[173] Y. J. Ko, *et al.*, *Phys. Chem. Chem. Phys.* **12**, 3535 (2010).

[174] L. Chomicz, *et al.*, *J. Chem. Phys.* **135**, 114301 (2011).

[175] J. Chen, *et al.*, *J. Phys. Chem. A* p. doi: 10.1021/jp303964j (2012).

[176] I. Compagnon, A.-R. Allouche, F. Bertorelle, R. Antoine, P. Dugourd, *Phys. Chem. Chem. Phys.* **12**, 3399 (2010).

[177] B. Bellina, *et al.*, *Int. J. Mass Spectrom.* **297**, 36 (2010).

[178] R. Antoine, P. Dugourd, *Phys. Chem. Chem. Phys.* **13**, 16494 (2011).

[179] L. Sheps, *et al.*, *Science* **328**, 220 (2010).

[180] G. M. Roberts, J. Lecointre, D. A. Horke, J. R. R. Verlet, *Phys. Chem. Chem. Phys.* **12**, 6226 (2010).

[181] L. Sheps, *et al.*, *J. Chem. Phys.* **134**, 184311 (2011).

[182] A. Sanov, W. Carl Lineberger, *Phys. Chem. Chem. Phys.* **6**, 2018 (2004).

[183] X. Chen, S. E. Bradforth, *Annu. Rev. Phys. Chem.* **59**, 203 (2008).

[184] Y.-L. Wang, H.-J. Zhai, L. Xu, J. Li, L.-S. Wang, *J. Phys. Chem. A* **114**, 1247 (2009).

[185] W. Huang, L.-S. Wang, *Phys. Chem. Chem. Phys.* **11**, 2663 (2009).

[186] R. Pal, L.-M. Wang, W. Huang, L.-S. Wang, X. C. Zeng, *J. Chem. Phys.* **134**, 054306 (2011).

[187] N. Shao, *et al.*, *J. Am. Chem. Soc.* **132**, 6596 (2010).

[188] R. Pal, L.-M. Wang, W. Huang, L.-S. Wang, X. C. Zeng, *J. Am. Chem. Soc.* **131**, 3396 (2009).

[189] W. Huang, L.-S. Wang, *Phys. Rev. Lett.* **102**, 153401 (2009).

[190] W. Huang, R. Pal, L.-M. Wang, X. C. Zeng, L.-S. Wang, *J. Chem. Phys.* **132**, 054305 (2010).
[191] L.-M. Wang, R. Pal, W. Huang, X. C. Zeng, L.-S. Wang, *J. Chem. Phys.* **132**, 114306 (2010).
[192] W. Huang, H.-J. Zhai, L.-S. Wang, *J. Am. Chem. Soc.* **132**, 4344 (2010).
[193] R. Hamouda, *et al.*, *J. Phys. Chem. Lett.* **1**, 3189 (2010).
[194] J. Li, X. Li, H.-J. Zhai, L.-S. Wang, *Science* **299**, 864 (2003).
[195] S. Bulusu, X. Li, L.-S. Wang, X. C. Zeng, *Proc. Natl. Acad. Sci. U. S. A.* **103**, 8326 (2006).
[196] G. B. Griffin, *et al.*, *Chem. Phys.* **350**, 69 (2008).
[197] G. B. Griffin, *et al.*, *J. Chem. Phys.* **130**, 231103 (2009).
[198] M. Y. Ryan, *et al.*, *Phys. Scr.* **80**, 048102 (2009).
[199] K. Majer, B. v. Issendorff, *Phys. Chem. Chem. Phys.* **14**, 9371 (2012).
[200] H. Xie, *et al.*, *J. Chem. Phys.* **136**, 184312 (2012).
[201] J. Bahn, *et al.*, *New J. Phys.* **14**, 075008 (2012).
[202] O. T. Ehrler, J. M. Weber, F. Furche, M. M. Kappes, *Phys. Rev. Lett.* **91**, 113006 (2003).
[203] O. T. Ehrler, *et al.*, *J. Chem. Phys.* **125**, 074312 (2006).
[204] B. Concina, M. Neumaier, O. Hampe, M. M. Kappes, *J. Chem. Phys.* **128**, 134306 (2008).
[205] X.-B. Wang, *et al.*, *J. Chem. Phys.* **128**, 114307 (2008).
[206] X.-B. Wang, *et al.*, *J. Phys. Chem. A* **114**, 1756 (2010).
[207] L.-M. Wang, *et al.*, *J. Am. Chem. Soc.* **132**, 14104 (2010).
[208] T. R. Galeev, *et al.*, *Phys. Chem. Chem. Phys.* **13**, 8805 (2011).
[209] W.-L. Li, C. Romanescu, T. R. Galeev, L.-S. Wang, A. I. Boldyrev, *J. Phys. Chem. A* **115**, 10391 (2011).
[210] A. P. Sergeeva, B. B. Averkiev, H.-J. Zhai, A. I. Boldyrev, L.-S. Wang, *J. Chem. Phys.* **134**, 224304 (2011).
[211] C. Romanescu, A. P. Sergeeva, W.-L. Li, A. I. Boldyrev, L.-S. Wang, *J. Am. Chem. Soc.* **133**, 8646 (2011).
[212] H.-J. Zhai, C.-Q. Miao, S.-D. Li, L.-S. Wang, *J. Phys. Chem. A* **114**, 12155 (2010).
[213] A. P. Sergeeva, D. Y. Zubarev, H.-J. Zhai, A. I. Boldyrev, L.-S. Wang, *J. Am. Chem. Soc.* **130**, 7244 (2008).
[214] W. Huang, *et al.*, *Nat. Chem.* **2**, 202 (2010).
[215] H.-J. Zhai, L.-S. Wang, *J. Am. Chem. Soc.* **129**, 3022 (2007).
[216] H.-J. Zhai, J. Dbler, J. Sauer, L.-S. Wang, *J. Am. Chem. Soc.* **129**, 13270 (2007).
[217] H.-J. Zhai, S. Li, D. A. Dixon, L.-S. Wang, *J. Am. Chem. Soc.* **130**, 5167 (2008).
[218] M. Sierka, J. Dbler, J. Sauer, H.-J. Zhai, L.-S. Wang, *ChemPhysChem* **10**, 2410 (2009).
[219] H.-J. Zhai, B. Wang, X. Huang, L.-S. Wang, *J. Phys. Chem. A* **113**, 9804 (2009).
[220] H.-J. Zhai, B. Wang, X. Huang, L.-S. Wang, *J. Phys. Chem. A* **113**, 3866 (2009).
[221] W.-J. Chen, H.-J. Zhai, Y.-F. Zhang, X. Huang, L.-S. Wang, *J. Phys. Chem. A* **114**, 5958 (2010).
[222] S. Li, H.-J. Zhai, L.-S. Wang, D. A. Dixon, *J. Phys. Chem. A* **113**, 11273 (2009).
[223] S. Li, H.-J. Zhai, L.-S. Wang, D. A. Dixon, *J. Phys. Chem. A* **116**, 5256 (2012).
[224] D. Wang, J. D. Graham, A. M. Buytendyk, J. K. H. Bowen, *J. Chem. Phys.* **135**, 164308 (2011).
[225] X. Li, J. K. H. Bowen, P. Jena, A. K. Kandalam, *J. Chem. Phys.* **135**, 204301 (2011).
[226] J. Atobe, K. Koyasu, S. Furuse, A. Nakajima, *Phys. Chem. Chem. Phys.* **14**, 9403 (2012).
[227] S. E. Waller, J. E. Mann, E. Hossain, M. Troyer, C. C. Jarrold, *J. Chem. Phys.* **137**, 024302 (2012).
[228] X.-B. Wang, X. Yang, J. B. Nicholas, L.-S. Wang, *Science* **294**, 1322 (2001).
[229] F. Mbaiwa, J. Wei, M. Van Duzor, R. Mabbs, *J. Chem. Phys.* **132**, 134304 (2010).
[230] M. Van Duzor, J. Wei, F. Mbaiwa, R. Mabbs, *J. Chem. Phys.* **133**, 144303 (2010).
[231] M. Van Duzor, F. Mbaiwa, J. Lasinski, N. Holtgrewe, R. Mabbs, *J. Chem. Phys.* **134**, 214301 (2011).
[232] M. Van Duzor, *et al.*, *J. Chem. Phys.* **134**, 184315 (2011).
[233] F. Mbaiwa, D. Dao, N. Holtgrewe, J. Lasinski, R. Mabbs, *J. Chem. Phys.* **136**, 114303 (2012).
[234] O. T. Ehrler, G. B. Griffin, R. M. Young, D. M. Neumark, *J. Phys. Chem. B* **113**, 4031 (2008).
[235] R. M. Young, M. A. Yandell, D. M. Neumark, *J. Chem. Phys.* **134**, 124311 (2011).
[236] M. A. Yandell, R. M. Young, S. B. King, D. M. Neumark, *J. Phys. Chem. A* **116**, 2750 (2011).
[237] R. M. Young, *et al.*, *Mol. Phys.* **110**, 1787 (2012).
[238] D. M. Neumark, *Mol. Phys.* **106**, 2183 (2008).
[239] O. T. Ehrler, D. M. Neumark, *Acc. Chem. Res.* **42**, 769 (2009).

[240] R. M. Young, D. M. Neumark, *Chem. Rev.* (2012).

[241] B. Winter, M. Faubel, *Chem. Rev.* **106**, 1176 (2006).

[242] Y. R. Shen, *Annu. Rev. Phys. Chem.* **40**, 327 (1989).

[243] G. B. Griffin, R. M. Young, O. T. Ehrler, D. M. Neumark, *J. Chem. Phys.* **131**, 194302 (2009).

[244] R. M. Young, G. B. Griffin, A. Kammrath, O. T. Ehrler, D. M. Neumark, *Chem. Phys. Lett.* **485**, 59 (2010).

[245] R. M. Young, M. A. Yandell, M. Niemeyer, D. M. Neumark, *J. Chem. Phys.* **133**, 154312 (2010).

[246] R. M. Young, M. A. Yandell, S. B. King, D. M. Neumark, *J. Chem. Phys.* **136**, 094304 (2012).

[247] P. D. Dau, *et al.*, *Chem. Sci.* **3**, 1137 (2012).

[248] X.-B. Wang, *et al.*, *J. Phys. Chem. A* **113**, 9579 (2009).

[249] X.-B. Wang, K. Kowalski, L.-S. Wang, S. S. Xantheas, *J. Chem. Phys.* **132**, 124306 (2010).

[250] X.-B. Wang, *et al.*, *Chem. Phys. Lett.* **477**, 41 (2009).

[251] X.-B. Wang, *et al.*, *J. Phys. Chem. A* **113**, 5567 (2009).

[252] X.-B. Wang, J. B. Nicholas, L.-S. Wang, *J. Chem. Phys.* **113**, 10837 (2000).

[253] X.-B. Wang, L.-S. Wang, *Phys. Rev. Lett.* **83**, 3402 (1999).

[254] L.-S. Wang, C.-F. Ding, X.-B. Wang, J. B. Nicholas, *Phys. Rev. Lett.* **81**, 2667 (1998).

[255] X.-B. Wang, C.-F. Ding, L.-S. Wang, *Phys. Rev. Lett.* **81**, 3351 (1998).

[256] A. Dreuw, L. S. Cederbaum, *Chem. Rev.* **102**, 181 (2001).

[257] X.-B. Wang, X. Yang, L.-S. Wang, *Int. Rev. Phys. Chem.* **21**, 473 (2002).

[258] X.-P. Xing, X.-B. Wang, L.-S. Wang, *J. Phys. Chem. A* **113**, 945 (2008).

[259] X.-B. Wang, K. Ferris, L.-S. Wang, *J. Phys. Chem. A* **104**, 25 (1999).

[260] J. Yang, *et al.*, *J. Chem. Phys.* **128**, 091102 (2008).

[261] X.-B. Wang, *et al.*, *J. Am. Chem. Soc.* **131**, 9836 (2009).

[262] X.-P. Xing, X.-B. Wang, L.-S. Wang, *Phys. Rev. Lett.* **101**, 083003 (2008).

[263] X.-P. Xing, X.-B. Wang, L.-S. Wang, *J. Chem. Phys.* **130**, 074301 (2009).

[264] C.-G. Ning, P. D. Dau, L.-S. Wang, *Phys. Rev. Lett.* **105**, 263001 (2010).

[265] D. A. Horke, A. S. Chatterley, J. R. R. Verlet, *J. Phys. Chem. Lett.* **3**, 834 (2012).

[266] D. A. Horke, A. S. Chatterley, J. R. R. Verlet, *Phys. Rev. Lett.* **108**, 083003 (2012).

[267] J. Fenn, M. Mann, C. Meng, S. Wong, C. Whitehouse, *Science* **246**, 64 (1989).

[268] K. Matheis, *et al.*, *J. Am. Chem. Soc.* **130**, 15903 (2008).

[269] M. Vonderach, *et al.*, *Phys. Chem. Chem. Phys.* **13**, 15554 (2011).

[270] O. T. Ehrler, J.-P. Yang, A. B. Sugiharto, A. N. Unterreiner, M. M. Kappes, *J. Chem. Phys.* **127**, 184301 (2007).

[271] C. Rensing, O. T. Ehrler, J.-P. Yang, A.-N. Unterreiner, M. M. Kappes, *J. Chem. Phys.* **130**, 234306 (2009).

[272] P. Weis, O. Hampe, S. Gilb, M. M. Kappes, *Chem. Phys. Lett.* **321**, 426 (2000).

[273] M. N. Blom, O. Hampe, S. Gilb, P. Weis, M. M. Kappes, *J. Chem. Phys.* **115**, 3690 (2001).

[274] P. D. Dau, *et al.*, *Phys. Rev. A* **85**, 064503 (2012).

Chapter 2

Experimental Setup

Experiments are the only means of knowledge at our disposal. The rest is poetry, imagination.

Max Planck

This chapter is partially based on the following publications:

J. Lecointre, G. M. Roberts, D. A. Horke and J. R. R. Verlet, *J. Phys. Chem. A* **114**, 11216 (2010)

D. A. Horke, G. M. Roberts, J. Lecointre and J. R. R. Verlet, *Rev. Sci. Instrum.* **83**, 063101 (2012)

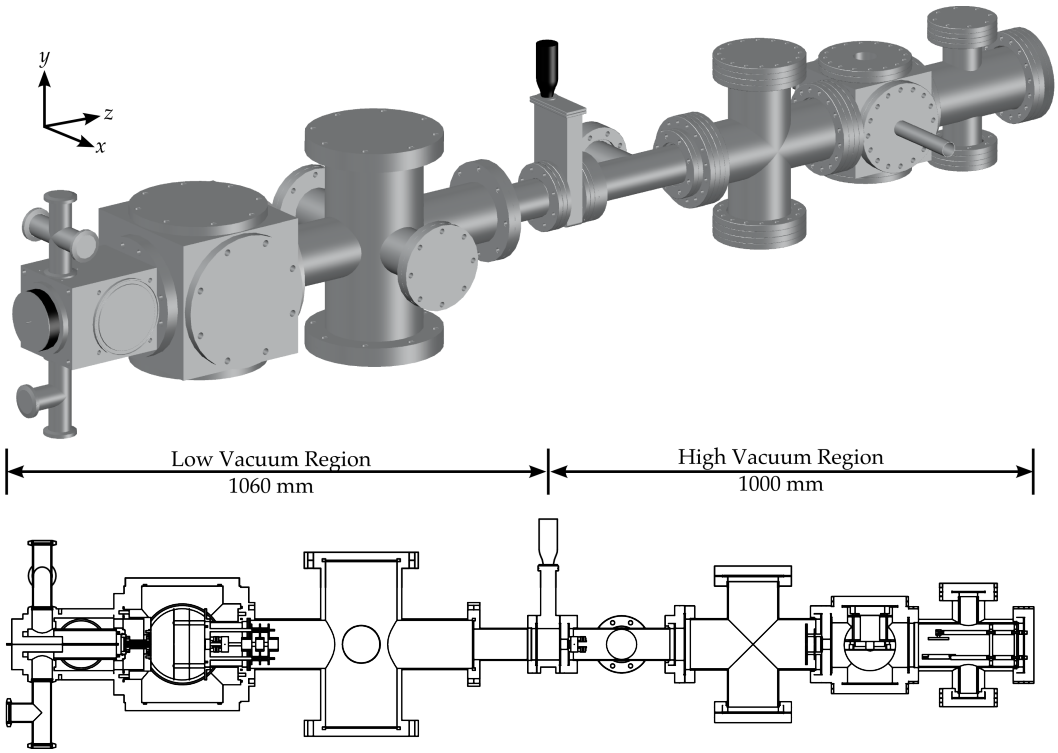

Figure 2.1: Overview of the anion beam machine, consisting of six differentially pumped regions. The top shows a 3 dimensional rendering of the entire machine, where vacuum pumps have been omitted for clarity. The bottom shows a cross-section along the *yz* direction of the machine, defined as the direction of flight for the anions.

This chapter offers a full description of the experimental apparatus in our laboratory. This machine was designed to allow the study of large anions and polyanions with femtosecond resolution using time-resolved photoelectron spectroscopy. More specifically, the use of photoelectron imaging techniques allows the extraction of photoelectron angular distributions, which carry information about the detaching orbitals (anions) or the location of excess charges within the molecular framework (polyanions). These prerequisites meant developing a machine that combines electrospray ionisation for the production of complex anions and polyanions with velocity-map imaging (VMI) techniques for high resolution photoelectron images. We have designed a new compact VMI setup, with a simpler electrode geometry but similar resolution to previous designs, specifically for use in anion experiments, as it utilises very low extraction fields, thereby minimising the effect on the primary ion beam. This chapter is organised as follows; the first section provides a detailed description of our ion beam machine, split into two parts: the low vacuum section, containing the ESI source, ion optics and mass spectrometer; and the high vacuum side containing the interaction region and detectors. Section 2.2 offers an overview of the laser setup in our laboratory, including frequency conversion techniques. Following this, section 2.3 describes the experimental timing and data acquisition routine in our laboratory, as well as the data analysis of raw photoelectron images, extracting

photoelectron spectra, angular distributions and their time-resolved equivalents. The last section contains a brief summary of this chapter.

2.1 Anion Beam Machine

The electrospray ionisation (ESI) photoelectron imaging spectrometer in our laboratory, a general schematic and rendering of which is shown in figure 2.1, consists of a total of 7 different pressure regions. This figure furthermore defines the cartesian coordinates used throughout this chapter; x and y describe the radial directions, whereas z is the axial coordinate, defining the flight direction of the anion beam. At the front of the machine, the ESI source operates at atmospheric pressure, and produced anions then enter a vacuum apparatus comprising a total of 6 differentially pumped regions. The first 4 regions, hereafter referred to as "low vacuum side", contain ion optics, an ion trap and a time-of-flight mass spectrometer. This region is separated from the remaining two chambers, the "high vacuum side", by a pneumatic gate valve. This second half of the machine contains the interaction region, where the ion packets are intersected by femtosecond laser pulses, the velocity-map imaging (VMI) detector and a reflectron mass spectrometer for the detection of fragment ions. The detailed design specifications will be discussed in the following sections, they have also been published recently.[1,2]

2.1.1 Low vacuum side

The low vacuum side of the spectrometer comprises the first four differentially pumped regions. A thin transfer capillary leads from atmospheric pressure into region 1 (R1), evacuated by a 100 m^3hr^{-1} mechanical pump (Oerlikon SV100B) to $\sim$1 Torr. This is connected to R2 by a 1 mm diameter pinhole, which is pumped down to 10^{-3} Torr by a 250 ls^{-1} turbomolecular pump (Oerlikon TW250S), backed by a 40 m^3hr^{-1} mechanical pump (Oerlikon D40B). A further pinhole of 1 mm diameter leads into R3, evacuated by a 3000 ls^{-1} diffusion pump (Oerlikon DIP3000, backed by a 25 m^3hr^{-1} Oerlikon D25B) to pressures of 10^{-6} Torr. Finally, a 5 mm pinhole leads into R4, at pressures of 10^{-7} Torr via a 250 ls^{-1} turbomolecular pump (Edwards EXT250H, backed by a 12 m^3hr^{-1} Edwards RV12 mechanical pump). At the end of R4 a pneumatic gate valve leads into the high vacuum side of the machine. The total length of the low vacuum part, from the beginning of the chamber to the gate valve, is 1060 mm. A technical drawing of the inner components of this section of the machine is shown in figure 2.2, and these will be explained in detail in the following sections.

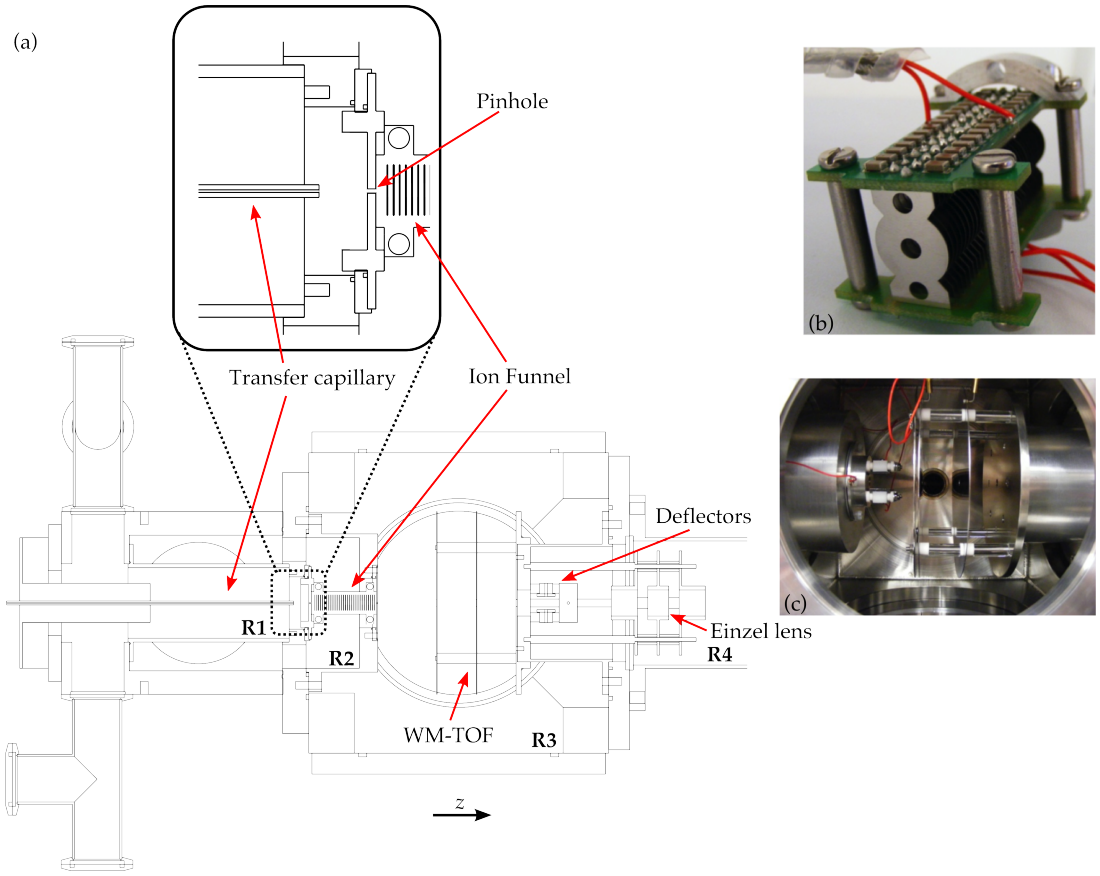

Figure 2.2: Overview of the low vacuum side of the machine, containing regions 1 to 4. (a) Technical drawing, with important parts labelled. Design and operation of these are explained in the text. The inset shows the interface between regions 1 and 2, separated by a pinhole with 1 mm inner diameter. Also shown are photos of the (b) ion funnel and (c) time-of-flight electrodes mounted inside the chamber.

Ion source

The use of electrospray ionisation (ESI),[3–5] a form of soft ionisation commonly used in mass spectrometers, was a natural choice for our experiment, as it allows the production of virtually any ion found in solution in the gas-phase (both anions and cations), including large complex anions and polyanions, solvent clusters and even entire proteins.[6–8] The basic operating principle of ESI is shown schematically in figure 2.3. A solution containing the target anion of interest, usually at concentrations of $\sim$ 1 mM in a solvent mixture of water and methanol or acetonitrile, is flowed through a fine electrospray needle (inner diameter (ID) 100 μm) using a commercial syringe pump (World Precision Instruments, Aladdin 1000) at flow rates of $\sim$200 μlhr^{-1}. This produces a fine mist of solvent/solute droplets at the end of the needle, which is placed $\sim$5 mm from a stainless steel transfer capillary (ID 600 μm) leading into the vacuum chamber. A high potential difference is applied between the ESI needle and the transfer capillary, typically $\sim$3 kV, with the polarity depending on whether anions or cations are desired. This potential difference is provided by a commercial ESI power supply (Applied Kilovolts) operating in a constant current mode. Thus a

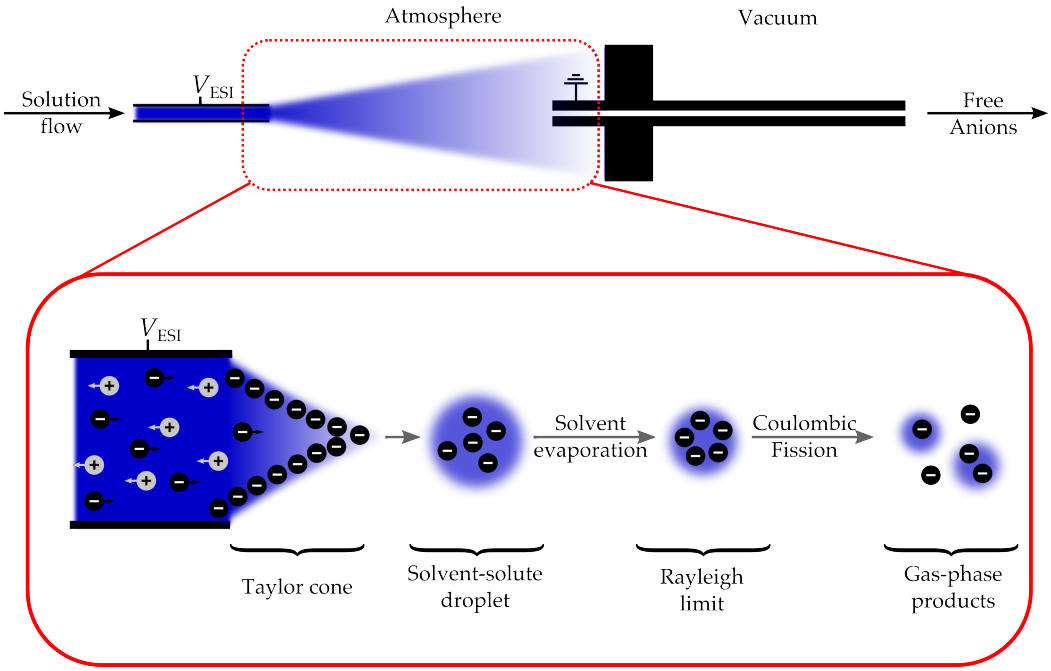

Figure 2.3: Schematic for the process of electrospray ionisation. A dilute solution is flowed through a thin ESI needle, biased at high voltage with respect to the transfer capillary into the vacuum chamber, typically placed 5 mm from the tip of the needle. The high electric field, and solvent flow, lead to the formation of a fine mist of solvent-solute droplets produced by the needle. These droplets subsequently undergo solvent evaporation and Coulombic fission processes while travelling towards and through the transfer capillary, eventually leading to the desired gas-phase products.

strong electric field is created between the ESI needle and the transfer capillary, leading to the formation of a Taylor cone at the tip of the ESI needle, due to the balance of electrostatic forces on the solute and the surface tension of the solution. The flow of the solution through the needle leads to small solvent-solute droplets being released from the tip of the needle and accelerated towards the capillary. During their motion towards (and inside) the capillary, solvent evaporation from the small droplets occurs. If sufficient solvent evaporates from a droplet that the Rayleigh limit is reached,[9] where the available solvent is not sufficient to stabilise the repulsive charges of the solute present, the droplet undergoes Coulombic fission into smaller constituents. These processes repeat until the gas-phase products, lone ions or small clusters, are formed. The efficiency of this process, and the distribution of gas-phase products, can be influenced by changing the pressure conditions in R1, by heating the transfer capillary (thereby aiding solvent evaporation) or through the use of different solvents. To aid alignment with the rest of the machine, both the ESI source and transfer capillary are placed on independent x, y, z-translation mounts.

Formed ions progress through the transfer capillary and into R1 of the vacuum chamber. They are subsequently accelerated from the biased capillary (~ -80 V) towards a pinhole (biased at ~ -60 V) with a ID of 1 mm and travel through this

pinhole into R2 of the vacuum chamber, entering the ion funnel. This is shown in detail in the inset in figure 2.2(a).

Ion funnel

At the beginning of the second differentially pumped chamber, ions enter an ion funnel device, a picture of which is shown in figure 2.2(b). One of the primary experimental challenges with using ESI is to improve transmission of ions into the ultra-high vacuum regime needed for photoelectron spectroscopy. Because ESI functions at atmospheric pressure, transition through a number of regions with intermediate pressures in the region of 10^{-2} Torr is practically unavoidable. In this pressure regime the collision rate with background gas is still very high, rendering standard ion optics, such as Einzel lenses, ineffective. The use of ion guiding devices utilising radio frequency (RF) voltages overcomes these problems.[10] One very compact ion guiding device is an ion funnel, based on previous designs.[11,12] Our version of this device consists of 33 stainless steel electrodes, with a central orifice of ID 3.2 mm, spaced 1.47 mm apart and mounted on two custom made printed circuit boards. Along the electrodes a direct current (DC) voltage ramp is applied, typically starting at -60 V near the end closest to R1, and dropping to -20 V at the other end of the device. This voltage ramp pushes anions along the device. Simultaneously a RF field is applied to all electrodes, with adjacent electrodes receiving potentials π out of phase. The RF field operates at frequencies of $\sim$1.5 MHz and potential differences of 300 V peak-to-peak, acting to radially confine ions along the axis of the device, similar to a two dimensional Paul trap.[13] The rapid switching of the field direction creates alternating saddle points of the electric field on the axis, switching between accelerating and decelerating the ions. Given a sufficiently high RF frequency, this confines and collimates ions along the central axis.

A further challenge with using ESI for photoelectron spectroscopy is the inherently continuous nature of ESI. Therefore, in order to create a pulsed beam of anions with a repetition rate matching that of the laser system, one needs to incorporate an ion trap for stopping and accumulating ions. As the repetition rate of our femtosecond laser system is 1 kHz, and high repetition rates are crucial for the duty cycle of the spectrometer, an ion trap capable of being emptied at that repetition rate is needed. This is not easily achieved with typical ion traps, such as Paul or multipole traps,[13–15] because they require the rapid switching of high RF voltages. In our design we have instead adopted a simple ring electrode trap between the last two electrodes of the ion funnel.[16] This allows us to use a constant RF field along the entirety of the device to radially confine ions, and an additional DC stopping potential is applied to the last electrode of the funnel, stopping ions from leaving the funnel and thus axially confining them.

In order to empty the device, and pulse ions into the next region, the voltage on the last electrode is dropped and ions pushed out through a 1 mm ID pinhole into R3, containing the time-of-flight spectrometer. While the ring electrode trap within the funnel allows for a compact and relatively simple design, a limitation of the current setup is the small trapping volume of around 1 mm^3, which can only hold approximately 10^3 charges due to the space-charge limit.[17,18] A planned redesign for this part of the machine has been manufactured, but not yet implemented. It will be presented, along with other suggested experimental improvements, in Chapter 6.

Time-of-flight

Following trapping and population accumulation in the ring electrode trap, ion packets are ejected into the third differentially pumped chamber (R3) at repetition rates up to 1 kHz. This region contains time-of-flight (TOF) electrodes in a Wiley-McLaren configuration, arranged co-linearly with the ion source.[19,20] The electrodes are mounted on stainless steel rods attached to a top hat mounted onto the flange separating R3 and R4, this entire assembly is shown in figure 2.4. This TOF geometry temporally focusses ions with the same mass-to-charge ratio, which can then be separated by arrival time at the detector (located in R6). The setup consists of three stainless steel electrodes (outer diameter 140 mm, 1 mm thick), arranged sequentially along the beam axis, separated from each other by 30 mm. The first electrode ("repeller") has an open 5 mm diameter orifice at the centre, allowing ion packets to pass through. The second ("extractor") and final ("ground") electrodes both have 5 mm central orifices covered by a high transmission (>88%) stainless steel mesh, allowing ions to pass through, while eliminating any electrostatic lensing effect from fringe fields leaking out the orifice. The electrodes are pulsed to high voltages when ions are located between the extractor and repeller plate, with potential differences of -2.3 kV and -1.9 kV applied to the repeller and extractor respectively, as indicated in figure 2.4. The timing sequence is controlled by a digital delay generator (see section 2.3), and the voltage pulses created by a custom build fast high voltage switch, delivering a fast falling edge (i.e. ground to $-$ve voltage) of $\sim$50 ns. Ion packets are therefore accelerated to kinetic energies of $\sim$ 2 keV along the spectrometer z-axis, and enter the fourth differentially pumped region, separated from R3 by the ground electrode of the TOF setup. The total flight path to the mass spectrometry detector is 1.3 m, and example spectra and calibrations will be given alongside the full description of the detector in section 2.1.2.

Ion optics

After acceleration in the TOF arrangements ion packets enter R4, the final region of the low vaccum part of the machine. Directly after entering R4 the ion

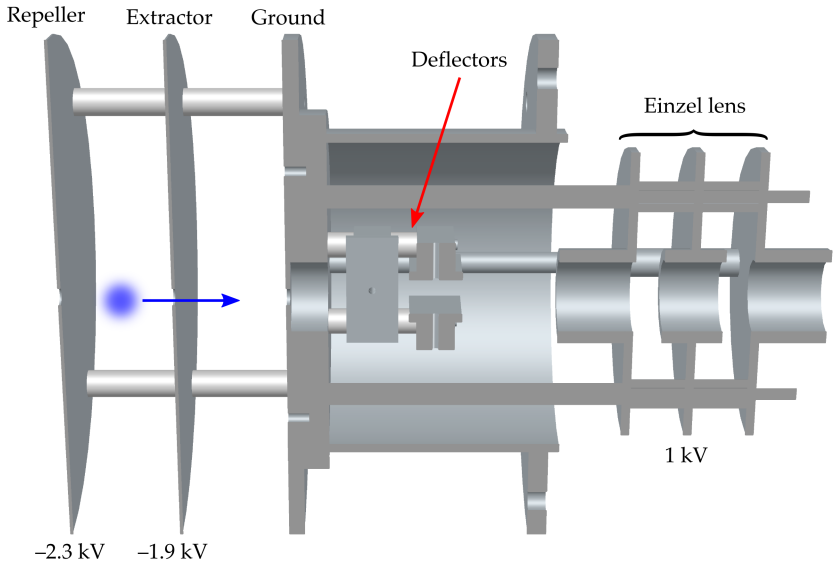

Figure 2.4: 3D rendering of the top hat and flange separating R3 and R4, mounted in this assembly are the time-of-flight (TOF) electrodes, the x,y deflector plates and Einzel lens. Ions are accelerated in the direction shown and temporally separated by mass-to-charge ratio. The deflector plates allow for small corrections to the beam path (x,y directions), while the Einzel lens spatially focusses ions onto the centre of the flight (z) axis.

packets encounter ion steering and focussing optics, shown in figure 2.4. A pair of deflector plates, arranged at right angles to each other and each consisting of two stainless steel plates (30 mm $\times$ 14 mm), are placed 20 mm apart around the beam axis. DC voltages of opposite polarity are applied to the two electrodes of each pair, to allow steering of the beam in the radial (x and y) directions, compensating for any possible misalignments along the setup. A second set of these deflector plates is located after the entrance into region 5, directly past the gate valve separating the low and high vacuum sections.

Directly after passing through the deflector plates, the ions enter a 3 electrode Einzel lens configuration, which spatially focusses ion packets onto the central beam axis, directly comparable to a convex optical lens.[21] The lens consists of three tubular electrodes (figure 2.4), the two outer electrodes are 20 mm long with a 30 mm ID and grounded, whereas the central inner electrode is 16 mm long (30 mm ID) and carries a high voltage, typically $\sim$1 kV. The focal point can be varied by changing the applied potential to the central electrode, and in practice is optimised for maximum signal during an experiment.

2.1.2 High vacuum side

After passing through the ion optics in R4, ion packets travel through a 5 mm pinhole into R5, pumped out by a 150 ls^{-1} turbomolecular pump (Oerlikon Tur-

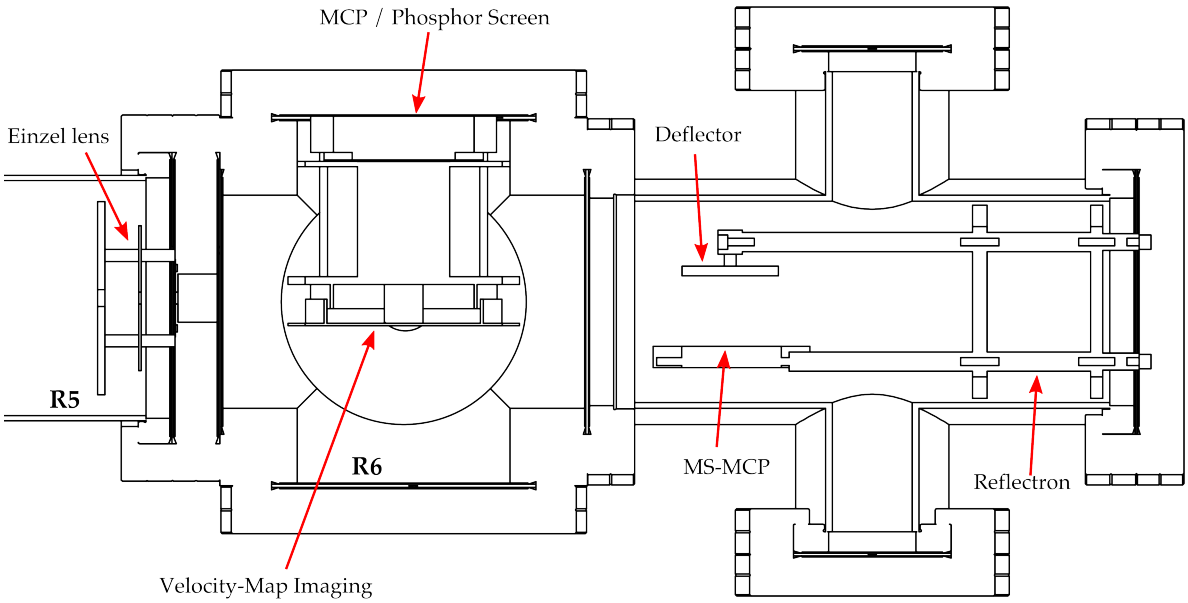

Figure 2.5: Overview of the high vacuum side of the spectrometer, contain regions 5 and 6 with the detector setup. A custom build velocity-map imaging detector is used for photoelectron imaging. The primary ion beam can be monitored by directly measuring ion current as a function of time-of-flight on the microchannel plate (MCP) detector. Alternatively, fragments produced by interaction between the laser and primary ion beam can be separated via a secondary reflectron mass spectrometer.

bovac 151) to typical pressures of 10^{-9} Torr, that can be separated from the low vacuum half of the machine by a pneumatic gate valve. Directly after the pinhole into R5 a second pair of x,y-deflector plates is located, identical to those in R3. The remainder of R5 contains a field-free drift region. At the entrance to the detection region (R6) a secondary Einzel lens is located as shown in figure 2.5. This comprises plate electrodes, the outer ones are grounded and 3 mm thick with OD 80 mm and a 5 mm orifice, and a central electrode of 1 mm thickness and OD 60 mm ID 3 mm that has a high voltage (typically $\sim$1 kV) applied. This lens is used to spatially focus the ion packet tightly into the centre of the interaction region, R6. This is evacuated by a 80 ls^{-1} turbomolecular pump (Oerlikon SL80) to ultimate pressures of 10^{-10} Torr and houses the detector setup, comprising a VMI detector for photoelectron imaging, and a microchannel plate (MCP) detector that can be used to monitor the primary ion beam as a function of TOF from the Wiley-McLaren setup in R3, or to monitor fragment ions produced by laser interactions via a secondary reflectron mass spectrometer.

The laser pulses enter the interaction region in R6 at right angles to the ion beam, and the two intersect in the centre of the VMI detector. In order to minimise any stray light, which could impinge on surfaces and release electrons there, the laser beams pass through a series of laser baffles before and after passing through the interaction region. A cross-sectional cut through a baffle unit is shown in figure 2.6, it consists of a conical skimmer with a central aperture of 4 mm and two

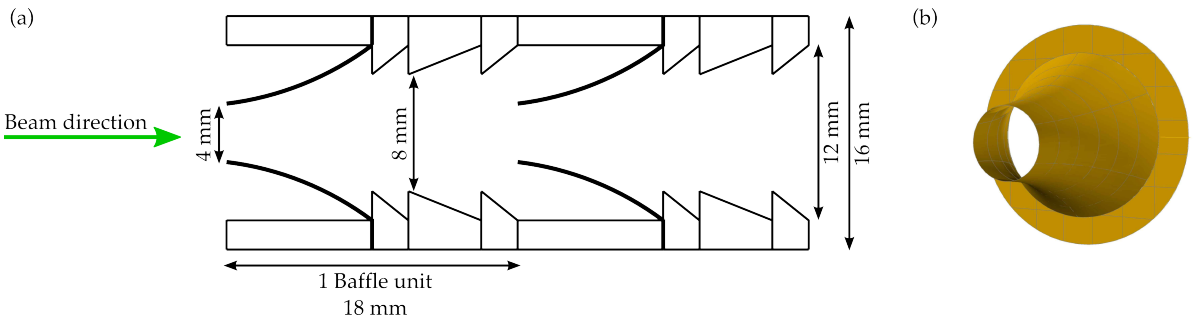

Figure 2.6: Schematic of the laser baffle setup used to minimise the effects of stray light. (a) Cut through the baffle setup with important dimensions indicated. All baffles and spacers are manufactured from oxygen-free copper and then oxidised. (b) Rendering of a single baffle, made by electroforming. The small 4 mm orifice is polished to a knife edge before oxidation, the thickness of the baffle is ∼200 μm.

types of spacers cut at different angles. This geometry was chosen to maximise the number of reflections needed for stray light to enter the interaction region, therefore maximising the chances of absorption. All baffles and spacers are machined from oxygen-free copper, which was chemically oxidised to maximise absorption.[22] The baffles were electroformed and the edges polished to a sharp finish. On entering the spectrometer through a 1 mm thick calcium fluoride window, the beams pass through a total of 8 baffle units arranged without gaps in between. After leaving the interaction region the beams travel through a further 7 baffle units before leaving the chamber through a fused silica window cut to Brewsters' angle to minimise back reflections.

Mass spectrometry detector

A 3D rendering of the ion detector is shown in figure 2.7. It consists of a MCP pair in a chevron geometry, coupled to a stainless steel anode, for the detection of charged particles. This is located parallel to the beam (z) direction, and therefore in order for ions to impact on the detector a deflector plate is located above it. This can be pulsed to high negative voltages (typically ∼1 kV), deflecting the trajectory of the anion beam so it strikes onto the detector. The reason for this seemingly complex arrangement is twofold: a secondary mass spectrometer is located further down the beam direction and ions need to be able to reach this without deflection from the interaction region. Secondly, the measurement of the primary ion beam should be taken as close as possible to the laser-ion beam interaction point, in order for the spatial and temporal focussing to be similar in both cases. This secondary mass spectrometer consists of a reflectron setup,[20] described in detail below, that allows the separation of ionic fragments produced by the laser-parent anion interaction. As all fragments originating from the same parent anion will carry the same velocity, a secondary mass spectrometer is necessary to separate them by mass-to-charge ratio. This reflectron detector also works with the primary ion MCP detector, by changing the timing for the de-

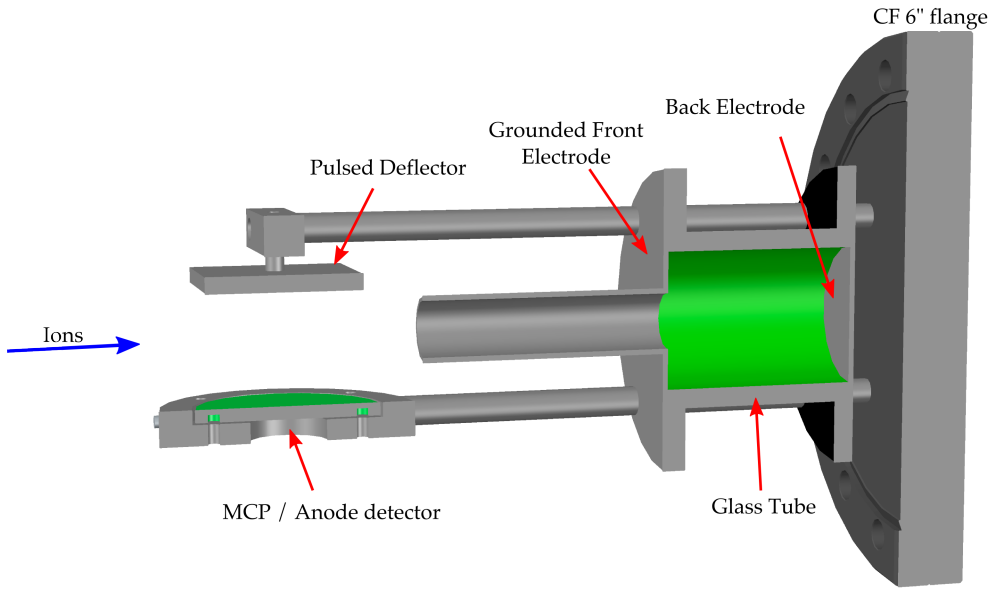

Figure 2.7: 3D rendering of the mass spectrometry setup. A deflector plate guides ions onto a MCP coupled anode detector mounted parallel to the beam direction. This allows monitoring of the primary ion beam via the Wiley-McLaren setup in R3, or analysis of laser produced ionic fragments via a secondary reflectron. This is mounted behind the MCP detector and consists of a resistive glass tube to create a smooth electric field gradient, separating ions by mass-to-charge ratio and turning them back towards the MCP detector where the are monitored. The timing of the high voltage deflection pulse determines which setup is used.

flector pulse, thereby allowing ions to enter the reflectron, be turned around according to their mass-to-charge ratio, and on their return trajectory they are deflected onto the detector by the deflector plate.

An example mass spectrum of the primary ion beam is shown in figure 2.8, collected by electrospraying a solution of Bromanil (tetrabromo-*p*-benzoquinone). The parent anion is observed between 49.0 μs and 49.5 μs, with a typical tetrabromo isotope pattern, as shown in the inset. The most abundant isotopic mass is 423.66 Da, and clearly separated peaks are observed for adjacent isotopes, yielding a mass resolution $\frac{m}{\Delta m} > 200$. The inset shows the effect of irradiation of the most abundant parent anion isotope with a nanosecond laser pulse, sufficiently energetic to detach an electron. Strong depletion of a single isotope is observed, therefore allowing, if desired, the collection of isotope specific photoelectron spectra.

The reflectron mass spectrometer, shown in figure 2.7, utilises a resistive glass tube (Photonis Inc., length 53 mm, ID 40 mm) for the production of a smooth electric field gradient inside. This tube is sandwiched between two stainless steel electrodes (OD 80 mm) at the front and back. The back electrode is solid and carries a high negative voltage (typically -2.8 kV), whereas the front plate has a central orifice of 15 mm diameter and is grounded. This orifice is covered

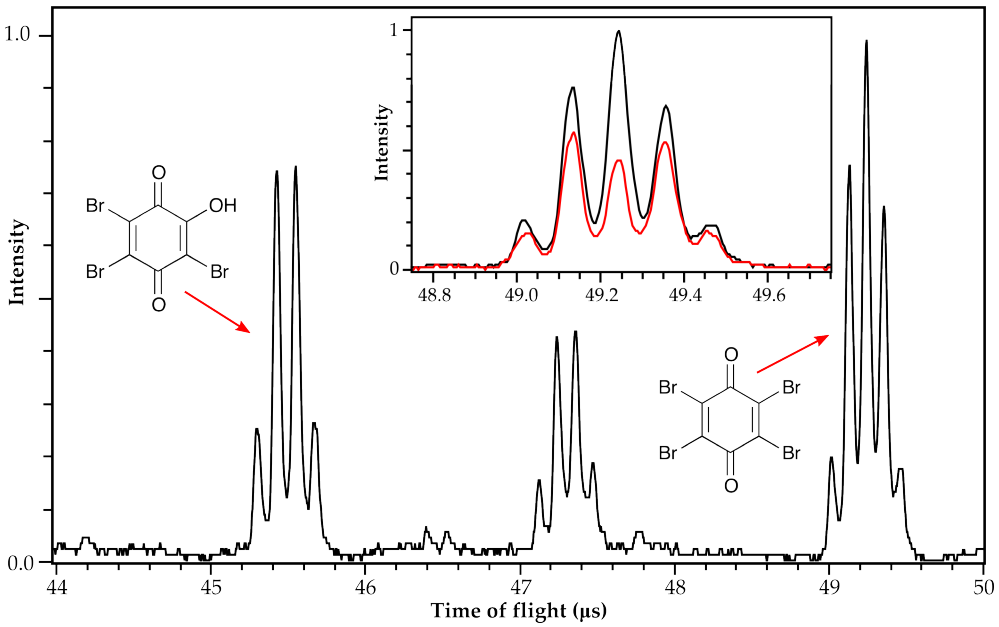

Figure 2.8: Example mass spectrum produced by electrospraying a solution of Bromanil, whose parent anion peak is observed around 49.2 μs, as indicated. Clear isotope patterns are observed, yielding a mass resolution > 200. The inset shows the parent anion peak (black) and the effect of irradiation of the most abundant isotope with a nanosecond laser pulse (red), showing strong isotope selective depletion.

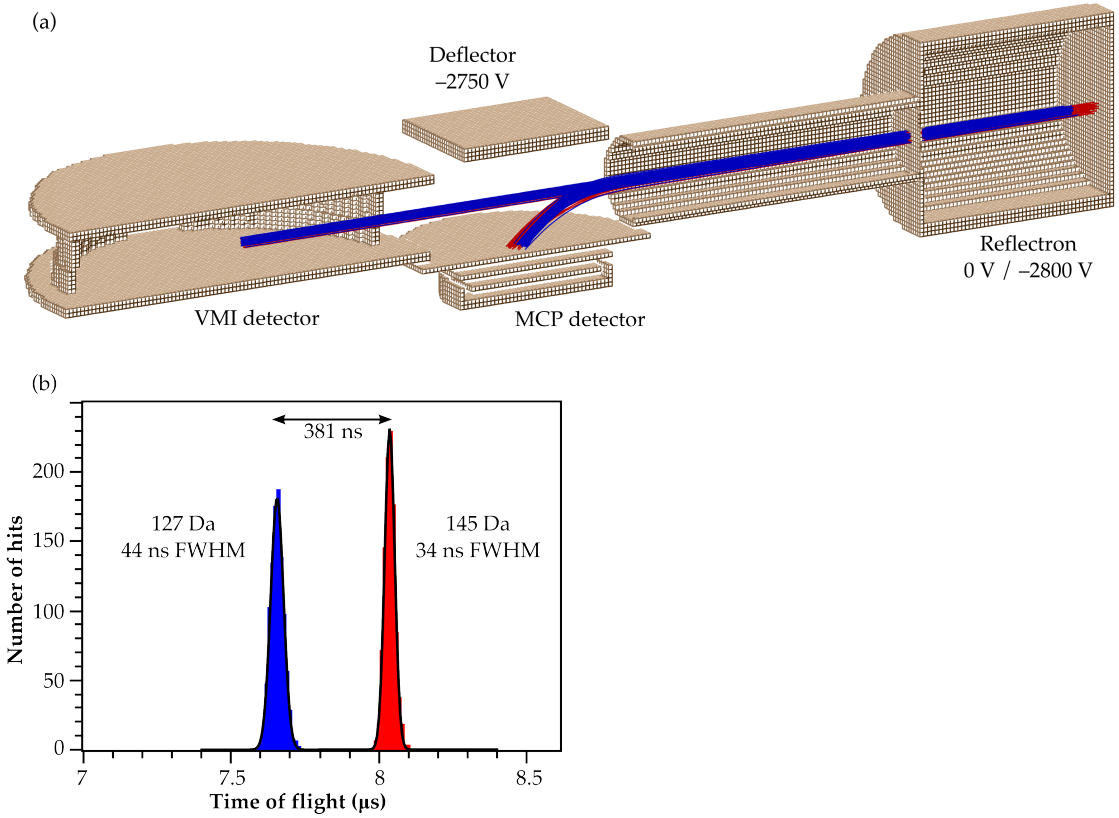

Figure 2.9: Simulation of the reflectron mass spectrometer. (a) SimIon geometry used. Ions of 127 Da (blue) and 145 Da (red) are generated in the centre of the VMI detector, with an initial velocity of 55 mmμs^{-1} towards the reflectron. The different mass-to-charge ratios penetrate the reflectron to different degrees before being turned around along their initial trajectories. (b) Histogram for the time-of-flight of 1000 trajectories each, showing a clear temporal separation between the two masses.

with a high transmission (88%) stainless steel mesh. The front plate furthermore has a stainless steel tube welded on and protruding away from the reflectron for 65 mm, to minimise the effect of stray fields on the anions on the way to the reflectron and back. The application of a strong potential difference across the glass tube creates a constant electric field gradient inside the tube, between the two ends, and this effectively acts like a stack of resistively coupled ring electrodes, albeit an infinite number of infinitely small ring electrodes. This setup acts like an "ion mirror", where incoming ions are decelerated and turned around, leaving the reflectron on the same trajectories they entered, before being deflected onto the detector.[20] How far an ion penetrates into the glass tube, and therefore its overall time of flight, will depend on the mass-to-charge ratio, as all incoming ions have the same initial velocity. Figure 2.9(a) shows a SimIon[23] simulation of the entire reflectron setup. Anions are generated in the centre of the VMI detector (described in detail in the next section) with a Gaussian distribution of initial positions (full width at half maximum, FWHM, of 0.5 mm) with masses of 127 Da (blue trajectories) and 145 Da (red trajectories), corresponding to I^- and $I^-(H_2O)$. The initial velocities are also distributed with a Gaussian distribution, centred around 55 mmμs^{-1} (corresponding to a kinetic energy of 2 keV for I^-), with a FWHM of 0.5 mmμs^{-1}. The shown trajectories are for the indicated voltages on the deflector and reflectron, which has been approximated as a stack of 25 ring electrodes. The deflector pulse is applied 5 μs after ion creation, when the ions are located inside the reflectron tube. Figure 2.9(b) shows a histogram of recorded flight times for 1000 trajectories each, and a Gaussian distribution fitted to the histogram. The peaks are well separated by 381 ns, and each have a FWHM of $\sim$40 ns, allowing easy discrimination between the two on a standard MHz oscilloscope.

Velocity-map imaging detector

The VMI detector in our machine, which has been described in detail in a recent publication,[2] has been designed specifically for use with a charged particle beam. The VMI technique significantly increases the quality of charged-particle images by focussing particles with the same initial velocity vector onto the same spot on the imaging detector, regardless of initial position. While typically VMI setups, such as the original one by Eppink and Parker,[24,25] utilise high voltages for the extraction of electrons, this is not practical for use with anions, whose trajectories will be affected by any static electric field. Furthermore, there are situations where large extraction fields are undesirable, such as for the investigation of Rydberg states, due to the large Stark effect in these system.[26] The design in our laboratory uses very small extraction fields, typically less than 5 Vcm^{-1}, and is significantly simpler and more compact than previous imple-

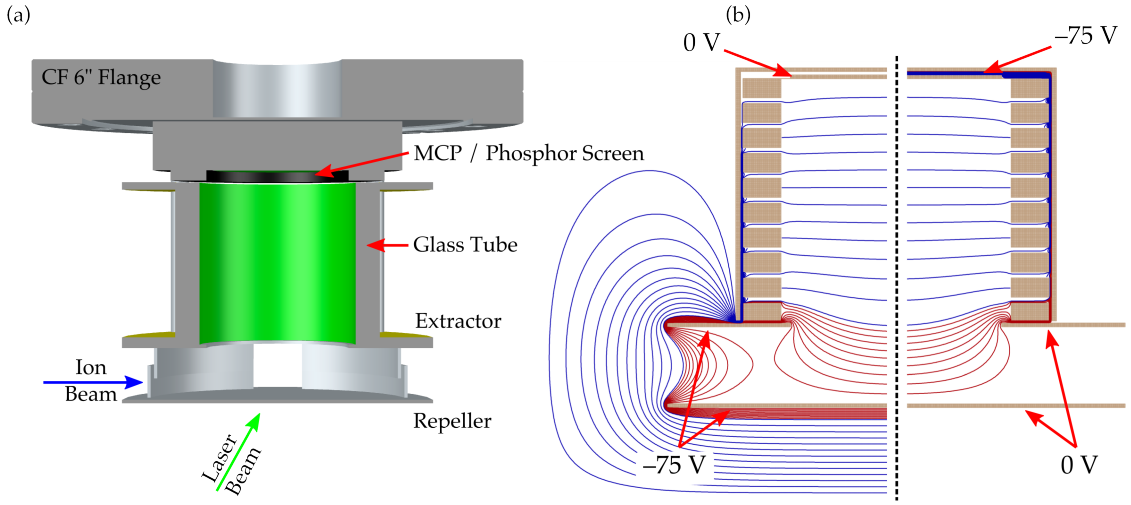

Figure 2.10: (a) 3D rendering of the velocity-map imaging (VMI) detector, consisting of two μ-metal electrodes and a resistive glass tube connecting the extractor electrode with the front of the position sensitive detector. For details and dimensions see text. (b) SimIon simulation of electric field lines inside the VMI setup, blue lines are spaced by 5 V, red lines by 1 V. Left: conventional imaging with a negative voltage on the electrodes and the detector grounded. An electrostatic lens is produced, however large stray electric field are created between the outside of the VMI and the surrounding vacuum chamber. Right: inverted voltages pulling electrons towards a positively charged detector, maintaining the lensing effect while avoiding stray fields.

mentations of VMI.

A 3D rendering of the VMI detector is shown in figure 2.10(a). It consists of two μ-metal electrodes (OD 96 mm, thickness 1 mm). The lower electrode (repeller) is solid, while the upper electrode (extractor) has a 44 mm orifice in the centre to allow electrons to pass through. The electrodes are separated by 16 mm and each has radial shielding (height 10 mm) to avoid any stray electric fields penetrating into the interaction region. This is welded (from the outside) onto the plates at ID 77 mm (extractor) and ID 81 mm (repeller), such that it overlaps without touching. Square holes of 16 mm are cut into this radial shielding perpendicular to each other, to allow the ion and laser beams to pass through. Located above the extractor plate, an in electrical contact with it, a resistive glass tube is situated (length 49.9 mm, OD 63.5 mm, ID 48.3 mm, Photonis Inc.), the other end of which is in electric contact with the front plate (2 mm thick stainless steel ring, ID 44 mm) of a position sensitive detector (chevron MCP pair coupled to a 40 mm diameter phosphor screen, Photek Inc.). Both ends of the glass tube are metallised to ensure good electrical conductivity between the touching surfaces. By applying a potential difference to the ends of the glass tube a region of constant electric field gradient is created inside, identical to the principles behind the reflectron. To eliminate stray magnetic fields, the outside of the glass tube is surrounded by a μ-metal cylinder. In our particular geometry no separate ground electrode is necessary, but the detector front face acts as the ground electrode. This forms the required electrostatic lens to achieve velocity mapping,

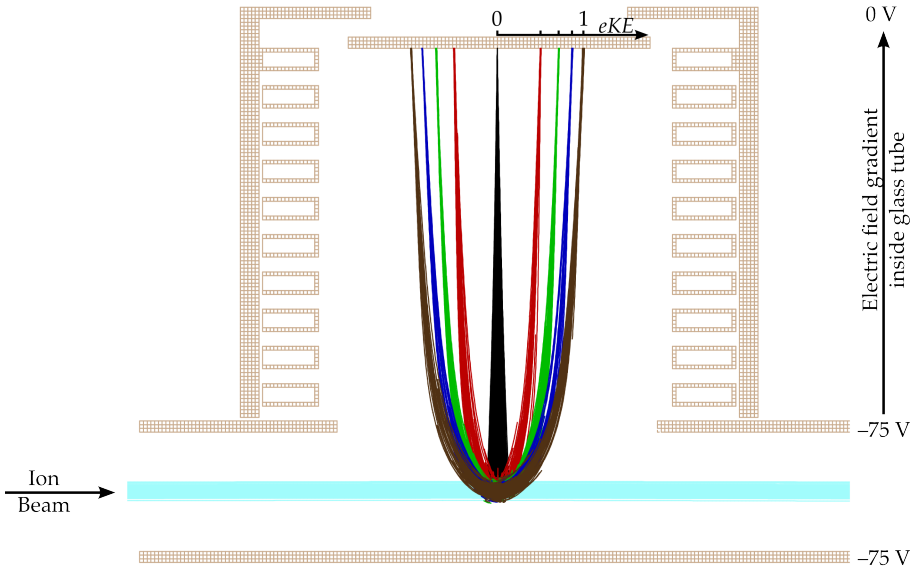

Figure 2.11: SimIon simulation of trajectories inside the VMI detector (shown is a thin slice through the centre of the detector), with both electrodes at −75 V. Shown in light blue is an anion beam of 2 keV energy and mass-to-charge ratio of 127 Da, this undergoes less than 0.1° deflection when passing through the setup. Inside the VMI, trajectories for electrons with 0.00, 0.25, 0.50, 0.75 and 1.00 eV kinetic energy are shown. Electrons are created with a Gaussian distribution (FWHM 0.5 mm) in the centre of the interaction region. The velocity mapping effect is clearly observed, with electrons focussing on the detector plane.

even when both VMI electrodes are held at the same potential. In these cases the focussing conditions can be varied by changing the ratio of the extractor orifice to the separation between the two electrodes.[2,27] For this design the ratio is 44 mm:16 mm = 2.75, which leads to velocity mapping conditions 60 mm from the centre of the electrodes, which is the location of the position sensitive detector. The entire setup is mounted onto a 6 inch CF flange, which fits into a 6 inch cube, with the interaction point at the centre of the cube. Due to the identical voltages on the electrodes, the actual voltage gradient, and therefore the electric field, is very small, thereby minimising the effect on the primary ion beam travelling through the setup. The achieved focussing condition, and the limited effect on the ion beam, can be seen in the trajectory simulations in figure 2.11. These SimIon[23] simulations include a primary ion beam of 2 keV kinetic energy and mass-to-charge ratio of 127 Da (corresponding to I^-), and electrons created with kinetic energies of 0.00, 0.25, 0.50, 0.75 and 1.00 eV. Electrons are formed with a Gaussian distribution of FWHM 0.5 mm around the centre of the interaction region. Both electrodes are set to −75 V, and the resistive glass tube is approximated by a stack of 10 identical ring electrodes, forming a constant electric field gradient between the extractor plate and the front of the position sensitive detector, which is grounded. Focussing of the electron trajectories at the detector plane is clearly observed, while the primary ion beam undergoes a deflection of less than 0.1°.

The utilisation of a resistive glass tube leads to the creation of a very smooth electric field gradient inside the tube, as can be seen from field line simulations in SimIon,[23] shown in figure 2.10(b). In these simulations the glass tube is again approximated by a stack of 10 equidistant ring electrodes. Shown on the left in figure 2.10(b) is the conventional imaging configuration, negative voltages (in this case -75 V) are applied to the repeller and extractor electrode, while the front of the detector is grounded. This creates the desired electrostatic lens from the inhomogeneous field leaking out through the orifice in the extractor. However, this also leads to significant stray electric fields surrounding the VMI setup, due to the grounded walls of the vacuum chamber. These can have a large effect on any charged particle beam, especially the lensing fields formed at the entrance and exit of the electrode plates. Stray fields can be completely avoided by "pulling" electrons towards the detector, rather than "pushing" them. This is achieved by reversing the applied fields and grounding both electrodes, while floating the entire position sensitive detector at a positive voltage. The resultant electric field lines are shown on the right of figure 2.10(b). This configuration eliminates all undesireable electric fields around the detector, while maintaining the electrostatic lens required for VMI detection.

The resultant photoelectron image on the phosphor screen is captured by a charge-coupled device (CCD) camera (Basler A312f, 512×512 pixels) and send to a computer for further data analysis and image deconvolution, which is described in detail in section 2.3, yielding photoelectron spectra (PES) and photoelectron angular distributions (PADs). A PES of iodide, collected with 268 nm (4.626 eV) femtosecond laser pulses, has already been presented in figure 1.14. This yields an energy resolution for our imaging setup of $\frac{\Delta E}{E} = 5\%$ as seen for the $^2P_{3/2}$ peak, which has a FWHM of 73 meV and an expected electron kinetic energy (*eKE*) of 1.567 eV (electron affinity of iodide is 3.059 eV[28]). The spin-orbit splitting in iodide is 0.943 eV, such that the $^2P_{3/2}$ peak is expected at 0.624 eV, as observed. Below *eKE*s of $\sim$1 eV the achieved energy resolution is limited by the bandwidth of the femtosecond detachment laser, explaining the slightly lower resolution achieved for the $^2P_{1/2}$ peak in figure 1.14.

Shown in figure 2.12 are PES and images for the photodetachment from iodide with a nanosecond laser pulse at 355 nm (3.496 eV). The spectra in 2.12(a) and (b) demonstrate the feasibility of "pulling" electrons towards the detector with ground VMI electrodes, as (a) shows the spectrum and photoelectron image for the conventional approach (electrodes at -75 V and grounded detector front), while (b) has the detector at $+75$ V. In this case a large amount of noise was observed on the imaging detector when the electrodes were grounded, due to stray electrons from surfaces or ionisation gauges entering the VMI setup and being

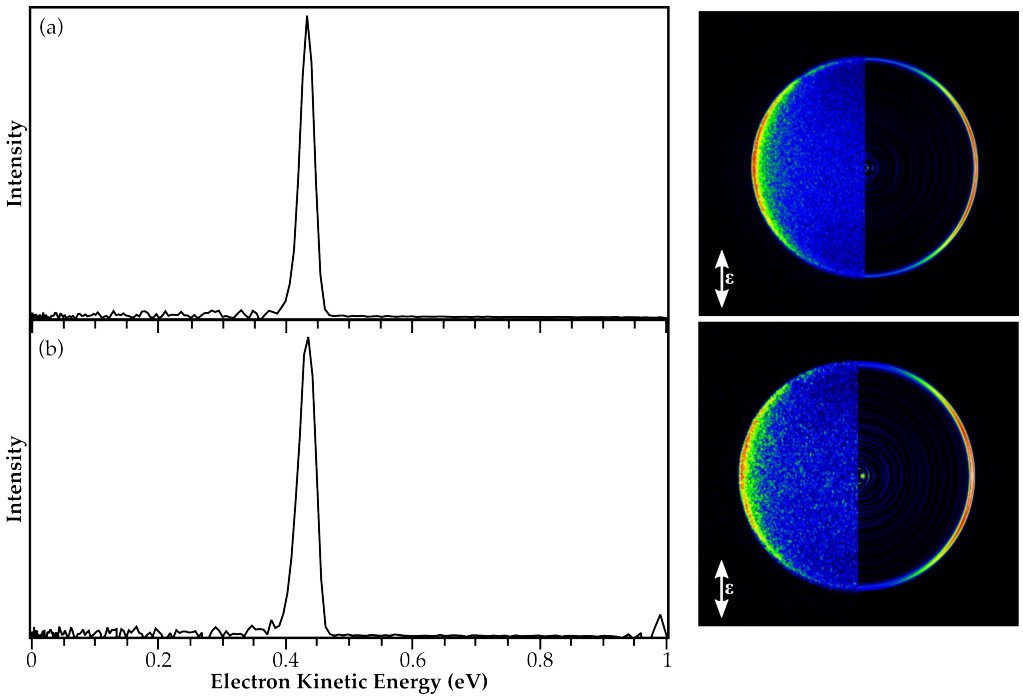

Figure 2.12: Photoelectron spectra for the detachment from iodide collected at 355 nm (3.496 eV). (a) Conventional VMI arrangement (electrodes at -75 V, detector front grounded) (b) inverted imaging voltages with the detector floating at $+75$ V and the electrodes at < 2 V. Shown on the right are the raw (left half) and reconstructed (right half) photoelectron images with the laser polarisation indicated by the arrow.

drawn up towards the detector. This could be completely avoided by applying a small negative voltage of -2 V to the electrodes, yielding the PES and photoelectron image shown in 2.12(b). Both of these spectra furthermore demonstrate the validity of using very low extraction fields for photoelectron imaging. Electrode voltages of -75 V lead to an extraction field in the interaction region of less than 4 Vcm^{-1}.

The ability of utilising even lower extraction voltages is shown in figure 2.13, showing the photoelectron image and PES for the detachment from bromide at 355 nm (3.496 eV). The electron affinity of Br^- is 3.364 eV,[29] leading to expected *eKE*s of 0.132 eV. This was imaged with the VMI electrodes at a voltage of -9 V, supplied by a household 9 V block battery, and the front of the detector grounded. This leads to an extraction field of < 0.5 Vcm^{-1} in the interaction region. Observed photoelectron intensities are significantly lower for these low fields, due to the reduced impact energy of electrons on the MCP detector. Nonetheless a satisfactory photoelectron image was collected, as shown in figure 2.13, and the PES yielded a peak with FWHM 10 meV, and therefore a resolution of $< 8\%$. However, some minor distortions are apparent in the photoelectron image (a minor stretching along the vertical axis and a tilt of the image with respect to the laser polarisation axis). These are primarily from stray electric fields which have a more pronounced effect on electrons which, due to the low

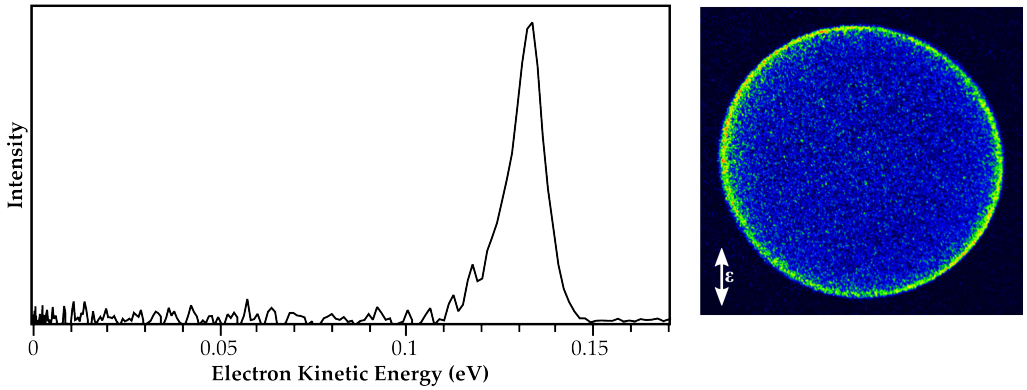

Figure 2.13: Detachment from bromide at 355 nm, collected with the electrodes at 9 V, provided by a block battery, and the detector grounded. Slight distortions are observed, but a resolution of $< 8\%$ is achieved. Shown on the right is the raw photoelectron image, with the laser polarisation indicated by the arrow.

extraction voltages, now have a significantly longer time-of-flight before striking the detector. More careful design and shielding should be able to reduce these artefacts and restore a resolution of 5%. While this low extraction field imaging is very sensitive to any stray electric fields, it is in principle less susceptible to magnetic fields, due to the lower velocity of the electrons and the resulting smaller Lorenz force acting on them.[30]

2.2 Laser Setup

Femtosecond laser pulses for pump-probe photoelectron spectroscopy are derived from a commercial solid-state laser system, based on a Ti:Sapphire oscillator and regenerative amplifier. A basic layout of the laser setup is shown in figure 2.14, it consists of a *Tsunami* series oscillator (Spectra Physics) that is pumped by a 5 W continuous wave diode pumped Nd:YAG laser (Spectra Physics *Millenia* series). The oscillator provides average output powers of 500 mW at a repetition rate of 76 MHz. These are seeded into a *Spitfire XP Pro* regenerative amplifier (Spectra Physics), where pulses are picked out at 1 kHz repetition rate by a Pockels cell and amplified in a Ti:Sapphire crystal, pumped by a diode pumped nanosecond Nd:YLF laser (Spectra Physics *Empower*), providing an average power output of 25 W. The fundamental output from the regenerative amplifier is 35 fs pulses, centred at 800 nm (1.55 eV), at a repetition rate of 1 kHz and with a pulse energy of 3 mJ. A typical fundamental spectrum from the regenerative amplifier is shown in figure 2.14(a)

The fundamental output is split into several beamlines. Half of the available power (1.5 W) is used to pump a *TOPAS* automated OPA (Spectra Physics), described in detail in the following section, providing tunable output in the infrared (IR). The remaining fundamental is split again, with half of the remainder

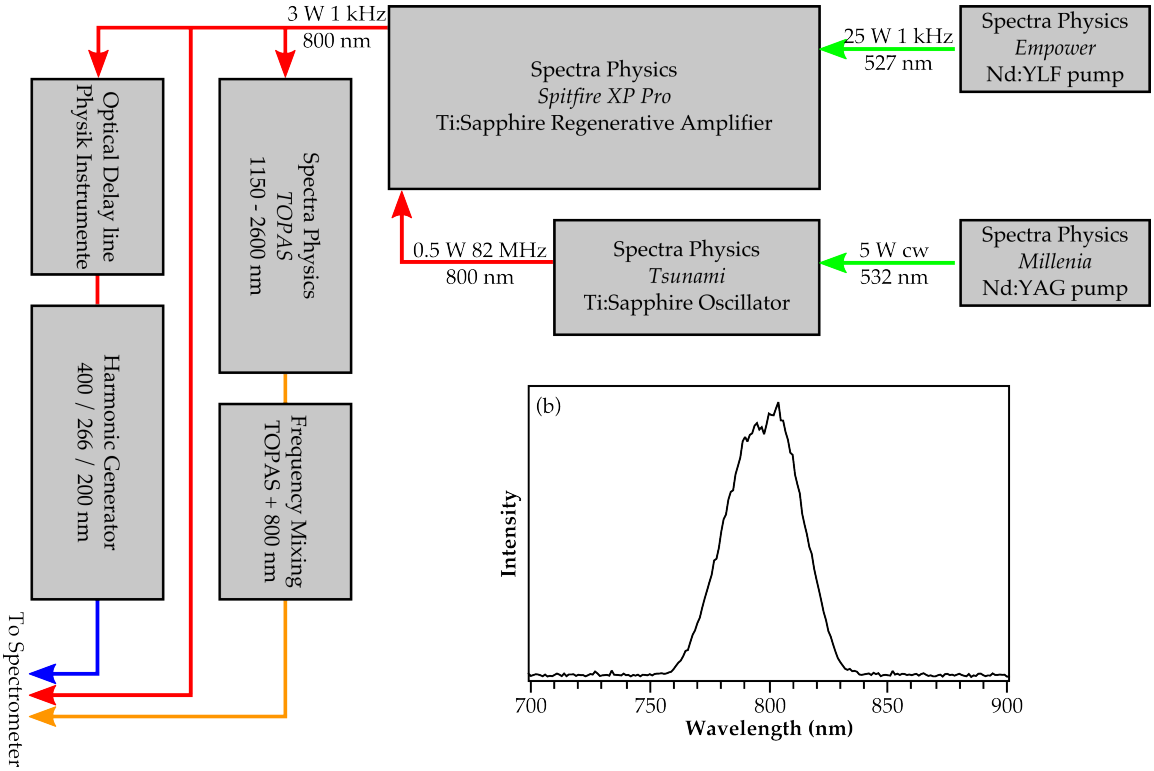

Figure 2.14: Overview of the laser setup. A commercial Ti:Sapphire oscillator and regenerative amplifier produce a fundamental output of 800 nm pulses with 3 mJ energy at a repetition rate of 1 kHz. Half of the available power is used to pump an automated optical parametric amplifier, the output of which is subsequently frequency mixed with remaining fundamental light to achieve tunability in the visible. The remaining fundamental power is split further, with half pumping a harmonic generator producing 2nd, 3rd and 4th harmonic light, and the remainder available as a high power 800 nm probe. All beams are recombined co-linearly before entering the spectrometer. Shown in (b) is a typical output spectrum of the fundamental beam.

(750 μJ) passing through a motorised optical delay line (Physik Instrumente) to provide a variable delay between pulses, before entering a harmonic generator for frequency doubling, tripling and quadrupling. The remaining 750 μJ of the fundamental beam remain unchanged and are recombined co-linearly with the output from the *TOPAS* and harmonic generator beamlines before entering the photoelectron imaging spectrometer through a 1 mm thick calcium fluoride window. Inside the machine the laser beams travel through a series of baffles before and after reaching the interaction point, and exit the spectrometer through a 2 mm thick window arranged at Brewsters' angle to minimise back reflections. The achieved time resolution in pump-probe experiments depends on the cross-correlation between the two pulses. Example cross-correlations are shown in figure 2.15 for 400 nm + 800 nm and 480 nm + 800 nm pump-probe pairs. The 400 nm is produced by the harmonic generator setup and the cross-correlation with the fundamental has a FWHM of 61 fs (2.15(a)), whereas the 480 nm pump pulse is produced via frequency mixing of the *TOPAS* output with 800 nm light and yields a cross-correlation of 108 fs with the fundamental (2.15(b)).

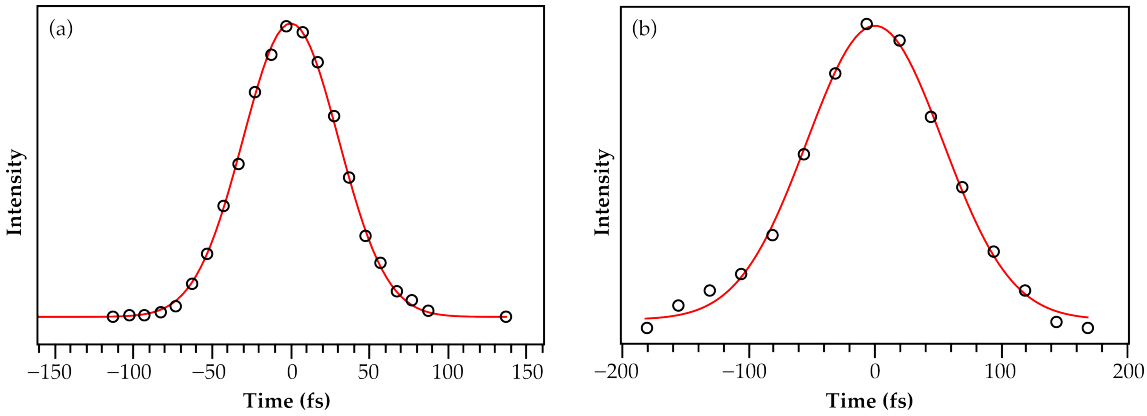

Figure 2.15: Measured intensity cross-correlations between pump and probe pulses at 400 nm + 800 nm (a) and 480 nm + 800 nm (b). The Gaussian fit yields a FWHM for the cross-correlations of 61 fs and 108 fs respectively.

2.2.1 Frequency conversion

In order to achieve photon energies in the ultraviolet (UV) part of the spectrum, and to gain tunable radiation in the visible part of the spectrum, several different frequency conversion schemes are employed, all of which are based on non-linear optical processes. Non-linear optics are based on the polarisation response $\vec{P}$ of a material, that becomes non-linear when high electric fields are incident, such as those produced from ultrafast lasers. In this case higher order contributions can have non-negligible effects and the polarisation vector becomes a summation of higher order terms,[31,32]

$$\vec{P} = \epsilon_0(\chi_1\vec{E} + \chi_2\vec{E}^2 + \chi_3\vec{E}^3 + ...) \tag{2.1}$$

where $\vec{E}$ represent the incident electric field, the constants χ_n are the n^{th} order susceptibilities and ϵ_0 is the permittivity of free space. This non-linear electric response can be utilised for the production of frequency multiples (harmonics) of an incident frequency. Consider an incident electric field $\vec{E}$ given by

$$\vec{E} = E_0 e^{-i\omega t} + E_0 e^{i\omega t}, \tag{2.2}$$

where ω is the frequency of the radiation. If this is incident on a material with a non-zero second order susceptibility χ_2 (such as a non-centrosymmetric optical crystal), the resulting polarisation response in the medium is obtained by substituting into equation 2.1;

$$\vec{P} = \epsilon_0(\chi_1(E_0 e^{-i\omega t} + E_0 e^{i\omega t}) + \chi_2(2E_0^2 + E_0^2 e^{-2i\omega t} + E_0^2 e^{+2i\omega t})) \tag{2.3}$$

$$\vec{P} = 2\epsilon_0\left(\chi_1 E_0 \cos(\omega t) + \chi_2 E_0^2 \cos(2\omega t) + 2E_0^2\right). \tag{2.4}$$

This process thus leads to the creation of an electric field with twice the incident

frequency, second harmonic generation (SHG). It furthermore becomes apparent that if two electric fields are incident on a non-linear optical material, a field is generated at the sum and the difference between the two incident frequencies, termed sum-frequency generation (SFG) and difference frequency generation (DFG). This is the basis for the harmonic generation stage. It is also possible to generate two photons at different frequencies from a single incident photon, subject to overall conservation of energy. This is the operational principle for the optical parametric amplifier (OPA). All non-linear optical processes are sensitive to phase matching between the involved photons, and the total sum of the wavevectors k of all photons must add up to zero. In the case of SHG, with k_1 and k_2 the wavevectors of the incident photons and k_3 the wavevector of the produced SHG photon, the phase matching relationship becomes

$$\Delta k = k_3 - k_2 - k_1 = 0. \tag{2.5}$$

In practice the phase matching can be tuned by rotating the non-linear medium used for the frequency conversion relative to the polarisation direction of the incident radiation. This property also allows the tuning of the frequencies produced in an OPA.

Optical parametric amplifier

A commercial automated optical parametric amplifier (OPA) is used for the production of tunable pulses across the near-IR and IR (1150 - 2600 nm). The OPA uses a small portion of the input fundamental to produce a white light continuum, via focussing to high intensities inside a sapphire plate. The resultant continuum is then used as a seed and spatially and temporally overlapped with a small part of the fundamental beam inside a β-Bariumborate (BBO) non-linear crystal, acting as a pre-amplifier. This leads to the production of a signal (1150 - 1600 nm) and idler (1600 - 2500 nm) beam, which are subsequently amplified with the large remainder of the fundamental pump beam inside a further BBO crystal.[33] The exact frequencies can be tuned by changing the phase matching conditions inside the BBO crystals, and signal and idler are linked by energy conservation.

In order to achieve tunable pulses across the visible part of the spectrum, the signal output from the OPA is frequency mixed with remaining 800 nm fundamental, or frequency doubled. The former is achieved with a type-I BBO crystal straight behind the output of the OPA, using the remainder of the OPA 800 nm pump beam, which is already temporally and spatially overlapped with the signal beam. This produces femtosecond pulses with energies of 50 - 100 μJ from 470 - 535 nm. For frequency doubling of the OPA signal beam, the remaining 800 nm pump is blocked inside the OPA and the signal passed through a type-

I BBO crystal, yielding pulses from 580 - 750 nm with $\sim$50 μJ pulse energies. In both cases the remaining IR radiation is split from the visible using a cold mirror, a dichroic material that transmits IR radiation but reflects across the visible. Pulses are then combined co-linearly with the output from the harmonic generator before being send into the spectrometer.

Harmonic Generator

The custom build harmonic generator utilises the principles of SHG and SFG and provides access to the second (400 nm), third (266 nm) and fourth (200 nm) harmonic of the 800 nm fundamental and is based on previous designs.[34,35] The incoming fundamental passes through a variable iris and a type-I BBO non-linear optical crystal, producing the second harmonic. The crystal is mounted on a two-axis rotation mount to optimise the phase matching and maximise the SHG output. The two frequencies are subsequently separated with a dichroic mirror, the remaining fundamental passes over a variable manual delay stage, to allow temporal overlap with the SHG pulse, and through a half-wave ($\lambda/2$) plate to rotate the polarisation by 90°, before being recombined with the 400 nm using a second dichroic mirror. The recombined pulses are then incident on second type-I BBO crystal, leading to frequency mixing and production of the third harmonic (266 nm). The output of the third harmonic can be optimised using the temporal delay between the fundamental and second harmonic pulses, as well as rotation of the crystal. To produce the fourth harmonic of the fundamental, the 266 nm beam is separated from the remainder in a dichroic mirror. The fundamental travels over a further manual delay line and through a $\lambda/2$ waveplate, before co-linear recombination of the pulses. They are then send into a third type-I BBO crystal, leading to production of 200 nm pulses. The efficiency of this process can be optimised by tuning the temporal delay and the phase matching. In practice, the desired harmonic is picked off from the setup with a dichroic mirror, or the process stopped once the harmonic of interest is produced by removing any further non-linear crystals. Produced harmonics are combined co-linearly with the *TOPAS* output before being send into the spectrometer.

2.3 Data Acquisition and Analysis

The data acquisition routine in our laboratory is controlled using a LabView (National Instruments Inc.) virtual instrument (VI), while the experimental parameters and timings of the anion beam machine are controlled through a digital delay generator (DDG, Highland Technologies P400). A flow diagram for the entire experimental routine is shown in figure 2.16. The master trigger that starts the experimental cycle is provided by the laser system, from the trigger output of the regenerative amplifier pump laser. This input defines t_0 for the DDG which

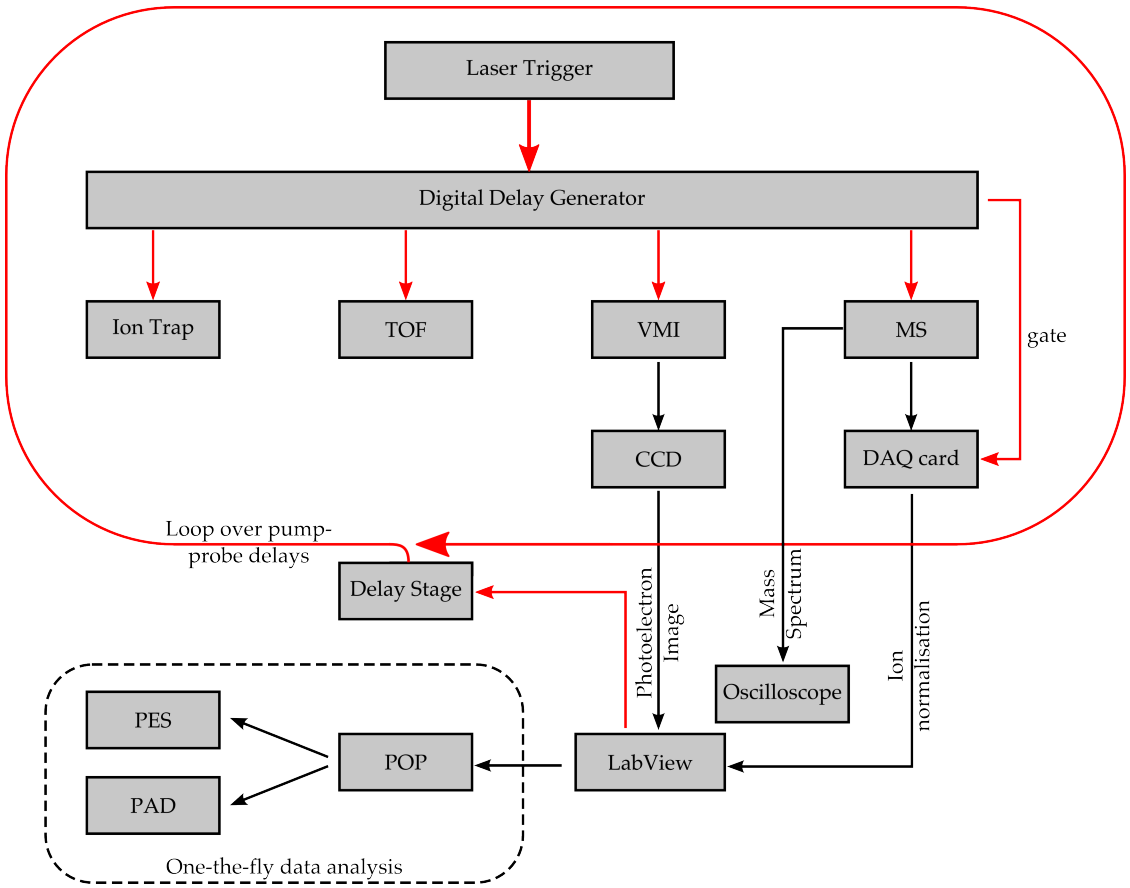

Figure 2.16: Flow diagram for the data collection process, red arrows indicate control of a process, and black arrows indicate flow of information. Data collection is controlled by a LabView VI and experimental timings by a digital delay generator (DDG), with the master trigger provided by the laser. The DDG controls the ion trap, time-of-flight (TOF), velocity-map imaging (VMI) and mass spectrometer (MS) . VMI images are recorded by a CCD camera and forwarded to LabView for processing. Collected MS can be viewed on an oscilloscope, but are also captured by a DAQ card to provide ion signal normalisation. This cycle is repeated for all pump-probe delays, controlled by LabView using the optical delay line. VMI images are analysed on-the-fly using the polar-onion peeling (POP) algorithm, providing photoelectron spectra (PES) and angular distributions (PAD).

controls the timings for the ion trap, Wiley-McLaren TOF electrodes, the VMI detector and the deflector guiding ions onto the mass spectrometry detector. As the ion trap and TOF need to be triggered before t_0, these are triggered by the previous laser pulse for the next laser pulse (i.e. if running at a repetition rate of 1 kHz a negative delay of -25 μs is achieved by applying a positive delay of 975 μs). The photoelectron image on the VMI screen is captured by a CCD camera, which is read out by the LabView VI. The recorded mass spectrum can be viewed on an oscilloscope. It is furthermore forwarded to a sample-and-hold circuit, which is also provided with a trigger from the DDG. This records the measured ion current at the time specified by the received gate pulse and forwards this value into the VI. This provides a measure of the ion current during the collection of the photoelectron image and allows the normalisation of VMI images with respect to ion current, automated in the VI. This cycle is repeated for all pump-probe delays, controlled by LabView by moving the optical delay

line. Typically all delays are scanned through several times to minimise the effect of long term instabilities. All collected photoelectron images for a specific delay are added together for analysis. The use of a fast deconvolution algorithm, described in detail in the next section, allows the on-the-fly analysis of photoelectron images (with the polar onion-peeling algorithm a full deconvolution of a 512×512 image takes less than 1 s) and provides on-screen views of the photoelectron spectrum. This enables the easy optimisation of experimental parameters for maximum photoelectron signal. All recorded data is stored (both raw and accumulated photoelectron images, as well as on-the-fly workups) for later data analysis.

2.3.1 Image reconstruction algorithm

In the process of collecting a VMI image, the 3D photoelectron cloud produced by the laser interaction is flattened and recorded on a 2D imaging detector. However, due to the inherent cylindrical symmetry in the system, induced by the linear polarisation of the laser pulse, no loss of information occurs as long as the polarisation vector is located in the plane parallel to the imaging detector. This allows the reconstruction of the full 3D Newton sphere of photoelectrons from the 2D VMI image through the use of reconstruction algorithms. The principle of any inversion algorithm is shown in figure 2.17, the basic premise is to recover the central slice (in the xz plane, parallel to the imaging detector) through the photoelectron cloud, from which the entire 3D distribution can be recovered through rotation around ϕ. The mathematically exact way of achieving this is an inverse Abel transform.[36] However, several other algorithms are now available, leading to reduced noise and faster image deconvolution.[37,38] We have developed our own deconvolution routine, which offers significantly faster deconvolution times, while maintaining the quality of reconstruction offered by other methods.[27,39] This is based on polar onion-peeling (POP).

The idea behind the POP algorithm is to remove the ϕ dependence throughout the recorded image from the outside (large radii) in. This is feasible because when a 3D sphere is flattened into 2D any radius r will only add contributions in the convoluted 2D image to any radii $< r$, and one can therefore "peel away" the convoluted contributions. In practice this is achieved by first converting the recorded Cartesian camera image into an array of polar coordinates. From this the largest (outermost) radius in the image is analysed, as it does not contain any contribution from smaller radii. The convoluted contribution this radius will make to all smaller radii is then evaluated and subtracted from the image. The algorithm then moves on to the next smaller radius; as all contributions from larger radii have already been accounted for and subtracted, this radius is now free of convoluted contributions. Hence it can be analysed, its contribution to

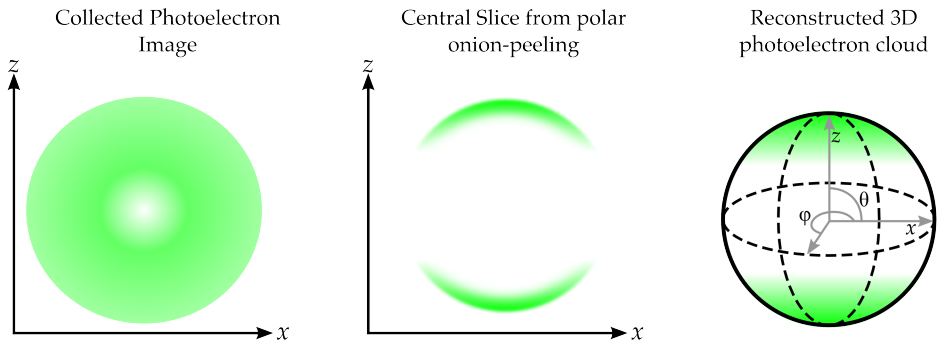

Figure 2.17: Basic principles of photoelectron image reconstruction. A 3D photoelectron cloud is flattened and recorded in 2D on an imaging detector, (a). The reconstruction algorithm recovers the central slice through the photoelectron cloud, using the cylindrical symmetry induced by the linearly polarised laser pulse, (b). From this the full 3D distribution can be recovered through rotation around ϕ, (c). The photoelectron spectrum can now be extracted by evaluating the intensity as a function of the radius, whereas the photoelectron angular distributions correspond to the intensity as a function of θ.

the image at smaller radii evaluated and subtracted. This loop is repeated until the contribution from all radii have been subtracted from the image, and therefore the ϕ contribution has been completely removed and the central slice (x,z coordinates in figure 2.17) through the photoelectron cloud is obtained. From this the full 3D photoelectron distribution can be recovered. The photoelectron velocity distribution can be evaluated through angular integration (intensity as a function of radius) and the photoelectron angular distributions can be evaluated through radial integration (intensity as a function of θ, the angle with respect to the laser polarisation). To obtain the usual photoelectron spectrum, the recovered velocity distribution needs to be converted into kinetic energy space. This is done by squaring the (arbitrary) velocity values (as $E \propto v^2$) and scaling the intensity accordingly by $1/v$. The obtained spectrum in kinetic energy space can now be calibrated against well-known standards.

2.3.2 Analysis of time-resolved data

The population dynamics associated with a specific electronic state can be extracted from photoelectron spectra by considering the spectral region of the photoelectron spectrum associated with that electronic state. To evaluated changes in the population of an electronic state with time, such as depletion or recovery of population, requires integration over the associated photoelectron feature, which is proportional to the population, in a series of spectra collected at different pump-probe delays. The correlation between photoelectron signal and pump-probe delay can then be fitted with an analytical expression to provide quantitative information, such as excited state lifetimes.

To integrate over a feature in a photoelectron spectrum (which is collected as discrete data points), one multiplies each data point in the spectrum with an as-

sociated width. However, as photoelectron spectra collected with imaging methods have data points distributed non-linearly in energy space, this associated width is different for each point in the spectrum. The width can be evaluated by considering the spacing between adjacent data points and using the average spacing between the data point that is being evaluated and the previous and following data point. Thus the i^{th} data point, c_i, has an associated width, Δc_i, of

$$\Delta c_i = \frac{c_i + c_{i+1}}{2} - \frac{c_i - c_{i-1}}{2} = \frac{c_{i+1} + c_{i-1}}{2}, \tag{2.6}$$

and one can evaluate the integral over a photoelectron feature as the sum of all data points within the feature, each multiplied with their respective width in energy space.

To extract quantitative information from the integrated data requires an analytical expression to fit the data. This needs to be convoluted with the instrument response function in the time domain, given by the pump-probe cross-correlation. For a single exponential decay the analytical solution is the exponentially modified Gaussian equation $\mathrm{G}(t, t_0, \sigma, \tau)$, where t denotes time, t_0 is the temporal overlap of pump and probe pulses, σ is the width of the cross-correlation (and related to the full-width at half maximum through FWHM$= 2\sqrt{2\ln 2}\sigma$) and τ the exponential decay time (lifetime). In general $\mathrm{G}(t, t_0, \sigma, \tau)$ is of the form[40]

$$\mathrm{G}(t, t_0, \sigma, \tau) = A \times \exp(B) \times C(t, t_0, \sigma, \tau). \tag{2.7}$$

Here A is simply an amplitude factor, B describes the exponential decay and C the convolution with a Gaussian function. The analytical expressions for these are

$$B = \left(\frac{\sigma^2}{2\tau^2} - \frac{t - t_0}{\tau} \right) \tag{2.8}$$

$$C = \mathrm{erf}\left(\frac{1}{\sqrt{2}} \left[\frac{t_0}{\sigma} + \frac{\sigma}{\tau} \right] \right) + \mathrm{erf}(z) \tag{2.9}$$

$$\text{where } z = \frac{1}{\sqrt{2}} \left(\frac{t - t_0}{\sigma} - \frac{\sigma}{\tau} \right), \tag{2.10}$$

where erf denotes the error function. The expression for C can be further simplified, without the introduction of significant calculational error,[40] as

$$C(t, t_0, \sigma, \tau) \cong 1 + \mathrm{erf}(z) = 1 - \mathrm{erf}(-z) = \mathrm{erfc}(-z), \tag{2.11}$$

where we have introduced the complimentary error function, erfc. This mathematical framework allows the extraction of exponential excited state lifetimes from integrated time-resolved photoelectron data, taking into account the pump-probe cross-correlation. We obtain the following expression for the photoelec-

tron intensity as a function of time, $I_{\mathrm{PE}}(t)$:

$$I_{\mathrm{PE}}(t) = I_0 + A_0 \times \exp\left(-\frac{t-t_0}{\tau} + \frac{\sigma^2}{2\tau^2}\right) \times \mathrm{erfc}(-z). \tag{2.12}$$

2.4 Summary

This chapter has given a detailed overview of the anion photoelectron imaging spectrometer in our laboratory. The first section described the electrospray ionisation process and how this methodology is used for the production of a stable, pulsed, focused and mass-selected beam of anions in the interaction region. Two different detectors are available, a mass spectrometer for the monitoring of the primary anion beam (using a Wiley-McLaren time-of-flight methodology) or secondary ionic fragments produced by the laser interaction (using a reflectron time-of-flight methodology) and a photoelectron imaging detector, where images are collected using a novel, compact and simple velocity-map imaging approach, specifically designed for use with anions. This features a resistive glass tube for the creation of a smooth electric field in the extraction region and has been designed for use with low extraction fields to minimise the effect on the primary ion beam. The entire data collection process is automated and controlled via a LabView VI, photoelectron images are captured by a CCD camera and monitoring of the ion signal during the collection of photoelectron images allows normalisation with respect to the ion current. Photoelectron spectra and angular distributions are reconstructed using the polar onion-peeling algorithm, providing real-time image deconvolution. Time-resolved photoelectron spectra can subsequently by analysed to yield population dynamics in electronic excited states, amongst other things. This experimental setup has been used to obtain all results in the following chapters, and reference will be made to the appropriate sections where applicable.

References

[1] J. Lecointre, G. M. Roberts, D. A. Horke, J. R. R. Verlet, *J. Phys. Chem. A* **114**, 11216 (2010).

[2] D. A. Horke, G. M. Roberts, J. Lecointre, J. R. R. Verlet, *Rev. Sci. Instrum.* **83**, 063101 (2012).

[3] R. L. Hines, *J. Appl. Phys.* **37**, 2730 (1966).

[4] J. Fenn, M. Mann, C. Meng, S. Wong, C. Whitehouse, *Science* **246**, 64 (1989).

[5] J. B. Fenn, M. Mann, C. K. Meng, S. F. Wong, C. M. Whitehouse, *Mass Spectrom. Rev.* **9**, 37 (1990).

[6] P. Jayaweera, A. T. Blades, M. G. Ikonomou, P. Kebarle, *J. Am. Chem. Soc.* **112**, 2452 (1990).

[7] K. Biemann, *Annu. Rev. Biochem.* **61**, 977 (1992).

[8] G. Schlosser, Z. Takts, K. Vkey, *J. Mass Spectrom.* **38**, 1245 (2003).

[9] L. Rayleigh, *Phil. Mag. Ser. 5* **14**, 184 (1882).

[10] T. Wyttenbach, P. R. Kemper, M. T. Bowers, *Int. J. Mass Spectrom.* **212**, 13 (2001).

[11] S. A. Shaffer, *et al.*, *Rapid Commun. Mass Spectrom.* **11**, 1813 (1997).

[12] T. Kim, *et al.*, *Anal. Chem.* **72**, 2247 (2000).

[13] W. Paul, H. S. Steinwedel, *Z. Naturforsch.* **8a**, 448 (1953).

[14] D. J. Douglas, A. J. Frank, D. Mao, *Mass Spectrom. Rev.* **24**, 1 (2005).

[15] R. Wester, *J. Phys. B: At., Mol. Opt. Phys.* **42**, 154001 (2009).

[16] D. Gerlich, *Inhomogeneous RF Fields: A Versatile Tool for the Study of Processes with Slow Ions* (John Wiley & Sons, Inc., 2007), pp. 1–176.

[17] E. Fischer, *Z. Phys.* **156**, 1 (1959).

[18] S. Guan, A. G. Marshall, *J. Am. Soc. Mass Spectrom.* **5**, 64 (1994).

[19] W. C. Wiley, I. H. McLaren, *Rev. Sci. Instrum.* **26**, 1150 (1955).

[20] A. G. Marshall, C. L. Hendrickson, *Annu. Rev. Anal. Chem.* **1**, 579 (2008).

[21] R. E. Imhof, F. H. Read, *J. Phys. E: Sci. Instr.* **1**, 859 (1968).

[22] P. Richharia, *Sol. Energ. Mater.* **20**, 199 (1990).

[23] *SimIon 8.0* scientific instrument services inc.

[24] A. T. J. B. Eppink, D. H. Parker, *Rev. Sci. Instrum.* **68**, 3477 (1997).

[25] D. H. Parker, A. T. J. B. Eppink, *J. Chem. Phys.* **107**, 2357 (1997).

[26] T. Gallagher, *Rydberg Atoms* (Cambridge University Press, 2005).

[27] G. M. Roberts, Development and construction of a new photoelectron imaging spectrometer for studying the spectroscopy and ultrafast dynamics of molecular anions, Ph.D. thesis, Durham University (2010).

[28] R. J. Pelaez, C. Blondel, C. Delsart, C. Drag, *J. Phys. B: At., Mol. Opt. Phys.* **42**, 125001 (2009).

[29] C. Blondel, P. Cacciani, C. Delsart, R. Trainham, *Phys. Rev. A* **40**, 3698 (1989).

[30] P. A. Tipler, G. Mosca, *Physics for Scientists and Engineers* (W. H. Freeman, New York, 2003), fifth edn.

[31] W. T. Silfvast, *Laser Fundamentals* (Cambridge University Press, Cambridge, 2004), second edn.

[32] C. Rulliere, *Femtosecond Laser Pulses* (Spinger, New York, 2005), second edn.

[33] M. Nisoli, *et al.*, *Opt. Lett.* **19**, 1973 (1994).

[34] A. Nebel, R. Beigang, *Opt. Lett.* **16**, 1729 (1991).

[35] J. Ringling, O. Kittelmann, F. Noack, G. Korn, J. Squier, *Opt. Lett.* **18**, 2035 (1993).

[36] L. Montgomery Smith, D. R. Keefer, S. I. Sudharsanan, *J. Quant. Spectrosc. Radiat. Transf.* **39**, 367 (1988).

[37] V. Dribinski, A. Ossadtchi, V. A. Mandelshtam, H. Reisler, *Rev. Sci. Instrum.* **73**, 2634 (2002).

[38] G. A. Garcia, L. Nahon, I. Powis, *Rev. Sci. Instrum.* **75**, 4989 (2004).

[39] G. M. Roberts, J. L. Nixon, J. Lecointre, E. Wrede, J. R. R. Verlet, *Rev. Sci. Instrum.* **80**, (2009).

[40] D. Hanggi, P. W. Carr, *Anal. Chem.* **57**, 2394 (1985).

Chapter 3

Relaxation Dynamics of Electron Acceptor Radical Anions

What is wanted is not the will to believe, but the will to find out, which is the exact opposite.

Bertrand Russell

This chapter is partially based on the following publications:

D. A. Horke, G. M. Roberts and J. R. R. Verlet, *J. Phys. Chem. A* **115**, 8369 (2011)

D. A. Horke and J. R. R. Verlet, *Phys. Chem. Chem. Phys.* **13**, 19546 (2011)

D. A. Horke, Q. Li, L. Blancafort and J. R. R. Verlet, *J. Am. Chem. Soc.* **(in preparation)**, (2012)

This chapter describes recent progress in a research project focussed on the elucidation of the ultrafast relaxation dynamics in electron acceptor radical anions. Electron transfer (ET) reactions are ubiquitous throughout chemistry and nature, and a radical anion can be considered the final step in an ET process. Specifically, we study the relaxation dynamics of electronic excited states of radical anions, as these can potentially play an important role in the ET process by providing an alternative reaction pathway.

Three systems have been investigated in our laboratory, all based on a common electronic and molecular backbone. The detailed descriptions of these systems are preceded by a joint introduction into the field and the questions we are trying to address, and the chapter is finalised with a conclusion and summary of all the findings in this research project and a brief outline of proposed future work in this area.

3.1 Introduction

Electron transfer reactions, involving the transfer of an electron from a donor (D) to an acceptor (A), are one of the most fundamental chemical interactions and are of crucial importance in nature,[1] such as the key processes of photosynthesis,[2,3] respiration,[4,5] energy conversion,[6] natural sensors,[7,8] metabolism[9] and technology, for example in artifical charge-transfer complexes.[10,11] The areas of redox and electrochemistry are devoted to the study of ET reactions, and have led to the development of solid state electronics[12] and are currently at the forefront of developing molecular electronics.[13]

A theoretical description of the rate of an ET reaction is provided by the seminal Marcus Theory.[14] This describes ET as being driven by the overall exergonicity, ΔG°, of the reaction, that is the free energy difference between the donor-acceptor system before (DA) and after (D^+A^-) the ET event. As ΔG° becomes more negative, i.e. the energetic driving force of the reaction increases, a barrier to reaction diminishes and eventually disappears when ΔG° equals the reorganisation energy, leading to an increase in the observed ET rate. However, as ΔG° increases further and the energetic driving force of the process is increased, the ET rate decreases as a reaction barrier re-emerges, as shown diagrammatically in figure 3.1(a). This rather unintuitive behaviour leads to the Marcus inverted region, the decrease of ET rate with increasing ΔG° for highly exergonic ET reactions and is now well established and has been experimentally verified.[15–18] Interestingly, numerous systems predicted to exhibit inverted region behaviour do not do so, and no decrease in ET rate occurs.[18–25] Instead, ET rates several orders of magnitude higher than predicted by Marcus theory are observed.

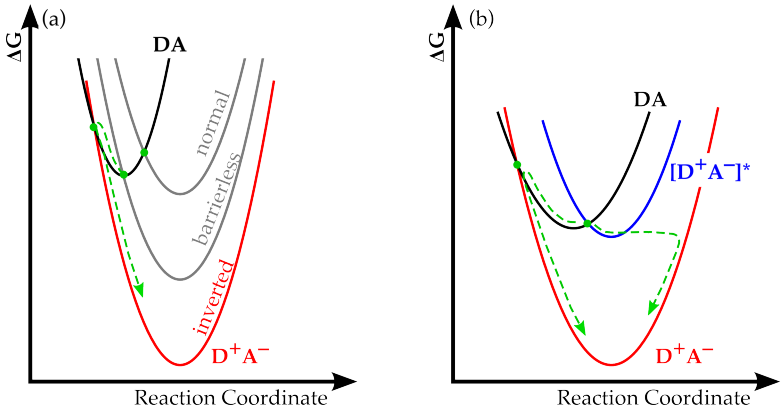

Figure 3.1: The Marcus inverted region. (a) The rate of electron transfer (ET) depends on the exergonicity, ΔG°, between the reactants and products and is limited by a barrier. As ΔG° increases this barrier initially decreases and eventually vanishes (barrierless region). However, as ΔG° increases further a barrier re-emerges and the ET rate drops (inverted region). (b) Excited electronic states of an electron acceptor can provide an alternative pathway for ET, avoiding the reaction barrier while maintaining the overall driving force ΔG°.

One mechanism used to explain this deviation from Marcus theory is the participation of excited states of the electron acceptor, vibrational or electronic, in the ET process.[12,20,26–31] These can effectively reduce the exergonicity of the reaction by providing an alternative reaction pathway. We consider here the case of electronic excited states, as shown in figure 3.1(b). If an electronic excited state is located at an energy that will allow an ET process into this state in the near-barrierless regime, and the excited state subsequently couples very strongly to the anionic ground state, then this could provide an alternative route to ET. It avoids the barrier to reaction present, but can maintain the overall driving force of the reaction, if the relaxation from the excited anion state to the ground state is sufficiently strong. Indeed, low-lying excited electronic states are common in many electron acceptor radical anions.[32,33] This alternative ET pathway has been considered in condensed-phase studies,[29,31,34–38] including dynamic investigations of excited states of common electron acceptors in their product state, suggesting very short lifetimes.[39–43] However, studies conducted in the condensed phase (in salt crystals or in solution) are strongly affected by their surroundings,[44] both energetically and dynamically, and the comparison with high-level theoretical calculations is correspondingly difficult. Furthermore, radical anions are generally highly reactive, making condensed phase studies of these short lived intermediates non-trivial. In this chapter we consider the dynamics of electronic excited states of several electron acceptor radical anions *in vacuo* using time-resolved photoelectron imaging.

In particular we investigate the ultrafast relaxation dynamics of various electronic excited states in electron acceptors based on the *para*-Benzoquinone (*p*BQ)

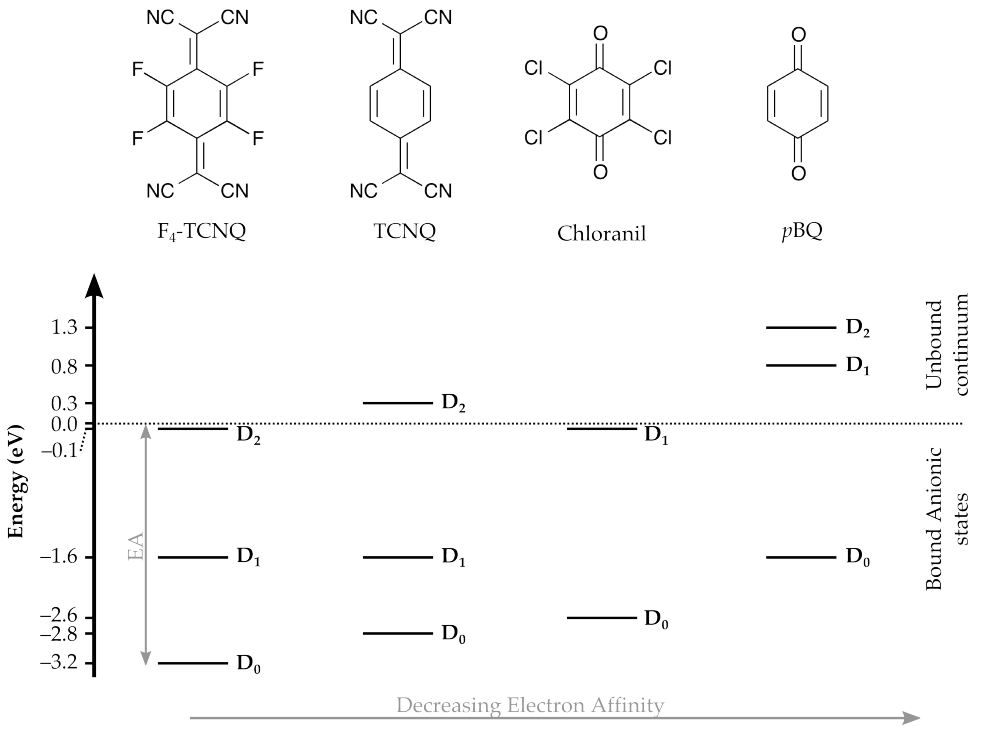

Figure 3.2: Electronic structure diagrams for several radical anions based on the quinone backbone. Referenced as 0 eV is the ground state of the corresponding neutral. The electron affinity is the energetic difference between the anion ground state (D_0) and the neutral ground state (0 eV) and decreases from left to right.

backbone. The quinones have received considerable scientific attention due to their importance in biological processes and artifical photosynthetic centres. Prominent biological examples of the quinone family are ubiquinone and plastoquinone, reaction intermediates in the proton coupled electron transfer reactions of biological systems.[1,45]

A number of quinoid systems have been investigated and a basic energy level diagram of their radical anion electronic states is shown in figure 3.2, where the ground state of the corresponding neutral is referenced at zero energy. We furthermore previously investigated 7,7,8,8-tetracyanoquinodimethane (TCNQ) radical anions.[46,47] The first systems studied were chosen to have a large electron affinity (EA), and consequently stable bound electronic excited states, such as the fluorinated version of TCNQ, 2,3,5,6-tetrafluoro-TCNQ (F_4-TCNQ), with an EA of 3.1 eV. Section 3.2 contains the detailed results of the investigation of F_4-TCNQ. The next system investigated in detail was Chloranil, which is structurally very similar to *p*BQ, but with the hydrogens replaced by chlorines, leading to a stabilisation of the anionic states relative to *p*BQ and consequently a larger electron affinity (figure 3.2), the dynamics of the bound D_1 excited state in Chloranil are presented in section 3.3. The final system investigated in this project was the *p*BQ radical anion itself. As is evident from the energy level diagram in figure 3.2, this does not possess any bound anionic electronic ex-

cited states. Instead the excited states are located within the electron detachment continuum, that is, unstable with respect to electron loss (autodetachment). Nonetheless, evidence for the internal conversion from these continuum states back to the anionic ground state has been collected and is presented in section 3.4. This is the first observation of above threshold dynamics in molecular anions. The final section of this chapter presents a joint conclusion and summary of all the findings across this project to date, and provides a brief outlook to future studies currently being undertaken or planned.

3.2 F_4-TCNQ

F_4-TCNQ is one of the most widely used electron acceptors,[48–50] with numerous technological applications in organic light emitting diodes[51,52] and organic molecular magnetism.[53,54] F_4-TCNQ is the fluorinated derivative of TCNQ, which was previously studied in our group.[46,47,55] The fluorination increases the electron affinity (EA) relative to TCNQ due to the electron withdrawing effect of the halogens around the central aromatic ring, leading to a stabilisation of the anionic states. Very few studies on the isolated F_4-TCNQ radical anion have been reported to date. A basic energy level diagram is shown in figure 3.3(a). *Ab initio* quantum calculations indicate that the doublet ground state of the anion (D_0) and the singlet ground state of the neutral (S_0) both have D_{2h} symmetry, and a vertical attachment energy of 2.89 eV is calculated at the MP4 level of theory.[56] Two bound anion excited states have been identified (D_1 and D_2 in figure 3.3(a)), the first is a core excited state, formed by excitation from the doubly occupied bound π orbital into the singly occupied corresponding anti-bonding orbital. The D_2 state corresponds to a valence excitation from the π^* anti-bonding orbital into a higher lying $2\pi^*$ orbital, calculated to be bound with respect to the neutral ground state by 0.24 eV. Calculations indicate that the minimum energy geometry for the anion excited state is not of D_{2h} character, leading to a large geometric rearrangement following excitation from D_0. The electronic properties of F_4-TCNQ are remarkably similar to those of TCNQ, except for the additional stabilisation of all anionic states relative to the ground state in F_4-TCNQ. Several experimental (gas-phase absorption[33] and photoelectron spectrum[46]) and theoretical studies[57–59] are available for TCNQ and a comparison with F_4-TCNQ will be made.

F_4-TCNQ radical anions are produced in the gas-phase via electrospraying a 1 mM solution of F_4-TCNQ in acetonitrile, using the apparatus described in detail in chapter 2. The electronic structure of F_4-TCNQ is probed using photoelectron spectroscopy. Specifically we report a spectrum collected at 400 nm (3.1 eV), resonant with the $D_2 \leftarrow D_0$ transition, and compare this to the spectrum

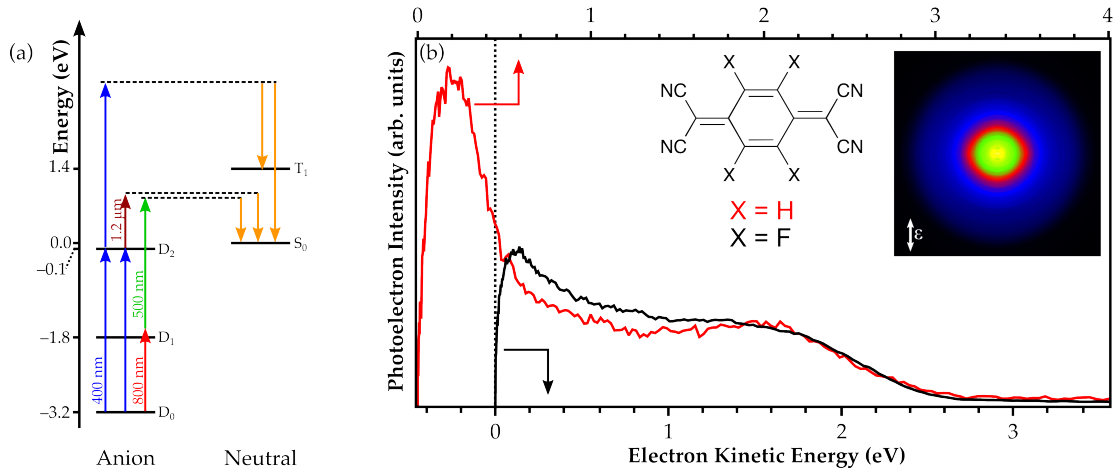

Figure 3.3: (a) Energy level diagram for F_4-TCNQ$^{\bullet-}$, indicating electronic states and excitation pathways. (b) Photoelectron spectrum of TCNQ$^{\bullet-}$ (red) and F_4-TCNQ$^{\bullet-}$ (black) collected with 400 nm (3.1 eV) photons. The two spectra are shifted with respect to each other to match the observed high electron kinetic energy (*eKE*) peak. This shift of 0.45 eV corresponds to the difference in electron affinity. In TCNQ the D_2 state is unbound, leading to a large peak at low *eKE*; this is absent in F_4-TCNQ, indicating that the D_2 is bound with respect to electron loss. Shown inset is the photoelectron image collect for F_4-TCNQ.

of non-fluorinated TCNQ reported previously. To directly probe the relaxation dynamics of the anionic excited states we use femtosecond time-resolved photoelectron imaging. Specifically, the D_1 state is excited at 800 nm (1.6 eV) and excited state population subsequently probed via electron detachment at 500 nm (2.5 eV) (typical cross-correlation 110 fs). Similarly, we excite population into the D_2 state at 400 nm (3.1 eV) and probe the dynamics with a 1200 nm (1.0 eV) pulse (cross-correlation 50 fs), sufficiently energetic to directly detach an electron into the S_0 neutral ground state. These excitation pathways are also indicated in figure 3.3(a).

3.2.1 Electronic structure calculations

In order to establish the electronic structure and state ordering of the radical anion and to acquire knowledge of the relevant orbital contributions, which can be crucial to understand to underlying Koopmans' correlations[60] in the photoelectron spectra, density functional theory (DFT) and time-dependent DFT (TD-DFT) calculations have been carried out on the radical anion, F_4-TCNQ$^{\bullet-}$. These can be compared to previous theoretical studies from the Simons group.[56] All calculations were carried out using the Gaussian03 software suite,[61] and utilised the B3LYP functional and correlation-consistent triple zeta basis set (cc-pVTZ). Geometry optimisation for the radical anion ground state was carried out (with D_{2h} symmetry) at the specified level and excited state energies, oscillator strengths and orbital contributions subsequently calculated at this optimised geometry of the anion ground state (corresponding to a vertical transition) using TD-DFT.

Table 3.1: Calculated excited states, excitation energies, oscillator strengths and orbital contributions for F_4-TCNQ$^{\bullet-}$. HOMO and LUMO refer to the neutral, such that the radical anion has a single electron residing in the LUMO.

State	Excitation Energy [eV]	Oscillator Strength	Orbital Contributions
1^2B_{3u} (D_1)	1.7	0.28	HOMO-1 → LUMO+2 0.01 LUMO → LUMO+1 0.15 HOMO → LUMO 0.81
2^2B_{3u} (D_2)	3.5	0.66	HOMO-1 → LUMO+2 0.10 LUMO → LUMO+1 0.77 HOMO-2 → LUMO+1 0.03 HOMO-1 → LUMO+2 0.03 HOMO → LUMO 0.03
^2A_g	4.1	0.00	HOMO → LUMO+4 0.08 LUMO → LUMO+3 0.88 HOMO-5 → LUMO 0.03

Results for the first three excited states, corresponding to those previously calculated, are summarised in table 3.1. We refer to the highest occupied molecular orbital (HOMO) and lowest unoccupied molecular orbital (LUMO) with respect to neutral F_4-TCNQ. Here the HOMO is doubly occupied and the LUMO vacant and in the anion the additional electron resides in the LUMO (of the neutral), making it singly occupied.

Both the D_1 and D_2 excited states are of $^2B_{3u}$ symmetry, with excitation energies of 1.7 eV and 3.5 eV, respectively. Both these states have appreciable oscillator strengths and can thus be considered optically bright states. A further excited state, calculated as bound in previous studies, was found to possess ^2A_g symmetry, and an excitation energy of 4.1 eV. However, this state has negligible oscillator strength and will not be considered further. The orbital contributions to the excited states reveal that the D_1 state is of primarily core-excited character, as expected, but does contain a ∼15% contribution from valence excitations. This state therefore primarily correlates (in a Koopmans' picture) to the neutral triplet ground state (T_1 in figure 3.3(a)). The contributions to the D_2 excited state are primarily from valence excitation into a higher lying π^* orbital. However, significant core-excited contributions are observed (∼10%), similar to those calculated in non-fluorinated TCNQ.[33,58]

3.2.2 Photoelectron spectroscopy

The photoelectron spectrum (PES) of F_4-TCNQ$^{\bullet-}$ collected at 400 nm (3.1 eV) is shown in figure 3.3(b). For comparison the PES of TCNQ$^{\bullet-}$, collected under identical conditions, is also shown.[46] The incident photon is resonant with the $D_2 \leftarrow D_0$ transition in both F_4-TCNQ$^{\bullet-}$ and TCNQ$^{\bullet-}$.[62,63] However, in the non-fluorinated variant the D_2 state is energetically unbound and a large photoelectron feature due to autodetachment from this state (or direct detachment

from the anion ground state) is observed around 0.2 eV electron kinetic energy (*eKE*) in the PES (red trace in figure 3.3(b)). In contrast to this, the spectrum for F_4-TCNQ$^{\bullet-}$ reveals no such peak (black trace), only a small part of the high energy shoulder of this peak is observed towards zero *eKE*. We therefore conclude that the D_2 state in F_4-TCNQ$^{\bullet-}$ is indeed bound with respect to electron loss. Comparison of the two PES immediately reveals the effect of the fluorine atoms, the spectra are very similar, but that of F_4-TCNQ$^{\bullet-}$ has been shifted towards lower *eKE* by $\sim$0.45 eV, due to the increased electron affinity in the presence of fluorine atoms, sufficient to bring the D_2 state below the detachment threshold.

The broad photoelectron feature at higher *eKE* is assigned to a resonant 2-photon detachment process via the D_2 state. Energetically, 2-photon detachment imparts 6.2 eV of energy into the system, given an EA of 3.2 eV, one might expect photoelectrons with kinetic energies up to $\sim$3 eV. However, the observed feature peaks around 1.6 eV, with a cut-off at $\sim$2.5 eV. We therefore assign this process primarily to the formation of the neutral triplet state, located 1.4 eV above the neutral ground state, as indicated in figure 3.3(a). An identical assignment has been made for the spectrum of TCNQ$^{\bullet-}$, where more detailed experimental[46,47,55] and theoretical[56,58] data are available. Our theoretical calculations show that the D_2 state in F_4-TCNQ does contain a contribution from core-excited orbitals (table 3.1), and can therefore correlate with the T_1 triplet state in a Koopmans' picture.[60] While this is only a minor contribution, the detachment cross-section from the D_2 into the T_1 appears to be very large, as has previously been observed for TCNQ. There is no indication in the PES for formation of the neutral ground state following detachment from the D_2, in either F_4-TCNQ$^{\bullet-}$ or TCNQ$^{\bullet-}$, despite the dominant electronic configuration of the D_2 corresponding to valence excitation and therefore correlating primarily with the S_0. This detachment channel thus appears to possess a very small cross-section.

3.2.3 D_1 excited state dynamics

The solution-phase absorption spectrum of F_4-TCNQ$^{\bullet-}$ suggests that the D_1 excited state is located approximately 1.4 eV above the anionic ground state,[63] whereas our TD-DFT calculations place this state 1.7 eV above D_0. To probe the relaxation dynamics of the D_1, we excite population into this state with a 800 nm (1.6 eV) laser pulse, and probe it a delay t later with a 500 nm (2.5 eV) probe pulse. This probe wavelength is sufficiently energetic to directly detach an electron from the D_1 excited state, as indicated in figure 3.3(a), yielding neutral ground state F_4-TCNQ, but insufficient to reach the triplet excited state of the neutral. Moreover, it is also not energetic enough for direct 1-photon detachment from the anion ground state (D_0). This significantly eases interpretation of the photoelectron signal and analysis of the time-resolved data, as no appreciable

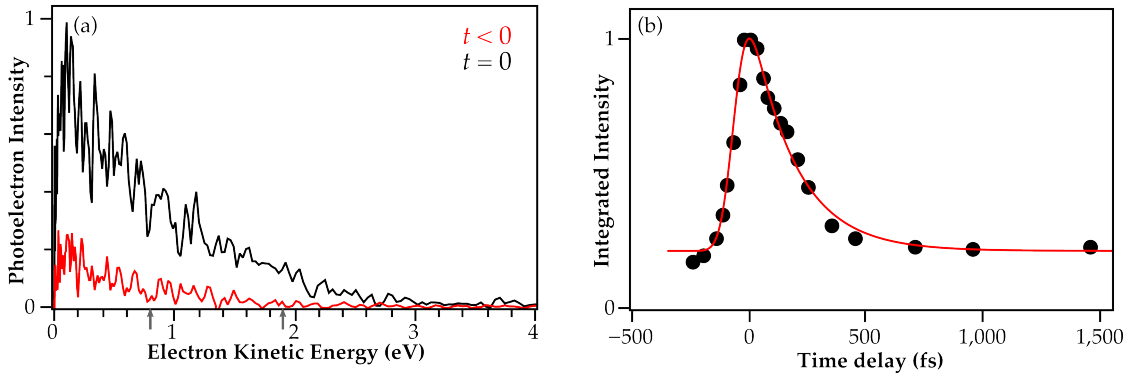

Figure 3.4: D_1 excited state dynamics in F_4-$TCNQ^{\bullet -}$. (a) Two representative photoelectron spectra taken at $t < 0$ (red trace) and $t = 0$ (black trace). (b) Total integrated photoelectron signal as a function of t. The fit to the data yields a lifetime of the D_1 state of 190 ± 35 fs.

signal is expected from the pump or probe pulse alone.

Figure 3.4(a) shows two representative photoelectron spectra, collected at $t < 0$ (probe before pump) and at $t = 0$ (pump and probe temporally overlapped). At negative delay (red trace) very little signal is observed, which we attribute to multiphoton processes leading to electron detachment. When pump and probe pulses arrive at the same time (black trace), a significant increase in photoelectron signal is observed and a broad spectrum, extending to *eKE* ~2 eV, is recorded. Electron detachment from the D_1 with a single probe photon yields photoelectrons with *eKE* up to 0.8 eV (indicated by the grey arrow in figure 3.4(a)), and we assign the low *eKE* signal to this process. More energetic photoelectrons are produced following the absorption of multiple probe photons. Specifically, the absorption of two 500 nm photons can access the triplet state of the neutral, yielding electrons with expected *eKE*s of up to 1.9 eV (grey arrow in figure 3.4(a)). We assign the observed higher energy electrons to this processes. The very large spectral width of this feature is most likely due to the large amount of vibrational energy imparted on the D_1 state by the pump pulse and consequently the observation of photoelectron signal from hot bands following detachment by the probe pulse. The high intensity of this 2-photon signal compared to the one photon process can be rationalised with the underlying Koopmans correlations. The D_1 is a core-excited state and as such correlates primarily with the neutral triplet state (T_1), rather than the singlet ground state of the neutral. Thus Koopmans' correlations favour the 2-photon process over the 1-photon process, leading to the sizeable intensity of the high energy feature compared to the single photon detachment channel.

The relaxation dynamics of D_1 population are studied by considering the total integrated photoelectron signal as a function of pump-probe delay, shown in figure 3.4(b). A very rapid loss of population following the initial excitation

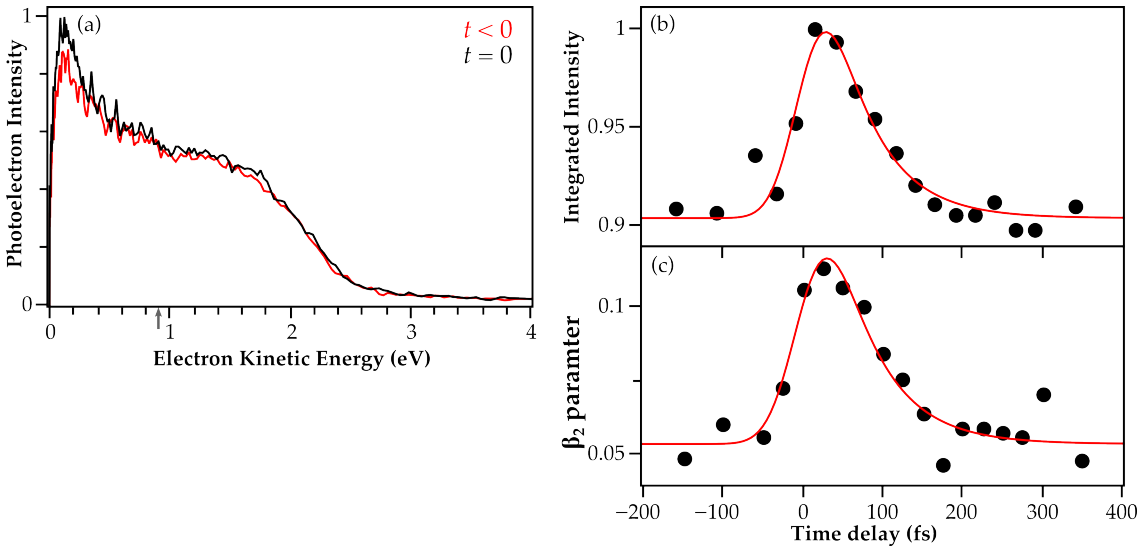

Figure 3.5: Dynamics of the D_2 excited state. (a) Two representative photoelectron spectra taken at $t < 0$ (red trace) and $t = 0$ (black trace). (b) Integrated photoelectron signal in the spectral region $0.0 \leq eKE \leq 0.5$ eV as a function of t. The fit yields an excited state lifetime of 57 ± 30 fs. (c) Extracted β_2 anisotropy parameters for the time-resolved photoelectron feature. The dynamics are clearly reflected in these and yield an excited state lifetime of 58 ± 30 fs.

is observed. To extract a quantitative timescale for the lifetime of the D_1 state, these data are fitted with an exponential decay, convoluted with a Gaussian instrument response function to account for the finite width of the pump-probe cross-correlation. The resulting fit (red trace in figure 3.4(b)) yields a characteristic lifetime of the D_1 core excited state of 190 ± 35 fs. This is a direct measure of the population dynamics in this state, and we assign the ultrafast relaxation observed to a direct internal conversion process, forming vibrationally hot anion ground state population.

3.2.4 D_2 excited state dynamics

From an electron acceptors point of view, perhaps the more relevant electronic state that could participate in an electron transfer reaction is the higher lying D_2 state; its electronic configuration ($\pi^2\ 2\pi^{*1}$) corresponds to that of the neutral with the addition of a single valence electron without any core excitations. Furthermore the D_2 state is energetically very close ($\sim$0.1 eV) to the neutral ground state, such that a very low energy electron could be captured into this state.

The dynamics of the D_2 state are investigated by exciting it with a 400 nm (3.1 eV) pump pulse, and probing the population a delay t later with a 1200 nm (1.0 eV) probe pulse, as indicated in figure 3.3(a). The choice of probe wavelength for this state was motivated by several factors: (i) The chosen wavelength is not resonant with any electronic transition in the system. (ii) The photon energy is insufficient to directly detach an electron from the D_0 or D_1 states of the anion.

(iii) The available energy enables direct detachment from the D_2 excited state, yielding the neutral S_0 ground state, with which the valence excited D_2 is correlated in a Koopmans' picture (table 3.1). (iv) The neutral triplet state T_1 cannot be reached from D_2 with this photon energy, easing interpretation of the photoelectron spectra.

Figure 3.5(a) shows two representative photoelectron spectra, collected at $t < 0$ and $t = 0$. As the probe is not sufficiently energetic to detach from the anion ground state, and not resonant with any transition, no photoelctron signal is observed from the probe alone, and the photoelectron spectrum at negative delays (red trace) is identical to the single colour spectrum at 400 nm (figure 3.3(b)). When the two pulses are temporally overlapped (black trace) a small increase in photoelectron yield is observed at low *eKE*. This arises from the additional detachment channel from the D_2 to the S_0 via a 1200 nm photon, expected to yield photoelectrons with *eKE* up to 0.9 eV (indicated by the grey arrow in figure 3.5(a)). The additional signal observed when $t = 0$ appears primarily at *eKE* < 0.9 eV, indicating that the neutral is formed with some internal energy. The signal increase is only on the order of 10% and we attribute this to the poor cross-section for detachment from D_2 to the neutral ground state, as discussed earlier.

The integrated photoelectron signal between 0.0 and 0.5 eV, containing the additional pump-probe feature, is shown in figure 3.5(b). It reveals a sharp rise upon excitation with the 400 nm pulse, followed by an exceptionally fast decay of the D_2 population. Fitting this data with a single exponential decay (convoluted with an instrument response function as discussed previously) yields a lifetime for the D_2 state of 57 ± 30 fs. Further evidence for this extremely fast excited state relaxation can be found in the time-resolved photoelectron angular distributions. We have previously shown that these can be sensitive to excited state dynamics,[55] and while they have a large systematic error (on the order of ± 0.1) and an error associated with the image deconvolution routine,[64] they are significantly less susceptible to overall intensity fluctuations, the primary source of noise in our experiment. Figure 3.5(c) shows the obtained β_2 parameter for the spectral region 0.0 to 0.5 eV as a function of pump-probe delay. This reveals an increase in anisotropy near $t = 0$, followed by a very fast decay back to the value observed at $t < 0$. Fitting these data with an exponential decay yields an excited state lifetime of 58 ± 30 fs, in excellent agreement with the energetic analysis. The data was fit with Legendre polynomials up to the 4^{th} order, as this is a two-photon process (section 1.3.2). The resulting β_4 parameters were found to be zero and showed no time dependence.

We assign the ultrafast relaxation observed to an internal conversion process to

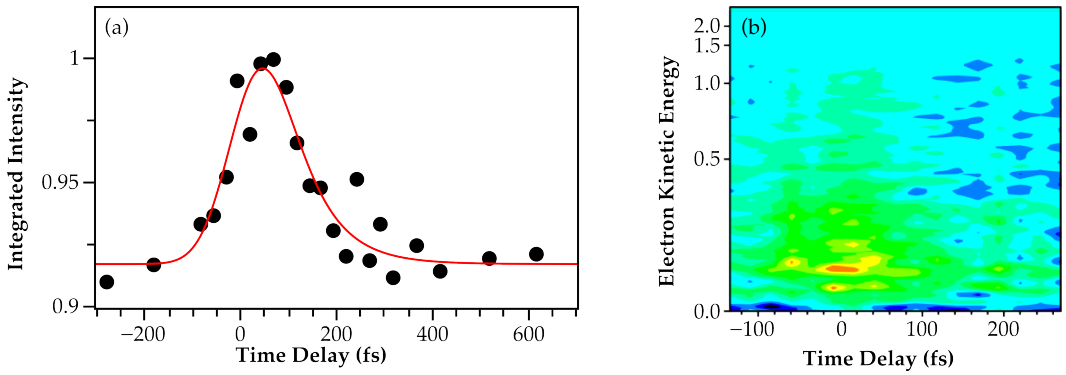

Figure 3.6: Dynamics of the D_2 state probed with photodetachment at 500 nm. (a) Integrated photoelectron signal in the spectral region $0.0 \leq eKE \leq 0.5$ eV, yielding an excited state lifetime of 71 ± 35 fs. (b) False colour intensity plot of the time-resolved photoelectron spectra with a background ($t \gg 0$) subtracted. No additional feature due to the transient population of the D_1 and no shift in kinetic energy with time delay is observed, indicative of minimal geometric changes in the D_2 state prior to relaxation.

a lower lying electronic state. This can proceed either directly to the D_0 anion ground state, or via intermediate population of the lower lying D_1 excited state. In order to gain further insight into the relaxation mechanism, pump-probe experiments were repeated with a more energetic probe beam at 500 nm (2.5 eV). This is sufficiently energetic to directly detach an electron from the D_1 state (as shown in the previous section), should it be transiently occupied from the D_2. Figure 3.6(a) shows the integrated photoelectron intensity at low *eKE* following excitation of the D_2 and probing at 500 nm. The observed dynamics are very similar to those observed with the 1200 nm probe pulse, and from this data we extract an excited state lifetime of 71 ± 35 fs. Given the broadened cross-correlation from the 500 nm pulse ($\sim$130 fs), this result is in good agreement with previously determined lifetimes. No evidence for transient population of the D_1 state is observed, which should manifest itself as a time-resolved photoelectron feature at low *eKE* with a rise-time governed by the D_2 decay from which it is populated and a relaxation time similar to that observed following direct excitation to the D_1. Shown in figure 3.6(b) is a false colour intensity plot showing the time-resolved photoelectron data after subtraction of a background spectrum ($t \gg 0$). This also shows no evidence for a photoelectron feature from the D_1 state. Furthermore, no change in kinetic energy is observed as a function of time delay, indicative of changing Franck-Condon factors due to vibrational wavepacket dynamics on the excited state.[65] Thus minimal geometric change is occurring in the D_2 state, perhaps not surprising given the very short lifetime observed.

3.2.5 Discussion

Excited state lifetimes in the sub-100 fs regime are typically attributed to relaxation via internal conversion through a conical intersection.[66,67] We attribute

the ultrafast dynamics observed here, for both the D_1 and D_2 anion excited states, to such a mechanism, as a simple golden rule expression fails to rationalise the ultrafast lifetimes. Previous calculations on F_4-TCNQ$^{\bullet-}$ indicated that both excited states are not of D_{2h} symmetry, although they are formed in the anion ground state geometry, exhibiting D_{2h} symmetry, following a vertical excitation.[56] The initial motion towards a geometric energy minimum in the D_2 state involves a mode of b_{3u} symmetry, with an out-of-plane motion of both the F atoms and the $C(CN)_2$ fragments, albeit in opposite directions. Aromatic systems commonly exhibit conical intersections involving an out-of-plane motion, and therefore symmetry breaking, leading to ultrafast internal conversion processes.[68,69] The final lowest energy structure of the D_2 excited state is calculated (at the MP2 level) to have a vertical detachment energy of 2.7 eV. Such a large energetic shift should be clearly distinguishable in the time-resolved photoelectron spectra, however no such shift is observed, as evidenced in figure 3.6(b). Moreover, such a large geometric rearrangement would take considerably longer than the observed 60 fs lifetime, and we conclude that the D_2 state internally converts through a conical intersection with the anion ground state before it could sample the entire excited state potential energy landscape. Similarly, the D_1 excited state undergoes rapid internal conversion to the D_0 ground state before it has time to explore the full excited state potential and reach a geometric energy minimum, as it is calculated to be energetically unstable with respect to electron loss at its minimum energy geometry.[44]

The observation of very fast internal conversion dynamics from the anion excited states back to the ground state reinforces the possibility of excited states of electron acceptors participating in the ET process. In this specific case, a neutral F_4-TCNQ molecule can readily accept a very low energy electron via the D_2 anion excited state, whose electronic configuration also corresponds to that of the neutral with an additional valence electron, and subsequently redistribute the excess energy into the vibrational modes of the anion ground state via ultrafast internal conversion. In a condensed phase environment the excess vibrational energy can then be dissipated into the bath. Along this alternative pathway the large (vibrational) energy barrier to electron transfer from reactants to products in highly exergonic systems (inverted region, figure 3.1(a)) is effectively transformed into electronic energy of the anion excited state (figure 3.1(b)). The Franck-Condon factors for a transition into an electronic excited state can also be more favourable than a vibrational transition, requiring a smaller geometric rearrangement to accommodate the excess charge. In the case of F_4-TCNQ$^{\bullet-}$ this excess charge is subsequently stabilised via internal conversion to the anion ground state, avoiding the reaction barrier while maintaining the overall exergonicity of the process.

3.3 Chloranil

Chloranil (CA) is the fully chlorinated derivative of *p*-benzoquinone (*p*BQ) and can serve as a representative quinoid based electron acceptor. CA itself is extensively used in artificial charge-transfer complexes and salts.[10,11] The addition of chlorine atoms around the carbon ring increases the electron affinity (EA) of CA relative to *p*BQ, and therefore stabilises all anionic states in this system (figure 3.2). CA shares much of its electronic and excited state properties with *p*BQ, as is evident from our electronic structure calculations. CA is a planar molecule of D_{2h} symmetry with an EA of 2.76 ± 0.2 eV.[70,71] The solution phase absorption spectrum of $CA^{\bullet-}$ exhibits two features around 450 nm and 320 nm, with a broad tail towards lower energy.[72] Brauman and co-workers have also previously recorded the gas-phase absorption spectrum of several radical anions, including $CA^{\bullet-}$.[33] They found a remarkable similarity with the solution phase spectrum, with strong absorbance below the threshold for electron detachment, providing further evidence for the presence of low-lying electronic excited states that are bound with respect to electron loss. Earlier experiments using the electron scavenger technique showed that thermal electrons can attach to neutral CA to form long lived (> 1 μs) radical anions, suggesting that at threshold CA can accept excess electrons.[70] In comparison with *p*BQ, the two absorption bands can be assigned to bright electronic transitions and the broad tail to nπ^* electronic states. In $p\text{BQ}^{\bullet-}$ the two bright electronic states are of ^2A_u and $^2B_{3u}$ character, with the former corresponding to a $\pi^* \leftarrow \pi^*$ transition from the singly occupied $\pi^*(b_{2g})$ molecular orbital (MO) to a higher lying empty π^* MO; and the latter corresponding to a transition form the double occupied $\pi(b_{3u})$ to the singly occupied $\pi^*(b_{2g})$ MO. We denote the latter as a core transition, which upon photodetachment leaves the neutral in an electronic excited state. The relative ordering of these two transitions remains unclear in $p\text{BQ}^{\bullet-}$ and is still subject to debate;[44,73] a similar debate has not been had for the much less studied $CA^{\bullet-}$. Using quantum chemical calculations (section 3.3.1) we show the electronic similarity between $p\text{BQ}^{\bullet-}$ and $CA^{\bullet-}$ and interpret the absorption spectrum accordingly, an overview of the involved electronic states is shown in figure 3.7(a).

Experimentally, $CA^{\bullet-}$ is introduced into the gas-phase via electrospraying of a 1 mM solution in acetonitrile, using the apparatus introduced in chapter 2, and a typical mass spectrum is shown in figure 3.7(b), clearly showing the isotopic mass resolution obtained and the hydrolysed form that is easily formed in the presence of trace amounts of water.[74] We subsequently collect photoelectron spectra (PES) and resonance enhanced PES confirming the nature of the excited state in the radical anion of CA. The excited state dynamics are then investigated using femtosecond time-resolved photoelectron imaging; population is

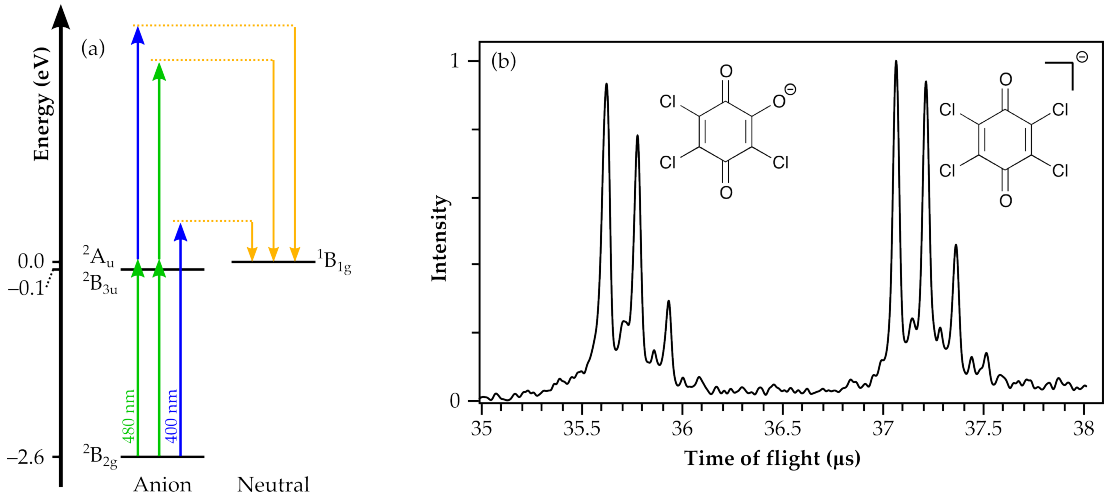

Figure 3.7: The chloranil radical anion. (a) Energy level diagram of $CA^{\bullet-}$ and excitation scheme used. (b) Typical mass spectrum of chloranil, showing the primary anion peak and the hydrolysed form, easily formed in the presence of trace amounts of water, both with isotopic resolution.

transferred into the excited state with a 2.58 eV (480 nm) pump photon, and the system probed via photodetachment with a 3.10 eV (400 nm) photon a delay t later. The temporal resolution of our experiments are limited by the pump-probe cross-correlation which was determined to be 130 fs in a thin type-II non-linear optical crystal.

3.3.1 Electronic structure calculations

In order to establish the electronic similarities between $CA^{\bullet-}$ and pBQ$^{\bullet-}$, and confirm the electronic structure of the CA radical anion, DFT and TD-DFT calculations have been performed. All calculations utilised the Gaussian09 software package,[75] with the B3LYP functional and correlation consistent triple zeta basis set (cc-pVTZ). Both the radical anions and neutral species of CA and pBQ have D_{2h} symmetry, and relevant calculated MOs for both are shown in figure 3.8. Here HOMO denotes the highest occupied molecular orbital of the neutral, such that the radical anion has a single electron in the LUMO (lowest unoccupied molecular orbital) of the neutral. The MOs are identical for the two species, with the exception of the MO of b_{1g} symmetry, which is destabilised in CA in comparison with pBQ. This can be rationalised by inspection of the MO iso-surfaces (figure 3.8), which show a strong repulsive interaction along the C-Cl bond in chloranil, which is absent in pBQ and much less pronounced for the b_{2u} and b_{3g} MOs. This interaction destabilises the MO and leads to a higher energy for the b_{1g} in CA compared to pBQ. Apart from this exception the MOs of the two systems are identical in terms of symmetry, orbital shape and relative MO ordering. However, we do note that the b_{1g}, b_{3g} and b_{2u} are very close in energy and small effects can alter the MO order. Indeed, using higher-level theory it has been shown that the b_{1g} is the HOMO of pBQ, and not the b_{3g} MO predicted here.[44]

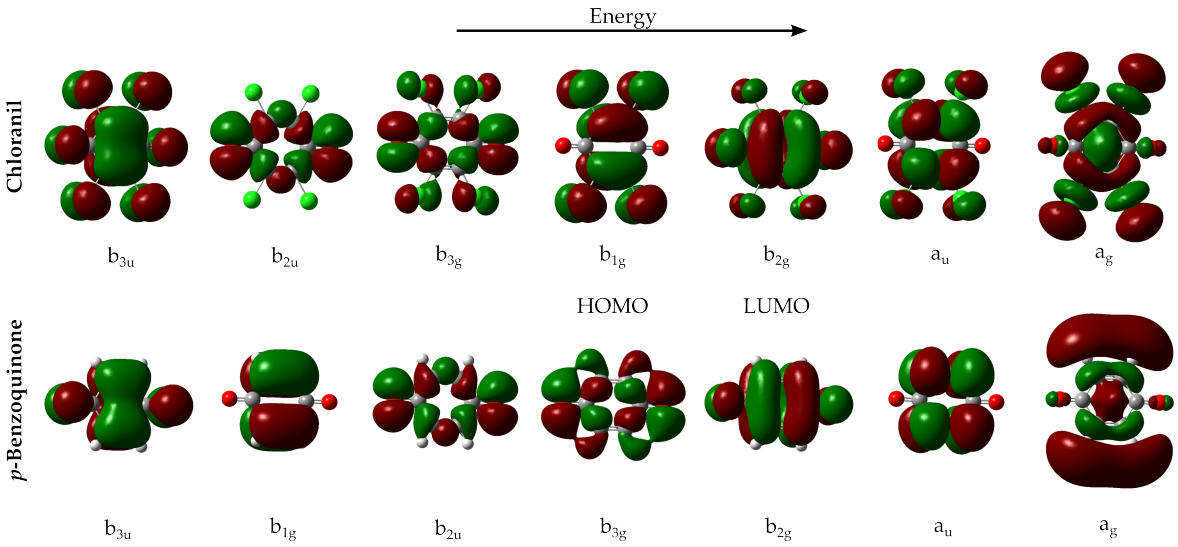

Figure 3.8: Calculated molecular orbitals for the chloranil and *p*BQ radical anions. Here HOMO and LUMO denote the highest and lowest occupied molecular orbital of the neutral respectively, such that the radical anion has a single electron residing in the LUMO.

As this b_{1g} orbital is destabilised further in CA relative to *p*BQ, it is expected that it is the HOMO of CA also, in agreement with other theoretical studies.[76] It should be noted however, that the HOMO is not involved in the anion excited states of interest here and hence its identity has no consequences for the analysis of the excited state dynamics in the radical anion.

To determine the nature of electronic transitions in $CA^{\bullet-}$, in particular the presence of ^2A_u and $^2B_{3u}$ excited states and their relative ordering, TD-DFT calculations were carried out, and the first 7 electronic excited states for $pBQ^{\bullet-}$ and $CA^{\bullet-}$ evaluated. These are summarised in table 3.2, showing the order of transitions, the term symbol of the formed electronic excited state and major orbital contributions to the transitions. As before, both systems appear very similar in their electronic excited states. The only difference arises due to the higher calculated energy of the b_{1g} MO in $CA^{\bullet-}$, which is not involved in the two transitions of interest in the current work. The first two excited states in both systems correspond to $n\pi^*$ states with $^2B_{3g}$ and $^2B_{2u}$ symmetry. These account for the low energy tail observed in the absorption spectra in both CA and *p*BQ radical anions.[72,77] The two bright states observed in the spectrum around 500 nm correspond to excited states of ^2A_u and $^2B_{3u}$ symmetries. These are calculated to be nearly isoenergetic, at 2.97 eV and 2.99 eV in $CA^{\bullet-}$ for the ^2A_u and $^2B_{3u}$, respectively. However they differ significantly in the nature of the transition. While the ^2A_u transition corresponds primarily to the excitation from the singly occupied LUMO to the next MO, the $^2B_{3u}$ involves excitation from a doubly occupied π orbital. Thus electron detachment from the ^2A_u leaves the remaining neutral in the ground electronic state, whereas detachment from $^2B_{3u}$ would require a 2-electron process to reach the neutral ground state, and therefore primarily

Table 3.2: Calculated electronic transitions, showing the excited state symmetries and major contributions for $CA^{\bullet-}$ and $pBQ^{\bullet-}$.

#	***p*-Benzoquinone**				**Chloranil**			
1	$^2B_{3g}$:	b_{3g}	$\rightarrow$	b_{2g}	$^2B_{3g}$:	b_{3g}	$\rightarrow$	b_{2g}
2	$^2B_{2u}$:	b_{2u}	$\rightarrow$	b_{2g}	$^2B_{2u}$:	b_{2u}	$\rightarrow$	b_{2g}
3	^2A_u:	b_{2g}	$\rightarrow$	a_u	$^2B_{1g}$:	b_{1g}	$\rightarrow$	b_{2g}
4	$^2B_{1g}$:	b_{1g}	$\rightarrow$	b_{2g}	^2A_u:	b_{2g}	$\rightarrow$	a_u
5	$^2B_{3u}$:	b_{3u}	$\rightarrow$	b_{2g}	$^2B_{3u}$:	b_{3u}	$\rightarrow$	b_{2g}
6	$^2B_{1g}$:	b_{1g}	$\rightarrow$	a_u	$^2B_{1g}$:	b_{1g}	$\rightarrow$	a_u
7	^2A_g:	b_{2g}	$\rightarrow$	a_g	^2A_g:	b_{2g}	$\rightarrow$	a_g

correlates with an excited state of neutral CA.

3.3.2 Photoelectron spectroscopy

We investigate the electronic structure of $CA^{\bullet-}$ via photoelectron spectroscopy at wavelengths of 400 nm (3.10 eV) and 480 nm (2.58 eV), the latter of which is resonant with the electronic transition from the anion ground state to a bright excited state of either ^2A_u or $^2B_{3u}$ symmetry. The photoelectron spectra, along with reconstructed central slices through the photoelectron cloud, are shown in figure 3.9. At 400 nm a broad unresolved feature is observed at low *eKE*, extending to $\sim$0.6 eV. Given the imparted photon energy of 3.10 eV, we estimate an adiabatic detachment energy of 2.6 ± 0.1 eV, in agreement with previous measurements that placed the electron affinity at 2.76 ± 0.2 eV.[70,71] The spectrum collected at 480 nm (shown in figure 3.9(b)) is markedly different from the 400 nm spectrum. Firstly, overall signal levels are significantly lower (by a factor of $\sim$12), secondly the bright feature at low *eKE* is nearly entirely absent. This indicates that 2.58 eV is indeed below the adiabatic detachment energy, and the small signal observed at low *eKE* is due to the broad bandwidth of the femtosecond laser pulse and the broad Franck-Condon window for detachment. The spectra shown in figure 3.9 have been shifted along the horizontal axis by the difference in photon energy (0.52 eV), as indicated by the vertical dashed line. Comparison with the 400 nm spectrum suggests that at 2.58 eV photon energy a small amount of direct detachment is expected. However the most prominent feature in the 2.58 eV PES is the very broad, anisotropic peak centred at 1.2 eV *eKE*, with a measured anisotropy of $\beta_2 = 0.6 \pm 0.3$ and $\beta_4 = -0.1 \pm 0.2$. We assign this feature to a resonance enhanced 2-photon detachment via the electronic excited state (either ^2A_u or $^2B_{3u}$), which has a maximum at 2.75 eV in solution. The assignment of this feature to a resonant process is supported by the absence of any high *eKE* feature in the 400 nm spectrum that would suggest a participation of non-resonant multiphoton detachment channels. Absorption of two photons at 480 nm imparts a total of 5.16 eV of energy into the system, given an adiabatic detachment energy of 2.6 eV, we expect this feature to extend to 2.56 eV *eKE* if the neutral is produced in the ground electronic state. This is in excellent agreement with the data, as

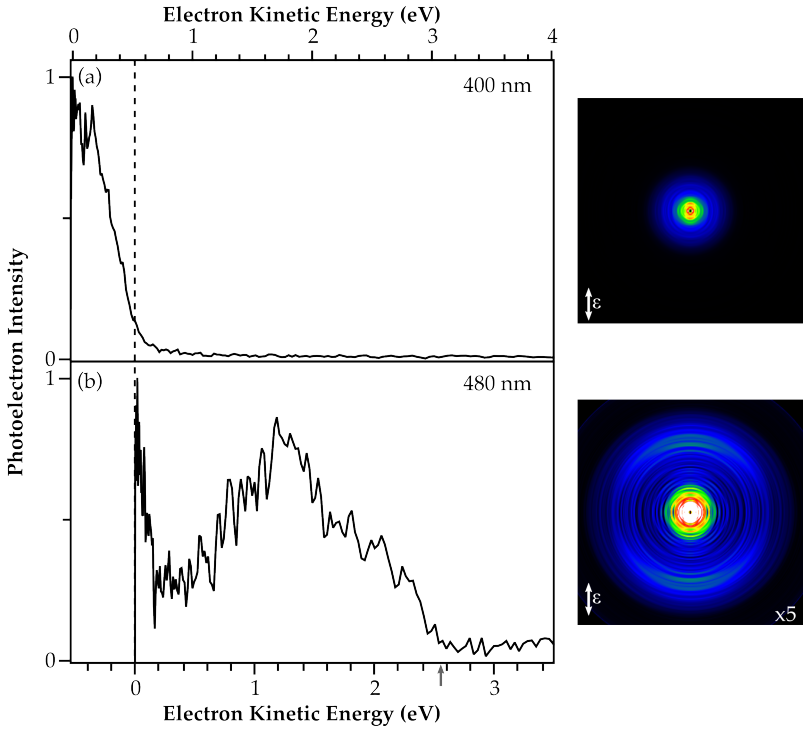

Figure 3.9: Photoelectron spectroscopy of $CA^{\bullet -}$. (a) Spectrum collected at 400 nm (3.10 eV), showing only direct detachment resulting in low electron kinetic energy (*eKE*) electrons. (b) Spectrum at 480 nm, resonant with the excited state in the anion. The broad peak corresponds to resonant detachment via this state. Shown inset are the reconstructed central slices through the photoelectron cloud, showing strong anisotropy in the resonance-enhanced feature in (b).

indicated by the grey arrow on the horizontal axis in figure 3.9(b).

While both the ^2A_u and the $^2B_{3u}$ state are energetically accessible and could partake in the dynamics, only the ^2A_u state fully correlates with the neutral ground state, as discussed earlier, and detachment from $^2B_{3u}$ would primarily result in the formation of neutral excited triplet state population. This would appear in the photoelectron spectrum at lower *eKE* if the triplet state is energetically accessible, or not at all if the triplet is located too high in energy to be accessed. We observe no evidence for neutral triplet formation, suggesting that the ^2A_u is primarily excited, although we do note that the $^2B_{3u}$ has a minor contribution from MOs that can correlate with the ground state neutral.

The large spectral width observed for the resonance enhanced feature in figure 3.9(b) suggests that either the excited state undergoes significant rearrangement following excitation, but prior to detachment, or that there is a large geometric change between the anion and neutral ground states (the excited state is initially formed in the ground state geometry). Given the short laser pulses employed here (∼100 fs), it seems unlikely that the excited state has sufficient time to undergo a large geometric motion. Thus this observation points to a large geometric rearrangement between the ground states of the neutral and anion. This

observation is consistent with the excitation of, and resonant detachment from, the ^2A_u state. This transition corresponds to removal of an electron from the b_{2g} orbital (table 3.2 and figure 3.8). Thus the transition from anion to neutral ground state removes the π^* character along the C=O bond, which is therefore expected to shorten significantly. This has has been noted in previous theoretical studies and is responsible for the large spectral width of the resonance enhanced feature.[76,78]

The use of femtosecond excitation pulses in photoelectron imaging studies usually does not offer sufficient spectral resolution to observe individual vibrational progressions. However, inspection of the resonance enhanced peak in figure 3.9(b) shows evidence of a vibrational progression at high *eKE*, with the observed peaks separated by ∼0.24 eV, corresponding to vibrational frequencies of around 1900 cm^{-1}. Calculated frequencies for the C=O stretch in neutral CA are between 1600 cm^{-1} and 1700 $^{-1}$.[78,79] We explain this only modest agreement with (i) the use of broadband femtosecond pulses, (ii) the internal temperature of the produced ions ($\geq$ room temperature) and (iii) the intrinsic resolution of our photoelectron imaging apparatus of ∼0.1 eV for *eKE*s of 2 eV. The quality of the observed vibrational progression in the photoelectron spectrum is not sufficient for a full vibrational analysis.

3.3.3 Excited state dynamics

The dynamics of the anion excited state (which is predominantly of ^2A_u character) were probed using time-resolved photoelectron spectroscopy, exciting population at 480 nm (2.58 eV) and probing the system a delay t later through electron detachment with a 400 nm (3.10 eV) pulse. The photon energy of the probe pulse has been chosen such that, in principle, excited state and ground state dynamics of the anion should be observable in coincidence. Excitation with the pump pulse alone produces the single colour spectrum shown in figure 3.9(b), probing at 3.10 eV imparts an additional 0.52 eV of energy, and therefore the observed resonance enhanced detachment peak is expected to blue-shift accordingly, extending the resonance feature to ∼3.1 eV *eKE*.

Two representative spectra, at negative (probe before pump, red trace) and at zero delay (pump and probe temporally overlapped, black trace) are shown in figure 3.10(a). While the signal-to-noise ratio in these spectra is rather poor, a clear shift to higher *eKE* is observed, along with a general increase in intensity for the high *eKE* feature. We attribute this signal to electron detachment from the excited state by the probe pulse, and it is therefore reflective of the excited state population dynamics. In order to extract quantitative excited state lifetimes, the photoelectron signal in the spectral region 1.0 eV $\leq$ *eKE* $\leq$ 3.1 eV is integrated

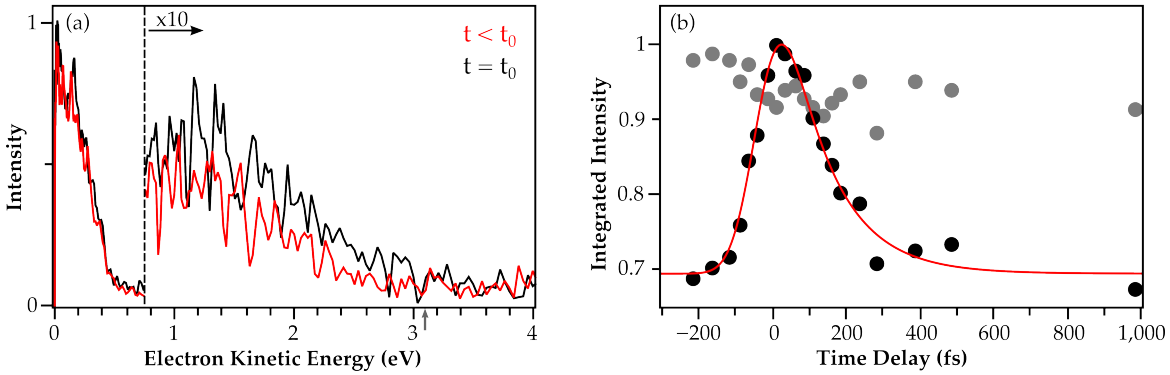

Figure 3.10: Dynamics of the ^2A_u state in $CA^{\bullet -}$. (a) Representative photoelectron spectra before and at $t = 0$ (red and black trace, respectively). The probe pulse extends the excited state feature to higher *eKE*. (b) Integrated photoelectron signal as a function of time for the spectral ranges 1.0 eV $\leq$ *eKE* $\leq$ 3.1 eV (black circles) and 0.0 eV $\leq$ *eKE* $\leq$ 0.4 eV (grey circles). The former represents the excited state population and an exponential fit (solid line) reveals a lifetime of 130 fs. The ground state (grey circles) shows no appreciable dynamics except for a depletion at $t = 0$.

and plotted as a function of pump-probe delay, figure 3.10(b). A sharp rise in signal is observed, due to the overlap of pump and probe pulses, around $t = 0$, followed by a rapid decay. Fitting of these data with an exponential decay, convoluted with a Gaussian instrument response function, yields the fit shown by the solid line in figure 3.10(b). From this an excited state lifetime of 130 ± 30 fs is extracted for the anion excited state.

The probe energy employed here should furthermore be sufficient to observe the anion ground state dynamics, which should manifest itself as changes in the integrated photoelectron signal at low *eKE*. Integrated photoelectron intensities in the low *eKE* region (0.0 eV $\leq$ *eKE* $\leq$ 0.4 eV) as a function of time are shown as grey circles in figure 3.10(b). A small depletion is observed around $t = 0$, as expected due to the removal of ground state population by the pump pulse, however no discernible time-dependence is observed in this data. We attribute this to the low excitation cross-section, such that the fraction of population transferred to the excited state is very small and observing such small signals on a large background is within the noise of our experiment. Moreover, the low *eKE* spectral window is convoluted with signals arising from other potential processes. Low-lying excited states of $n\pi^*$ character, identified in the electronic structure calculations to be dark with respect to optical excitation from the ground state, could be populated via internal conversion from the initially excited electronic state. Electron detachment from these states by the probe pulse would then lead to additional signal in the low *eKE* window. Furthermore, the probe photon is sufficiently energetic to access the neutral triplet state from the ^2A_u state, potentially leading to small additional photoelectron signal in the low *eKE* region of the spectrum. Hence we conclude that the ^2A_u excited state is short-lived and decays via internal conversion, but cannot definitively assign the pathway of re-

laxation. This may be via a series of intermediate electronic states of the anion, or directly to the anionic ground state. We can furthermore reinforce the argument that the electronic state primarily excited is the ^2A_u; as the neutral triplet is now energetically accessible, any population in the $^2B_{3u}$ excited state should strongly correlate to this, and lead to an increase in photoelectron signal 0.0 eV $\leq eKE \leq$ 0.4 eV. We actually observe a slight decrease in this region when pump and probe pulses are overlapped, indicating that our assignment of primarily exciting the ^2A_u state is valid.

Vibrational dynamics are observable in time-resolved photoelectron spectroscopy as changes in the average *eKE* with time. In the present case no such shifts are observed, indicating that no appreciable geometric rearrangements are taking place in the excited state. This is perhaps not surprising, given the spectral width of the excited state feature, and the very short lifetime. We note furthermore that these dynamics will only be observable if the difference in energy of the involved electronic states (in this case the ^2A_u excited and $^1B_{1g}$ ground state) changes along the vibrational coordinate of interest, which is not necessarily the case. Nevertheless, the lack of spectral changes with time indicates that the excited state population is not lost due to autodetachment, which could occur if the excited state shifts above the neutral ground state in energy along a vibrational coordinate, but detachment from the probe pulse. Furthermore, excited state autodetachment would be accompanied by very low energy electrons, but no discernable dynamics are observed in this spectral region.[80]

3.3.4 Discussion

Internal conversion on these ultrafast timescales observed here is usually associated with relaxation via a conical intersection.[66,67] We attribute the observed dynamics to this process, the excited state will initially be formed in the anion ground state geometry, and subsequently evolve towards a conical intersection with either a lower-lying excited state, or the electronic ground state. We cannot conclusively specify the pathway of internal conversion following excitation to the ^2A_u excited state, but observe no evidence for transient population in another excited state of the system. Conical intersections in aromatic systems often involve out-of-plane deformations,[68,69] and this is the active mode predominantly excited following $^2B_{2g} \rightarrow ^2A_u$ excitation in $CA^{\bullet -}$.[44] From an electron acceptors perspective, this conical intersection leads to a rapid exchange of electronic to vibrational energy following electron attachment into the ^2A_u state of the anion. In a condensed phase environment this excess vibrational energy can then be dissipated to the surroundings. This mechanism makes the ^2A_u state an ideal candidate for a doorway state in electron transfer reactions in the highly exergonic inverted region. The observation of long lived radical anions following electron

capture of slow electrons by CA[70] complements this observation and confirms the rapid redistribution of energy across the available vibrational modes. The behaviour observed in CA is very similar to that in F_4-TCNQ previously studied, a threshold excited state of the anion can undergo very rapid internal conversion to the electronic ground state of the anion. The backbone of both these systems is *p*-Benzoquinone, which dominates their electronic properties. The observation of very similar dynamics in several quinoid based electron acceptors then points to the electronic properties of the *p*BQ backbone to be responsible for the exceptional electron accepting abilities, similar to the behaviour of chromophores that frequently represent the dynamics of much larger systems.

3.4 *p*-Benzoquinone

p-Benzoquinone (*p*BQ) is the backbone and active site of many electron acceptors common in nature and technology,[45,81–85] such as the ones studied in the previous sections. It is furthermore the acceptor site in important biological species, such as ubiquinone or plastoquinone, which act as electron transfer (ET) intermediates in the proton-coupled ET reactions of biological systems. These systems have a long aliphatic side chain attached to *p*BQ, which acts to enhance their membrane solubility, the ET process itself however occurs on the quinone moiety. Given that the primary biological function of *p*BQ is that of an electron acceptor, properties such as its electron affinity (EA) and electronic details of its radical anion, $p\text{BQ}^{\bullet-}$, provide important benchmark information to understand the underlying ET process. Using our tool of anion time-resolved photoelectron spectroscopy (which can be considered the reverse of an electron transfer process), we probe the electronic structure of $p\text{BQ}^{\bullet-}$ and the relaxation dynamics of two electronic excited states of the radical anion. If these states are strongly coupled to the anion ground state, they could provide an alternative pathway to ET, going some way in explaining the unusually high ET efficiency of quinoid systems.[18,20,86]

Numerous theoretical[44,73,87–91] and experimental[77,92–98] studies have investigated neutral and radical anions of *p*BQ, with the most accurate value of the EA determined to be 1.860 ± 0.005 eV using photodetachment spectroscopy of $p\text{BQ}^{\bullet-}$.[77] The electronic structure of the radical has been studied using quantum chemical *ab initio* methods at various levels recently.[44,73,90] The electronic ground state of $p\text{BQ}^{\bullet-}$ is a $^2B_{2g}$ state with D_{2h} symmetry. In this anion ground state a single electron resides in a π^* orbital that is the lowest unoccupied molecular orbital (LUMO) of neutral *p*BQ. The first two excited electronic states of the radical are dipole forbidden (dark) $n\pi^*$ states of $^2B_{3g}$ and $^2B_{2u}$ symmetry (see also section 3.3.1), calculated at energies of 2.38 eV and 2.44 eV above the anion ground state

(at the symmetry adapted cluster configuration interaction level of theory, SAC-CI).[44] These states are hence predicted to be higher in energy than the EA of *p*BQ and therefore located in the electronic continuum of the radical anion and unstable with respect to electron loss. The first bright electronic state is a $\pi^*\pi^*$ state of ^2A_u character, corresponding to the promotion of the single electron in the π^* orbital to a higher lying, previously empty, π^* orbital. This state is predicted at 2.71 eV above the anion ground state.[44] The following two excited states are both of $^2B_{3u}$ symmetry, but considerably different electronic character, and the exact ordering and energies of these states remains the subject of debate. Honda *et al.*[44] calculate the first of them, denoted 1^2B_{3u}, to be 3.50 eV above the anion ground state and corresponding to a $\pi\pi^*$ transition, the promotion of an electron from a doubly filled core orbital to the singly occupied π^* frontier orbital. In contrast to this, the second state (2^2B_{3u}) is placed 3.74 eV above the anion ground state and corresponds to the transition of the electron in the singly occupied π^* orbital to a higher lying π^* orbital. As all these excited states lie within the unbound continuum of the radical anion, they can be classed as either Feshbach or shape resonances.[99] The former arise from the excitation of an electron from a doubly occupied core orbital to the singly occupied π^* molecular orbital (SOMO). These resonances therefore require a two-step mechanism to undergo autodetachment to the electronic ground state of neutral *p*BQ, leading to picosecond lifetimes despite being formally unbound.[77] Shape resonances on the other hand, corresponding to the promotion of the lone electron in the SOMO to higher π^* orbitals, require no rearrangement to undergo autodetachment to the ground state of the neutral and consequently are expected to be very short lived. From an ET point of view however, it is the shape resonances that are of particular interest as they can be formed by electron capture from the neutral ground state, potentially leading to alternative routes for ET processes.

An overview of the electronic state structure of the *p*BQ radical anion is shown in figure 3.11(a), with dark states shown in grey. Experimentally, both the dark $n\pi^*$ states and the ^2A_u were observed by Schiedt and Weinkauf using photodetachment spectroscopy on $p\text{BQ}^{\bullet-}$ in a cold molecular beam.[77] The dark states were identified as Feshbach resonances, at energies of 2.27 eV and 2.41 eV above the anion ground state. Based on the observed relatively narrow linewidth, these states have lifetimes in the order 0.2 to 1.0 ps. A much broader feature was observed in the detachment spectrum at 2.50 eV, with an intensity $\sim$50 times greater than the dark states. This was assigned to the vibrational origin of the ^2A_u shape resonance, and from the measured 200 cm^{-1} linewidth a lifetime of 25 fs inferred. At higher photon energies the observed detachment spectrum rapidly gains intensity, but unfortunately the data reported by Schiedt and Weinkauf does not extend far enough to observe additional resonances. Recently Fu *et al.*[98] reported a UV photoelectron spectrum of $p\text{BQ}^{\bullet-}$, produced

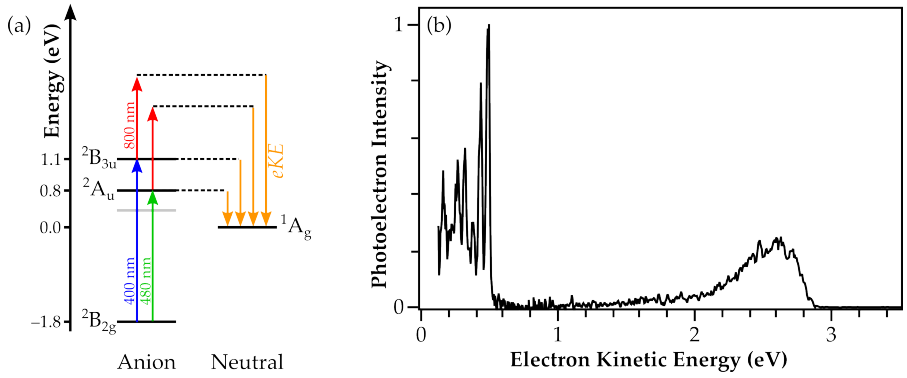

Figure 3.11: Electronic structure of *p*-Benzoquinone. (a) Electronic state diagram, referenced to the neutral ground state at 0.0 eV. Shown in grey are the optically dark nπ^* states; arrows indicate the excitation schemes used. (b) Photoelectron spectrum of pBQ$^{\bullet-}$ collected by Fu *et al.* at 4.66 eV (266 nm) photon energy.[98] This places the first neutral excited state 2.32 eV above the ground state, inaccessible with our probe energies.

via electrospray ionisation and cooled to 70 K in an ion trap, and the recorded spectrum at photon energies of 4.661 eV (266 nm) is shown in figure 3.11(b).* Their measurements confirm the previously determined EA, and they furthermore observe the first two excited states of neutral *p*BQ at 2.32 eV and 2.49 eV above the ground state.

The presence of multiple exited states in close proximity gives rise to a dense manifold of electronic and vibrational states, enabling radiationless relaxation processes to compete with electronic autodetachment.[100–102] As the identified electronic states are of very different character, one might anticipate significant differences in geometry also, leading to the possibility of excited state surface crossings and conical intersections, typically associated with excited state lifetimes of sub-100 fs.[66] Previous experiments on neutral *p*BQ using the SF_6 electron scavenger technique have indeed shown that electron attachment is feasible and leads to the formation of long-lived ($\sim$30 μs) anionic states of *p*BQ, with a sharp resonance for electron capture identified at 0.7 eV above the neutral ground state,[100,101,103] coinciding with the ^2A_u anion excited state identified by Schiedt and Weinkauf,[77] and indicating that indeed internal conversion can compete with electronic autodetachment on this very fast timescale and lead to the formation of stable anions of *p*BQ. This electron capture process by the excited anionic state could therefore by a viable alternative pathway for electron acceptance by *p*BQ.

Experimentally, pBQ$^{\bullet-}$ is produced by electrospraying a 20 mM solution of *p*BQ (98%, Sigma-Aldrich), as described in detail in chapter 2. Resonant photoelectron spectra are collected for both the ^2A_u and $^2B_{3u}$ states using 480 nm (2.58 eV) and 400 nm (3.10 eV) photons. Time-resolved pump-probe photoelectron spectra

*We thank Prof. X. B. Wang for sharing the photoelectron spectrum of *p*BQ at 4.661 eV.

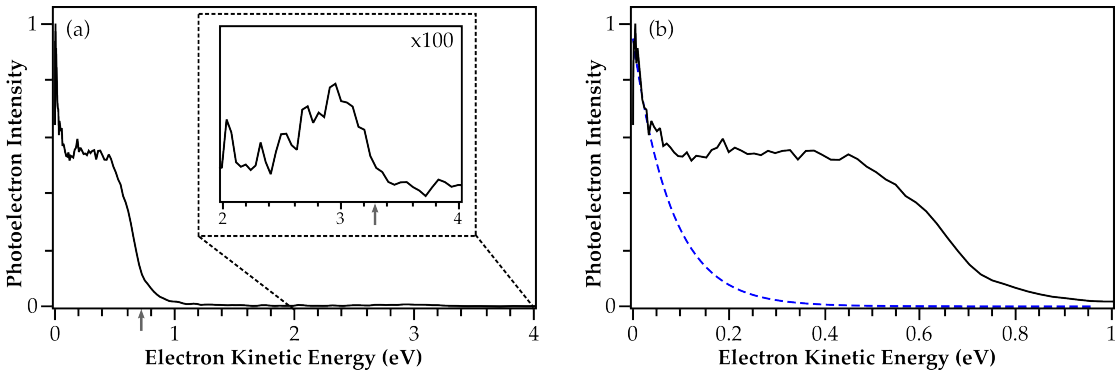

Figure 3.12: Photoelectron spectrum of pBQ$^{\bullet-}$ collected with 2.58 eV (480 nm) photons, resonant with the ^2A_u state. (a) Spectrum with the inset showing the observed resonance enhanced 2-photon detachment feature. (b) Low energy part of the spectrum shown in (a), thermionic emission is observed at threshold, and can be fit with an exponential fit (dashed blue line).

are collected by exciting the state of interest and subsequently probing population with a 800 nm (1.55 eV) probe pulse, these excitation pathways are also indicated in figure 3.11(a). The time resolution of our experiments are limited by the pump-probe cross-correlation, which was determined inside a type II non-linear crystal to be 130 fs for a 480 nm pump beam, and 65 fs for a 400 nm pump beam, both correlated with the 800 nm probe.

3.4.1 Dynamics of the ^2A_u excited state

To experimentally confirm the energetic location of the ^2A_u excited state, figure 3.12 shows the photoelectron spectrum of pBQ$^{\bullet-}$ collected with 480 nm (2.58 eV) photons. While the origin of this state has been determined to be 2.50 eV, we observe a significant increase in overall photoelectron signal at higher energies, while the shape of the spectrum remains unchanged, consistent with the observation of an increasing photoelectron yield observed by Schiedt and Weinkauf at higher energies.[77] We are therefore preparing the excited state with some amount of vibrational energy. It should furthermore be noted that, in comparison with previous studies, our laser bandwidth is ∼30 meV, and our ions are not as cold as those produced in a molecular beam source. From the spectrum shown in figure 3.12(a) we identify three main features; (i) a very weak feature centred at an electron kinetic energy (*eKE*) of around 3 eV and extending to ∼3.3 eV; (ii) a broad peak extending to *eKE*∼0.8 eV and (iii) an intense peak at zero *eKE* and falling of quickly towards higher *eKE*.

As the incident photon energy is 2.58 eV, the observation of feature (i), with an *eKE* significantly higher than this, indicates a multiphoton process. The absorption of two photons imparts a total of 5.12 eV into the system, given the EA of 1.86 eV, this should result in photoelectrons with maximum *eKE* of ∼3.3 eV, consistent with the high energy cut-off for feature (i), as indicated by the grey arrow

in figure 3.12(a). We therefore assign this peak to resonant two-photon detachment via the ^2A_u excited anion state. Moreover, the shape of this photoelectron feature is very similar to that observed in the one-colour spectrum of Fu *et al.*,[98] shown in figure 3.11(b).

A more detailed view of the low *eKE* spectral region is shown in figure 3.12(b). The lower *eKE* peak, feature (ii), is assigned to a direct detachment process from the anion ground state to the neutral ground state, given an EA of 1.86 eV, this should yield photoelectrons extending to *eKE* $\sim$0.72 eV, consistent with the data and indicated by the grey arrow on the horizontal axis of figure 3.12(a). The very broad nature of this feature is consistent with the previously recorded UV photoelectron spectrum[98] shown in figure 3.11(b), indicating a large geometric difference between the anion and neutral ground states. The recorded spectrum is furthermore consistent with the photodetachment spectrum collected by Schiedt and Weinkauf at 485 nm, although clearly we cannot reproduce the vibrational resolution.[77] Lastly, it is important to note that this feature also contains a contribution from electronic autodetachment from the ^2A_u state. As this state lies in the unbound continuum of the anion, it is prone to undergo autodetachment to form the neutral ground state, and loose an electron with *eKE* $\leq$0.72 eV.

We also observe a narrow and intense feature at zero *eKE*. As the photodetachment cross-section vanishes at threshold for anionic systems,[104,105] this cannot arise from a direct detachment process. Instead we assign this feature to thermionic loss of electrons from vibrationally very hot anion ground state population (see section 1.2.3), as has been observed in a number of anionic systems.[80,106–108] This hot anion ground state is formed via internal conversion from the initially excited ^2A_u electronic excited state, whose excess electronic energy will be transferred into vibrational energy in the $^2B_{2g}$ anion ground state following internal conversion. Due to the high density of states at these vibrational energies, a statistical Boltzmann-type electron loss occurs, leading to the emission of very low *eKE* electrons. This delayed form of autodetachment furthermore explains the long lifetimes ($\sim$30 μs) observed for anions formed following above threshold electron attachment to neutral *p*BQ.[103] This statistical loss process depends primarily on the temperature of the autodetaching system and can be described, to a good approximation, by a Boltzman distribution (section 1.2.3).[108,109] Such a fit is shown as the dashed blue line in figure 3.12(b), and we extract an ion internal temperature of approximately 1500 K. Considering the ions have 2.58 eV of excess internal vibrational energy, and assuming an equipartition between the 36 available degrees of freedom in *p*BQ, we expect an ion equilibrium temperature of $\sim$1660 K. This is in reasonable agreement, given the rather crude approximations made, and indicates that the thermionic emission occurs from the anionic ground state, and not a transiently populated

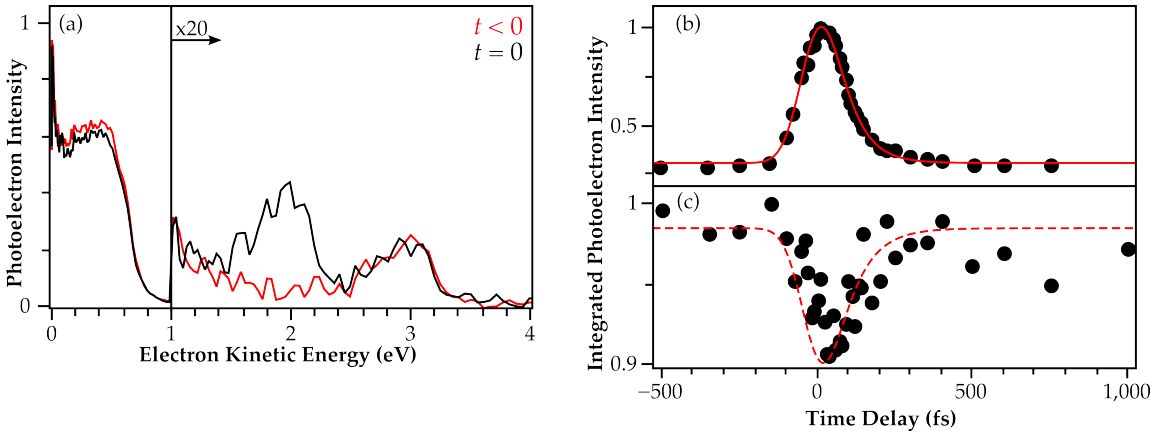

Figure 3.13: Dynamics of the ^2A_u state of pBQ$^{\bullet-}$, excited at 2.58 eV (480 nm) and probed at 1.55 eV (800 nm). (a) Representative photoelectron spectra at $t < 0$ (red trace) and $t = 0$ (black trace). A large additional feature is observed at $t = 0$, due to detachment from the excited state by the probe, and a depletion in the low *eKE* feature. (b) Integrated excited state signal as a function of t, indicating a very fast decay with typical lifetime of 65 fs (exponential fit shown as solid line). (c) Integrated signal at $eKE \leq 0.1$ eV, containing primarily the thermionic emission feature. A depletion and subsequent recovery is observed, on similar timescales to the excited state. The dashed line is a guide to the eye only and represents the fit from the top panel.

lower-lying electronic excited state, such as one of the dark $n\pi^*$ states. The observation of thermionic emission confirms that the ^2A_u state is indeed excited with a 480 nm photon, it furthermore indicates that non-radiative relaxation channels are accessible and active from the ^2A_u state and the signal from thermionic emission acts as a direct probe for hot anion ground state population.

In order to investigate these non-radiative relaxation pathways, we employ time-resolved photoelectron spectroscopy. The ^2A_u state is populated with a 480 nm (2.58 eV) pump pulse, and the system probed a delay t later with a 800 nm (1.55 eV) probe pulse. Two representative photoelectron spectra, collected at negative delays (probe before pump) and at $t = 0$ (pump and probe temporally overlapped) are shown in figure 3.13(a). The spectrum at negative delays is identical to the single colour photoelectron spectrum in figure 3.12, indicating that the probe pulse alone is not sufficient to detach an electron. This is confirmed by the absence of any photoelectron signal when only the 800 nm beam is used. When the two pulses are temporally overlapped, an additional feature is observed in the spectrum, centred at ~2 eV *eKE* and extending to 2.3 eV. We assign this feature to electron detachment following the absorption of a single pump and a single probe photon, which impart a total of 4.13 eV of energy into the system, given the EA of 1.86 eV, this should yield electrons with a maximum *eKE* of 2.27 eV, consistent with the data. This feature therefore arises from photodetachment by the probe from the ^2A_u excited state, populated by the pump pulse, and is a direct measure of the excited state population. Concomitantly to the appearance of this new feature, a depletion is observed at low *eKE* in figure 3.13(a). These depleted features were previously assigned to direct autodetachment from

the excited state (extending to 0.72 eV), and thermionic emission from hot anion ground state (peaking at threshold, 0 eV). Both these are depleted as they are dependent on the excited state population. If the probe pulse de-populates the excited state via electron detachment, less population is available to undergo direct autodetachment, and hence a depletion in this spectral region is observed. Similarly, depletion by the probe pulse directly competes with the internal conversion channel, which is a prerequisite for thermionic emission and monitored through the thermionic emission signal, and hence the threshold photoelectron signal is depleted also.

In order to evaluate the population dynamics within the ^2A_u state, the photoelectron intensity is integrated over the spectral range 1.5 eV $\leq eKE \leq$ 2.5 eV and plotted as a function of time in figure 3.13(b). This spectral region contains the feature due to 1+1′ resonance enhanced detachment and is therefore a measure of the excited state population as a function of time. The data shows a sharp rise in population with the arrival of the pump pulse, followed by a very rapid exponential decay. Fitting the data with an exponential decay convoluted with the instrument response function yields an excited state lifetime of 65 fs. This is significantly shorter than the measured cross-correlation between pump and probe pulses (130 fs) and we note that fitting the data with a slightly longer cross-correlation can reduce the measured lifetime significantly. However, the data cannot be reproduced with a lifetime longer than 65 fs and this timescale should therefore be considered an upper limit for the lifetime of the ^2A_u. Figure 3.13(c) shows the integrated signal in the thermionic emission peak ($eKE \leq 0.1$ eV) as a function of time. While the data here are more noisy, a clear depletion is observed, followed by a very fast recovery on timescales similar to those observed for the excited state decay. Note that the dashed line in this figure is not a fit, but just a guide to the eye and is the inverted fit from (b). Close inspection of the two dynamics traces suggests a small temporal shift between the appearances of the features, with thermionic emission exhibiting a slight delay in comparison with excited state depopulation. Whilst the data for the recovery dynamics is too noisy to definitively assign this, this shift could be attributed to the finite time required for the internal conversion from the excited state to the hot anion ground state, which then subsequently undergoes thermionic emission. As thermionic emission is a clear signature of hot anion ground state population, the recovery observed is evidence that internal conversion is an active relaxation pathway. Therefore if the probe arrives 300 fs after the pump pulse, internal conversion has already occured and hence the excited state population appears depleted whilst the anion ground state population has recovered.

The timescale for internal conversion from the ^2A_u state cannot be determined directly, as the measured lifetime contains contributions from two competing

processes, internal conversion, IC, and autodetachment, AD. While in principle IC is proportional to the integrated signal of the thermionic emission feature, the thermionic emission process is very slow (μs) and therefore only a fraction of the thermionic emission signal is actually recorded on the detector. The yield of AD is contained within the low *eKE* feature in figure 3.12(a), however this feature also contains a contribution from direct detachment (anion ground state to neutral ground state). While some insight into the relative contributions of the two processes can be gained from the photodetachment spectrum recorded by Schiedt and Weinkauf,[77] their measurements do not cover the entire spectral width considered here. Hence we can only conclude that internal conversion is operative from the ^2A_u state, as evidenced by the observation of thermionic emission. It furthermore proceeds on a timescale comparable to that of autodetachment, yielding an overall observed lifetime for this state of less than 65 fs.

Finally, we consider the pathway for internal conversion. In principle, photoelectron spectroscopy is also sensitive to dark states, therefore if any of the lower lying $n\pi^*$ electronic states of the anion were transiently populated, then a probe photon could detach an electron from them, if it is sufficiently energetic. Although the 1.55 eV probe is energetic enough to access the neutral ground state from either of the $n\pi^*$ states, both of them require a two-electron rearrangement to form the neutral ground state, and therefore these states are uncorrelated in Koopmans' picture. Instead, these core-excited states correlate with the first triplet state of the neutral (located 2.31 eV above the ground state), which is too energetic to be accessed at this probe wavelength. Consequently, we cannot conclusively assign if the IC pathway involves further electronic excited states, or proceeds directly to the anion ground state.

3.4.2 Dynamics of the $^2B_{3u}$ excited state

The photoelectron spectrum of pBQ$^{\bullet-}$ collected at 400 nm (3.10 eV), resonant with the $^2B_{3u}$ excited state, is shown in figure 3.14(a). We identify three spectral components, as indicated by the dashed lines in the spectrum; (i) a peak centred at $\sim$0.9 eV *eKE* and extending to 1.2 eV, (ii) overlapping with this peak on the low *eKE* side a feature centred around 0.3 eV and (iii) at threshold we observe a feature due to thermionic emission, analogous to that observed following excitation to the ^2A_u state. No feature due to 2-photon resonant detachment via the $^2B_{3u}$ excited state is distinguishable.

The highest *eKE* feature (i) is assigned to direct photodetachment from the anion ground to the neutral ground state, given the photon energy of 3.10 eV and the EA of 1.86 eV, this should yield electrons with an energetic cut-off at 1.24 eV, in good agreement with the data, as indicated by the grey arrow in figure 3.14(a).

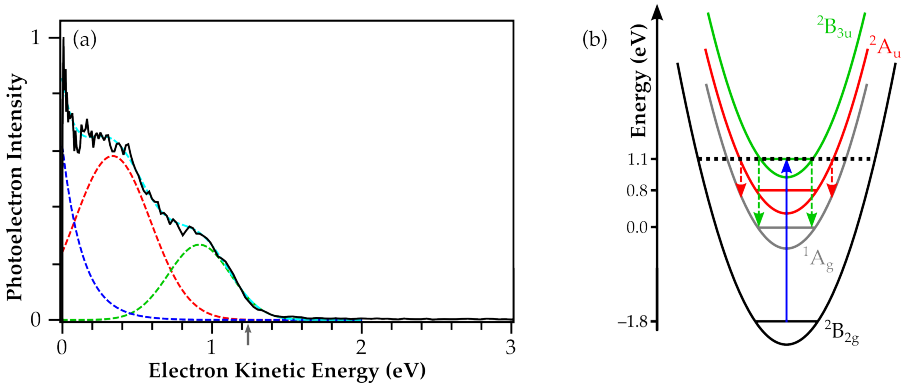

Figure 3.14: Photoelectron spectroscopy of pBQ$^{\bullet-}$ at 3.10 eV (400 nm). (a) Photoelectron spectrum with dashed lines indicating the contributions from direct detachment or autodetachment from the $^2B_{3u}$ (green), autodetachment from the transiently populated ^2A_u (red) and from thermionic emission from hot anion ground state (blue). (b) Overview of the anion dynamics following excitation to the $^2B_{3u}$; internal conversion to the lower lying ^2A_u is observed, which can subsequently undergo autodetachment to the neutral ground state, or internally convert further. This populated state can then undergo thermionic emission due to the large amount of internal energy present.

The presence of a thermionic emission feature at threshold indicates that we are indeed resonant with an excited state following 3.10 eV excitation, and that this excited state leads to the production of hot anion ground state population, which subsequently looses an electron. Similar to the situation encountered when the ^2A_u state was directly excited, this indicates that internal conversion from the $^2B_{3u}$ must be an operative relaxation pathway, competing with autodetachment.

The observation of a photoelectron feature centred around 0.3 eV *eKE* is unexpected, especially in comparison with the UV photoelectron spectrum (figure 3.11(b)),[98] which shows that no neutral excited states can be accessed at this photon energy. We therefore assign this feature to dynamics within the anion following excitation of the $^2B_{3u}$ state and the population of lower lying anion excited states from the initially excited $^2B_{3u}$ state, which can subsequently undergo autodetachment and yield the observed photoelectrons. While no energy is lost from the system in the gas-phase, the observed feature may appear at a different *eKE* due to a shift in Franck-Condon overlap and a change in geometry between the involved states. Specifically, population in an excited state with considerable amounts of internal energy may be expected to conserve some of that energy following autodetachment, leading to vibrationally excited products and a shift in the observed *eKE* to lower energy. The only available electronic states of the anion that can be populated by internal conversion from the $^2B_{3u}$ are the two dark $n\pi^*$ states and the ^2A_u state discussed above. As the latter is energetically closest to the originally excited state, and we have shown that further internal conversion from this state is possible, this is the most likely state to be populated. Comparison of the photoelectron spectra collected following excitation of the ^2A_u (figure 3.12(a)) and $^2B_{3u}$ (figure 3.14(a)) furthermore reveals a strong

resemblance between the additional features in the 400 nm spectrum and those seen in the 480 nm spectrum. Specifically, the low *eKE* peak observed in figure 3.14(a) is almost identical in energy and shape to the feature assigned to autodetachment from the ^2A_u in figure 3.12(a). If the ^2A_u state is indeed transiently populated, this can then undergo internal conversion to hot anion ground state, as evidenced by the thermionic emission feature in both photoelectron spectra. An overview of the dynamics in the anion following excitation to the $^2B_{3u}$ is shown in figure 3.14(b) and further evidence for the transient population of the ^2A_u state can be gained from the time-resolved data presented below.

To estimate the fraction of population that undergoes internal conversion from the $^2B_{3u}$ state, rather than autodetachment, the relative contributions to the photoelectron spectrum can be considered. This is physically meaningful as both processes only depend upon a single photon and one molecular cross-section. To estimate the peak areas, the spectrum has been fitted with the sum of two Gaussian functions and an exponential decay, representing the two autodetachment channels and the thermionic emission, as shown in figure 3.14(a). The feature arising from autodetachment from the ^2A_u (red dashed Gaussian) and from thermionic emission (blue exponential) require population to undergo internal conversion from the initially populated $^2B_{3u}$, whereas autodetachment directly from the $^2B_{3u}$ (green dashed Gaussian) is in direct competition with the internal conversion process. By comparing these peak areas, we estimate that at least 75% of population in the $^2B_{3u}$ undergoes internal conversion, rather than autodetachment. Furthermore, this estimate is likely to be significantly too small, because (i) the long timescale of thermionic emission[103] means that only a fraction of this feature is observed, such that the peak area of the exponential should be significantly larger and (ii) the feature due to autodetachment from the $^2B_{3u}$ (green Gaussian) also contains a contribution from direct detachment from the anion ground state, such that autodetachment is only responsible for a fraction of this peak. From this (rather crude) analysis we conclude that at least 75% of the $^2B_{3u}$ population primarily undergoes internal conversion to lower lying electronic states of the anion, despite being unbound with respect to autodetachment by 1.1 eV.

To probe the dynamics of the $^2B_{3u}$ resonance, population is coherently excited into the $^2B_{3u}$ with a 400 nm (3.10 eV) laser pulse and the system probed a delay t later with a 800 nm (1.55 eV) probe pulse (as indicated in figure 3.11(a)). Absorption of a probe photon and subsequent photodetachment into the neutral ground state should yield photoelectrons with higher *eKE* than observed from the 400 nm only spectrum. Two representative photoelectron spectra, collected at $t < 0$ (blue trace) and $t = 0$ (black trace) are shown in figure 3.15(a). The spectrum at negative delays (probe before pump) is identical to the 400 nm only

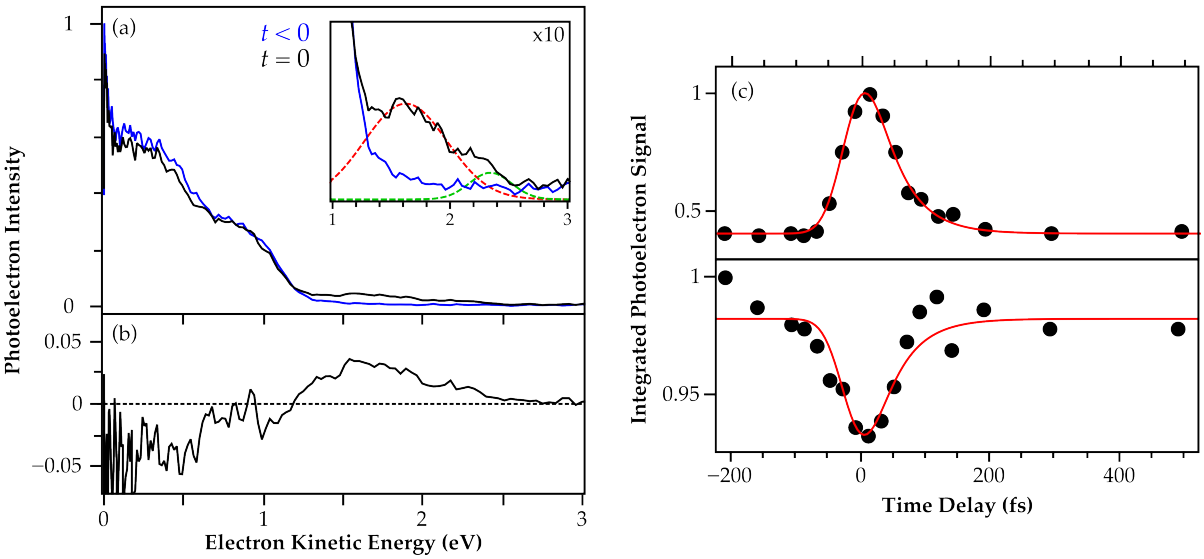

Figure 3.15: Dynamics of $p\text{BQ}^{\bullet-}$, excited at 3.10 eV (400 nm) and probed at 1.55 eV (800 nm). (a) Two representative photoelectron spectra collected at $t < 0$ (red) and $t = 0$ (black), (b) difference spectrum. An additional, bimodal feature is observed when pump and probe are overlapped (see inset in (a)), arising from probe detachment from either of the excited electronic states. Concomitantly a depletion in the low kinetic energy signal is observed. (c) Integrated photoelectron signal as a function of t. Top panel shows the additional signal (1.2 eV $\leq$ *eKE* $\leq$ 2.5 eV) and lower panel shows the depletion between 0.2 eV $\leq$ *eKE* $\leq$ 0.6 eV. Both data were fitted jointly (solid red line) and revealed a typical lifetime of 40 fs.

spectrum in figure 3.14(a), indicating that the probe alone is not sufficiently energetic to detach an electron from $p\text{BQ}^{\bullet-}$ and is furthermore not resonant with any transition. The pump-probe spectrum however shows additional features. An additional bimodal feature is observed between 1.2 eV and 2.5 eV *eKE*, as shown in the inset and further highlighted in the difference spectrum shown in figure 3.15(b). Concomitantly we observe a depletion of photoelectron signal at *eKE* $<$ 0.5 eV. We assign the additional high *eKE* feature to the absorption of a probe photon from an excited electronic state, yielding photoelectrons shifted to higher energy by the additional 1.55 eV imparted into the system by the probe. Depletion is observed for those photoelectron features dependent on internal conversion from the initially excited $^2\text{B}_{3u}$ state; the low *eKE* feature from autodetachment from the $^2\text{A}_u$ state and the thermionic emission feature. These channels are depleted as the absorption of a probe photon directly competes with the internal conversion from the $^2\text{B}_{3u}$, thereby reducing the fraction of population that reaches the $^2\text{A}_u$ state. The feature attributed to direct detachment or autodetachment from the $^2\text{B}_{3u}$, centred at 0.9 eV *eKE*, shows now appreciable depletion. If this feature were primarily due to autodetachment from the $^2\text{B}_{3u}$ following excitation by the pump pulse, a depletion should be observed as autodetachment is in direct competition with absorption of a probe photon at $t = 0$. The lack of depletion then indicates that this peak arises primarily from a direct detachment process from the anion ground state at 3.10 eV, rather than excitation of the $^2\text{B}_{3u}$ followed by autodetachment.

The extract quantitative information from the time-resolved spectra, the photoelectron intensity is integrated over the observed features and plotted as a function of t in figure 3.15(c), where the top panel shows the signal for 1.2 eV $\leq eKE \leq$ 2.5 eV and the lower panel for 0.2 eV $\leq eKE \leq$ 0.6 eV. Both data are fitted jointly with a single exponential fit convoluted with the instrument response function, given by the pump-probe cross-correlation that was measured as 65 fs. A sharp rise in excited state population is observed when pump and probe pulses are overlapped, followed by an exceptionally fast decay and the observed depletion dynamics in the ^2A_u state (lower panel) mirror this behaviour. A fit to the data revealed a characteristic lifetime of $\tau = 40$ fs, which is less than the measured cross-correlation of pump and probe pulses and should be considered an upper limit.

Close inspection of the additional feature observed between 1.2 eV $\leq eKE \leq$ 2.5 eV shows that this bimodal peak mirrors the appearance of the low *eKE* peak, which has been attributed to the autodetachment from the $^2B_{3u}$ and ^2A_u states. Indeed the features appear identical, but shifted in kinetic energy by 1.55 eV, the probe photon energy. This suggests that, in addition to the initially excited $^2B_{3u}$ state, the ^2A_u is also probed following its formation via internal conversion. The fact that the feature arising from direct detachment from the ^2A_u is already observed at $t = 0$ suggests that the internal conversion $^2B_{3u} \rightarrow ^2A_u$ occurs within the cross-correlation of the pulses of 65 fs. Further insight into these dynamics can be gained by considering the two features separately, as indicated by the dashed Gaussian functions shown in the inset of figure 3.15(a). Here the green dashed Gaussian at high *eKE* corresponds to detachment from the $^2B_{3u}$ by a probe photon, whilst the red dashed Gaussian at lower energies corresponds to detachment from the ^2A_u populated via internal conversion. Integration of the photoelectron signal over these two features separately (1.2 eV $\geq eKE \geq$ 2.0 eV and 2.0 eV $\geq eKE \geq$ 3.0 eV) is shown in figure 3.16(a) and reveals a clear temporal shift between the appearance of the two. The feature due to detachment from the initially excited $^2B_{3u}$ excited state (green) appears first, and approximately 20 fs later the detachment from the ^2A_u is observed (red). Both features then decay on a 40 fs timescale. We attribute this finite time difference between the two features to the time taken for the internal conversion, and therefore the population of the ^2A_u required for detachment from it, to take place. While this shift is much smaller than the cross-correlation, temporal shifts can be measured to much higher accuracies than lifetimes.[110]

The delay observed between the appearance of features from the $^2B_{3u}$ and ^2A_u states can be related to the internal conversion time between the two using a simple sequential kinetic model.[111] The population decays exponentially from

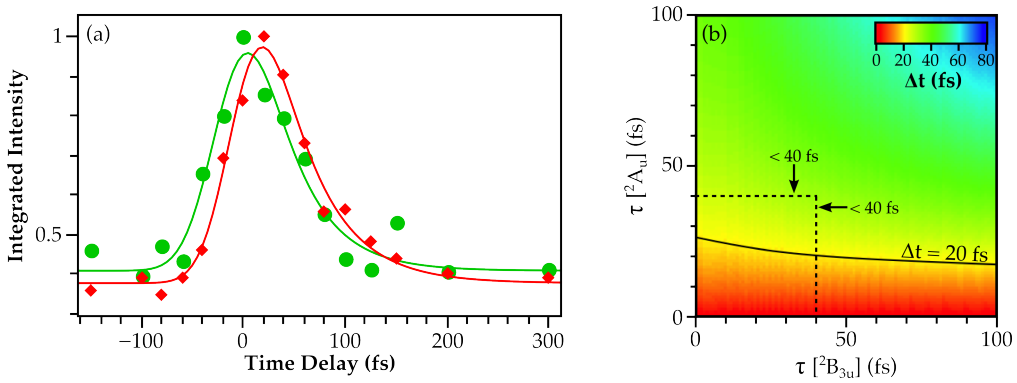

Figure 3.16: Analysis of the bimodal feature in figure 3.15(a) reveals the presence of two separate dynamics. (a) Separate integration of the photoelectron signal due to the two contributions reveals a temporal shift between them, attributed to time taken for the internal conversion from the $^2B_{3u}$ to the ^2A_u state. (b) Kinetic simulation of two sequentially decaying exponential processes. The contour map shows the observed temporal delay Δt between the maximum population in either state, for excited state lifetimes between 0 and 100 fs. The solid line indicates the experimentally observed shift of 20 fs in (a).

the initially populated $^2B_{3u}$ to the ^2A_u, which in turn decays exponentially to a final state(s) not monitored here. The populations of the two excited states can then be expressed as

$$N[^2B_{3u}] = \exp\left(-\frac{t}{\tau[^2B_{3u}]}\right) \tag{3.1}$$

$$N[^2A_u] = \frac{\tau[^2B_{3u}]^{-1}}{\tau[^2A_u]^{-1} - \tau[^2B_{3u}]^{-1}}\left[\exp\left(-\frac{t}{\tau[^2B_{3u}]}\right) - \exp\left(-\frac{t}{\tau[^2A_u]}\right)\right] \tag{3.2}$$

To model the observed temporal shift, the kinetics according to these equations are convoluted with a Gaussian instrument response function of FWHM 65 fs and the delay between the maximum of the $^2B_{3u}$ and the ^2A_u states measured as the respective lifetimes ($\tau[^2B_{3u}]$ and $\tau[^2A_u]$) are scanned. The simulation results are shown in figure 3.16(b), where the measured delay in populations is shown as a contour plot and function of the lifetime of the two states. Indicated by the solid line within the contour plot is the experimentally determined delay of 20 fs, from which one can assess the possible combinations of the $^2B_{3u}$ and ^2A_u lifetime that will lead to this measured shift. This shows that the measured shift is significantly more sensitive to the ^2A_u lifetime than that of the $^2B_{3u}$ state. The feasible timescales are furthermore restricted by the measured excited state lifetimes of $\tau < 40$ fs, and must therefore lie within the quadrant marked by the dashed lines. We find that if the lifetime of the ^2A_u is set to 40 fs, the *minimum* value of the temporal shift is 24 fs. To obtain a delay of 20 fs, the lifetime of the ^2A_u excited state must be <27 fs, in excellent agreement with the 25 fs lifetime inferred from the linewidth in the photodetachment spectra by Schiedt and Weinkauf.[77] The lifetime of the $^2B_{3u}$ can also be restricted by considering that the ^2A_u lifetime cannot be shorter than the 25 fs supported by the spectral

width. This would suggest a lifetime of the $^2B_{3u}$ of <10 fs. However, given the large uncertainty in determining spectral width accurately, and considering that a small change in the ^2A_u lifetime will have a large effect on the $^2B_{3u}$, this will have a large error associated with it. If the maximum width of the ^2A_u is in fact closer to 250 cm^{-1}, rather than 200 cm^{-1}, this would support a lifetime of 21.2 fs for the ^2A_u, leading to an excited state lifetime for the $^2B_{3u}$ of <30 fs. These extremely fast internal conversion time-scales then point to the involvement of conical intersections in the relaxation pathway.

3.4.3 Electronic structure calculations

To confirm the existence and location of the conical intersections between the excited and ground anion states of pBQ$^{\bullet-}$ observed experimentally in our laboratory, electronic structure calculations were carried out in the group of Lluis Blancafort, in a collaborative effort. Potential energy surfaces were calculated using the complete active space second-order perturbation theory (CASPT2), coupled with complete active space self-consistent field (CASSCF) calculations. Geometries of critical points (minima and conical intersections) were optimised at the CASSCF level, and energies recalculated using CASPT2 theory, to account for dynamic correlation effects. All CASSCF optimisations used an augmented and correlation-consistent double-zeta basis set (aug-cc-pVDZ), whilst CASPT2 utilised the large atomic natural orbitals (ANO-L[112]) basis, contracted to C,O[4s,3p,2d,1f]/H[3s,2p,1d].

The complete active space of pBQ$^{\bullet-}$ consists of 13 electrons in 10 orbitals (13,10 active space), comprising 8π orbitals and the 2n orbitals of oxygen. The full active space was used in the geometry optimisation of the $^2B_{2g}$ state and nπ^* minima. All further optimisations (state minima and conical intersections) were carried out with a reduced active space of 9 electrons in 10 orbitals, excluding the two n orbitals located on the oxygen to reduce computational effort and avoid convergence issues. This reduced active space still provides a balanced description of the electronic excited and ground state, and energy differences between the CASPT2 and CASSCF level are less than 0.1 eV. The CASPT2 energies at all critical geometries were evaluated with the (13,10) active space, averaging over 9 states with equal weights in the CASSCF reference calculations. All CASPT2 calculations utilised an IPEA parameter of 0.25[113] and a 0.1 imaginary level shift.[114] Gaussian09 A.02[75] was used for CASSCF calculations and Molcas 7.2[115] for CASPT2. The coupling strength between two states i and j was evaluated as the CASSCF interstate coupling vector, $\mathbf{ic}_{ij}$;

$$\mathbf{ic}_{ij} = \Delta \langle \Psi_i | \hat{H} | \Psi_j \rangle . \tag{3.3}$$

A summary of the calculated potential energy surfaces of the radical anion is

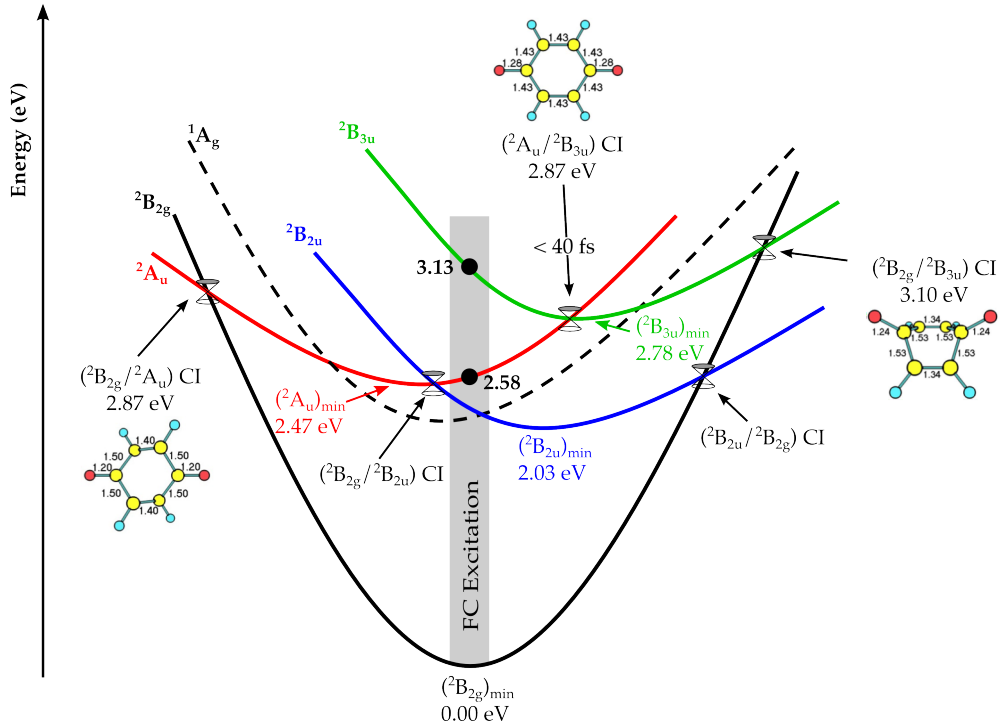

Figure 3.17: Potential energy surfaces for the $^2B_{3u}$, ^2A_u, $^2B_{2u}$ and $^2B_{2g}$ radical anion states and the ^1A_g neutral state of pBQ. Several conical intersections (CIs) are identified between the anion excited states, and between the anion states and the neutral ground state. Their energies and geometries are indicated. The most likely decay pathway following excitation to the $^2B_{3u}$ is $^2B_{3u} \rightarrow {}^2A_u \rightarrow {}^2B_{2u}$. These calculations were carried out in the group of Lluis Blancafort.

shown in figure 3.17, with calculated energies at critical points indicated. The electron affinity of pBQ$^{\bullet-}$ was furthermore calculated as 2.04 eV (CASPT2 / CASSCF level), in good agreement with the experimental value of 1.86 eV. Excitation energies in the Franck-Condon region of the $^2B_{2g}$ state to the optically bright anion excited states were calculated as 2.58 eV and 3.13 eV for the ^2A_u (red) and $^2B_{3u}$ (green) states respectively, in excellent agreement with the experimental data. The latter state was identified as being primarily a Feshbach type excitation from the ground state (67% wavefunction contribution), with only a minor (∼15%) contribution from a shape resonance excitation. Also shown is the potential energy surface for the $^2B_{2u}$ nπ^* state (blue), which is optically dark but could be populated via internal conversion.

The calculations furthermore revealed several conical intersections (CIs) accessible at the experimentally employed excitation energy of 3.1 eV; (i) a CI between the $^2B_{3u}$ and ^2A_u excited states at 2.87 eV. While one might expect a very small coupling through this CI as the $^2B_{3u}$ is primarily of Feshbach character, the contribution of a valence excitation to the wavefunction increases this coupling somewhat, and the interstate coupling vector is evaluated as 0.014 hartree bohr^{-1}, corresponding to an intermediate coupling strength. (ii) A further CI is identified between the ^2A_u and the dark $^2B_{2u}$ nπ^* state, the exact intersection

energy and geometry is still being investigated, but is close to the ^2A_u minimum at 2.47 eV. The coupling between the states is again of an intermediate strength (0.02 hartree bohr^{-1}). Three further conical intersections were identified between the excited and the anion ground state of $^2B_{2g}$ symmetry, (iii) a CI between the $^2B_{3u}$ excited state and the $^2B_{2g}$ at 3.10 eV, (iv) a CI between the ^2A_u and $^2B_{2g}$ state at 2.87 eV and (v) a CI between the $^2B_{2u}$ nπ^* and the $^2B_{2g}$, whose exact energy and geometry is still being evaluated. All crossings with the anion ground state have an out-of-plane distorted geometry, leading to loss of the D_{2h} symmetry. These CIs are shown in figure 3.17 along with their respective intersection geometries. For comparison the energy of the neutral ground state (^1A_g) is shown as a dashed line.

3.4.4 Discussion

Based on the preceding sections of experimental evidence and theoretical calculations, a detailed insight into the dynamics of pBQ$^{\bullet-}$ following excitation at 3.10 eV can be gained. Initial excitation populates a state of $^2B_{3u}$ symmetry, which is predominantly of Feshbach character, consistent with the low autodetachment yield observed experimentally. Once this state is formed, the nuclear motion on the excited state involves a stretching along the principal axis of the molecule as a π^* orbital is populated. Near the minimum energy geometry of the $^2B_{3u}$ a CI with the lower lying ^2A_u excited state is located at 2.78 eV, and population internally converts to the ^2A_u state through this CI. Experimentally, this is evidenced by the large transient population observed in the ^2A_u following excitation at 3.1 eV. From a theoretical point of view, motion through this CI is the more likely decay pathway due to the calculated intermediate coupling strength and the location of the CI very close to the $^2B_{3u}$ minimum geometry, requiring only a minimal geometry distortion, consistent with the very efficient internal conversion ($\geq$75%) and fast lifetime ($<$40 fs) measured experimentally.

Once population is in the ^2A_u state, the nuclear motion involves a recompression of the molecule, as the system evolves on the potential energy surface and towards the ^2A_u minimum geometry. Near the state minimum a CI with the (optically dark) $^2B_{2u}$ is located, and population internally converts to this state via this crossing. This process is energetically allowed and dynamically favoured because it retains the D_{2h} symmetry in the system as it does not involve any non-totally symmetric modes. The lifetime of the ^2A_u is sub-30 fs with contributions from internal conversion (via the CI) and autodetachment. While the latter is expected to be very fast from this shape resonance, the photoelectron spectrum following direct excitation of the ^2A_u clearly shows the formation of significant population of hot anion ground state, evidence for an efficient internal conversion mechanism that competes with the direct autodetachment. The population

in the $^2B_{2u}$ will hence evolve towards the minimum geometry of this state, calculated at 2.03 eV. At this geometry the energy of the neutral ground state is 2.73 eV and the anion therefore becomes bound with respect to electron loss. From the $^2B_{2u}$ state there are two possible decay pathways; either the system undergoes a further internal conversion event to form the anion ground state, with which a CI exists, or alternatively if this $n\pi^*$ state is long lived, thermionic emission can occur from this state due to the excess energy that has not been dissipated in the gas-phase environment. However, in a condensed phase situation this energy can be efficiently dissipated to the surroundings, leading to the formation of stable $p\text{BQ}^{\bullet-}$.[103]

In addition to the most likely pathway outlined above, direct internal conversion from the excited states ($^2B_{3u}$ or ^2A_u) to the anion ground state is also feasible, through a number of CIs that are energetically accessible at 3.10 eV excitation energy (figure 3.17). However, given the very short timescales observed experimentally, this pathway appears less likely, due to the large distortion in nuclear geometry required to access these intersections. Optical excitation primarily activates the totally symmetric vibrations, whereas the CI geometries involve a symmetry breaking and out-of-plane motion. Hence a large amount of intramolecular vibrational energy transfer is necessary to reach the CIs, which is expected to take significantly longer than the observed lifetimes. Thus the most likely decay route appears to be $^2B_{3u} \rightarrow {}^2A_u \rightarrow {}^2B_{2u}$, in excellent agreement with the experimental data.

Dynamics of the competition between autodetachment and internal conversion in above threshold excited states have previously been observed in cluster systems,[116] but we believe this to be the first observation of these competitive dynamics in isolated molecular anions. Due to the nature of the competing decay channels only a single lifetime can be observed, however the consideration of asymptotic yields in the photoelectron spectrum allows further insight into the yields of the individual relaxation pathways. While this analysis is rather qualitative in the current experiment, it does allow the placement of quantitative upper limits on the individual decay rates.

The observed ultrafast dynamics through a series of CIs show that population in above threshold electronic excited states in $p\text{BQ}^{\bullet-}$ is efficiently funnelled into the anion ground state, converting excess electronic energy into vibrational energy. The observation of internal conversion from states located in the electronic continuum highlights the efficiency of this process in pBQ, as it effectively competes with ultrafast autodetachment. From an electron acceptors point of view this suggests that these excited states may indeed play a crucial role in electron transfer processes, allowing the capture of a free electron from the electronic

continuum, and stabilising this excess charge on an ultrafast timescale in the anionic ground state, thereby avoiding the barrier to electron transfer characterising the Marcus inverted region by initially populating an electronic excited state, acting as a doorway state for the electron transfer process.

3.5 Conclusion

This chapter investigated several common electron acceptors, based on *p*BQ and its derivatives. Due to the large electron affinity of these systems, ET is a highly exergonic process. This places them in the Marcus inverted region, where a free energy barrier slows down the ET process. However, for many electron acceptors based on *p*BQ this is not observed, and ET rates do not indicate the presence of any barrier. The present work tries to understand the absence of a measurable barrier by investigating the dynamics of electronic excited states in these systems, which have previously been suggested to participate in the electron transfer event by providing an alternative pathway.

Three common electron acceptors have been investigated, F_4-TCNQ, Chloranil an *p*BQ. All these systems are based on the central quinone moiety, where the primary effect of substituents is to stabilise anionic states to differing degrees. This leads to the excited electronic states in F_4-TCNQ and Chloranil being bound, while in *p*BQ they are located in the electronic continuum for electron detachment. However, our calculations have shown that electronically these systems are remarkably similar. This similarity is also reflected in the measured excited state dynamics. Following optical excitation to a bright electronic excited state of the radical anion, all systems studied undergo ultrafast internal conversion to lower lying (and bound) anionic states. Following valence excitation, most relevant to electron transfer processes as it is analogous to capture of an excess electron by the neutral, F_4-TCNQ undergoes internal conversion in $\sim$60 fs, Chloranil in $\sim$130 fs and *p*BQ in $\sim$40 fs. In the case of *p*BQ this internal conversion is so efficient that it even out-competes autodetachment, despite being $>$1 eV above the detachment threshold.

Given the remarkable electronic similarity between the systems studied, we speculate that the mechanism identified for the *p*BQ radical anion is likely to be similar to that operational in all quinone based electron acceptors. For this system we were able to show that following population of an excited state of the system, the radical anion undergoes radiationless decay through a series of internal conversions, facilitated by conical intersections between the dense manifold of available electronic states, forming a stable radical anion. This mechanism is compatible with the idea of electronic states providing an alternative pathway

to electron acceptance that was introduced in figure 3.1(b); a free low energy electron can easily be captured by these continuum resonances, and the excess charge subsequently stabilised (and brought below the detachment threshold) in sub-100 fs. It is the quinone backbone that is responsible for these fast dynamics and therefore the functioning of these electron acceptors. This moiety really acts as the *electrophore* in these system which, in analogy to the term chromophore, is responsible for the electronic dynamics observed, crucial to the electron accepting abilities.

A number of further investigations within this research project are currently under way or being planned:
(i) We are planning on repeating the experiments on the *p*BQ radical anion with an improved time-resolution for photoelectron spectroscopy. The quoted experimental lifetimes of the current results are all upper limits, as they are considerably shorter than then the pump-probe cross-correlations. We are currently improving our laser setup, details of which will be given in section 6.2, such that these lifetimes can be refined and determined to a better accuracy.
(ii) The conical intersections identified to be responsible for the fast internal conversion dynamics in $p\text{BQ}^{\bullet -}$ are associated with a symmetric stretch of the entire molecule. In an attempt to experimentally verify this, we are currently investigating the relaxation dynamics in a series of halogenated derivatives. These are identical to the already studied Chloranil, but with bromine, fluorine or iodine substituents around the central benzene ring. The introduction of heavier substituents on the ring should slow down the molecular stretch considerably, leading to a systematic increase in the observed timescales for internal conversion from unsubstituted *p*BQ to fluoranil, chloranil, bromanil and finally iodanil. This novel methodology provides an experimental way of determining the nature of a conical intersection in an aromatic system and experiments are currently under way in our laboratory.
(iii) Having studied the dynamics of isolated electron acceptors, a logical next step is the introduction of an entire electron transfer system, including a donor and an acceptor into the gas-phase, with the intent of investigating the dynamics of the entire process, including any intermediate states that might be involved. The difficulty here is the stable introduction of such a large system into the gas-phase. Due to the nature of our experimental apparatus the system is furthermore required to be negatively charged, in order to allow for mass-selection and trapping to acquire population (see chapter 2). Two possible species are currently being investigated for their feasibility: transition metal complexes, where a charge transfer process between two metal centres occurs, and small organic mixed-valence systems. The simplest of these appears to be dinitrobenzene (DNB), in this system the location of the nitro-groups around the benzene ring determines the behaviour of the mixed valance system. 1,4-DNB shows

strong charge delocalisation (class III mixed-valence compound), whereas the 1,2-DNB system shows more localised behaviour.[117] We hope to study in detail the dynamics of both systems in order to compare them and understand the underlying electron-transfer process in detail.
(iv) The final aim of this project would be to study an electron transfer process, and associated dynamics, between a separate donor and acceptor moiety in the gas-phase. This could be achieved using donor-spacer-acceptor systems, such as those studied in the seminal solution-phase works by the groups of Closs and Miller.[16,18,22,24,25] Here an electron donor and acceptor are separated by a rigid saturated hydrocarbon spacer, allowing the study of different combinations of donor and acceptor (and hence different exergonicities), as well as investigating the dependence on the charge separation by varying the length of the spacer molecule. The electron transfer can be induced with a pump laser pulse, and the ET or recombination dynamics subsequently probed through electron detachment.

References

[1] J. P. Klinman, D. Mu, *Annu. Rev. Biochem.* **63**, 299 (1994).

[2] P. R. Chitnis, *Annu. Rev. Plant. Physiol. Plant. Mol. Biol.* **52**, 593 (2001).

[3] G. Renger, T. Renger, *Photosynth. Res.* **98**, 53 (2008).

[4] T. M. Iverson, C. Luna-Chavez, G. Cecchini, D. C. Rees, *Science* **284**, 1961 (1999).

[5] V. Yankovskaya, *et al.*, *Science* **299**, 700 (2003).

[6] G. Yu, J. Gao, J. C. Hummelen, F. Wudl, A. J. Heeger, *Science* **270**, 1789 (1995).

[7] J. J. Hickman, D. Ofer, P. E. Laibinis, G. M. Whitesides, M. S. Wrighton, *Science* **252**, 688 (1991).

[8] I. Willner, A. Riklin, *Anal. Chem.* **66**, 1535 (1994).

[9] C. C. Moser, J. M. Keske, K. Warncke, R. S. Farid, P. L. Dutton, *Nature* **355**, 796 (1992).

[10] W. L. Peticolas, *J. Chem. Phys.* **26**, 429 (1957).

[11] J. J. Mayerle, J. B. Torrance, J. I. Crowley, *Acta Cryst. B* **35**, 2988 (1979).

[12] P. F. Barbara, T. J. Meyer, M. A. Ratner, *J. Phys. Chem.* **100**, 13148 (1996).

[13] A. Nitzan, *Annu. Rev. Phys. Chem.* **52**, 681 (2001).

[14] R. A. Marcus, N. Sutin, *Biochim. Biophys. Acta* **811**, 265 (1985).

[15] C. Creutz, N. Sutin, *J. Am. Chem. Soc.* **99**, 241 (1977).

[16] J. R. Miller, J. V. Beitz, R. K. Huddleston, *J. Am. Chem. Soc.* **106**, 5057 (1984).

[17] M. R. Wasielewski, M. P. Niemczyk, W. A. Svec, E. B. Pewitt, *J. Am. Chem. Soc.* **107**, 1080 (1985).

[18] G. L. Closs, J. R. Miller, *Science* **240**, 440 (1988).

[19] D. Rehm, A. Weller, *Ber. Bunsen-Ges. Phys. Chem.* **73**, 834 (1969).

[20] D. Rehm, A. Weller, *Isr. J. Chem.* **8**, 259 (1970).

[21] J. V. Beitz, J. R. Miller, *J. Chem. Phys.* **71**, 4579 (1979).

[22] L. T. Calcaterra, G. L. Closs, J. R. Miller, *J. Am. Chem. Soc.* **105**, 670 (1983).

[23] M. T. Indelli, R. Ballardini, F. Scandola, *J. Phys. Chem.* **88**, 2547 (1984).

[24] J. R. Miller, L. T. Calcaterra, G. L. Closs, *J. Am. Chem. Soc.* **106**, 3047 (1984).

[25] G. L. Closs, L. T. Calcaterra, N. J. Green, K. W. Penfield, J. R. Miller, *J. Phys. Chem.* **90**, 3673 (1986).

[26] R. A. Marcus, P. Siders, *J. Phys. Chem.* **86**, 622 (1982).

[27] P. F. Barbara, G. C. Walker, T. P. Smith, *Science* **256**, 975 (1992).

[28] P. Suppan, *The marcus inverted region* (Springer Berlin / Heidelberg, 1992), vol. 163 of *Topics in Current Chemistry*, pp. 95–130.

[29] A. Morandeira, L. Engeli, E. Vauthey, *J. Phys. Chem. A* **106**, 4833 (2002).

[30] N. Mataga, H. Chosrowjan, S. Taniguchi, *J. Photochem. Photobiol., C* **6**, 37 (2005).

[31] J. Petersson, M. Eklund, J. Davidsson, L. Hammarstrom, *J. Phys. Chem. B* **114**, 14329 (2010).

[32] T. Shida, E. Haselbach, T. Bally, *Acc. Chem. Res.* **17**, 180 (1984).

[33] E. A. Brinkman, E. Gunther, O. Schafer, J. I. Brauman, *J. Chem. Phys.* **100**, 1840 (1994).

[34] P.-A. Muller, E. Vauthey, *J. Phys. Chem. A* **105**, 5994 (2001).

[35] A. S. Lukas, Y. Zhao, S. E. Miller, M. R. Wasielewski, *J. Phys. Chem. B* **106**, 1299 (2002).

[36] S. Pags, B. Lang, E. Vauthey, *J. Phys. Chem. A* **108**, 549 (2003).

[37] E. Vauthey, *J. Photochem. Photobiol., A* **179**, 1 (2006).

[38] N. Van Anh, *et al.*, *J. Phys. Chem. C* **113**, 18358 (2009).

[39] J.-C. Gumy, E. Vauthey, *J. Phys. Chem. A* **101**, 8575 (1997).

[40] D. Gosztola, M. P. Niemczyk, W. Svec, A. S. Lukas, M. R. Wasielewski, *J. Phys. Chem. A* **104**, 6545 (2000).

[41] P. Brodard, A. Sarbach, J.-C. Gumy, T. Bally, E. Vauthey, *J. Phys. Chem. A* **105**, 6594 (2001).

[42] D. Mandal, T. Tahara, S. R. Meech, *J. Phys. Chem. B* **108**, 1102 (2004).

[43] M. J. Hope, *et al.*, *Chem. Phys. Lett.* **474**, 112 (2009).

[44] Y. Honda, M. Hada, M. Ehara, H. Nakatsuji, *J. Phys. Chem. A* **106**, 3838 (2002).

[45] H. Nohl, W. Jordan, R. J. Youngman, *Adv. Free Radical. Bio.* **2**, 211 (1986).

[46] G. M. Roberts, J. Lecointre, D. A. Horke, J. R. R. Verlet, *Phys. Chem. Chem. Phys.* **12**, 6226 (2010).

[47] G. M. Roberts, Development and construction of a new photoelectron imaging spectrometer for studying the spectroscopy and ultrafast dynamics of molecular anions, Ph.D. thesis, Durham University (2010).

[48] R. C. Wheland, E. L. Martin, *J. Org. Chem.* **40**, 3101 (1975).

[49] T. J. Emge, *et al.*, *J. Chem. Phys.* **77**, 3188 (1982).

[50] M. Fourmigue, V. Perrocheau, R. Clerac, C. Coulon, *J. Mater. Chem.* **7**, 2235 (1997).

[51] M. Pfeiffer, *et al.*, *Org. Electron.* **4**, 89 (2003).

[52] K. Walzer, B. Maennig, M. Pfeiffer, K. Leo, *Chem. Rev.* **107**, 1233 (2007).

[53] J. S. Miller, *Dalton Trans.* pp. 2742–2749 (2006).

[54] N. Lopez, *et al.*, *Chem. Commun.* pp. 4611–4613 (2007).

[55] J. Lecointre, G. M. Roberts, D. A. Horke, J. R. R. Verlet, *J. Phys. Chem. A* **114**, 11216 (2010).

[56] M. Sobczyk, P. Skurski, J. Simons, *J. Phys. Chem. A* **107**, 7084 (2003).

[57] I. Zanon, C. Pecile, *J. Phys. Chem.* **87**, 3657 (1983).

[58] P. Skurski, M. Gutowski, *J. Mol. Struct. Theochem* **531**, 339 (2000).

[59] M. Makowski, M. T. Pawlikowski, *Int. J. Quantum Chem.* **106**, 1736 (2006).

[60] T. Koopmans, *Physica* **1**, 104 (1934).

[61] M. J. Frisch, *et al.*, *Gaussian03* revision c.02 (2003).

[62] I. Haller, F. B. Kaufman, *J. Am. Chem. Soc.* **98**, 1464 (1976).

[63] S. Panja, *et al.*, *J. Chem. Phys.* **127**, 124301 (2007).

[64] G. M. Roberts, J. L. Nixon, J. Lecointre, E. Wrede, J. R. R. Verlet, *Rev. Sci. Instrum.* **80**, (2009).

[65] A. E. Bragg, J. R. R. Verlet, A. Kammrath, O. Cheshnovsky, D. M. Neumark, *J. Chem. Phys.* **122**, 054314 (2005).

[66] H. Köppel, *Chem. Phys. Lett.* **205**, 361 (1993).

[67] G. Stock, *Chem. Phys. Lett.* **224**, 131 (1994).

[68] A. L. Sobolewski, W. Domcke, *Chem. Phys.* **259**, 181 (2000).

[69] S. Perun, A. L. Sobolewski, W. Domcke, *J. Am. Chem. Soc.* **127**, 6257 (2005).

[70] C. D. Cooper, W. F. Frey, R. N. Compton, *J. Chem. Phys.* **69**, 2367 (1978).

[71] P. Kebarle, S. Chowdhury, *Chem. Rev.* **87**, 513 (1987).

[72] J. J. Andre, G. Weill, *Mol. Phys.* **15**, 97 (1968).

[73] R. Pou-Amerigo, L. Serrano-Andrs, M. Merchn, E. Ort, N. Forsberg, *J. Am. Chem. Soc.* **122**, 6067 (2000).

[74] D. H. Sarr, C. Kazunga, M. J. Charles, J. G. Pavlovich, M. D. Aitken, *Environ. Sci. Technol.* **29**, 2735 (1995).

[75] M. J. Frisch, *et al.*, *Gaussian09* revision a.02 (2009).

[76] C. Katan, P. E. Blöchl, P. Margl, C. Koenig, *Phys. Rev. B* **53**, 12112 (1996).

[77] J. Schiedt, R. Weinkauf, *J. Chem. Phys.* **110**, 304 (1999).

[78] S. E. Boesch, R. A. Wheeler, *J. Phys. Chem. A* **101**, 8351 (1997).

[79] A. Girlando, I. Zanon, R. Bozio, C. Pecile, *J. Chem. Phys.* **68**, 22 (1978).

[80] B. Baguenard, J. C. Pinar, C. Bordas, M. Broyer, *Phys. Rev. A* **63**, 023204 (2001).

[81] P. Seta, *et al.*, *Nature* **316**, 653 (1985).

[82] M. S. Graige, M. L. Paddock, J. M. Bruce, G. Feher, M. Y. Okamura, *J. Am. Chem. Soc.* **118**, 9005 (1996).

[83] G. Kurisu, H. Zhang, J. L. Smith, W. A. Cramer, *Science* **302**, 1009 (2003).

[84] A. Osyczka, C. C. Moser, F. Daldal, P. L. Dutton, *Nature* **427**, 607 (2004).

[85] N. El-Najjar, *et al.*, *Phytochem. Rev.* **10**, 353 (2011).

[86] R. A. Marcus, *Rev. Mod. Phys.* **65**, 599 (1993).

[87] S. E. Boesch, A. K. Grafton, R. A. Wheeler, *J. Phys. Chem.* **100**, 10083 (1996).

[88] Y. H. Mariam, L. Chantranupong, *J. Comput.-Aided Mol. Des.* **11**, 345 (1997).

[89] P. Mohandas, S. Umapathy, *J. Phys. Chem. A* **101**, 4449 (1997).

[90] R. Pou-Amerigo, M. Merchan, E. Ort, *J. Chem. Phys.* **110**, 9536 (1999).

[91] T. K. Manojkumar, H. S. Choi, P. Tarakeshwar, K. S. Kim, *J. Chem. Phys.* **118**, 8681 (2003).

[92] T. Itoh, *Chem. Rev.* **95**, 2351 (1995).

[93] S. Siegert, F. Vogeler, R. Weinkauf, *Z. Phys. Chem. (Muenchen, Ger.)* **225**, 507 (2011).

[94] J. Weber, K. Malsch, G. Hohlneicher, *Chem. Phys.* **264**, 275 (2001).

[95] M. Puranik, S. Umapathy, *Bull. Chem. Soc. Jpn.* **75**, 1057 (2002).

[96] M. O. A. El Ghazaly, A. Svendsen, H. Bluhme, S. B. Nielsen, L. H. Andersen, *Chem. Phys. Lett.* **405**, 278 (2005).

[97] A. Ohrn, F. Aquilante, *Phys. Chem. Chem. Phys.* **9**, 470 (2007).

[98] Q. Fu, J. Yang, X.-B. Wang, *J. Phys. Chem. A* **115**, 3201 (2011).

[99] J. Simons, *Roles Played by Metastable States in Chemistry* (American Chemical Society, 1984), vol. 263 of *ACS Symposium Series*, chap. 1, pp. 3–16.

[100] L. G. Christophorou, J. G. Carter, A. A. Christodoulides, *Chem. Phys. Lett.* **3**, 237 (1969).

[101] P. M. Collins, L. G. Christophorou, E. L. Chaney, J. G. Carter, *Chem. Phys. Lett.* **4**, 646 (1970).

[102] A. R. Cook, L. A. Curtiss, J. R. Miller, *J. Am. Chem. Soc.* **119**, 5729 (1997).

[103] C. D. Cooper, W. T. Naff, R. N. Compton, *J. Chem. Phys.* **63**, 2752 (1975).

[104] E. P. Wigner, *Phys. Rev.* **73**, 1002 (1948).

[105] D. J. Pegg, *Rep. Prog. Phys.* **67**, 857 (2004).

[106] B. Baguenard, J. C. Pinare, F. Lepine, C. Bordas, M. Broyer, *Chem. Phys. Lett.* **352**, 147 (2002).

[107] K. Hansen, K. Hoffmann, E. E. B. Campbell, *J. Chem. Phys.* **119**, 2513 (2003).

[108] M. Kjellberg, *et al.*, *Phys. Rev. A* **81**, 023202 (2010).

[109] C. E. Klots, *Z. Phys. D: At., Mol. Clusters* **20**, 105 (1991).

[110] R. d. Nalda, J. G. Izquierdo, J. Dura, L. Banares, *J. Chem. Phys.* **126**, 021101 (2007).

[111] J. R. R. Verlet, A. E. Bragg, A. Kammrath, O. Cheshnovsky, D. M. Neumark, *J. Chem. Phys.* **121**, 10015 (2004).

[112] P.-O. Widmark, P.-. Malmqvist, B. O. Roos, *Theo. Chem. Acc.* **77**, 291 (1990).

[113] G. Ghigo, B. O. Roos, P.-. Malmqvist, *Chem. Phys. Lett.* **396**, 142 (2004).

[114] N. Forsberg, P.-. Malmqvist, *Chem. Phys. Lett.* **274**, 196 (1997).

[115] G. Karlström, *et al.*, *Comp. Mater. Sci.* **28**, 222 (2003).

[116] A. E. Bragg, J. R. R. Verlet, A. Kammrath, O. Cheshnovsky, D. M. Neumark, *J. Am. Chem. Soc.* **127**, 15283 (2005).

[117] J. P. Telo, A. S. Jalilov, S. F. Nelsen, *J. Phys. Chem. A* **115**, 3016 (2011).

Chapter 4

Electronic Dynamics of Polyanions

There is no harm in doubt and skepticism for it is through these that new discoveries are made.

Richard P. Feynman

This chapter is partially based on the following publications:

D. A. Horke, A. S. Chatterley and J. R. R. Verlet, *Phys. Rev. Lett.* **108**, 083003 (2012)

D. A. Horke, A. S. Chatterley and J. R. R. Verlet, *J. Phys. Chem. Lett.* **3**, 834 (2012)

D. A. Horke, A. S. Chatterley and J. R. R. Verlet, *J. Chem. Phys.* **(in preparation)**, (2012)

This chapter contains recent experimental results from investigations of polyanions (multiply-charged anions) in the gas-phase. A general introduction into the area is given, highlighting the recent interest in studies of polyanions, both because of their wide use in nature and technology, and for the study of fundamental interactions between charged particles on a molecular scale. Section 4.2 investigates the Repulsive Coulomb Barrier (RCB) in detail, a characteristic property of polyanions. It specifically looks at the effect of excess internal energy on the RCB and the mechanism of electron loss via tunnelling through the barrier. The following section 4.3 is concerned with the effect of the RCB on the photodetachment process, looking at how it affects photoelectron spectra and angular distributions. It furthermore highlights the differences between spectra collected with femtosecond or nanosecond laser pulses. We demonstrate how the unusual properties of the RCB affect the trajectories of outgoing photoelectrons, leading to photoelectron angular distributions that can be used to probe large-amplitude structural dynamics in polyanions, with data shown for the ultrafast dephasing of a rotational wavepacket in a dianion. Following this will be a summary and conclusion of the findings presented within this chapter and a brief outlook onto future experiments in this area.

4.1 Introduction

Polyanions, that is anions with multiple excess charges (sometimes referred to as multiply-charged anions), are ubiquitous throughout nature, biology and chemistry. While the study of polyanions in the condensed phases (such as solution or salt crystals) is relatively common, little is known about these systems in the gas-phase. This is partly due to the technological difficulties with introducing large polyanions into the gas-phase, and also because many polyanions commonly encountered in solution are unstable with respect to electron loss or fragmentation in the gas-phase.[1–4] While suitable experimental techniques, most importantly electrospray ionisation (see chapter 2),[5–7] now routinely allow one to transfer polyions ions into the gas-phase, the issue of stability *in vacuo* remains. Small and highly-charged systems, such as sulfonate or phosphate, that are ubiquitous in solution phase chemistry, are unstable when isolated, due to the strong repulsion between the excess charges and the lack of stabilising solvent.[8,9] However, despite this intrinsic electronic instability arising from the Coulombic repulsion between excess charges, polyanions also have a fundamental electronic stability due to the electron-nuclear attraction.[2,10–16] This balance of forces makes polyanions an interesting system to study for gaining an understanding of these fundamental interactions at the molecular level and how they influence, for example, outgoing photoelectrons. This interplay of interactions furthermore gives rise to several unusual properties of polyanions, most impor-

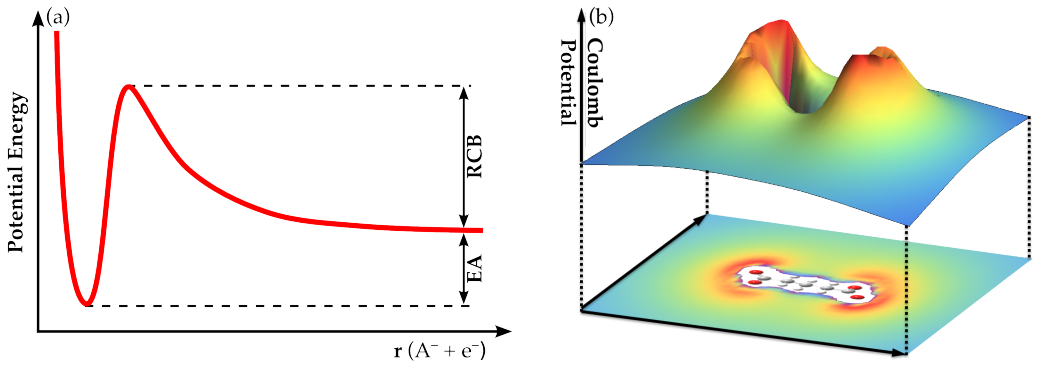

Figure 4.1: The Repulsive Coulomb Barrier (RCB), arising from the balance of electron-electron repulsion and nuclear-electron attraction. (a) 1-dimensional sketch of the potential encountered when an electron approaches an anion. (b) Calculated RCB surface for pentanedioic acid, calculated in the plane of the carbons, demonstrating the spatial dependence of the RCB on the location of excess charges.

tantly the presence of a repulsive Coulomb barrier (RCB) to photodetachment, figure 4.1(a).[14,17–20] The RCB can be most intuitively understood by considering the reverse process to electron detachment from a polyanion, that is the addition of an electron to an already negatively charged species. As the excess electron approaches the system from a distance it will interact with the existing ion as though it were a point charge and feel a repulsive force according to the distance between the charges, r, leading to a repulsive potential scaling as r^{-1}. Thus the repulsion between the two will increase until, when the distance between the two is sufficiently small, the point-charge approximation is no longer valid and the nuclear attraction out-competes the Coulomb repulsion. The excess electron will be attracted to the system and form a bound state, with a barrier to electron detachment. The presence of this potential barrier leads to several interesting and unusual observations in polyanions, such as the direct observation of electron tunneling[11,12,14,21] or species with negative electron binding energies.[16,22]

While the height of the RCB (see figure 4.1(a)) depends on the magnitude of the Coulomb repulsion between the excess charges, and therefore the distance between them,[15] the RCB itself is of course a three-dimensional (3D) potential in space. An example of this is shown in figure 4.1(b), which depicts the 2D potential barrier (within the plane containing the Carbon atoms) to photodetachment from a pentanedioic acid. A maximum potential barrier is observed around the areas where the negative charges reside, around the terminal dicarboxylate groups. The barrier falls off rapidly towards the centre of the molecule, and is lowest furthest away from the charges, around the central carbon atom. The RCB therefore depends on the spatial location, or geometry, of the excess charges within the molecular framework. As has been shown by experiments in the Wang group, this spatial distribution of the RCB has a large effect on the trajectory of outgoing photoelectrons.[23–25] We show that indeed by probing

the shape of the RCB, information about the molecular geometry, or specifically the location of excess charges within the molecule, can be gained.[26] While the exact calculation of the potential experienced by an electron within the RCB is computationally very challenging, due to the non-locallity and energy dependence of the potential, the introduction of suitable approximations allows for the calculation of local and non-energy dependent RCBs of sufficient quality to agree quantitatively with experimental findings (see section 4.3).[27] Seminal contributions to the theoretical study of polyanions and RCBs have been made by the groups of Lorenz Cederbaum[2,27–35] and Jack Simons,[1,8,13,36–40] who have calculated electronic properties and RCBs for numerous atomic and molecular dianions. One approximative approach that yields non-energy dependent RCBs is the *Local Static Approximation* (LSA), which we utilise in section 4.3 to calculate 2D RCB surfaces for dianions. This quantum chemical approach relies on calculating the energy difference between a system in the presence of a point charge at position **r** and the same system in the absence of the point charge.[27] By scanning the position **r** a multidimensional map of the RCB is acquired. However, a few technical details need to be taken into account. For calculating an RCB for photodetachment from a dianion, the remaining electronic configuration should be that of the monoanion, however in the optimised geometry of the dianion (as electron detachment is a vertical process). Furthermore, the presence of the point charge close to the remaining monoanion should not introduce any polarisation effects on the electron density around the monoanion, as in reality the outgoing electron will leave the system too fast to disturb it. The easiest way to practically implement this in quantum chemical calculations is to consider the point charge as infinitesimally small for the purposes of the calculation, and subsequently scale the obtained results to represent the repulsion of a unit charge. With these considerations in mind, the LSA can be applied to any *ab initio* method that calculates the total energy.[27]

Despite the huge importance and influence of the RCB on the electronic properties of polyanions, nothing is known about the effect of ro-vibrational excitation (excess internal energy) on the RCB. We investigate this in section 4.2, using the fluorescein dianion as a model system.[41] We furthermore study the tunnelling dynamics through the RCB in the fluorescein dianion, following excitation to an electronic state bound solely by the RCB. A similar situation is encountered in the study of the pyrromethene-556 dianion, which again possesses a bright electronic excited state bound only by the RCB. We use this system in section 4.3 to first investigate the effect of the RCB on photoelectron spectra, such as kinetic energy cut-offs and peak shapes, as well as providing a detailed comparison between photoelectron spectra collected with a femtosecond or a nanosecond laser pulse, and the additional information that can be gained by having both sets of data. We secondly use the RCB in pyrromethene dianions to study

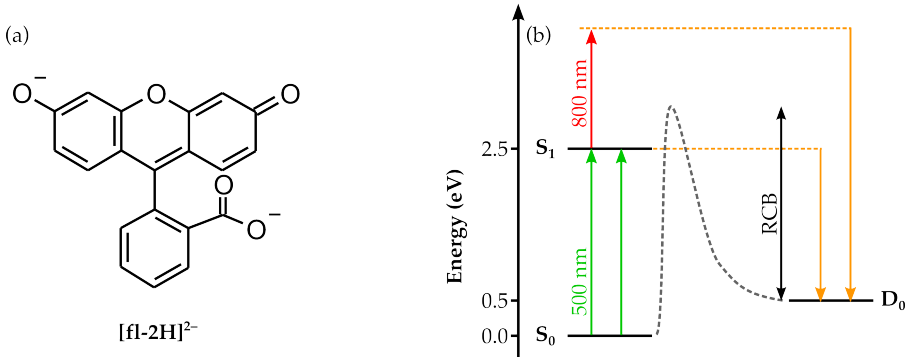

Figure 4.2: (a) Structure of the doubly deprotonated fluorescein dianion, $[fl\text{-}2H]^{2-}$. (b) Basic electronic structure diagram of $[fl\text{-}2H]^{2-}$, indicating the presence of a potential barrier to photodetachment and the excitation schemes used.

the effect of the barrier shape on the trajectories of outgoing photoelectrons. We demonstrate that by creating a spatially aligned sample of polyanions in the gas-phase, the measured photoelectron angular distributions are highly dependent on the RCB, which in turn carries information about the geometry of the excess charges within the anion. This new technique can be used for the study of large-amplitude structural dynamics with femtosecond resolution and we show proof-of-principle data for this with the rotational dephasing dynamics of pyrromethene-556 dianions at different degrees of excess internal energy.[26] This chapter is concluded with a summary of the experimental findings presented throughout and a brief outlook onto future experiments on gas-phase polyanions in our laboratory.

4.2 Effect of Internal Energy on the RCB

Despite the general interest in polyanions and especially the RCB in the recent literature, there has been no detailed investigation of the dependence of the RCB on internal energy, i.e. ro-vibrational excitation, and the associated effect of tunnelling through it. In principle, for a given electronic state, there is not a single RCB, but rather every ro-vibrational level of the electronic state will have an associated RCB. This then leads to the question of how the RCB changes as more internal energy is imparted in a given electronic state, and how do these changes affect the photoelectron spectrum, which has emerged as the primary tool for studying polyanionic systems *in vacuo*.[4]

In order to address these questions and understand the fundamental relationship between excess internal energy and the observed RCB, we have studied the doubly deprotonated fluorescein dianion ($[fl\text{-}2H]^{2-}$, figure 4.2(a)) using a combination of photoelectron spectroscopy and time-resolved photoelectron spec-

troscopy. A basic electronic state diagram of $[\text{fl-2H}]^{2-}$ is shown in figure 4.2(b). The fluorescein dianion has a bright $S_1 \leftarrow S_0$ transition around 2.5 eV, which is highly fluorescent in solution (Φ=0.92)[42] but has recently been shown to be non-fluorescent in the gas-phase.[43] Instead the isolated $[\text{fl-2H}]^{2-}$ undergoes electron loss following $S_1 \leftarrow S_0$ excitation. While this is not surprising, given that the excitation energy is above the electron affinity of $[\text{fl-2H}]^{2-}$, it still remains unclear if the S_1 state is completely unbound with respect to electron loss, or if the electron is bound by an RCB (as indicated in figure 4.2(b)) and the electron subsequently lost through an indirect process, such as tunnelling through the barrier.[11,12,21] We address these questions here by exciting the S_1 state with different amounts of internal energy (using tunable nanosecond or femtosecond laser pulses) and measuring the resulting photoelectron spectrum (section 4.2.1), thereby probing the energetics of the RCB and the photodetachment process. We subsequently employed time-resolved spectroscopy to probe the dynamics of the S_1 excited state (section 4.2.2) and specifically the tunnelling process. As this is sensitive to the size and shape of potential being tunnelled, it yields further insight into the nature of the RCB observed at different amounts of ro-vibrational excitation.

Experimentally, $[\text{fl-2H}]^{2-}$ is produced via electrospray ionisation of a 1 mM solution of fluorescein in methanol, brought to pH$\sim$11 through the addition of NaOH (see chapter 2 for details). Mass selected $[\text{fl-2H}]^{2-}$ dianions are subsequently intersected by laser pulses from a femtosecond or nanosecond laser. Nanosecond pulses are generated using an Nd:YAG pumped optical parametric oscillator, producing $\sim$5 mJ pulses of 10 ns duration across the visible, yielding intensities in the interaction region of $I_{ns} \sim 7 \times 10^6$ Wcm^{-2}. Femtosecond pulses in the visible spectral region are produced as described in chapter 2, and typical intensities for single colour photoelectron spectra are $I_{fs} \sim 1 \times 10^{10}$ Wcm^{-2}. Time-resolved experiments utilise a 800 nm (1.55 eV) probe beam, as well as the visible pump. Typical cross-correlations are on the order of 140 fs and pump and probe pulses are co-linearly combined before being loosely focused into the interaction region, reaching intensities on the order of $I_{pump} \sim 8 \times 10^{11}$ Wcm^{-2} and $I_{probe} \sim 5 \times 10^{12}$ Wcm^{-2}.

4.2.1 Photoelectron spectroscopy of the fluorescein dianion

The energetics of the $[\text{fl-2H}]^{2-}$ dianion are probed using photoelectron spectroscopy at various wavelengths, and several photoelectron spectra collected with nanosecond laser pulses between 540 nm (2.30 eV) and 430 nm (2.88 eV) are shown in figure 4.3(a). Also shown is a spectrum collected with a 400 nm (3.10 eV) femtosecond laser pulse. There are no apparent differences between photoelectron spectra collected with a femtosecond or nanosecond light source, confirming that the observed features arise from the absorption of a single pho-

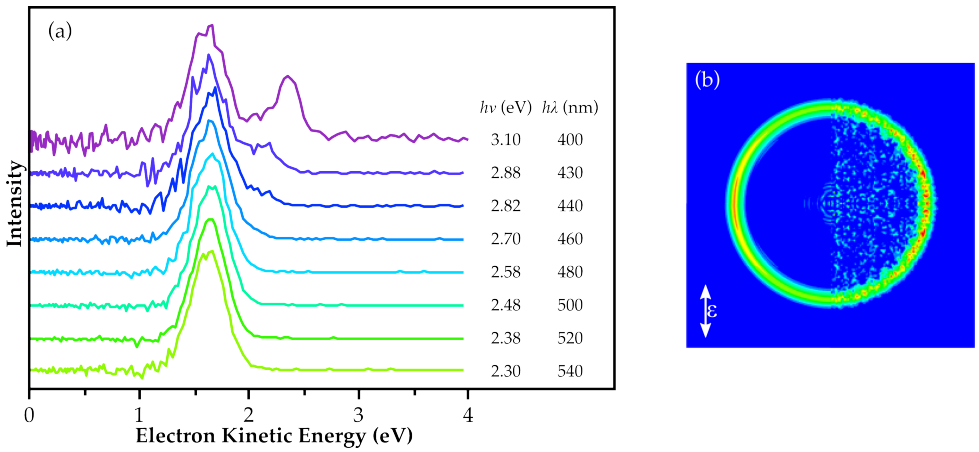

Figure 4.3: Photoelectron spectroscopy of the fluorescein dianion. (a) Spectra collected at various excitation wavelengths (430-540 nm, as indicated) with a nanosecond laser pulse, also shown is the spectrum at 400 nm collected with a femtosecond laser pulse. A feature at constant *eKE* = 1.64 eV persists in all spectra, despite the changing excitation energy. (b) Central slice through the photoelectron cloud following excitation at 2.48 eV (500 nm); showing the reconstructed (left) and raw (right) image.

ton. A deconvoluted photoelectron image, collected with nanosecond 500 nm (2.48 eV) laser pulses is shown in figure 4.3(b) and reveals a single, slightly anisotropic feature ($\beta_2 = -0.2 \pm 0.1$). The most striking aspect of the data shown in figure 4.3(a) is the persistence of a photoelectron peak at an electron kinetic energy (*eKE*) of 1.64 eV, regardless of excitation energy. Typically in photoelectron spectroscopy the electron binding energy (*eBE*) is defined as $eBE = h\nu - eKE$ (equation 1.56). However, despite an increase in photon energy of 0.8 eV in going from 540 nm to 400 nm, no concomitant increase in *eKE* is observed and the feature persists at *eKE* = 1.64 eV, suggesting a clearly unphysical increase of the binding energy with increasing photon energy. If photon energies in excess of 2.60 eV (480 nm) are used, an additional feature emerges, first appearing as a small shoulder to the high energy side of the dominant peak in the 480 nm spectrum, and increasing in *eKE* as the photon energy is increased. This feature also gains intensity relative to the feature with constant *eKE* as the photon energy rises. To quantitatively evaluate the energetics, the observed photoelectron spectra have been fitted with the sum of two Gaussian functions, which accurately describe the observed photoelectron peaks. This yields an average *eKE* for the non-shifting peak of 1.64 ± 0.01 eV, although we note that our spectrometer resolution in this spectral region is 0.08 eV. The higher *eKE* feature shifts to higher energy with increasing photon energy, as typically observed in photoelectron spectroscopy, and from this we extract an adiabatic binding energy (*ABE*) of 0.5 ± 0.1 eV for $[\text{fl-2H}]^{2-}$.

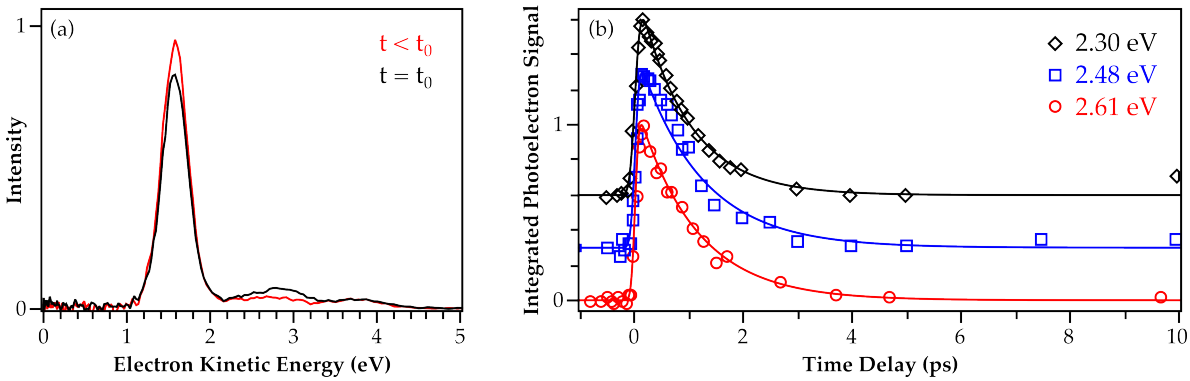

Figure 4.4: Time-resolved photoelectron spectroscopy of the S_1 excited state of$[fl\text{-}2H]^{2-}$. (a) Two representative photoelectron spectra at $t < 0$ (red) and $t = 0$ (black), an additional feature is observed at high *eKE*, along with a depletion in the tunnelling peak. (b) Integrated photoelectron signal over the additional feature observed for various excitation wavelengths, corresponding to different amounts of internal energy in the excited state. All data sets exhibit similar tunnelling lifetimes.

4.2.2 Excited state dynamics of the fluorescein dianion

In order to gain further insight into the S_1 excited state properties, and to understand the nature of the non-shifting photoelectron feature, we have performed time-resolved photoelectron spectroscopy. Population is excited into the S_1 with a pump photon in the visible (2.30 eV, 2.48 eV or 2.61 eV) and subsequently probed at various delays t with a 800 nm (1.55 eV) probe pulse. Two representative photoelectron spectra, collected at $t < 0$ (probe before pump) and at $t = 0$ (pump and probe temporally overlapped) are shown in figure 4.4(a). Due to the higher photon intensities employed in these studies, small multiphoton peaks are observed at higher *eKE* in both photoelectron spectra. An additional feature can be identified in the spectrum with pump and probe temporally overlapped, centred at ∼2.9 eV *eKE*. We attribute this feature to the removal of an electron from the S_1 excited state by a probe photon. At the same time a depletion is observed in the low *eKE* peak at 1.64 eV, indicating that this features is dependent on the S_1 population and is depleted around $t = 0$ due to the competition with photodetachment from the S_1 by the probe photon. In order to quantitatively evaluate the lifetime of the excited state, the collected photoelectron spectra are integrated over the additional feature (2.2 eV $\leq$ *eKE* $\leq$ 3.5 eV) and plotted as a function of pump-probe delay t. This is show in figure 4.4(b) for three different pump wavelengths. All datasets show a rapid rise around $t = 0$, corresponding to the overlap of pump and probe pulses, followed by an exponential decay of population. Fitting these data with a single exponential, convoluted with a Gaussian instrument response function, yields characteristic lifetimes for the S_1 state of 0.9, 1.1 and 1.1 $\pm$0.2 ps, for excitation at 2.30 eV (538 nm), 2.48 eV (500 nm) and 2.61 eV (475 nm), respectively.

4.2.3 Discussion

The time-resolved photoelectron data presented in the previous section clearly shows that the feature observed at a constant *eKE* in figure 4.3(a) cannot arise from direct photodetachment, as this would be instantaneous on the timescale of our experiment. Instead the data shows that the S_1 state, while energetically located in the detachment continuum, is actually bound by a RCB, and the observed lifetime of the S_1 state corresponds to the tunnelling lifetime through this potential barrier.[11] The relatively short lifetime on the order of 1 ps indicates that the excited state is likely located close to the top of the barrier. It is this tunnelling electron loss that leads to the observation of a photoelectron peak at 1.64 eV *eKE*. We explain the absence of a shift to higher *eKE* with increasing photon energy by considering that the total energy within the system must be conserved. The *eKE* in a photodetachment process can then be expressed as

$$eKE = h\nu - ABE - E_{int}, \tag{4.1}$$

where $h\nu$ is the energy of the incident photon, *ABE* indicates the adiabatic binding energy of the electron and E_{int} is the internal energy of the remaining anion (following detachment from the dianion). Accordingly, the observed invariance in *eKE* with changing $h\nu$ must be accompanied by a change in E_{int} of the remaining anion. Therefore the remaining anion must be produced with increasing amounts of excess internal energy as the photon energy is increased. Typically in photoelectron spectroscopy, the detachment of an electron is considered a vertical transition and the E_{int} in the remaining anion determined by the Franck-Condon factors between the dianion and anion and is independent of $h\nu$. The observed photoelectron spectra in figure 4.3(a) therefore show that electron loss via tunneling through the RCB from the S_1 excited state of the dianion is not a vertical transition, but rather can be considered a diagonal transition that obeys a propensity rule conserving internal energy.

For a dianion A^{2-}, each vibrational level of the photodetachment product A^- will have an associated RCB leading to the formation of the dianion. This RCB can either be viewed from the perspective of the dianion (inner RCB) or from the perspective of an electron approaching a monoanion (outer RCB).[44] This leads to two possible scenarios for the relationship between the RCB of different vibrational states, as depicted in figure 4.5(a); (i) The height of the outer RCB is constant while the inner RCB increases with E_{int} or (ii) the inner RCB is constant while the height of the outer RCB decreases with increasing E_{int}. The Wang group have previously presented arguments favouring the latter,[14] however if this were the case then for photon energies that exceed the height of the inner RCB, direct detachment would be the only accessible electron loss channel. This is clearly not the case here, because the photoelectron spectrum at *all* photon

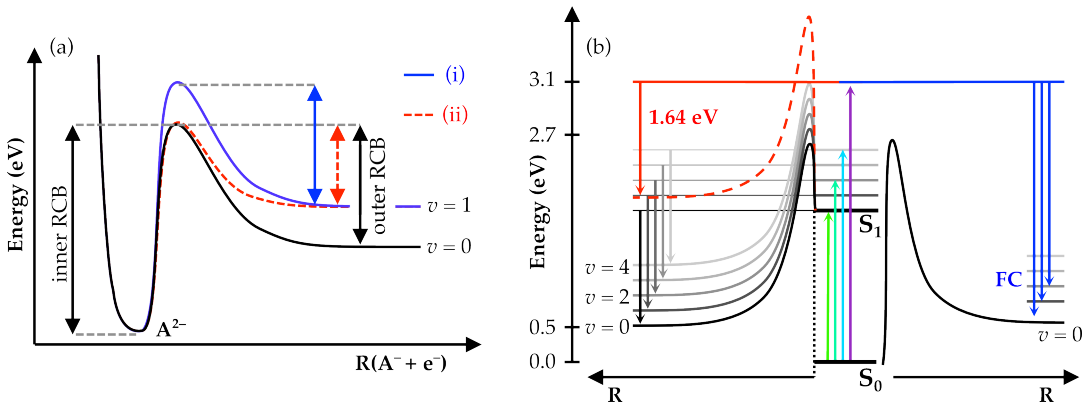

Figure 4.5: Effect of internal energy on the RCB. (a) Two scenarios are depicted, (i) constant outer RCB or (ii) outer RCB varies with internal energy. Experimental data points to the former being the case and this is depicted in (b) for the fluorescein dianion, where **R** indicates the $[\text{fl-2H}]^-$ to e^- distance. With increasing internal energy in the excited state the inner RCB increases, leading to a constant outer RCB (left side of figure). Tunnelling through this constant RCB is strongly adiabatic and yields a photoelectron feature at a fixed *eKE* of 1.64 eV. If the excitation energy is sufficient to directly overcome the RCB from the S_0 to the monoanion, a second decay channel opens up and direct photodetachment is observed (right side of figure), governed by Franck-Condon (FC) factors.

energies (figure 4.3(a)) exhibits a feature due to tunnelling at 1.64 eV *eKE*. Even at photon energies of 3.10 eV, where a feature due to direct detachment is observed, a clear signature of tunnelling through the RCB is present. Therefore, based on our experimental findings, we evoke case (i), a constant RCB height for every vibrational level.

The observed diagonal nature of the tunnelling transition is depicted in figure 4.5(b). If the system is excited to the lowest part of the S_1 band at 2.30 eV, electron tunnelling adiabatically correlates to the formation of a low vibrational level of the monoanion $[\text{fl-2H}]^-$. It should be noted with reference to figure 4.5(b) that the RCB leading to the S_1 state is not the same as that leading to the S_0 state of the dianion.[27] However they are identical at long range, as they share the same product state ($[\text{fl-2H}]^- + e^-$) and differences are only expected to arise at very short range. Thus we anticipate that the height of the S_1 outer RCB is similar to that of the S_0 outer RCB, as indicated. Increasing the excitation (pump) energy beyond 2.30 eV accesses higher vibrational levels of the S_1 electronic state. As E_{int} is conserved during the tunnelling event, the monoanion product $[\text{fl-2H}]^-$ will be formed vibrationally excited, leading to the observation of a constant *eKE* despite increasing photon energy. Once the employed photon energy is sufficiently energetic to directly overcome the RCB to detachment from the S_0 state, a new photon loss channel opens up, as indicated on the right hand side of figure 4.5(b), and direct photodetachment into the continuum becomes a possibility. This secondary detachment pathway gives rise to the additional feature observed in the photoelectron spectra (figure 4.3(a)) at higher *eKE*, first observed for photon energies 2.58 eV $< h\nu <$ 2.70 eV. This direct detachment

is a vertical transition, as commonly observed in photoelectron spectroscopy, and hence the vibrational excitation in the product is determined by the Franck-Condon factors between the S_0 state of the dianion and the D_0 ground state of the monoanion, and independent of excitation energy. This feature behaves as expected, shifting to higher *eKE* as the photon energy is increased. Concomitant to the direct detachment channel accessed at 2.70 eV, this is still resonant with the $S_1 \leftarrow S_0$ transition, exciting high vibrational levels of S_1, consequently leading to high vibrational excitation in the monoanion following the adiabatic electron loss through tunnelling. Indeed, even at photon energies of 3.10 eV, more than 0.4 eV above the RCB for direct detachment from the S_0 state, excitation into the S_1 still preferentially adiabatically tunnels through the RCB, although we do note that signal levels are significantly lower than those observed at lower excitation energies. As the S_1 state excited at 3.10 eV is located within the electronic detachment continuum, adiabatic autodetachment might be expected to compete with tunnelling electron loss, this would manifest itself in a broadening of the observed photoelectron feature. We observe no evidence for this, even in the 3.10 eV photoelectron spectrum, and conclude that this loss channel must be a very minor one. Hence the physical picture that emerges is one of a dense progression of RCB potential energy surfaces, each corresponding to a ro-vibrational state in the anion, while the effective outer RCB height is approximately constant.

Further evidence for this conceptual framework of a constant RCB independent of E_{int} can be gained from the time-resolved dynamics of the S_1 state. The tunnelling rate through the barrier following excitation with various amounts of internal energy in the excited state was found to be constant over a 0.3 eV window. The rate of tunnelling is strongly dependent on the height and width of the potential, and this suggests the barrier encountered by the electron in the excited state is very similar in all cases and independent of E_{int}.[45] This observation strongly supports the concept of a constant outer RCB and an inner RCB that increases with increasing E_{int}, case (i) in figure 4.5(a). We can estimate the height of the outer RCB by considering the *ABE* of the system, determined to be 0.5 ± 0.1 eV, and the appearance of the direct detachment feature. This was first observed following excitation with photon energies between $2.6 - 2.7$ eV, and hence we estimate the height of the outer RCB as $2.1 - 2.2$ eV.

The emerging physical picture of a dense ladder of vibrational RCB potential surfaces furthermore explains tandem mass spectra of $[\text{fl-2H}]^{2-}$.[43] Following excitation of the $S_1 \leftarrow S_0$ transition an electron is lost, leading to the formation of $[\text{fl-2H}]^-$. However, this is not observed for thermal activation methods, such as off-resonance irradiation collisionally activated dissociation or infra-red multiphoton dissociation, despite the low *ABE* of 0.5 eV. Instead fragmentation with

loss of the CO_2^- group is favoured.[43] This is consistent with the picture presented here; as vibrational energy is deposited into the dianion the electron is prevented from leaving as the inner RCB increases with E_{int}. Eventually sufficient energy is deposited into the system to break the weakest bond, leading to fragmentation as the dominant decay channel, not electron loss. Indeed, dissociation in favour of electron loss is a common feature of tandem mass spectrometry using activation methods through collisions or photons.[46,47]

Using time-resolved photoelectron spectroscopy to probe the dynamics of an electronic excited state bound solely by the RCB we have shown that one cannot consider a single barrier for a system, but instead an RCB exists for every ro-vibrational state. This dense ladder of potential energy surfaces explains the observation of strongly adiabatic tunnelling, which can be viewed as a diagonal transition and exhibits dramatically different behaviour to that normally observed in photoelectron spectroscopy, such as the observation of a constant *eKE* feature, independent of excitation energy. The physical picture of an increasing inner RCB as more internal energy is deposited into the excited state even remains valid above the lowest (v=0) barrier to electron loss, and tunnelling is observed to compete with direct detachment of an electron. These results highlight the complexity of the RCB in polyanions and its importance for interpreting photoelectron spectra, which will be further explored in the following section.

4.3 Influence of RCBs on photoelectron spectra

Photoelectron spectroscopy has emerged as a key tool for the study of gaseous polyanions, their energetics and dynamics.[4] While several new and exciting properties of polyanions have been investigated with this technique, such as energetic cut-offs and electron tunnelling processes,[11,12,14,21] no detailed studies have investigated the effect of these unique properties on the observed photoelectron spectra. In particular the presence of a Repulsive Coulomb Barrier (RCB) has a large influence on the photodetachment processes observable,[14,15] such as the strongly adiabatic tunnelling mechanism through the RCB,[41] which cannot be rationalised within the commonly used framework for photoelectron spectroscopy. This section not only focusses on explaining the photoelectron spectra from polyanions, and how they are influenced by the RCB and associated dynamics, but we furthermore compare spectra collected with femtosecond and nanosecond laser pulses, and explain the marked differences between them. It is only through the combined results from long and short pulse excitation, as well as ultrafast time-resolved experiments, that a complete picture of the dynamics can be gained. In the following sections we therefore present the spectra collected under several different conditions, before discussing and interpreting

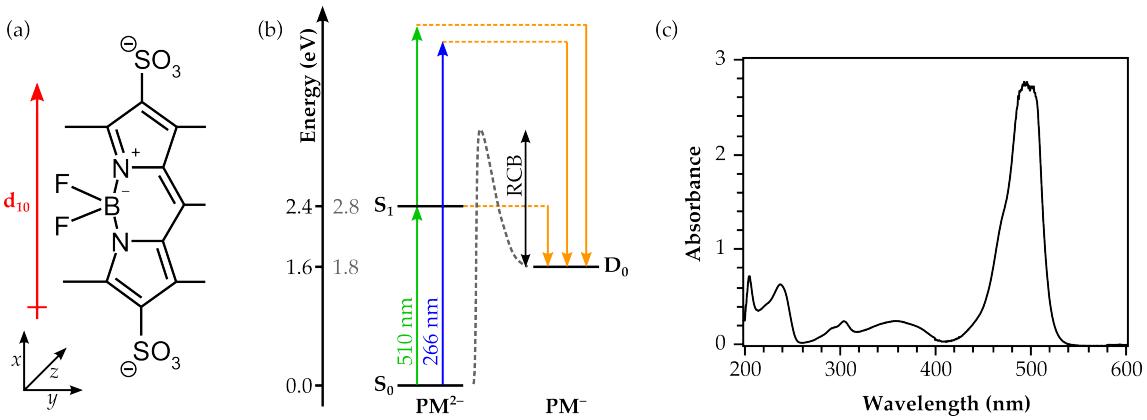

Figure 4.6: The pyrromethene-556 dianion. (a) Molecular structure indicating the direction of the $S_1 \leftarrow S_0$ transition dipole moment $\mathbf{d_{10}}$. (b) Basic electronic state diagram showing the presence of the excited state that is bound solely by the RCB. The axis values indicate the experimental (black) and theoretical (grey) energies. (c) Absorption spectrum of PM^{2-} in methanol, showing the strong $S_1 \leftarrow S_0$ transition around 498 nm.

them jointly in section 4.3.4. Following this will be an analysis and discussion of the observed photoelectron angular distributions for both one-colour and time resolved data in section 4.3.5.

The prototypical dianion used in these studies is pyrromethene-556 (PM^{2-}), figure 4.6(a).[48,49] This commonly used laser dye consists of a central boron-dipyrromethene (BODIPY) chromophore, on which the highest occupied molecular orbital (HOMO) is located, and two terminal SO_3^- groups that carry the excess charge. The BODIPY chromophore has been widely studied in solution[50,51] and has a strong $S_1 \leftarrow S_0$ transition around 498 nm in methanol,[52] as shown in the absorption spectrum in figure 4.6(c). The $S_1 \leftarrow S_0$ transition dipole moment, $\mathbf{d_{10}}$, is located along the molecular axis as indicated in figure 4.6(a). Similar to the fluorescein dianion studied previously,[41] this excited state is formally unbound with respect to electron loss to form the monoanion, but the electron is prevented from leaving by the presence of the RCB, as indicated in the electronic structure diagram in figure 4.6(b). The choice of PM^{2-} as a model dianion has several reasons; (i) the presence of a strong, optically bright excited state that primarily decays via fluorescence in solution ($\Phi = 0.90$ in methanol),[49,53] implying that internal conversion and intersystem crossing may be minor decay channels. (ii) The rigid structural backbone of PM^{2-} does not change significantly upon excitation, ruling out any major structural changes between the charged sulfate groups and the BODIPY chromophore. (iii) The location of the terminal sulfate groups is well defined with respect to the transition dipole moment $\mathbf{d_{10}}$.

Experimentally, PM^{2-} is produced from electrospray ionisation of a 1 mM solution of PM disodium salt in methanol, and formed dianions subsequently trapped and mass-selected before being intersected by laser pulses in the cen-

tre of the velocity-map imaging detector (chapter 2). Nanosecond laser pulses across the visible spectrum are derived from a Nd:YAG pumped optical parametric oscillator and attenuated to ∼5 mJ per pulse at 10 Hz, yielding intensities in the interaction region of 7×10^6 Wcm^{-2}. Femtosecond laser pulses at 800 nm (40 fs duration) are either frequency tripled to yield UV radiation at 266 nm, or used to seed an optical parametric amplifier to produce light in the visible range. Typical intensities in the interaction region are on the order of 1×10^{10} Wcm^{-2}. For time-resolved experiments, a remainder of the fundamental 800 nm beam is used as a probe, following excitation in the visible, and typical pump-probe cross-correlations are on the order of 130 fs, as determined in a thin non-linear crystal.

4.3.1 Quantum chemistry calculations

Electronic structure calculations were used to gain an understanding of the underlying electronic states in PM^{2-}. All calculations were carried out within Gaussian09,[54] utilising the B3LYP functional and 6-311++g(2d,2p) basis set for density functional theory (DFT) and time-dependent DFT (TD-DFT) calculations. The vertical detachment energy is evaluated as the total energy difference between the monoanion and the dianion electronic configurations in the dianion optimised geometry and was calculated to be 1.95 eV. The adiabatic energy difference, between the anion and dianion in their respective optimised structures, was found to be 1.79 eV. To aid in the assignment of photoelectron spectra, TD-DFT was used to calculate excited electronic states and the corresponding excitation energies. For the dianion the bright $S_1 \leftarrow S_0$ transition was predicted at 2.75 eV (oscillator strengths $f = 0.42$), and with a transition dipole moment, $\mathbf{d}_{10}$, aligned along the defined x direction, as indicated in figure 4.6(a). The calculated transition energy is in reasonable agreement with experiment given the level of theory employed here. For the monoanion the first 5 electronic excited states were calculated and all found to lie within 1.6 eV of the electronic ground state. Therefore a dense manifold of electronic final states is available in the monoanion following detachment from the dianion.

In order to evaluate the RCB present in PM^{2-} the *Local Static Approximation* (LSA) approach of Dreuw and Cederbaum is employed.[27] The dianion geometry was optimised at the B3LYP/6-311++g(2d,2p) level. Due to the large number of individual calculations required, a two dimensional (2D) RCB scan was carried out using the smaller 3-21+g* basis, evaluating the RCB potential in the xy plane (as defined in figure 4.6(a) and containing $\mathbf{d_{10}}$). One dimensional slices through the RCB surface were evaluated at the higher B3LYP/6-311++g(2d,2p) level of theory and show the RCB potential along the three principal axis starting from the

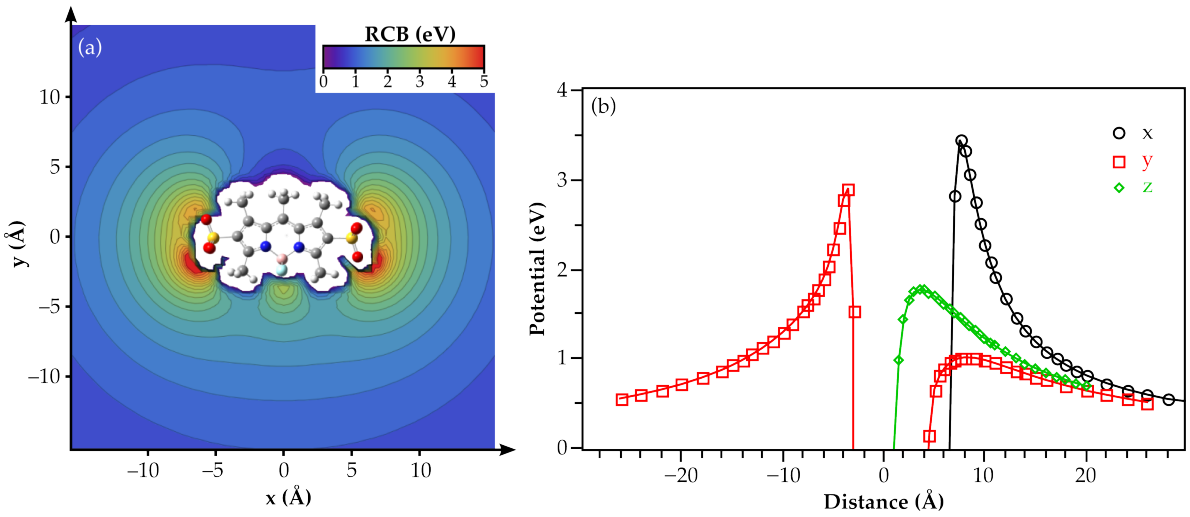

Figure 4.7: Calculated RCBs for PM^{2-}. (a) Contour plot of the RCB potential in the xy plane, as defined in figure 4.6(a). (b) Slices through the RCB potential in the three principal directions and passing through the origin, defined as the centre of the BODIPY chromophore.

origin, taken as the centre of the BODIPY chromophore. The excess point charge used to evaluate the RCB in the LSA approximation was given a magnitude of $-0.01\ e^-$ in order to minimise polarisation effects, and the resulting potentials subsequently scaled to represent the potential of a unit charge. A 2D contour plot of the RCB potential in the xy plane is shown in figure 4.7(a). Due to the inherent symmetry of this system, the surface was scanned in the x direction only from $0 \rightarrow 15$ Å and the results reflected onto the negative x direction. As the two SO_3^- groups are not in exactly the same orientation on both sides of the molecule, the shown RCB surface does not describe the RCB accurately close to the terminal sulfate groups. However, the SO_3^- groups can freely rotate about the C−S bond in vacuum, such that the local potential in this area is smeared out around the oxygens anyway. The same symmetry arguments were applied to the 1D cuts through the potential, shown in figure 4.7(b).

Analysis of the 2D contour map of the RCB in figure 4.7(a) reveals that, as intuitively expected, the largest barrier is closest to the terminal SO_3^- groups that carry the excess negative charge and falls off towards the centre of the molecule. The maximum of the RCB is approximately 5 eV, but this will be smeared out due to rotation around the C−S bonds. An asymmetric RCB is observed in the y direction, with a secondary local maximum around the electron rich Boron centre on the BODIPY chromophore. The lowest RCB is found opposite the Boron (positive y direction), and the more accurate 1D slices shown in figure 4.7(b) put this lowest barrier at ∼1.1 eV.

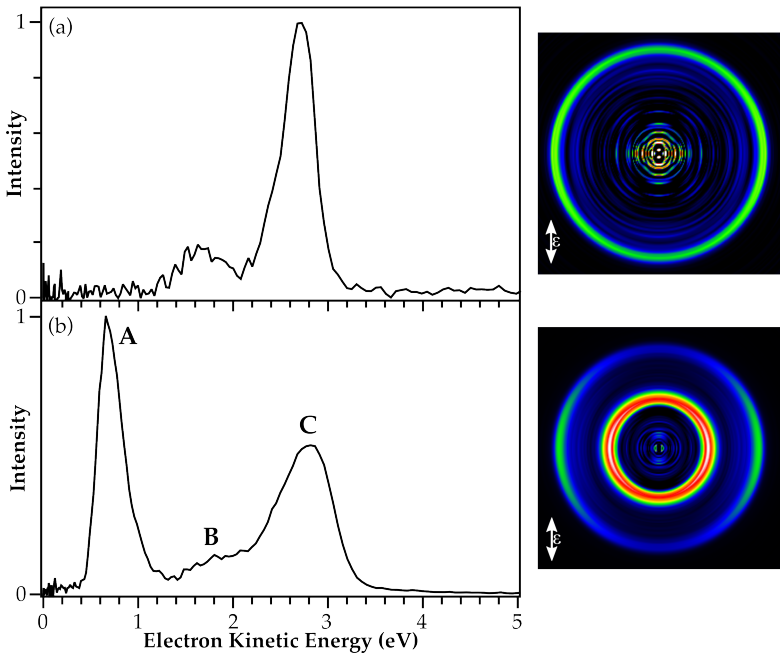

Figure 4.8: Single-colour photoelectron spectra of PM^{2-} collected with a femtosecond laser. (a) UV spectrum at 4.66 eV (266 nm), sufficient to directly detach an electron over the RCB. (b) Spectrum at 2.43 eV (510 nm), resonant with the $S_1 \leftarrow S_0$ transition. Also shown are the reconstructed photoelectron images.

4.3.2 One-colour photoelectron spectra

In order to ascertain the underlying electronic structure of PM^{2-} we use ultraviolet (UV) photoelectron spectroscopy. A single-colour photoelectron spectrum collected with femtosecond UV pulses of 4.66 eV (266 nm) is shown in figure 4.8(a). This is sufficiently energetic to detach an electron directly over the RCB (as indicated in figure 4.6(b)). The spectrum exhibits two distinctive features; a less intense broad peak centred at 1.6 eV *eKE* and with a measured anisotropy of $\beta_2 = 0.2 \pm 0.2$ and a more intense higher energy feature centred at 2.7 eV *eKE* with $\beta_2 = -0.12 \pm 0.05$. A photoelectron spectrum collected at 2.43 eV (510 nm) is shown in figure 4.8(b), this photon energy is resonant with the $S_1 \leftarrow S_0$ transition as indicated in figure 4.6(b). We observe three distinct features, labelled A,B and C in the spectrum. Feature A is a sharp and slightly asymetrically shaped peak around 0.7 eV *eKE* ($\beta_2 = -0.15 \pm 0.08$); B corresponds to a weaker peak centred at *eKE*$\sim$2.0 eV ($\beta_2 = -0.60 \pm 0.10$ and $\beta_4 = 0.11 \pm 0.13$) and feature C is a broad peak centred at 2.8 eV *eKE* with $\beta_2 = -0.56 \pm 0.05$ and $\beta_4 = 0.02 \pm 0.05$.

As the observed feature C in the resonant photoelectron spectrum corresponds to electrons of higher kinetic energy than the photon energy used, it must arise from a resonant 2-photon process via the S_1 excited state of the dianion. Further confirmation for this assignment comes from comparison with the UV spectrum in figure 4.8(a). The photon energy of 4.66 eV employed here is close to the energy imparted into the system when two 2.43 eV photon are absorbed. Given

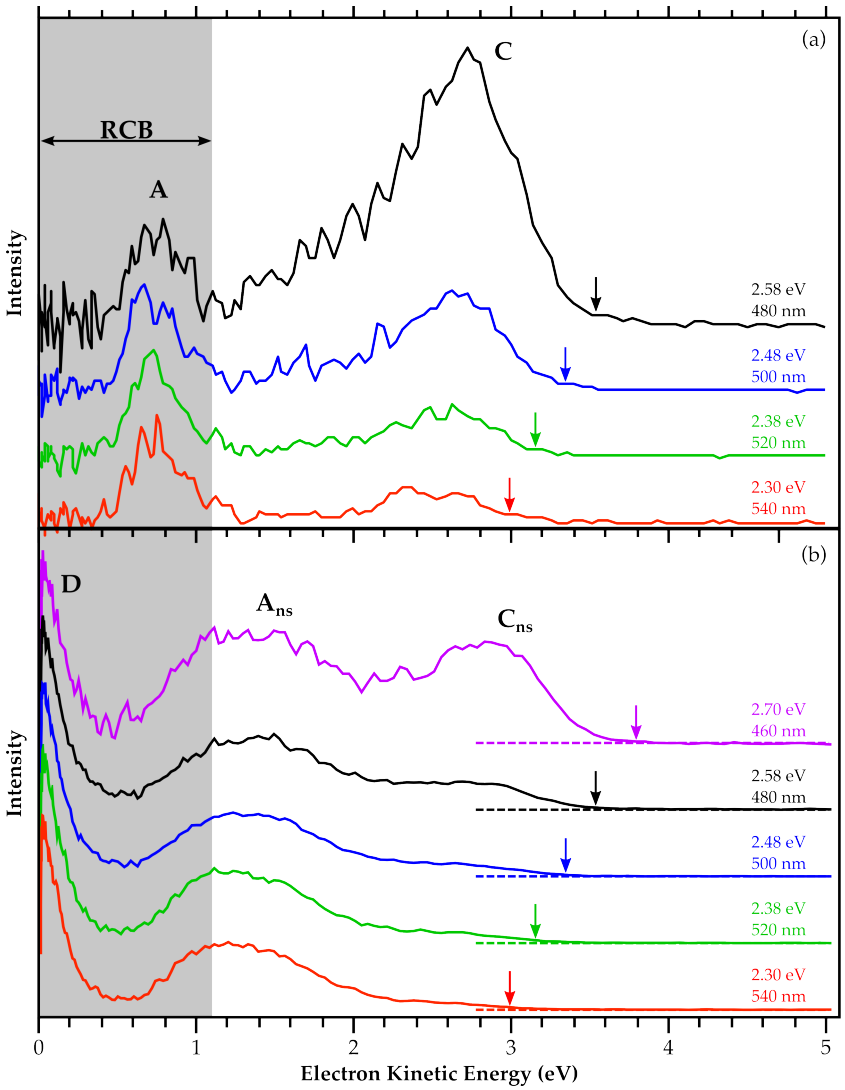

Figure 4.9: Single-colour photoelectron spectra of PM^{2-} collected with (a) femtosecond pulses and (b) nanosecond pulses. Arrows indicate the expected energetic cut-off for feature C based on the known electron affinity and photon energy employed. The shaded area represents the RCB of 1.1 eV, below which no direct electron detachment is possible from the dianion.

the large similarity in shape and peak position of features B and C with those observed in the UV spectrum, we assign both B and C to a 2-photon process, the relative intensity of these features is due to the resonance enhancement via the $S_1 \leftarrow S_0$ transition, such that B and C can be ascribed to a resonance enhanced 2-photon detachment (R2PD). The feature observed at low *eKE* in the 2.43 eV spectrum (A) is not reproduced in the UV spectrum.

Several femtosecond photoelectron spectra are shown in figure 4.9(a), these were collected with photon energies from 2.30 eV (539 nm) to 2.58 eV (479 nm), all resonant with the $S_1 \leftarrow S_0$ transition in the dianion. All spectra are similar in appearance to the spectrum collected with 2.43 eV photons shown in figure 4.8(b), with clearly distinguishable features A and C, with the weaker peak B not reproduced as clearly due to the lower signal-to-noise ratio in these data. With

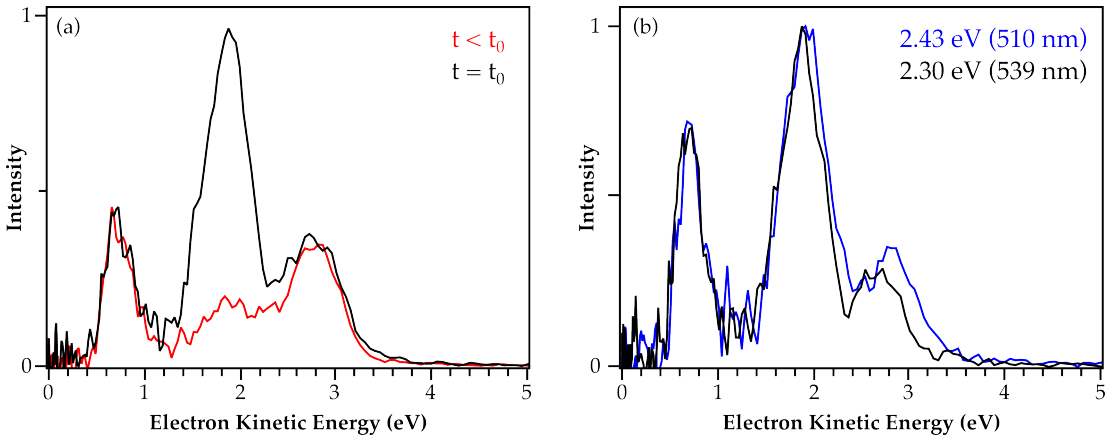

Figure 4.10: Time-resolved photoelectron spectroscopy of PM^{2-}. (a) Two representative photoelectron spectra collected with a 2.43 eV (510 nm) pump and 1.55 eV (800 nm) probe at $t < 0$ (red) and for $t = 0$ (black). A large additional pump-probe feature is observed. (b) Two photoelectron spectra collected at $t = 0$ for pump energies of 2.30 eV (black) and 2.43 eV (blue). The low *eKE* feature shows no spectral shift, whereas the pump-probe feature and the high *eKE* feature move to higher energies as expected.

increasing photon energy the relative intensity of feature C increases in comparison to A. Furthermore, feature A shows no spectral shift as the photon energy is increased, in contrast to C which shifts to higher energies, consistent with a vertical 2-photon transition.

Resonant photoelectron spectra were also collected with nanosecond laser pulses, ranging from 2.23 eV (540 nm) to 2.70 eV (460 nm), and these are shown in figure 4.9(b). All spectra are similar in appearance and exhibit three distinctive features; (i) at very low *eKE* a large isotropic peak is observed that is not present in any of the femtosecond spectra, we label this feature D, (ii) a broad peak centred around *eKE* ∼1.3 eV, that shows no spectral shift with increasing photon energy, labelled A_{ns}. This feature exhibits slight anisotropies, with $\beta_2 = -0.17 \pm 0.09$ at 2.58 eV (480 nm). Lastly a peak is observed at higher *eKE* between 2.0 eV and 3.5 eV *eKE*, this feature shifts to higher energies and gains intensity relative to feature A_{ns} as the photon energy is increased, we label this C_{ns}. Given that the observed *eKE* is higher than the employed photon energy, this feature must arise from the absorption of multiple photons and, in comparison with the femtosecond spectra previously presented, we assign C_{ns} to a R2PD process via the S_1 excited state. This peak is significantly more isotropic than the previous features, with typical values of $\beta_2 = -0.49 \pm 0.08$ and $\beta_4 = 0.01 \pm 0.12$ at 480 nm.

4.3.3 Time-resolved photoelectron spectroscopy

In order to probe the dynamics of the S_1 electronic state in PM^{2-}, population was excited with a pump pulse of either 2.43, 2.34 or 2.30 eV (corresponding to

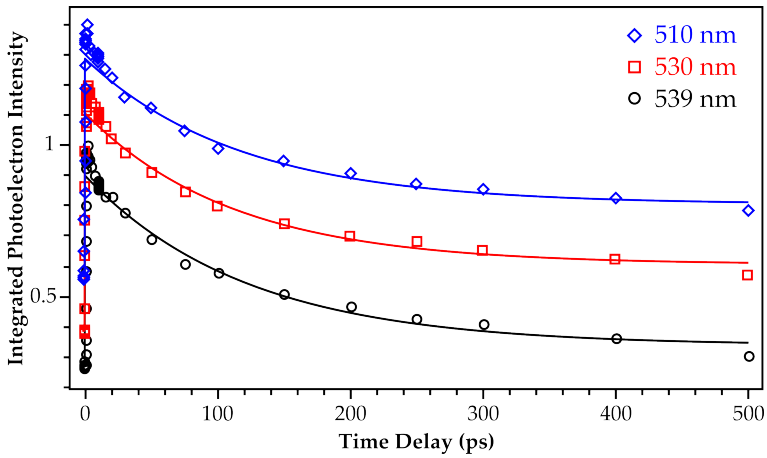

Figure 4.11: Dynamics of the S_1 excited state of PM^{2-} following excitation with different amounts of excess internal energy. Data were fitted with a single exponential deacy, convoluted with a Gaussian instrument response function, and yielded characteristic lifetimes of 121, 112 and 117 $\pm$10 ps for pump wavelengths of 510, 530 and 539 nm, respectively.

510, 530 and 539 nm) and subsequently probed a delay t later with a 1.55 eV (800 nm) probe pulse. Changing the excitation energy leads to different amount of internal energy within the excited state. Figure 4.10(a) shows two representative photoelectron spectra, collected when the probe (2.43 eV) arrives before the pump ($t < 0$) and with pump and probe pulses temporally overlapped ($t = 0$). The former is identical to the pump-only spectrum shown in figure 4.8(b), indicating that the probe alone is not sufficiently energetic to detach an electron directly and not resonant with any transition. When the two pulses are overlapped, a very intense additional feature is observed at eKE $\sim$1.9 eV , between features A and C assigned previously. The effect of changing the pump pulse energy is illustrated in figure 4.10(b), which shows two photoelectron spectra collected at $t = 0$ for pump energies of 2.43 eV (510 nm, blue trace) and 2.30 eV (539 nm, black trace). As previously observed, no spectral shift is present for the pump-only feature A. A small shift to higher energies is apparent for the pump-probe feature, as expected, and this is even more pronounced for the R2PD feature C, where the observed shift of $\sim$0.25 eV is consistent with the additional energy imparted by the absorption of two 510 nm photons, rather than 539 nm photons.

To evaluate the lifetime and dynamics of the S_1 state, photoelectron spectra were collected for various pump-probe delays t, and the photoelectron signal integrated over the additional pump-probe feature and plotted as a function of delay in figure 4.11 for the three pump energies employed. The integrated intensities have been fitted with a single exponential decay, convoluted with a Gaussian instrument response function, and yielded lifetimes of 121, 112 and 117 $\pm$10 ps for pump wavelengths of 510, 530 and 539 nm, respectively, equivalent within the experimental error.

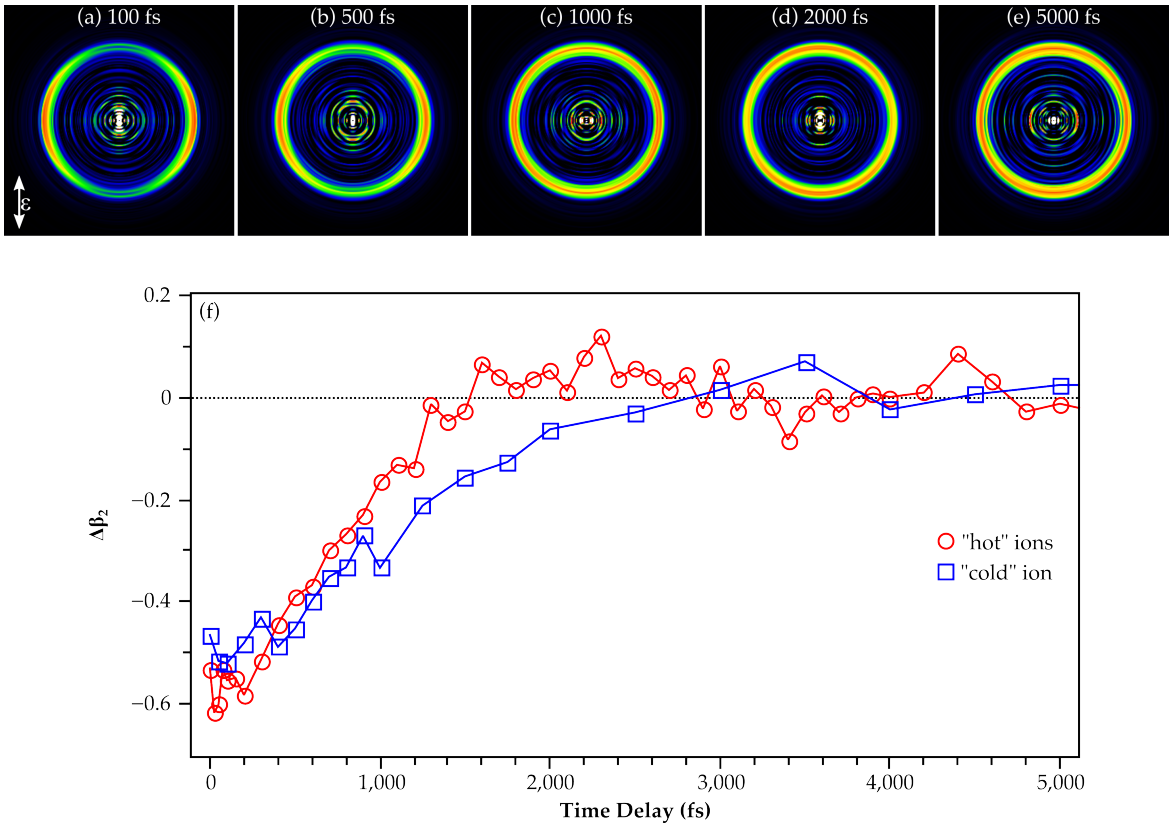

Figure 4.12: Time-resolved photoelectron angular distributions in PM^{2-} following excitation to the S_1 state. (a)-(e) Background subtracted reconstructed photoelectron images at various delays t showing the loss of anisotropy with time. A brief moment of positive anisotropy is observed around 2 ps, after which an isotropic image is obtained. (f) Change in β_2 parameter as a function of t for hot (∼1000 K) and cold (room temperature) parent ions. The loss of anisotropy is significantly slowed down by the lower excess internal energy in the cold sample.

Inspection of the photoelectron anisotropies in the excited state feature yields dynamic information in these data at early time delays (sub-5 ps).[26] For clarity a background spectrum at long time delay $t \gg 0$ was subtracted from all data, leaving only the pump-probe feature, and resulting photoelectron images are shown in figure 4.12(a)-(e) for selected delays t. At very early delays (t = 100 fs) a strong negative anisotropy is observed, similar to that in the single-colour resonant femtosecond photoelectron spectrum in figure 4.8(b). However this anisotropy is rapidly lost within the first few picoseconds after excitation. Approximately 2 ps after the pump pulse a slight positive anisotropy is measured (figure 4.12(d)), before a fully isotropic image emerges for all subsequent delays. This experiment has been repeated under different ion source conditions, varying the amount of internal energy present in the produced ions. This is shown in figure 4.12(f), which shows the measured change in anisotropy parameter β_2 as a function of pump probe delay t. Shown in red is the case of "hot" ions, carrying a large amount of excess internal energy, and shown in blue that of "cold" ions which are approximately at room temperature.[26] The degree of internal energy in the parent ion can be controlled via the conditions in the

electrostatic ring ion trap (see chapter 2 for details), most importantly through changing the buffer gas used. The use of heavier buffer gases, such as nitrogen, leads to a faster cooling of the anions due to quicker momentum transfer.[55] However, by the same arguments this also leads to an increased heating of the stored ions during ejection from the trap. This is maintained at a constant buffer gas pressure and during the unloading stored ions get electrostatically accelerated through the background buffer gas and ejected from the trap. A heavy gas (e.g. Nitrogen) transfers significant momentum to the ions during the unloading and leads to substantial heating of the ions. This can be avoided by using light buffer gases, ideally helium, which leads to colder ions being ejected from the trap, at the expense of taking longer to reach a colder temperature within the trap. Using a helium buffer gas ions get ejected at approximately room temperature, whereas the use of nitrogen produces an ion packet with significant thermal excitation, on the order of 1000 K. As the data in figure 4.12 shows, the use of a colder ion sample slows down the loss of photoelectron anisotropy significantly, and this will be discussed in section 4.3.5 in the context of rotational coherence spectroscopy.[56–58]

4.3.4 Discussion of photoelectron spectra

Non-resonant photoelectron spectrum

The single-colour UV photoelectron spectrum of PM^{2-} was shown in figure 4.8(a), collected at a photon energy of 4.66 eV. The higher energy peak observed here has already been assigned to a single-photon detachment. For this to occur in a dianion, the available energy must be sufficient to overcome the electron affinity and the RCB of the system.[14] Based on the electronic structure calculations presented earlier, it is reasonable to assume that this is indeed the case given excitation at 4.66 eV and the observed peak can be related to the intrinsic energetics of the system in the usual fashion. The peak is centred at 2.7 eV, yielding a vertical detachment energy for PM^{2-} of 2.0 eV. The adiabatic detachment energy (*ADE*) can be estimated by extrapolation of the high-energy cut-off for the peak,[59] yielding an approximate *ADE* of 1.6 eV. These results compare favourably with DFT calculations presented in section 4.3.1, where the vertical energy gap between the ground dianion state (S_0) and the ground state of the monoanion (D_0) has been evaluated as 1.95 eV, and the *ADE* for this transition as 1.79 eV. The D_0 electronic state corresponds to removal of an electron from the π-system of the BODIPY chromophore, and hence photodetachment from the S_0 dianion state correlates with the D_0. The weaker feature at lower *eKE* observed in the UV spectrum of figure 4.8(a) most likely corresponds to the formation of an excited state of the monoanion following photodetachment from PM^{2-}. This feature is observed 1.2 eV below that of the ground state transition,

and TD-DFT calculations have identified several low lying excited states in the monoanion that could be populated. It appears most likely that the observed state corresponds to an excitation from the HOMO−3 to the HOMO of the anion, calculated at 1.20 eV above the anion ground state. This state contains minor contributions from several transitions and is weakly correlating with both the S_0 and the S_1 state of the dianion.

In the UV photoelectron spectrum no features are observed below an *eKE* of ∼1.1 eV, despite the existence of several low lying electronic excited states of the anion in this region. However, a low energy cut-off is expected in photoelectron spectra of polyanions due to the presence of the RCB, below which no photoelectrons due to direct detachment processes can be observed.[4] This arises from the condition that the incident photon energy must be sufficient to overcome the *ABE* and the RCB of the system.[14,15] Based on the 4.66 eV spectrum in figure 4.8(a) we estimate an RCB height of 1.1 eV, which could indicate that a large fraction of the feature around 1.6 eV *eKE* is not observed in the spectrum due to the RCB. This barrier height is furthermore in very good agreement with RCB simulations, which estimated the lowest barrier at 1.1 eV.

Resonant femtosecond photoelectron spectra

The resonant photoelectron spectrum collected at 2.43 eV shown in figure 4.8(b) can partially be rationalised by comparison with the UV spectrum at 4.66 eV (figure 4.8(a)). Features B and C are analogous in both spectra, but now proceed via a resonance enhancement from the S_1 state. However, the low *eKE* feature A is not observed in the UV photoelectron spectrum. Indeed this feature is located within the RCB of PM^{2-}, such that a direct detachment process is not possible. We attribute this peak to tunnelling through the RCB following single photon excitation to the S_1 state,[11,12,21] as has previously been observed for the fluorescein dianion (section 4.2).[41] As the S_1 state in PM^{2-} is highly fluorescent in solution,[52] it is not unreasonable to assume a gas-phase lifetime sufficiently long for tunnelling to occur. We therefore assign feature A to tunnelling through the RCB, producing photoelectrons with significantly less *eKE* than the RCB and leaving the monoanion in the D_0 ground state, a process that is allowed by Koopmans correlations.[60,61]

Comparison of the resonant photoelectron spectra collected with femtosecond pulses of varying energy, shown in figure 4.9(a), reveals the presence of a tunnelling feature A at all photon energies. However, no spectral shift in this feature is observed as the incident energy increases, similar to the situation encountered in the fluorescein dianion.[41] This has been explained with a strongly adiabatic tunnelling mechanism through the RCB, conserving any excess internal energy

(cf. figure 4.5). The same situation is encountered here and tunnelling should be considered a diagonal transition. All photoelectron spectra shown in figure 4.9(a) show the presence of a broad feature C. This shifts to higher kinetic energies with increasing photon energy, as expected for a 2-photon detachment process and arrows in figure 4.9(a) indicate the anticipated high energy cut-off and are in good agreement with the data. The relative intensities of features A and C change as the photon energy is increased, with feature C gaining intensity relative to A. Feature C corresponds to a R2PD process, and we explain the relative increase in intensity of this feature with the presence of a 2-photon resonance. An indication for this can be gained from the solution phase absorption spectrum, figure 4.6(c), showing the onset of a resonance at $\sim$250 nm with a maximum at 230 nm, explaining the increase in intensity as the incident photon energy approaches the maximum of the resonance.

Excited state dynamics

Time-resolved photoelectron spectroscopy data following excitation of the S_1 state was shown in figures 4.10 and 4.11. A clear pump-probe feature was observed, which decreased in intensity as a function of pump-probe delay t. No other noticeble changes in this feature (such as spectral shifts) were observed. The intensity of the pump-probe feature is a direct measure of the S_1 population and hence the reduction in signal is direct evidence for a loss of excited state population with time, but the decay mechanism from the S_1 cannot be unambiguously determined. Given the presence of a tunnelling feature (A) in the resonant photoelectron spectra, this is clearly an operative loss mechanism. However, internal conversion (IC) or intersystem crossing (ISC) to a lower triplet state are in principle also possible. We rule out the participation of fluorescence as this occurs on a nanosecond timescale and therefore can only contribute a very small fraction within the picosecond lifetime observed.[52] The occurrence of ISC is rather improbable as dyes based on the BODIPY chromophore are well known for their very low rate of $S_1 \rightarrow T_1$ conversion.[48,49] Lastly, IC is a possible decay pathway but it should be noted that the fluorescence quantum yield in solution is very high, indicating that, at least in the condensed phase environment, no ultrafast radiationless processes contribute significantly to the relaxation from the S_1.

Some indication of the dominant relaxation pathway can be gained by considering the dynamics of the tunnelling feature A. If tunnelling was the only (or major) decay channel, a large depletion should be observed in this feature at $t = 0$, followed by a recovery that is mirroring the population decay in the pump-probe peak.[62,63] No discernible dynamics are observed for feature A (figure 4.10), al-

though we note that the data are quite noisy. Nonetheless, the integrated photoelectron signal for this peak should show a depletion of similar magnitude to the additional pump-probe feature observed, if tunnelling was a primary decay route. In previous studies on the tunnelling dynamics in the fluorescein dianion this depletion was clearly observed (figure 4.4(a)).[41] The lack of these dynamics then suggests that tunnelling is not primarily responsible for the observed dynamics, leaving internal conversion as the primary decay pathway from the S_1 state in the gas-phase. While this is surprising given the lack of radiationless decay in solution, there are several differences between isolated and solvated PM^{2-}, mainly the stabilisation of the charged SO_3^- groups. Environmental effects have been noted on PM in different solvents, but these have been primarily attributed to effects of the resonance structures of the BODIPY chromophore, with the terminal SO_3^- groups acting as spectators only.[53] Nonetheless, the lack of stabilisation of the charged terminal groups in the gas-phase introduces much stronger Coulombic interactions with the chromophore and can have a considerable effect on the electronic dynamics. Further evidence for an active internal conversion mechanism can be found in the nanosecond photoelectron spectra discussed below.

As there are 2 active and competing decay pathways from the S_1 state, the measured lifetime contains contributions from both internal conversion (τ_{IC}) and tunnelling (τ_{tun}) and only an overall observed lifetime is measured, that is related to the individual components;

$$\frac{1}{\tau_{obs}} = \frac{1}{\tau_{IC}} + \frac{1}{\tau_{tun}}. \tag{4.2}$$

The measured $\sim$120 ps lifetime is thus faster than both the individual components, however given the arguments above, IC is expected to be the dominant relaxation channel with a lifetime close to (but slower) than the observed lifetime and tunnelling could be significantly slower. The group of Kappes were the first to directly measure the tunnelling dynamics through the RCB using time-resolved photoelectron spectroscopy and they observed a timescale of $\sim$100 ps in phtalocyanine-tetrasulfonate tetra-anions.[11]

Effect of pulse duration on photoelectron spectra

Comparison of the photoelectron spectra collected with femtosecond and nanosecond laser pulses, shown in figures 4.9(a) and (b) respectively, highlights marked differences between the two. The nanosecond spectra show a very intense feature at low *eKE* (labelled D), that is completely absent when femtosecond pulses are used. This feature is furthermore located within the RCB and thus cannot stem from a direct detachment process. Low energy features have previously been observed following nanosecond excitation of dicarboxylate dianions by

the Wang group, and were assigned to a dissociative autodetachment processes from a monoanion formed following photodetachment from the parent dianion.[64] Specifically, it was proposed that the parent radical can exothermically undergo decarboxylation to form a $(CH_2)_nCO_2^-$ radical, which subsequently looses an electron yielding signal at very low *eKE*. Similarly in the present case the observed feature D must arise from monoanions; this can be appreciated by the fact that the feature is completely absent when femtosecond pulses are employed, and therefore the origin of feature D is related to the extended timescale of the nanosecond excitation. Feature D appears completely structureless and isotropic, and decays exponentially with increasing *eKE*, which is typically associated with thermionic emission or autodetachment processes.[65–68] It cannot arise from direct detachment as the photodetachment cross-section vanishes at threshold.[69,70] Considering the fact that no fragmentation is observed following single-photon excitation to S_1, evidenced by the absence of photoelectron signal at threshold following femtosecond excitation, we recognise that the system must be acquiring excess amounts of internal energy, eventually leading to dissociation followed by electron loss. The mechanism by which PM^{2-} gains excessive internal energy can be explained by the prolonged exposure to a resonant photon field during nanosecond excitation and the presence of a fast internal conversion channel from the S_1 excited state that proceeds significantly faster than the duration of the laser pulse. This leads to a situation where photon cycling can occur, similar in spirit to infra-red multiphoton dissociation, but via an electronic transition.[71,72] Thus the system is excited to the S_1 state, undergoes internal conversion, thereby acquiring 2.5 eV of excess internal energy, followed by intramolecular vibrational redistribution. This hot PM^{2-} can then proceed to absorb another photon resonant with the $S_1 \leftarrow S_0$ transition and the cycle repeats until fragmentation sets in, as shown schematically in figure 4.13. This forms a vibrationally hot anion which can subsequently undergo statistical electron loss, either directly or through the absorption of additional photons if the BODIPY chromophore remains intact. Specifically, one could imagine loss of a terminal SO_3^- group due to excess internal energy, thereby removing the RCB from the system and placing the S_1 excited state in the electronic continuum, leading to statistical autodetachment and the observed low *eKE* signal.

Feature A_{ns} observed in the nanosecond spectra and centred around *eKE* = 1.3 eV shows no spectral shift with increasing photon energy and can be correlated with feature A in the femtosecond spectra. We have shown previously that the (apparently unphysical) behaviour of a feature's invariance on incident photon energy can be explained with a strong adiabatic tunnelling mechanism through the RCB, which obeys a propensity rule and conserves internal energy throughout the electron loss process.[41] This is indeed observed here, for both features A and A_{ns}. However, some clear differences are immediately apparent between

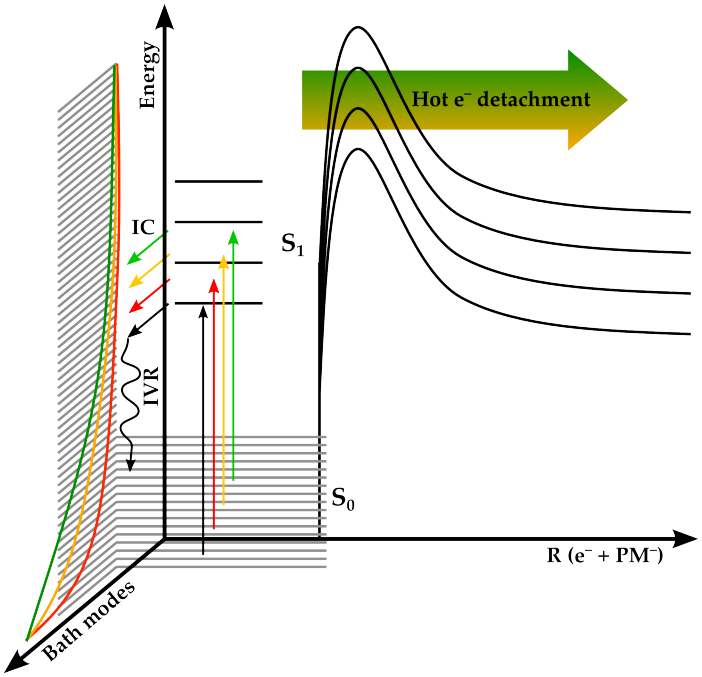

Figure 4.13: Photon cycling mechanism and statistical electron loss in PM^{2-}. A cycle of photoexcitation and rapid internal conversion followed by intramolecular vibrational redistribution (IVR) leads to an increased internal temperature, similar to IR multiphoton excitation experiments but utilising an electronic transition. This process can continue until fragmentation sets in, forming a hot monoanion that can subsequently undergo statistical electron loss (autodetachment) or absorb additional photons if the BODIPY chromophore remains intact. An additional electron loss mechanism from the dianion arises if during the IVR process modes are sampled that can lead to direct electron loss over the RCB at ∼1.1 eV. This leads to the observed shift of the tunnelling feature to higher *eKE* in the nanosecond photoelectron spectra.

the feature in the femtosecond and nanosecond spectra, figures 4.9(a) and (b) respectively. The peak maxima are located at *eKE* = 0.7 eV and 1.3 eV for features A and A_{ns} respectively, furthermore the peak width has increased significantly for nanosecond excitation. This is in direct contrast with the situation in doubly deprotonated fluorescein anions (section 4.2) where femtosecond and nanosecond excitation yields identical photoelectron spectra. The crucial difference between these two systems is the very fast tunnelling mechanism in fluorescein (1 ps), ruling out the possibility of any photon cycling regardless of pulse duration. A similar situation has recently been recorded in a tetra-anion.[73] In contrast to this is PM^{2-} where a fast internal conversion mechanism leads to the build up of excess amounts of internal energy in the dianion.

The observed spectral broadening in the case of PM^{2-} is therefore a consequence of the high amount of internal energy present due to the photon cycling mechanism operative with nanosecond excitation. The low *eKE* cut-off for the tunnelling features (A and A_{ns}) is identical and the broadening is only observed on the high *eKE* side of the nanosecond spectrum. Moreover, the nanosecond feature is located close to the top of the RCB (∼1.1 eV) and peaks just above it at 1.3 eV, suggesting that a significant fraction of A_{ns} may contain contributions

from direct detachment above the lowest RCB, enabled by the high excess internal energy. While this would contradict the adiabatic tunnelling picture derived for fluorescein dianions, the timescale of electron loss in the present case is significantly longer. Specifically, complete IVR of the internal energy in PM^{2-} may be expected, such that bath modes leading to electron emission over the lowest barrier can be statistically sampled, a decay pathway that is inaccessible in fluorescein due to the fast tunnelling lifetime. This leads to a spectral broadening of feature A_{ns} relative to A and spectral shift of the feature towards the lowest point of the RCB. This proposed statistical electron loss mechanism is shown schematically in figure 4.13. Following photoexcitation the RCB experienced by the system increases. However, IVR on the excited state could sample the correct mode for electron loss above the lowest RCB, leading to the observation of photoelectrons near 1.1 eV *eKE*. Alternatively, the relaxation through IC allows photon cycling via the S_1 electronic resonance and thus the build up of excess internal energy in the system, eventually leading to statistical emission of electrons over the RCB from the S_0 state. It is not known if the broadening of A_{ns} arises from electron emission from the S_0 or the S_1, nonetheless these statistical mechanism are crucial for understanding electron loss and excitation from thermally activated polyanions in tandem mass-spectrometry experiments.[46,47]

Summary

A thorough investigation using femtosecond and nanosecond photoelectron spectroscopy, as well as time-resolved pump-probe experiments, has yielded several important insights into the nature of repulsive Coulomb barriers in polyanions and their effect on photoelectron spectra. In contrast to the experiments on the fluorescein dianion, a large difference was observed between spectra collected with femtosecond or nanosecond pulses when these were resonant with an electronic excitation. While both yielded a peak due to strongly adiabatic tunnelling through the RCB, as previously observed, additional features were present in the nanosecond spectrum. We attribute these to the presence of a fast internal conversion mechanism which opens up the possibility of mulitple photon excitations, or photon cycling, via the resonant $S_1 \leftarrow S_0$ transition. This leads to the accumulation of internal energy within the dianion until fragmentation sets in, leading to statistical electron loss from the formed monoanion in the presence of a nanosecond excitation field. As this mechanism is not accessible with femtosecond laser pulses, the corresponding feature is entirely absent in this case. The build up of internal energy furthermore leads to the possibility of IVR sampling bath modes that allow electron loss over the lowest RCB in the system, leading to a shift of the tunnelling feature towards the maximum of the RCB and a significant broadening of the tunnelling peak. This is in stark contrast to previous work on the fluorescein dianion, where nanosecond and femtosecond

spectra appeared identical.

4.3.5 Discussion of photoelectron angular distributions

Angular distributions in one-colour photoelectron spectra

While the RCB in PM^{2-} is strongly anisotropic in space (figure 4.7), and it has been shown previously that the RCB shape can influence the direction of outgoing photoelectrons,[23–25] the features observed here in the UV spectrum appear nearly isotropic. This implies that the detachment cross-section for PM^{2-} is almost isotropic, leading to an equal probability for photodetachment from any molecular orientation in space and therefore making any inherent anisotropy in electron emission unobservable in the laboratory frame. In order to observe the guiding effect of the RCB on electrons, a connection between the frames of reference of the molecule and the laboratory needs to be established; this can be achieved if the photodetachment cross-section is strongly peaking along one molecular direction, as is commonly the case in long chain-like molecules,[74] and has been shown by the Wang group,[23–25] or through molecular alignment.[75–78]

In contrast to the UV photoelectron spectrum, the resonant femtosecond photoelectron spectrum in figure 4.8(b) shows large negative anisotropies in the high *eKE* features ($\beta_2 = -0.56$ for feature C). As the initial and final states involved in this transition are identical to those in the UV spectrum, the observation of negative anisotropies must be related to the resonant nature of the detachment process. The probability of an electronic excitation depends upon the relative orientation between the polarisation of the incident photon (ϵ) and the electronic transition dipole moment ($\mathbf{d_{10}}$). Specifically, the excitation probability depends on the angle θ between ϵ and $\mathbf{d_{10}}$ and is proportional to $\cos^2\theta$. Therefore those dianions are primarily excited that have their transition dipole moment (indicated in figure 4.6(a)) parallel to the incident polarisation, and overall a $\cos^2\theta$ distribution of excited molecules is created by the linearly polarised excitation pulse. It should be noted that this methodology is not alignment of an entire sample, but rather selective excitation of those molecules that happen to be aligned with the laser polarisation at the instance of absorption. As the observed R2PD feature in the resonant photoelectron spectrum in figure 4.8(b) arises exclusively from detachment from the (aligned) excited state population, the effect of the RCB on the outgoing photoelectron is now observable, due to the link between the molecular frame ($\mathbf{d_{10}}$) and the laboratory frame (ϵ).

The observed negative anisotropy can be rationalised by comparison with the calculated RCB surface in figure 4.7(a). Following R2PD at 2.43 eV the outgoing photoelectron will have an asymptotic *eKE* of $\sim$3.1 eV. This available kinetic en-

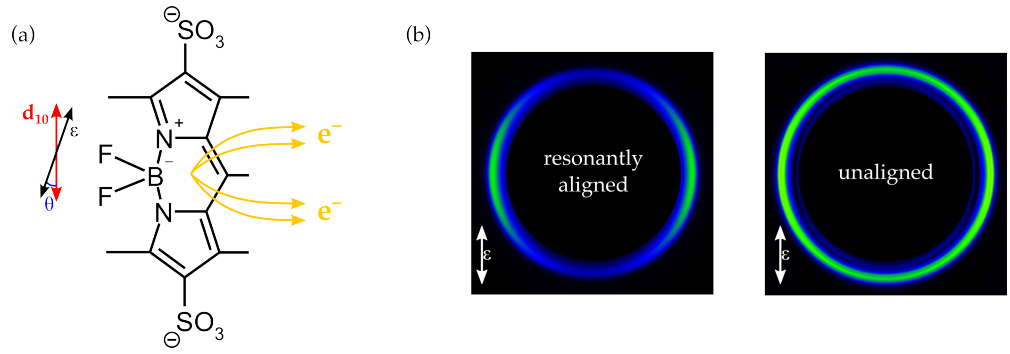

Figure 4.14: (a) Following resonant alignment of $\mathbf{d_{10}}$ with ϵ a $\cos^2\theta$ distribution of molecules in the excited state is created, leading to emission of photoelectrons primarily parallel to ϵ, away from the excess negative charges. (b) Photoelectron images of a 2-photon resonant detachment process (left) , equivalent to emission from an aligned sample and therefore showing strong anisotropy, and a single photon detachment (right), where an isotropic emission of electrons occurs.

ergy is not sufficient to overcome the RCB in the molecular x direction (along the SO_3^- groups, as defined in figure 4.6(a)), leading to electrons being primarily ejected along the $+y$ direction and hence yielding a negative anisotropy. The lowest point on the RCB is not tightly confined in the x direction, leading to an angular spread in the emission of electrons and hence the extreme anisotropy parameter of $\beta_2 = -1$ is not observed. Inspection of the calculated slices through the RCB in figure 4.7(b) indicates that the barrier in the $-y$ direction, along the boron, is approximately 3.2 eV and therefore no emission of electrons should occur in this direction (as $eKE \leq 3.1$ eV). However, on either side of the boron saddle points are located allowing electrons to pass through as the RCB height here is on the order of 2 eV. Figure 4.14(a) shows a schematic of PM^{2-} indicating the alignment axis and the preferred emission direction of photoelectrons based on the location of excess charges and the calculated RCB. Shown in part (b) of figure 4.14 are two single-colour photoelectron images with only the relevant features to this discussion shown. The image on the left has been collected with 510 nm photons, yielding a resonant 2-photon detachment process and thus an aligned sample and exhibits strong anisotropy, whereas the right image corresponds to detachment from a randomly oriented sample of PM^{2-} with a single UV photon, and an isotropic feature is observed. The angular distributions of emitted electrons qualitatively match the predictions based on analysis of the calculated RCB surfaces.

Considering the creation of an aligned sample following excitation to the S_1 excited state, one might expect the tunnelling feature (A) in the femtosecond photoelectron spectra to exhibit similar anisotropies as the R2PD peak. However, this is not observed and the tunnelling peak appears (near) isotropic with $\beta_2 = -0.15$. We attribute this to the long timescale of the tunnelling process and loss of alignment within this time. Following the selective excitation and

thus creation of a coherent rotational wavepacket in the S_1 electronic state, the rotational coherences evolve independently in free space and the individual rotational phases become scrambled again, leading to a dephasing of the aligned population.[56–58] This typically occurs on the order of a few to 10s of picoseconds and thus significantly faster than the measured S_1 lifetime.[79–81] The tunnelling process hence does not occur from an aligned sample of molecules and the effect of the RCB on outgoing electrons is no longer observable. This rotational dephasing can be tracked in real-time through the evolution of the photoelectron anisotropy as a function of time in time-resolved photoelectron spectroscopy experiments, as discussed below.

The photoelectron feature attributed to a resonant 2-photon detachment process following nanosecond excitation (feature C_{ns} in figure 4.9(b)), exhibits strong negative anisotropies on the order of $\beta_2 = -0.5$ for all employed nanosecond photon energies. While this is very similar to the anisotropy observed for the same process following femtosecond excitation, in the femtosecond case the system has no time to rotationally dephase and the rotational wavepacket created through the absorption of the first photon is still in-phase, leading to the detachment from an aligned state by the second photon, as outlined above. For a nanosecond excitation process, however, this argument does not hold as the second photon can be absorbed significantly later (given an excited state lifetime on the order of 100s of picoseconds), after rotational dephasing has occurred and leading to an isotropic distribution of photoelectrons, similar to that observed for the delayed electron tunnelling process. Thus the measured negative anisotropy for C_{ns} is rather unexpected. A possible explanation for this observation could be that the second (detaching) photon must be absorbed within the first few picoseconds following excitation. This could be the case if fast motion on the excited state potential energy surface following excitation leads to a geometry change and a reduced cross-section for detachment from the excited state. A further possible explanation could be the involvement of a 2-photon resonance in this process. We have already made this argument for a possible rationalisation of the changing intensities of the A_{ns} and C_{ns} features and if this is the case, then the resonance could lead to a non-isotropic absorption cross-section for the second photon, leading to a preferential 2-photon detachment from a particular molecular orientation. We have no experimental evidence for either of these possible explanations.

Finally, it should be noted that the discussion of PADs presented here is founded entirely on classical arguments, based on the long-range interaction between an outgoing electron an the remaining charge on the anion. For a photodetachment process from a monoanion or neutral, the observed PADs arise from the interference of outgoing partial photoelectron waves, an entirely quantum me-

chanical phenomenon that cannot be explained in classical terms. For example the observation of negative anisotropy following detachment from an anion (e.g. iodide, figure 1.14) can only be rationalised with quantum arguements, as classically electrons should be emitted in the direction of the ejecting force - the laser polarisation - and hence always exhibit positive anisotropies. However, the situation is different for polyanions. Here the long-range interaction dominates the photoelectron trajectories and a classical description is, at least qualitatively, valid.

Time-resolved photoelectron angular distributions

The temporal evolution of the measured photoelectron anisotropy of the pump-probe feature was shown in figure 4.12 and a rapid loss in the anisotropy observed with increasing pump-probe delay t. This can again be rationalised with the creation of a rotational wavepacket by the resonant pump excitation pulse. This creates an ensemble of excited state molecules aligned in free space such that their transition dipole moment $\mathbf{d_{10}}$ is parallel to the polarisation of the pump pulse, ϵ. However this is only an instantaneously aligned sample and in the gas-phase the PM^{2-} molecules are free to rotate. Due to the population of many different rotational states in the sample, molecules will rotate at different speeds, leading to a rapid loss of alignment.[80] This is exactly the behaviour observed in the time-resolved anisotropy measurements shown in figure 4.12(f), where the anisotropy is lost within a few picoseconds following the pump pulse. The observed anisotropy parameter β_2 is thus a measure of the degree of alignment within the sample. This assignment of rotational dephasing dynamics has been confirmed by repeating these measurements with a different amount of internal energy (or initial temperature) in the parent dianions. This will lead to a different population distribution in the rotational states and therefore a different timescale for rotational dephasing.[56–58] Indeed the use of a colder primary ion target, as shown by the blue data in figure 4.12(f), slows down the loss of anisotropy (i.e. rotational dephasing) be a factor of $\sim$2 compared to the sample prepared with significant amounts of internal energy (red data).

Shown in figure 4.15(a) are the measured β_2 parameters of the excited state feature as a function of time for the sample of "hot" ions. Following a fast decay of the initially highly negative anisotropy, a positive value is observed approximately 2 ps after excitation, which subsequently decays to yield an isotropic distribution. This can be clearly seen in the photoelectron images shown in 4.15(b) (further photoelectron images were shown earlier in figure 4.12(a)-(e)). This data can be crudely modelled as a function of the rotational constants involved and the internal temperature by considering the population and interference of the populated rotational states in the system. The rotational level populations, $D(J)$,

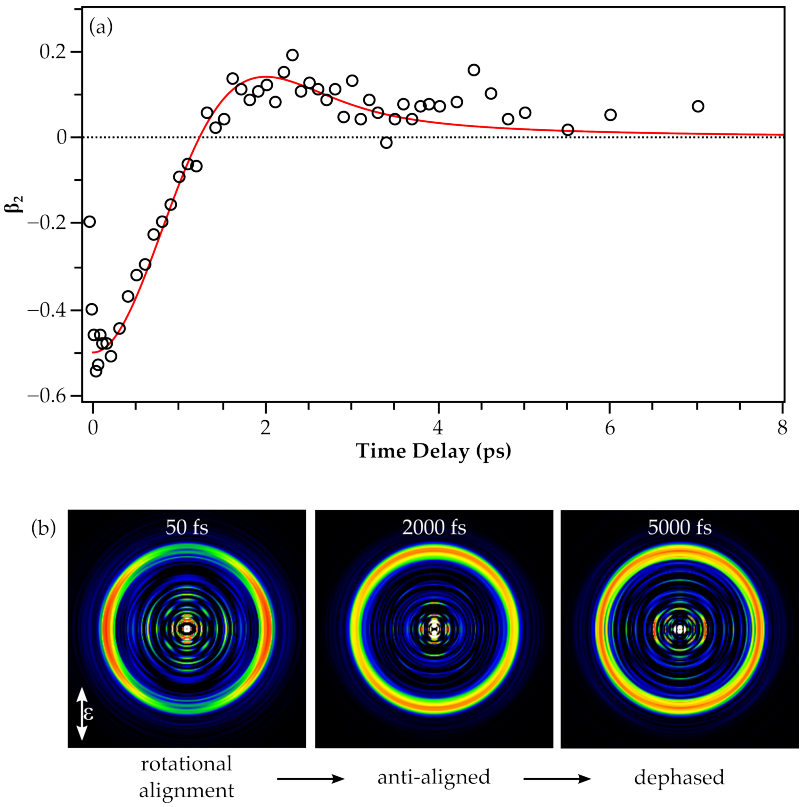

Figure 4.15: (a) Measured β_2 parameter as a function of pump-probe delay following resonant excitation by the pump. A rapid loss in anisotropy is observed that can be modelled as a dephasing of the created rotational wavepacket. (b) Selected background subtracted photoelectron images at key delays during the dephasing process.

can be evaluated from a Boltzmann distribution;

$$D(J) = (2J+1)\exp\left(-\frac{hBJ(J+1)}{k_B T}\right), \tag{4.3}$$

where J is the rotational quantum number, B the rotational constant of the system, k_B is the Boltzmann constant and T the rotational temperature. Considering all rotational states are in phase following coherent excitation (i.e. $\phi = 0$ at $t = 0$), one can now evaluate the phase ϕ for each level as a function of rotational quantum number J and time t according to

$$\phi(t, J) = D(J) \times \cos\left(2B(2J+1) \times 2\pi t\right). \tag{4.4}$$

The overall rotational dephasing can now be evaluated by summation over all rotational states and evaluation as a function of time.[56–58] In order to model the data shown in figure 4.15(a) an effective rotational constant of $B = 153$ MHz was used, corresponding to the sum of the two rotational constants from the observable molecular rotations in the current geometry (due the the inherent cylindrical symmetry no rotation about the ϵ axis is observable). The resultant calculated rotational anisotropy was then scaled by a constant to match the photoelectron anisotropy observed at early time delays. The resultant simulation is shown as a

red trace in figure 4.15(a) and reproduces the observed photoelectron anisotropy remarkably well, considering the simplistic approach taken. We extract an approximate internal temperature for the ions of 1000 K ("hot" sample). The brief moment of anti-alignment (positive β_2) observed is reproduced well and further reinforces the assignment of the observed dynamics to rotational dephasing following the creation of a rotational wavepacket in a resonantly aligned sample.

Summary

The measured photoelectron angular distributions show that while the RCB has a profound effect on the trajectories of outgoing photoelectrons, this is only observable if there is a connection between the molecular and laboratory frame. In previous investigations by the Wang group this was given by the strongly anisotropic photodetachment cross-section,[23–25] leading to preferential detachment from one molecular orientation. This was not that case here and photoelectron spectra appeared isotropic unless an electronic resonance was excited, which leads to the creation of an aligned ensemble of electronically excited molecules, thereby connecting the two frames of reference and making the guiding effect of the RCB observable. The nature and extent of this alignment can be probed using time-resolved photoelectron angular distributions, allowing the real-time observation of rotational dephasing in the gas-phase.[26]

4.4 Conclusion

This chapter investigated in detailed the electronic structure, properties and dynamics of polyanions, using two dianions as model systems. Of particular interest is the study of the repulsive Coulomb barrier in these systems, which is responsible for several unusual properties of gas-phase polyanions. By studying metastable electronic states, formally unbound (higher in energy than the corresponding monoanion), but given metastability by the RCB preventing the excess electron from escaping, we have investigated the properties of the RCB and how it affects the electron detachment process and outgoing photoelectrons.

It is not sufficient to describe polyanion systems in terms of a single RCB, but rather every ro-vibrational state has its own RCB associated with it, leading to a dense manifold of potential energy surfaces. Populating excited ro-vibrational levels in a polyanion has the effect of increasing the inner RCB, that is despite excess internal energy the electron will still be bound by the RCB surface. This observation helps to rationalise tandem mass spectrometry results of polyanions using thermal activation methods, where fragmentation often occurs prior to electron loss. In the case of the fluorescein dianion, the outer RCB was found to be approximately constant and independent of vibrational excitation. This leads

to the tunnelling process through the RCB being strongly adiabatic, adhering to a strict propensity rule and conserving any vibrational energy present.

This strongly adiabatic nature of the electron tunnelling process was confirmed using femtosecond excitation of the pyrromethene-556 dianion, but this was not the case for nanosecond excitation of this system. If a fast (in comparison to tunnelling through the RCB) internal conversion decay pathway is operative, this leads to a photon cycling mechanism in the presence of a long (nanosecond) excitation field and hence the build-up of large amounts of internal energy in the dianion. The prolonged timescale of irradiation furthermore enables the redistribution of the vibrational energy in the system, eventually sampling modes that lead to detachment over the lowest part of the RCB. This shifts the measured photoelectron signal towards the minimum energy of the RCB. Hence the timescale of the excitation and the available decay routes from the excited state have a very large effect on the recorded photoelectron spectrum, both in terms of intensities and peak positions. Thus while the vibrational propensity rule for electron tunnelling has been confirmed in several polyanionic systems now, it can be broken given an operative internal conversion mechanism and sufficient time for complete IVR.

The direction of outgoing photoelectrons is strongly influenced by the shape of the RCB potential. This long-range interaction out-competes the inherent angular distributions due to partial wave interferences and can be qualitatively understood in a simple classical picture. The RCB surface, which depends on the relative location of excess charges within the molecular framework, can therefore be probed using photoelectron imaging. This yields the possibility of extracting structural information from photoelectron imaging experiments by probing the RCB surface of polyanions.

This presents a new methodology for studying large amplitude structural dynamics in gas-phase polyanions with femtosecond resolution, which is generally applicable through the use of molecular alignment techniques.[75–78] Any structural change that alters the relative position of the excess charges should be observable in such a fashion and experiments are currently under way in our laboratory to exploit this new technique. Specifically we are looking at observing the *cis-trans* isomerisation of a large system in the gas-phase, such as a stilbene or azobenzene, as shown schematically in figure 4.16. By placing negatively charged groups (sulfate or carboxyl) at the far ends of the molecule, they act as spectators only and provide the RCB necessary for observing dynamics through the angular distributions. The excitation of the *cis-trans* isomerisation will then lead to a change in the distribution of the excess charges and thus to a different shape of the RCB and hence influence the direction of outgoing pho-

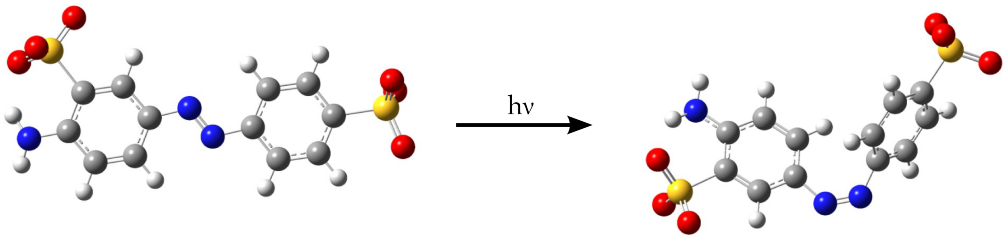

Figure 4.16: *Cis-trans* isomerisation of acid yellow 9 leads to a change in the distance between, and relative orientation of, the excess charges located on the SO_3^- groups, changing the inherent RCB. This effect should be observable in the photoelectron angular distributions.

toelectrons in a different fashion. This technique is generally applicable to any structural motion in the gas-phase that sufficiently changes the geometry of the excess charges and could become a general tool for the laboratory based study of gas-phase structural dynamics.[82,83]

In order to extract detailed information about the molecular structure from the measured angular distributions a more quantitative way of predicting the effect of RCBs on outgoing photoelectrons is needed. Specifically, using a calculated RCB surface (or hypersurface) should enable one to simulate the resulting photoelectron angular distributions. Work to this effect is currently under way in our research group. To a first approximation a simulation of classical electron trajectories should suffice. The difficulty in these simulations is the choice of starting point for the exiting electrons. Thus a more appropriate methodology is to treat the problem in reverse, that is deal with electron attachment rather than detachment. The idea here is to launch electrons with a given *eKE* towards the molecule (RCB surface) from a distance and from all directions. A trajectory simulation is then used to determine which spatial directions yield electrons that get captured by the molecule, rather than turn around. These directions should then equally correspond to electrons that can escape the molecular RCB potential, given they are ejected with the specified amount of kinetic energy. This framework can later be extended to a quantum mechanical treatment, with photoelectrons incident as interfering partial waves. A way of accurately simulating and understanding the effect of the RCB on photoelectron angular distributions should allow the extraction of detailed structural information with femtosecond time resolution from polyanions or larger molecular systems where excess charges can be introduced purely as spectators and to provide a measurable RCB.

References

[1] A. I. Boldyrev, M. Gutowski, J. Simons, *Acc. Chem. Res.* **29**, 497 (1996).

[2] A. Dreuw, L. S. Cederbaum, *Chem. Rev.* **102**, 181 (2002).

[3] M. K. Scheller, R. N. Compton, L. S. Cederbaum, *Science* **270**, 1160 (1995).

[4] X.-B. Wang, L.-S. Wang, *Annu. Rev. Phys. Chem.* **60**, 105 (2009).

[5] R. L. Hines, *J. Appl. Phys.* **37**, 2730 (1966).

[6] J. Fenn, M. Mann, C. Meng, S. Wong, C. Whitehouse, *Science* **246**, 64 (1989).

[7] J. B. Fenn, M. Mann, C. K. Meng, S. F. Wong, C. M. Whitehouse, *Mass Spectrom. Rev.* **9**, 37 (1990).

[8] A. I. Boldyrev, J. Simons, *J. Phys. Chem.* **98**, 2298 (1994).

[9] X.-B. Wang, J. B. Nicholas, L.-S. Wang, *J. Chem. Phys.* **113**, 10837 (2000).

[10] O. T. Ehrler, J. M. Weber, F. Furche, M. M. Kappes, *Phys. Rev. Lett.* **91**, 113006 (2003).

[11] O. T. Ehrler, J. P. Yang, A. B. Sugiharto, A. N. Unterreiner, M. M. Kappes, *J. Chem. Phys.* **127**, 184301 (2007).

[12] K. Matheis, *et al.*, *J. Am. Chem. Soc.* **130**, 15903 (2008).

[13] J. Simons, *J. Phys. Chem. A* **112**, 6401 (2008).

[14] X. B. Wang, C. F. Ding, L. S. Wang, *Phys. Rev. Lett.* **81**, 3351 (1998).

[15] L. S. Wang, C. F. Ding, X. B. Wang, J. B. Nicholas, B. Nicholas, *Phys. Rev. Lett.* **81**, 2667 (1998).

[16] X.-B. Wang, L.-S. Wang, *Nature* **400**, 245 (1999).

[17] R. L. Hettich, R. N. Compton, R. H. Ritchie, *Phys. Rev. Lett.* **67**, 1242 (1991).

[18] C. Yannouleas, U. Landman, *Chem,. Phys. Lett.* **210**, 437 (1993).

[19] C. Jin, *et al.*, *Phys. Rev. Lett.* **73**, 2821 (1994).

[20] R. N. Compton, A. A. Tuinman, C. E. Klots, M. R. Pederson, D. C. Patton, *Phys. Rev. Lett.* **78**, 4367 (1997).

[21] X.-B. Wang, C.-F. Ding, L.-S. Wang, *Chem. Phys. Lett.* **307**, 391 (1999).

[22] J. M. Weber, *et al.*, *J. Am. Chem. Soc.* **126**, 8585 (2004).

[23] C.-G. Ning, P. D. Dau, L.-S. Wang, *Phys. Rev. Lett.* **105**, 263001 (2010).

[24] X.-P. Xing, X.-B. Wang, L.-S. Wang, *J. Phys. Chem. A* **113**, 945 (2008).

[25] X. P. Xing, X. B. Wang, L. S. Wang, *Phys. Rev. Lett.* **101**, 083003 (2008).

[26] D. A. Horke, A. S. Chatterley, J. R. R. Verlet, *J. Phys. Chem. Lett.* **3**, 834 (2012).

[27] A. Dreuw, L. S. Cederbaum, *Phys. Rev. A* **63**, 049904 (2001).

[28] H. G. Weikert, L. S. Cederbaum, F. Tarantelli, A. I. Boldyrev, *Z. Phys. D* **18**, 299 (1991).

[29] T. Sommerfeld, M. K. Scheller, L. S. Cederbaum, *Chem. Phys. Lett.* **209**, 216 (1993).

[30] M. K. Scheller, L. S. Cederbaum, *J. Chem. Phys.* **99**, 441 (1993).

[31] M. K. Scheller, L. S. Cederbaum, *J. Chem. Phys.* **100**, 8934 (1994).

[32] M. K. Scheller, L. S. Cederbaum, *J. Chem. Phys.* **100**, 8943 (1994).

[33] A. Dreuw, L. S. Cederbaum, *J. Chem. Phys.* **112**, 7400 (2000).

[34] A. Dreuw, H. Schweinsberg, L. S. Cederbaum, *J. Phys. Chem. A* **106**, 1406 (2002).

[35] S. Feuerbacher, L. S. Cederbaum, *J. Am. Chem. Soc.* **125**, 9531 (2003).

[36] A. I. Boldyrev, J. Simons, *J. Chem. Phys.* **97**, 2826 (1992).

[37] A. I. Boldyrev, J. Simons, *J. Chem. Phys.* **98**, 4745 (1993).

[38] M. Gutowski, A. I. Boldyrev, J. V. Ortiz, J. Simons, *J. Am. Chem. Soc.* **116**, 9262 (1994).

[39] M. Gutowski, A. I. Boldyrev, J. Simons, J. Rak, J. Baejowski, *J. Am. Chem. Soc.* **118**, 1173 (1996).

[40] J. Simons, *Annu. Rev. Phys. Chem.* **62**, 107 (2011).

[41] D. A. Horke, A. S. Chatterley, J. R. Verlet, *Phys. Rev. Let.* **108**, 083003 (2012).

[42] D. Magde, R. Wong, P. G. Seybold, *Photochem. Photobiol.* **75**, 327 (2002).

[43] P. D. McQueen, S. Sagoo, H. Yao, R. A. Jockusch, *Angew. Chem. Int. Ed.* **49**, 9193 (2010).

[44] J. C. Marcum, J. M. Weber, *J. Chem. Phys.* **131**, 194309 (2009).

[45] P. Atkins, R. Friedman, *Molecular Quantum Mechanics* (Oxford University Press, Oxford, 2005), fourth edn.

[46] H. J. Cooper, K. Håkansson, A. G. Marshall, *Mass Spectrom. Rev.* **24**, 201 (2005).

[47] S. Ard, *et al.*, *J. Chem. Phys.* **132**, 094301 (2010).

[48] T. G. Pavlopoulos, M. Shah, J. H. Boyer, *Opt. Commun.* **70**, 425 (1989).

[49] S. C. Guggenheimer, *et al.*, *Appl. Opt.* **32**, 3942 (1993).

[50] F. Lopez Arbeloa, J. Bauelos, V. Martnez, T. Arbeloa, I. Lpez Arbeloa, *Int. Rev. Phys. Chem.* **24**, 339 (2005).

[51] A. Loudet, K. Burgess, *Chem. Rev.* **107**, 4891 (2007).

[52] Y. Assor, Z. Burshtein, S. Rosenwaks, *Appl. Opt.* **37**, 4914 (1998).

[53] T. Lopez Arbeloa, F. Lopez Arbeloa, I. Lopez Arbeloa, *Phys. Chem. Chem. Phys.* **1**, 791 (1999).

[54] M. J. Frisch, *et al.*, *Gaussian09* revision a.02 (2009).

[55] E. de Hoffmann, V. Stroobant, *Mass Spectrometry - Principles and Applications* (Wiley & Sons, Chichester, 2002), second edn.

[56] P. M. Felker, J. S. Baskin, A. H. Zewail, *J. Phys. Chem.* **90**, 724 (1986).

[57] P. M. Felker, A. H. Zewail, *J. Chem. Phys* **86**, 2460 (1987).

[58] J. S. Baskin, P. M. Felker, A. H. Zewail, *J. Chem. Phys.* **86**, 2483 (1987).

[59] D. A. Horke, J. R. R. Verlet, *Phys. Chem. Chem. Phys.* **14**, 8511 (2012).

[60] T. Koopmans, *Physica* **1**, 104 (1934).

[61] A. Stolow, *Annu. Rev. Phys. Chem.* **54**, 89 (2003).

[62] J. R. R. Verlet, *Chem. Soc. Rev.* **37**, 505 (2008).

[63] G. M. Roberts, J. Lecointre, D. A. Horke, J. R. R. Verlet, *Phys. Chem. Chem. Phys.* **12**, 6226 (2010).

[64] X.-P. Xing, X.-B. Wang, L.-S. Wang, *J. Phys. Chem. A* **114**, 4524 (2010).

[65] B. Baguenard, J. C. Pinar, C. Bordas, M. Broyer, *Phys. Rev. A* **63**, 023204 (2001).

[66] B. Baguenard, J. C. Pinar, F. Lpine, C. Bordas, M. Broyer, *Chem. Phys. Lett.* **352**, 147 (2002).

[67] K. Hansen, K. Hoffmann, E. E. B. Campbell, *J. Chem. Phys.* **119**, 2513 (2003).

[68] M. Kjellberg, *et al.*, *Phys. Rev. A* **81**, 023202 (2010).

[69] E. P. Wigner, *Phys. Rev.* **73**, 1002 (1948).

[70] A. Sanov, R. Mabbs, *Int. Rev. Phys. Chem.* **27**, 53 (2008).

[71] N. Basov, E. Markin, A. Oraveski, A. Pankrato, A. Skachkov, *JETP Lett.* **14**, 165 (1971).

[72] D. P. Little, J. P. Speir, M. W. Senko, P. B. O'Connor, F. W. McLafferty, *Anal. Chem.* **66**, 2809 (1994).

[73] H.-T. Liu, *et al.*, *Phys. Rev. A* **85**, 064503 (2012).

[74] D. Dill, *J. Chem. Phys.* **65**, 1130 (1976).

[75] H. Stapelfeldt, T. Seideman, *Rev. Mod. Phys.* **75**, 543 (2003).

[76] K. F. Lee, D. M. Villeneuve, P. B. Corkum, A. Stolow, J. G. Underwood, *Phys. Rev. Lett.* **97**, 173001 (2006).

[77] Z. Lu, R. E. Continetti, *Phys. Rev. Lett.* **99**, 113005 (2007).

[78] L. Holmegaard, *et al.*, *Nat. Phys.* **6**, 428 (2010).

[79] N. F. Scherer, L. R. Khundkar, T. S. Rose, A. H. Zewail, *J. Phys. Chem.* **91**, 6478 (1987).

[80] P. M. Felker, *J. Phys. Chem.* **96**, 7844 (1992).

[81] A. Blokhin, M. Gelin, E. Khoroshilov, I. Kryukov, A. Sharkov, *Opt. Spectrosc.* **95**, 346 (2003).

[82] H. Ihee, *et al.*, *Science* **291**, 458 (2001).

[83] C. Bressler, M. Chergui, *Annu. Rev. Phys. Chem.* **61**, 263 (2010).

Chapter 5

Spectroscopy and Dynamics of the Green Fluorescent Protein Chromophore

The universe is full of magical things patiently waiting for our wits to grow sharper.

Eden Phillpotts

This chapter is partially based on the following publications:

D. A. Horke and J. R. R. Verlet, *Phys. Chem. Chem. Phys.* **14**, 8511 (2012)

D. A. Horke, C. R. S. Mooney, A. S. Chatterley, A. Simperler, H. H. Fielding and J. R. R. Verlet, *Chem. Sci.* **accepted** (2012)

This chapter describes recent work conducted in our laboratory on the electronic spectroscopy and dynamics of the chromophore of the green fluorescent protein. We use ultra-violet (UV) photoelectron spectroscopy to probe the electronic structure of the anionic chromophore and corresponding neutral radical and with the aid of electronic structure calculations assign several excited states of the neutral. We furthermore show that the bright excited state of the anionic form is bound with respect to electron loss, the first experimental evidence for this. In the second half of this chapter we investigate the relaxation dynamics of this bright anionic state, work conducted in Durham but in collaboration with the group of Helen Fielding (UCL), who provided high level *ab initio* calculations and assistance during data analysis. We find that the gas-phase behaviour of the chromophore is similar to that observed in solution, but differs from the protein environment. Ultrafast relaxation via internal conversion is observed and the chromophore is non-fluorescent when isolated.

5.1 Introduction

The discovery of fluorescent proteins, the first of which was the green fluorescent protein (GFP),[1,2] has revolutionised molecular biology. Their ability to be fused to other proteins without disturbing their function has lead to the widespread use of fluorescent proteins for *in vivo* monitoring of biological processes.[3–5] The optical properties of GFP can be attributed to a central chromophore that is buried inside a 11-stranded β-barrel in the protein. The GFP chromophore itself is based on p-hydroxybenzylidene-2,3-dimethylimidazoline (HBDI) and exists in an anionic and neutral form, as shown in figure 5.1. This chromophore is responsible for the optical properties of GFP, including its two broad absorption bands centred at 395-397 nm (A band) and 470-475 nm (B Band) in the protein.[6,7] The A band is assigned to absorption by the neutral form of the chromophore, which subsequently undergoes excited state proton transfer to form the anionic form.[8,9] The B band corresponds to absorption by the anionic chromophore, forming the highly fluorescent S_1 excited state. In contrast to the protein environment, in solution $HBDI^-$ was found to be virtually non-fluorescent unless cooled below the glass-transition temperature, when fluorescence returned.[10,11] The differences between wild-type and solvated HBDI excited state relaxation are however not surprising, given the differences in absorption spectra between the two media. Isolated gas-phase $HBDI^-$, on the other hand, exhibits absorptions that are very similar to those in the natural protein environment (and consequently differ from the solvated absorption spectrum).[12] This was attributed to the effect of the β-barrel structure of the protein backbone, which sits tightly around the chromophore in the protein, excluding water molecules from the vicinity and effectively providing a solvent-free gas-phase like environment around the

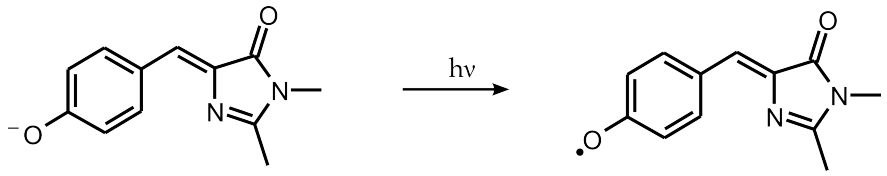

Figure 5.1: Structure of the HBDI anion and the radical formed following photodetachment.

chromophore.[12,13] However, recent experiments have shown that, despite the similarity in absorption spectra, isolated $HBDI^-$ is non-fluorescent and the primary decay channels from the S_1 excited state (located 2.57 eV above the anion ground state in the gas-phase) are fragmentation and electron detachment.[14,15]

Despite the huge importance and effect of GFP in biology and the life sciences, relatively little is known about the underlying photophysics and photochemistry of the HBDI chromophore that underpins the operation of GFP as a fluorescent marker. By studying the isolated chromophore in the gas-phase, we experimentally determine several previously unknown properties of $HBDI^-$, which aid to explain the observed behaviour and can act as benchmarks for future studies. Using UV photoelectron spectroscopy the vertical and adiabatic detachment energies are determined. These are crucial values as they influence the fate of the excited state of the chromophore and determine whether this is bound with respect to electron loss or resides in the electronic continuum. We furthermore identify several electronic excited state of the neutral radical formed following photodetachment and using density functional theory calculations these are assigned to detachment from lower lying orbitals in the anion. These values again provide key benchmarks for current theoretical investigations of HBDI and GFP. We find experimentally that the S_1 excited state is indeed bound in the gas-phase, in disagreement with theoretical studies,[16,17] and proceed to investigate the excited state relaxation of the S_1 state using time-resolved photoelectron spectroscopy. The observed dynamics are interpreted with the aid of high-level *ab initio* calculations (conducted in the group of Helen Fielding) and the primary relaxation path is found to be very similar to that observed in solution, despite the differences in absorption spectra between the two media. This highlights the importance of the protein backbone for the function (i.e. fluorescence) of GFP in nature.

Experimentally, $HBDI^-$ was produced via electrospray ionisation of a 1 mM solution of HBDI. This was synthesised using published methods[18,19] in the groups of Steven Cobb (single-colour photoelectron spectroscopy experiments) and Helen Fielding (time-resolved experiments), and provided for use in our anion photoelectron spectrometer. Solutions were brought to pH$\sim$10 through the addition of NaOH. Following trapping and mass selection using time-of-flight

spectrometry (see chapter 2 for details), HBDI anions are intersected by laser pulses in the centre of our velocity-map imaging detector. For single-colour photoelectron spectroscopy we utilise femtosecond laser pulses at 2.58 eV (480 nm), 4.62 eV (268.1 nm) and 6.15 eV (201.5 nm) and nanosecond pulses at 3.496 eV (355 nm). Femtosecond pulses correspond to the third (268.1 nm) and fourth harmonic (201.5 nm) of the Ti:Sapphire system used, and visible pulses were created by frequency mixing the output of an optical parametric amplifier with residual fundamental light, as outlined in chapter 2. Nanosecond pulses used are the third harmonic of a Nd:YAG laser. Typical intensities in the interaction region are 1.6×10^9 Wcm^{-2}, 1.4×10^9 Wcm^{-2} and 2.8×10^8 Wcm^{-2} for the 480, 268.1 and 201.5 nm, respectively and 5×10^6 Wcm^{-2} for the nanosecond pulses. For time-resolved photoelectron spectroscopy experiments the system is pumped with a visible excitation pulse (2.48 eV, 500 nm) and probed a delay t later with a 1.55 eV (800 nm) pulse (typical intensities 2.0×10^{10} Wcm^{-2}). The pump-probe cross-correlation was determined to be 130 fs in a thin non-linear crystal.

5.2 Electronic Structure of the GFP Chromophore

5.2.1 Photoelectron spectroscopy of HBDI$^-$

Photoelectron spectra of HBDI$^-$ collected at three different detachment energies (3.496, 4.62 and 6.15 eV) are shown in figure 5.2(a)-(c). To accurately determine the intrinsic vertical detachment energy (*VDE*) care was taken to avoid any unnecessary heating of anions within the anion beam machine. To achieve this, Helium buffer gas was used within the ion trap and all trapping voltages reduced to the lowest operable levels, this yields ions at approximately room temperature (as outlined in section 4.3.3).[20] As this reduces the ion current in the interaction region, the spectrum at 201.5 nm (5.2(c)), where a significantly lower photon flux is available, was collected under slightly hotter ion source conditions. Nonetheless the measured *VDE* is identical across all three spectra at 2.8 ± 0.1 eV, as indicated by the grey shaded area in figure 5.2. These findings furthermore agree with other experimental values published after these results.[21,22]

The experimentally determined *VDE* is significantly higher in energy than the $S_1 \leftarrow S_0$ absorption maximum (2.57 eV).[14] Shown in figure 5.3 is a comparison of our photoelectron spectrum (collected at 3.496 eV photon energy and shown in figure 5.2(a))) with the action spectra recorded by Forbes and Jockusch.* This shows the measured photofragmentation yield (red circles) as a function of excitation wavelength, collected over a range of photon energies resonant with the

*We thank Prof. R. Jockusch for sharing the photofragement yield spectra for HBDI$^-$.

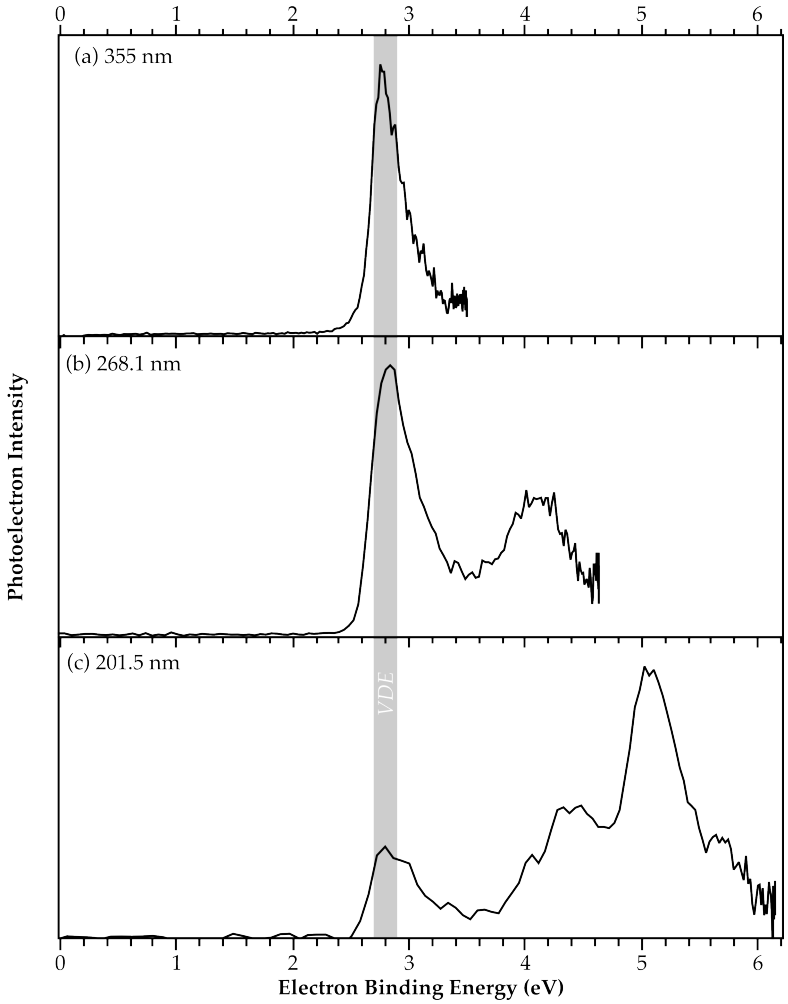

Figure 5.2: Photoelectron spectrum of $HBDI^-$ at photon energies of (a) 3.496 eV (355 nm), (b) 4.62 eV (268.1 nm) and (c) 6.15 eV (201.5 nm). The vertical shaded bar indicates the determined *VDE* of 2.8 ± 0.1 eV, the *ADE* is determined by interpolation of the rising edges as 2.6 ± 0.1 eV.

$S_1 \leftarrow S_0$ transition. The authors furthermore infer the photoelectron detachment yield (green squares) by comparison of the total ion current measured before and after optical excitation.[14] The fragmentation channel exhibits a single maximum, peaking at 2.57 eV, while the electron yield exhibits a similar shape, but with an additional feature peaking at 2.76 eV. Forbes and Jockusch assigned the peak around 2.57 eV to the origin of the $S_1 \leftarrow S_0$ transition, while the secondary feature at higher energy was assigned to a vibrational excitation of the S_1 state. However, comparison of the electron yield data with the photoelectron spectrum in 5.2(a) shows that the position and onset of the second peak in the yield spectrum correlates remarkably well with the onset of the photoelectron feature. Given that this peak is entirely absent in the fragmentation data, this suggests that the feature around 2.76 eV in the electron yield spectrum corresponds primarily to direct detachment or autodetachment into the continuum. Importantly, the correlation between the two independent data sets reinforces the conclusion that the S_1 state origin lies below the detachment threshold (*VDE*), making the S_1 state bound with respect to the neutral in the Franck-Condon region of opti-

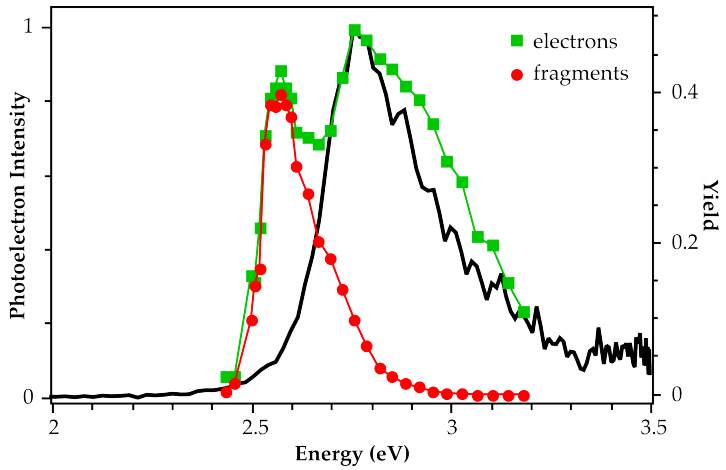

Figure 5.3: Comparison between the photoelectron spectrum at 355 nm (3.496 eV) and the fragmentation yield (red circles) and electron yield (green squares) spectra collected by Forbes and Jockusch.[14] The horizontal axis represents the electron binding energy (photoelectron spectrum) or excitation energy (yield spectra).

cal excitation. The adiabatic detachment energy (*ADE*) can be extracted from the photoelectron spectrum be extrapolation of the rising edge of the feature; for all spectra shown in figure 5.2 this yields a value of 2.6 ± 0.1 eV for the *ADE*. This coincides with the measured maximum of the $S_1 \leftarrow S_0$ transition.[14]

$HBDI^-$ and related chromophores have been the subject of several theoretical studies, investigating both electronic structure and dynamics, and these have been recently reviewed.[23] The best theoretical estimates for the values of the *VDE* and *ADE* are 2.54 eV and 2.39 eV, respectively.[16,17] These values place the S_1 state in the electronic continuum (unbound with respect to electron loss) and do not agree with the experimental values determined here, that have been reproduced in other laboratories.[21,22] While the origin of this discrepancy remains unclear, very recent theoretical investigations report a *VDE* = 2.62 eV and an *ADE* = 2.52 eV, confirming the bound nature of the excited state in the Franck-Condon region.[22] The fact that three photoelectron spectra collected at different excitation energies yield identical values for the *VDE* and *ADE*, as well as identical peak shapes, rules out the possibility of accessing resonances in the photoelectron spectrum. We furthermore note that the employed energies are so far above the $S_1 \leftarrow S_0$ transition that an excitation of the S_1 state is inconceivable. The only difference between the theoretical studies and the experimental investigations presented here is then the finite internal temperature inherent to any experimental investigation. However, we have induced significant thermal excitation in $HBDI^-$ and observe no effect on the photoelectron spectra, as is shown in figure 5.4(a) and (b), for photoelectron spectra collected with 3.496 eV (355 nm) and 4.62 eV (268.1 nm) excitation energies. Furthermore, the extrapolated *ADE*s are likely to increase as zero internal energy is approached, because the participation from hot bands is reduced. The presence of hot bands is clearly

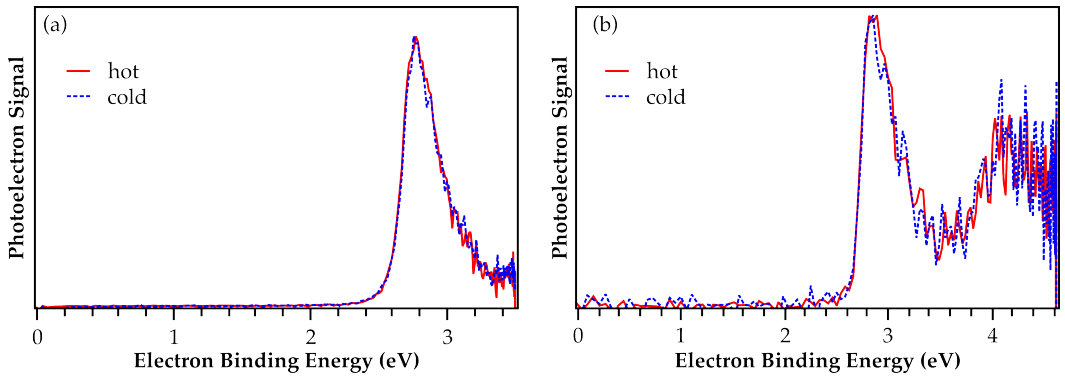

Figure 5.4: Photoelectron spectra collected with different amounts of internal energy in the parent anion, controlled by changing the trapping conditions in the beam machine. No effect of excess internal energy on the *VDE* or *ADE* is observed. (a) Spectra collected at 3.496 eV (355 nm) and (b) spectra at 4.62 eV (268.1 nm).

discernible in other investigations of the HBDI anion, with a significantly worse signal-to-noise ratio than the data presented here.[22] Therefore we conclude from our experimental evidence, and that from other laboratories, that the S_1 state of $HBDI^-$ is bound with respect to electron loss, despite recent theoretical studies suggesting otherwise.[16,17]

The photoelectron spectrum collected with 4.62 eV photons (figure 5.2(b)) indicates the presence of an excited state of neutral HBDI with an electron binding energy (*eBE*) of ∼4.1 eV. This is confirmed by the spectrum shown in 5.2(c), collected at 6.15 eV. This furthermore shows the presence of additional excited states of the neutral at *eBE*s of ∼4.4 eV and ∼5.1 eV. We assign the accessed states with the aid of density functional theory (DFT) calculations.

5.2.2 Electronic structure calculations of HBDI

To assign the observed excited states of neutral HBDI, formed following photodetachment from $HBDI^-$, we use DFT and time-dependent DFT (TD-DFT) calculations to gain an understanding of the underlying electronic structure. All calculations utilise the CAM-B3LYP functional, where the Coulomb attenuated method (CAM) is specifically employed to account for intra-molecular charge transfer in excited states.[24] An augmented and correlation-consistent double-zeta basis set is used (aug-cc-pVDZ) and all calculations run within the Gaussian09 software suite.[25] To assign the photoelectron spectra all energies and excited states were evaluated at the optimised geometry of the anion, given that photodetachment is a vertical process.

The calculated electronic excited states of the neutral HBDI are shown as red bars in figure 5.5, superimposed on the UV photoelectron spectrum first shown in figure 5.2(c). The shown *VDE*s of the excited states are evaluated as the anion-

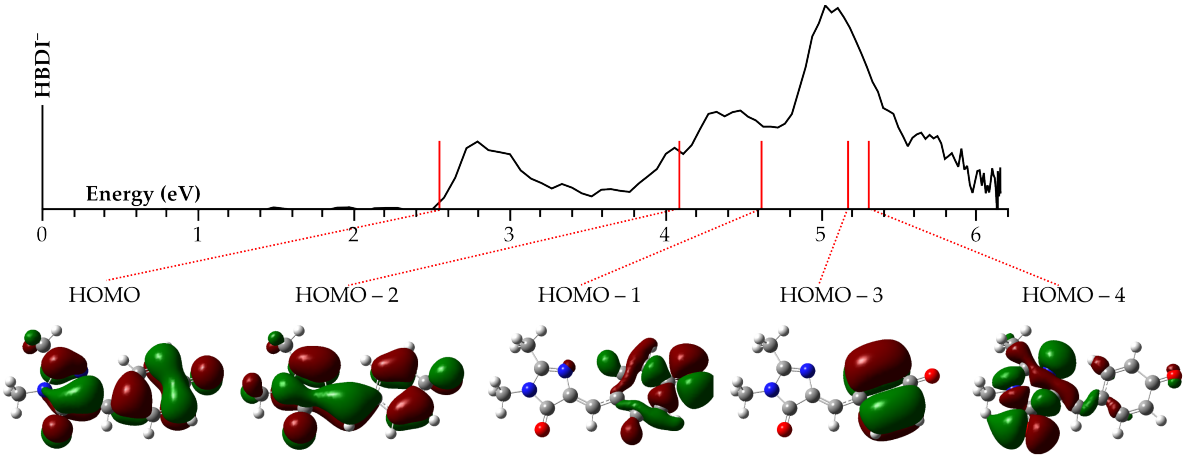

Figure 5.5: Calculated electronic excited states of neutral HBDI (red bars) in the anion geometry, superimposed on the photoelectron spectrum collected with 6.15 eV photons. Shown molecular orbitals correspond to the anion orbital from which an electron is removed in the detachment process, yielding the indicated neutral excited state.

to-neutral vertical energy separation, for which the robust high-level literature value of 2.54 eV is used,[16] plus the excitation energy within the neutral, calculated using TD-DFT as outlined above. The predicted peak positions match the recorded spectrum remarkably well and, assuming that all detachment processes have a similar cross-section, we can assign each feature in the spectrum to a specific transition into a neutral excited state. Details of the calculated excited states, their excitation energies and orbital contributions are given in table 5.1, where molecular orbital (MO) 57 corresponds to the highest occupied MO (HOMO) of both neutral (singly occupied HOMO) and anionic (doubly occupied HOMO) HBDI. Analysis of the dominant contributions to the calculated excited states (highlighted in bold) shows that the first four excited states can be assigned to transitions from successively more bound doubly occupied MOs to the singly occupied HOMO of the neutral. From the anions perspective the formed excited states therefore correspond to the removal of an electron from successively more bound anion MOs, leaving the neutral in an excited state with a hole in successively lower lying MOs. The anion orbitals (which are identical to those of the neutral) from which an electron is removed to form a specific neutral excited state are also shown in figure 5.5.

The ground state of neutral HBDI corresponds to detachment of a single electron from the (doubly occupied) HOMO in the anion, leaving the neutral with a singly-occupied (radical) HOMO. While we calculate a *VDE* of 2.79 eV, in remarkable agreement with the experimental data, this is significantly higher then previous electronic structure calculations (using high-level Multireference Moller-Plesset Perturbation theory) placing the *VDE* at 2.54 eV.[16] The first neutral excited state is calculated at 1.51 eV above the neutral ground state and

Table 5.1: Excited states and orbital contributions of neutral HBDI following photodetachment from $HBDI^-$. The HOMO in both forms is MO 57.

Excitation Energy	Orbitals	Relative Contribution
1.5047 eV	**55 → 57**	**0.74**
	55 → 58	0.19
	55 → 60	0.01
	55 → 62	0.03
2.1053 eV	57 → 58	0.23
	52 → 58	0.01
	56 → 57	**0.71**
	56 → 58	0.03
2.7189 eV	53 → 58	0.01
	56 → 59	0.01
	57 → 59	0.02
	54 → 57	**0.84**
	54 → 58	0.08
2.7520 eV	**53 → 57**	**0.76**
	53 → 58	0.18
	53 → 62	0.01

corresponds to the removal of an electron from the HOMO−2 of the anion, as indicated in figure 5.5. The predicted *VDE* for this transition is 4.08 eV, in excellent agreement with the observed peak in the photoelectron spectrum at 4.1 eV. Detachment from the HOMO−1 of the anion corresponds to the removal of an electron with a calculated *eBE* of 4.61 eV, most likely corresponding to the feature at 4.4 eV in the photoelectron spectrum. Two further excited states are calculated to be very close in energy at *VDE*s of 5.17 and 5.30 eV and correspond to detachment from the HOMO−3 and HOMO−4 of the anion, respectively. We assign both these transitions to the photoelectron peak at 5.1 eV *eBE* and the presence of two near-degenerate features accounts for the increased intensity in this peak, which has approximately doubled with respect to all other transitions observed in the spectrum. However it should be noted that this is a very simplified explanation of the larger photoelectron intensity observed for this feature and does not take into account the relative magnitude of absolute detachment cross-sections. The overall good agreement between theory and experimental data provides some confidence in these assignments and highlights the use of photoelectron spectroscopy as a sensitive probe for the MOs of the $HBDI^-$ chromophore and hence a benchmark for future calculations.

5.2.3 Nature of the S_1 excited state

Analysis of the UV photoelectron spectra of $HBDI^-$ in section 5.2.1 revealed a *VDE* of 2.8 eV, significantly higher than the maximum of the $S_1 \leftarrow S_0$ absorption maximum in the gas-phase.[14] These relative values are crucial as they determine the role of autodetachment in the relaxation processes following excitation of isolated $HBDI^-$ to the S_1 state, which is responsible for the strong fluorescence in wild-type GFP. The observation of a *VDE* in excess of the absorption energy

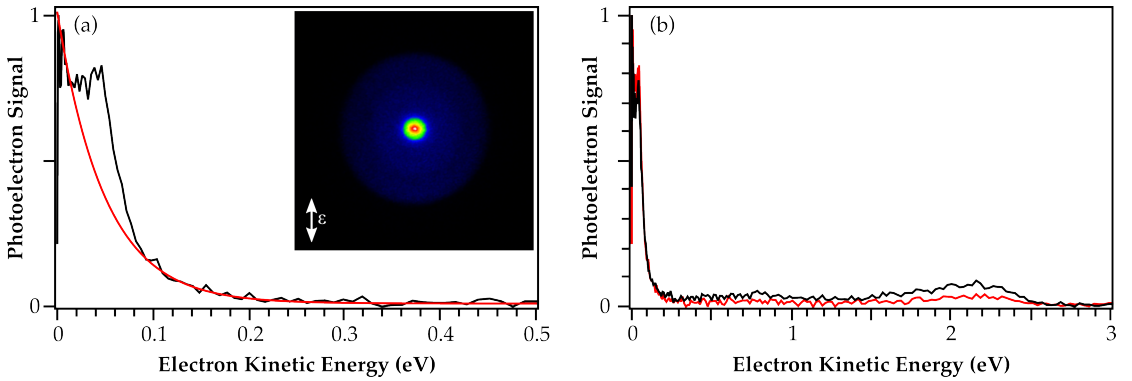

Figure 5.6: Photoelectron spectrum of $HBDI^-$ collected at 2.58 eV (480 nm), resonant with the $S_1 \leftarrow S_0$ transition. (a) Observation of electrons at threshold is indicative of thermionic emission, which is modelled by the red line. Shown inset is the raw photoelectron image, indicating the very intense feature at zero electron kinetic energy. (b) Spectrum at 480 nm collected with high (black) and low (red) laser intensities.

makes the S_1 state bound and thus implies that autodetachment into the continuum is a minor channel at most, at least in the Franck-Condon region. However the extrapolated *ADE*s coincide with the origin of the $S_1 \leftarrow S_0$ transition, indicating that there might be an energetically accessible continuum following motion on the S_1 excited state energy surface.[26,27] Indeed, the action spectra acquired by Jockusch and co-workers (figure 5.3) indicate that following excitation at 480 nm both fragments and electrons are observed.[14,15] Comparison of the action spectrum with the photoelectron spectrum shows that at higher energies both autodetachment and direct photodetachment are clearly active decay paths.

To gain additional insight into the nature and fate of the S_1 state following photoexcitation, a photoelectron spectrum at 2.58 eV (480 nm), and therefore resonant with the $S_1 \leftarrow S_0$ transition, is shown in figure 5.6(a). The most striking feature in this spectrum is the observation of photoelectrons with $eKE \sim 0$ eV, as is clearly visible in the raw photoelectron image shown inset in figure 5.6(a). Photoelectrons at threshold cannot originate from a direct detachment process as the cross-section for photodetachment from an anion vanishes at threshold.[28,29] This feature must therefore arise from an indirect process, such as (i) autodetachment from the excited state or (ii) thermionic emission from hot anion ground state population, following internal conversion from the excited state.[30–33] Thermionic emission manifests itself as a falling exponential in the photoelectron spectrum and between 0.1 eV $< eKE <$ 0.2 eV clear evidence of an exponentially decaying intensity is observed. The spectral shape of thermionic emission can be crudely modelled according to[33,34]

$$I(eKE) = \exp\left(-\frac{eKE}{k_B T}\right), \tag{5.1}$$

and this is shown as a red line in figure 5.6. Here a temperature of 575 K has

been used for the fit, which reproduces the observed intensity distribution very well. The extracted temperature however is not meaningful in this case, due to the contribution of competing decay mechanisms (fragmentation as observed by Forbes and Jockusch[14]). The observation of thermionic emission on the other hand is a clear indication that internal conversion is an operative relaxation mechanism following S_1 excitation, reinforcing the argument that the S_1 state is bound with respect to electron loss.

A recent photoelectron spectrum collected by the group of Andersen confirms the presence of a very low *eKE* peak ($\sim$0.05 eV), however their data suggests that no electrons are observed at threshold and the photoelectron signal vanishes at *eKE* = 0 eV .[22] The authors attribute the observed peak to a vibrational autodetachment feature from the S_1 excited state. Such an indirect electron emission can occur if, following excitation, population in the S_1 undergoes motion on the excited state potential energy surface, such that its energy shifts above that of the neutral ground state. Despite the disagreement with our interpretation, this study agrees with the bound nature of the S_1 state in the Franck-Condon region and the operation of an internal conversion mechanism.[22]

At higher *eKE* multi-photon processes are observed in the resonant photoelectron spectrum, as is clear from the spectra in figure 5.6(b) and from the weaker rings observed at larger radii in the photoelectron image. These 2-photon processes are enabled by the resonance enhancement via the S_1 state and energetically can be assigned to 2-photon detachment to form the neutral ground state (feature at $\sim$2.4 eV) or the first excited state observed previously (feature at $\sim$0.8 eV). In order to ascertain that the feature attributed to thermionic emission does not arise due to a resonant 2-photon process, a photoelectron spectrum at 480 nm was collected for two different laser intensities. These are shown in figure 5.6(b) as the black (high intensity, 2×10^{10} Wcm^{-2}) and red (low intensity, 4×10^{9} Wcm^{-2}) traces. While the multiphoton features at higher *eKE* appear severely depleted in comparison to the single photon peak when lower intensities are used, the exponential tail around the energetic threshold shows no such depletion. This indicates that the low *eKE* feature does indeed arise from a single-photon process, confirming the assignment to thermionic emission.

In addition to the thermionic emission feature at threshold, the resonant photoelectron spectrum appears to contain a further feature due to direct or autodetachment, peaking around 0.05 eV *eKE*, equivalent to that observed by Andersen *et al*.[22] Direct detachment could occur due to the finite bandwidth of the femtosecond laser ($\sim$40 meV full width at half-maximum) or the presence of hot bands in the spectrum due to finite anion temperatures prior to detachment. Alternatively, autodetachment is feasible following motion on the excited state

potential energy surface and shifting of the S_1 anion energy below that of the D_0 neutral ground state, as suggested above.[26,27] However, no direct detachment process contributes to the photoelectron spectrum at $eKE = 0$ eV according to the Wigner threshold laws.[28,29] Although it has been suggested that this might be a too simplistic approach for complex polar molecules such as $HBDI^-$ that posses a large dipole moment, where the charge-dipole interaction can dominate over the centrifugal barrier to detachment.[22,35]

5.2.4 Discussion

The observation that the *VDE* of $HBDI^-$ is larger than the maximum of the $S_1 \leftarrow S_0$ transition, and the S_1 state hence is bound in the Franck-Condon region, is consistent with experiments in the Jockusch and Andersen groups.[12–15] A major channel observed in both these studies is fragmentation. Experiments by the Jockusch group indicate the presence of an electron loss channel following excitation at 480 nm.[14] Through power-dependence studies the authors attempted to discern the possible mechanism for this electron loss by considering the number of photons absorbed.[15] Here we have shown that, in addition to multi-photon processes, the emission of thermionic electrons occurs after 480 nm excitation, and as the excitation energy is increased direct and autodetachment processes start to contribute to the observed photoelectron signal, although their relative contributions remain unknown. This interpretation is consistent with a bound S_1 state and an operative internal conversion mechanism in the gas-phase, quenching the strong fluorescence observed in wild-type GFP. This naturally leads to the question of the operative relaxation pathway of $HBDI^-$ in the gas-phase, and the effect of the protein environment that effectively suppresses this non-radiative relaxation and leads to strong fluorescence in GFP.

5.3 Dynamics of the GFP Chromophore

While the bound nature of the S_1 excited state in HBDI anions has now been confirmed by several experimental groups around the world,[21,22,36] very little is known about the dynamics of the excited state. Specifically, the relaxation pathway following population of the S_1 via absorption of a photon from the S_0 anion ground state is unknown in the gas-phase, but has been the focus of several theoretical studies.[26,37–42] In natural GFP in the protein environment fluorescence is the dominant decay, leading to the outstanding uses of GFP and related chromophores as markers in biology and the life sciences.[1,2] Isolated $HBDI^-$, however, was found to be non-fluorescent and thus must primarily decay by an alternative route.[14,15]

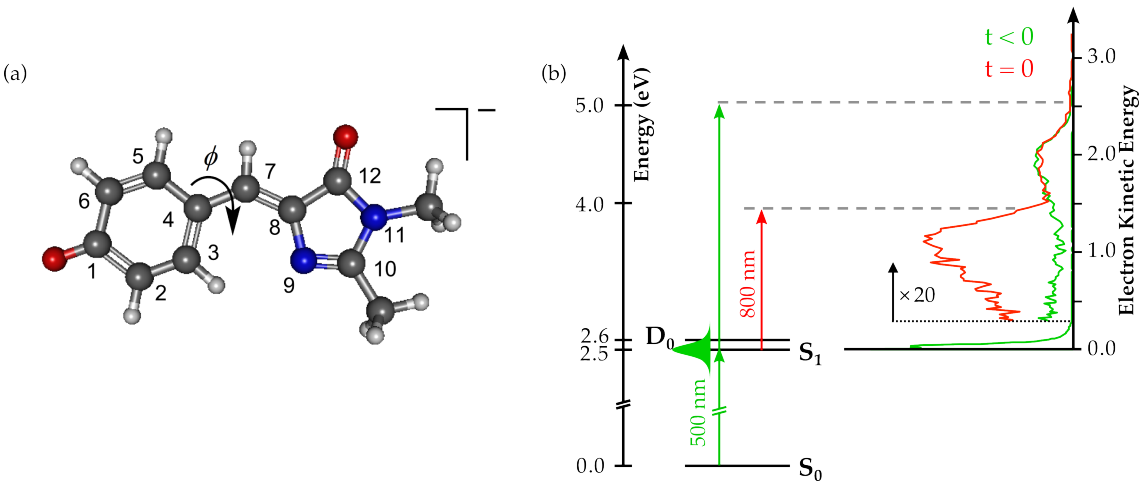

Figure 5.7: (a) Molecular structure of the isolated HBDI anion, indicating the atomic labelling used throughout and the torsion angle ϕ. (b) Basic electronic state diagram of $HBDI^-$ and the pump-probe scheme used in time-resolved experiments. Shown inset are two representative photoelectron spectra collected at $t < 0$ (green) and at $t = 0$ (red). The additional feature is assigned to photodetachment from the S_1 state by the probe and hence monitors the excited state population.

In contrast to the gas-phase, GFP (and the HBDI chromophore) has been extensively studied in solution. Upon de-naturisation the protein was found to loose its fluorescent properties,[10] which only returned when the protein was re-naturised or cooled below the glass-transition temperature.[11] The loss of fluorescence was attributed to a fast radiationless decay pathway becoming available. Using the fluorescence upconversion technique the S_1 anion excited state of $HBDI^-$ was found to decay bi-exponentially in solution, with characteristic lifetimes in methanol of 340 fs and 1.1 ps.[43–45] These timescales were found to be almost independent on the choice of solvent or the solvent viscosity, with the exception of extremely viscous solvents which significantly increased the excited state lifetime.[45–47] Theoretical studies suggest that this ultrafast decay involves motion on the excited state potential energy surface that moves population away from the fluorescent state (FS) geometry via a rotation around the C4−C7 torsion angle ϕ (as indicated in figure 5.7(a)), followed by fast internal conversion to the anion ground state.[26,45] To achieve the highly efficient fluorescence observed in natural GFP, this rotation about ϕ must be inhibited by the protein environment, and thus population trapped in the FS geometry. Solvating the chromophore in highly viscous solvents, or freezing it below the glass-transition temperature, similarly inhibits the free rotation about the C4−C7 axis, thereby leading to the return of the fluorescence as population is prevented from leaving the FS geometry in the S_1 state.[47,48]

While the rotation about ϕ will naturally be uninhibited in the gas-phase environment, the electronic absorption spectrum of isolated $HBDI^-$ and that of the native protein are very similar, suggesting that the protein does not induce

any significant changes in electronic character or excitation energy (at least in the Franck-Condon region).[12,13] This is in stark contrast to solution phase data, which shows marked differences in absorption spectra of the protein and the solvated environment, most noticeably a blue-shift of ∼0.3 eV in water.[10] Despite the similarities in absorption spectra, the gas-phase relaxation mechanism clearly differs from that of the protein, as no fluorescence is observed from isolated $HBDI^-$.[14] In order to probe the decay pathway in the gas-phase, following excitation to the S_1 state, we use time-resolved photoelectron spectroscopy. The $S_1 \leftarrow S_0$ transition is resonantly excited with a 2.48 eV (500 nm) femtosecond pump pulse and the system probed a variable delay t later with a 1.55 eV (800 nm) probe pulse, as indicated in figure 5.7(b).

5.3.1 Time-resolved photoelectron spectroscopy of $HBDI^-$

Two representative photoelectron spectra are shown in figure 5.7(b), superimposed on the electronic structure diagram of $HBDI^-$. Shown in green is a spectrum collected at $t < 0$ (probe before pump), which is identical to a pump-only photoelectron spectrum, indicating that the probe is insufficient to directly detach an electron from $HBDI^-$ and is not resonant with any transition. This spectrum is dominated by a large signal at $eKE < 0.2$ eV, arising from the indirect emission of electrons following S_1 excitation as discussed in section 5.2.3.[22,36] A second much weaker feature is evident in this spectrum, centred at 1.96 eV *eKE*. This is consistent with resonant 2-photon detachment via the S_1 state, as has been previously observed. Shown in red in figure 5.7(b) is a photoelectron spectrum with pump and probe pulses temporally overlapped ($t = 0$). Here an additional photoelectron feature emerges, peaking at an *eKE* of 1.1 eV. Given the probe photon energy of 1.55 eV, this feature is consistent with excitation to the S_1 state by the pump, followed by photodetachment by the probe pulse. This therefore represents a direct measure of the S_1 excited state population.

Time-resolved photoelectron spectra at various delays are shown in figure 5.8(a), with a pump-only photoelectron spectrum subtracted from the data at all delays, leaving only the excited state signal. A contour plot of the same data is shown in (b). A very fast rise in signal is observed around $t = 0$, corresponding to the temporal overlap of pump and probe pulses. The observed time-resolved feature peaks around *eKE* = 1.1 eV at $t = 0$ and is asymmetrically shaped with a decaying edge towards higher *eKE*. With increasing time delay the high energy side of the feature decays on a sub-picosecond timescale, leaving only intensity at lower kinetic energies, centred around 0.6 eV *eKE*. This signal subsequently decays on a picosecond timescale. The observed dynamics are clearly not well described by a single exponential decay model and instead were fitted with a global fitting routine comprising two exponentially decaying profiles, convoluted with a

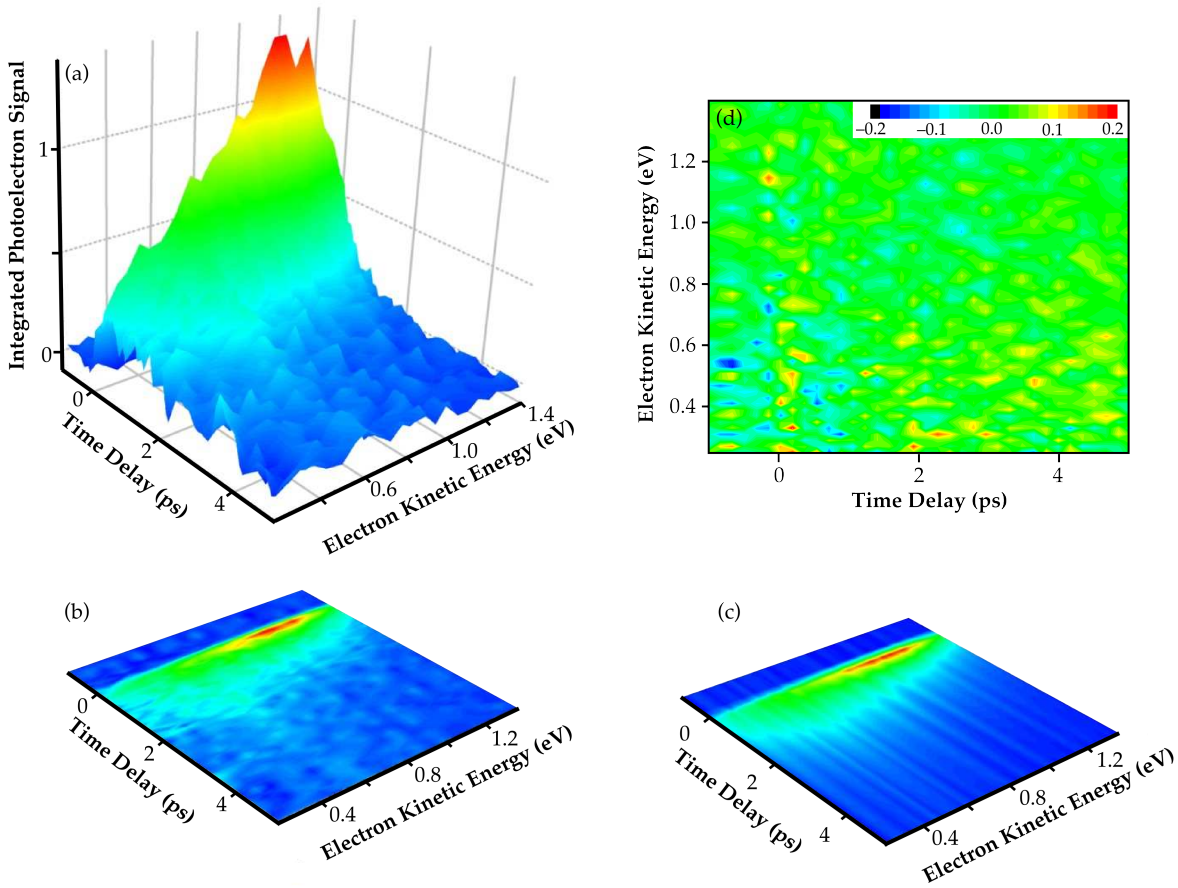

Figure 5.8: (a) Time-resolved photoelectron spectra of $HBDI^-$ with a pump-only spectrum subtracted, leaving only the excited state feature; (b) contour map of time-resolved data; (c) reconstructed time-resolved data from the global fit, showing excellent agreement with the experimental data in (b); (d) residuals of the global fitting routine with two exponential components.

Gaussian instrument response function;

$$S(eKE,t) = \sum_i g(t) \otimes c_i(eKE) e^{-t/\tau_i}. \tag{5.2}$$

Here the overall observed signal $S(eKE,t)$ is described in terms of the coefficients $c_i(eKE)$ that describe the amplitude of the i^{th} decay at a given eKE and with an associated lifetime $\tau_i = k_i^{-1}$. Two exponential contributions (c_1 and c_2) describe the experimental data remarkably well and the resultant $S(eKE,t)$ is shown in figure 5.8(c), with the residuals from data fitting shown in (d). The overall fit yields an adjusted R^2 parameter of 0.98. The extracted lifetimes are τ_1=330 fs and τ_2=1.4 ps. This model also allows the extraction of the individual photoelectron spectra corresponding to the contributions c_1 and c_2, and these are shown in figure 5.9(a), where positive intensity indicates an exponential decay, and negative intensity an exponential growth at a given eKE for that contribution.

The photoelectron spectrum associated with the fast decay component c_1 (green trace in figure 5.9(a)) shows a decay of intensity in the spectral region above

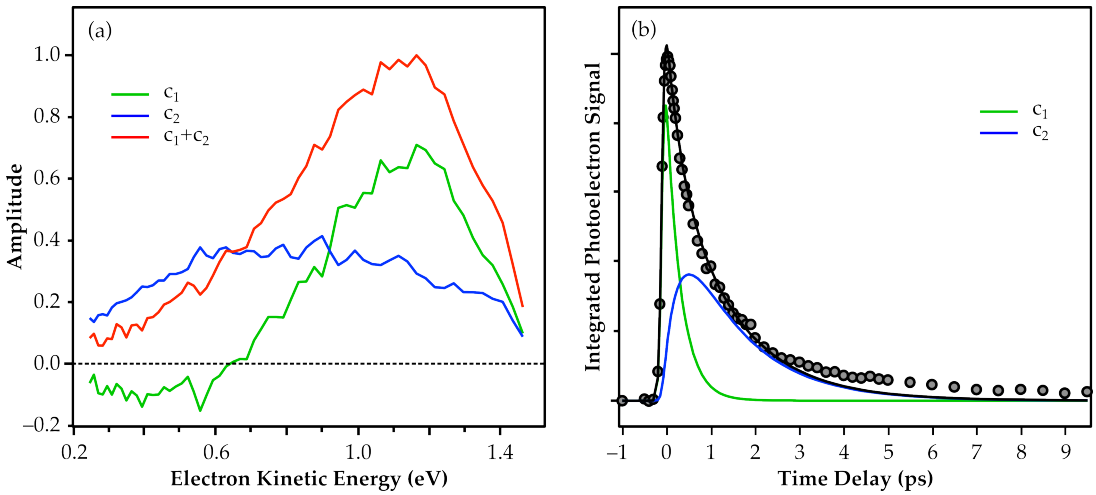

Figure 5.9: (a) Spectra of the fast (c_1, green trace) and slow (c_2, blue trace) components of the bi-exponential decay, extracted from the time-resolved data using a global fit. The photoelectron spectrum associated with the initially excited intermediate is shown in red. (b) Total integrated photoelectron intensity of the excited state feature (grey circles) and extracted fit (solid black line). Also shown are the two components, corresponding to timescales of 330 fs (green) and 1.4 ps (blue). At long times a slight deviation is observed from the model fit as around 2% of the population remain in the excited state.

0.6 eV, with a simultaneous growth in photoelectron signal with $eKE < 0.6$ eV. This suggests a motion on the S_1 excited state potential energy surface, from the initially excited Franck-Condon (FC) region towards a region leading to emission of photoelectrons with lower kinetic energies, with a characteristic 330 fs timescale. The remaining population subsequently decays on a 1.4 ps timescale (τ_2), producing a broad distribution of photoelectrons peaking at $\sim$0.6 eV *eKE*, as shown by the c_2 spectrum in figure 5.9(a) (blue trace). No spectral shifts are observed for this feature. The photoelectron spectrum corresponding to the decay occurring on a 330 fs timescale can be reconstructed by summing the two individual contributions c_1 and c_2 and this is shown as a red trace in 5.9(a).

The results from the global fitting analysis have furthermore been used to reproduce the total integrated photoelectron signal, as shown by the solid line in figure 5.9(b). The bi-exponential nature of the decay is clear from the data, and both the fast and the slow components reproduced well by the fit, which is overall in excellent agreement with measured data. A small discrepancy is however observed at long time delays, where experimentally the signal does not decay back to zero, but approximately 2% remains and decays on a timescale significantly longer than the current experimental data (10 ps). This indicates that a small fraction of population remains trapped in the excited state and decays on a much slower timescale, for example through fluorescence.

5.3.2 *Ab initio* calculations of potential energy surfaces

These calculations were carried out in the group of Helen Fielding (UCL) and with help from the EPSRC UK National Service for Computational Chemistry Software. All calculations were carried out on a simplified GFP model chromophore, *p*-hydroxybenzylidene -imidazoline (HBI^-), featuring hydrogen terminated imidazole groups. While this was chosen to reduce the computational expense, given that the terminal methyl groups are unlikely to have any significant effect on the chromophore energetics,[42] in our view little added computational expense would have been introduced by inclusion of the methyl groups. A molecular potential energy surface scan was used to determine the molecular geometries along the excited state reaction coordinate of HBI^-.

Calculations used the complete active space self-consistent field (CASSCF) level of theory, employing a 6-31G* basis set and carried out in the MOLPRO 2010.1 software suite.[26,49] The complete active space for HBI^- should encompass all p-orbitals antisymmetric to the molecular plane, a total of 16 electrons in 14 orbitals (16,14 active space). To reduce computational effort, an incomplete active space of (12,11) is employed, with the orbitals deemed to have least influence on the conjugation excluded. These are the lowest and highest sets of benzene valence p-orbitals on the phenol moiety (equivalent to the lowest HOMO and highest LUMO), as well as the lone pair on the N11 atom (see figure 5.7(a) for atom labels).[26] To avoid CASSCF convergence problems, a two-root (S_0,S_1) state averaged procedure was employed in all calculations. The potential energy surface was scanned with respect to torsional motion around ϕ, the angle responsible for the ultrafast non-radiative decay in solution. The single state CASSCF energies for the neutral radical were obtained by removal of a single electron from the anion state and in the anion calculated geometries. The energy profile at key molecular geometries was furthermore improved by using single-state, single-point multiconfigurational second-order perturbation theory (CASPT2) calculations, utilising the ANO-pVDZ basis set, for both anion and neutral radical configurations, carried out using MOLCAS 7.6.[50–52]

A summary of the results from these calculations is shown in figure 5.10. Specifically we evaluated the energies of the S_0 and S_1 anion states and the D_0 neutral states at key geometries along the S_1 excited state potential energy surfaces. These key geometries were identified as (i) the Franck-Condon (FC) geometry, corresponding to the geometry initially excited from the S_0, (ii) a fluorescent state (FS) geometry, a shallow minimum on the S_1 surface and (iii) a twisted intermediate (TI), formed following rotation around ϕ (C4−C7 axis) by 90°. This is in agreement with previous theoretical studies.[26,45] A further TI geometry can be reached by torsional motion around the C7−C8 axis, however this was found

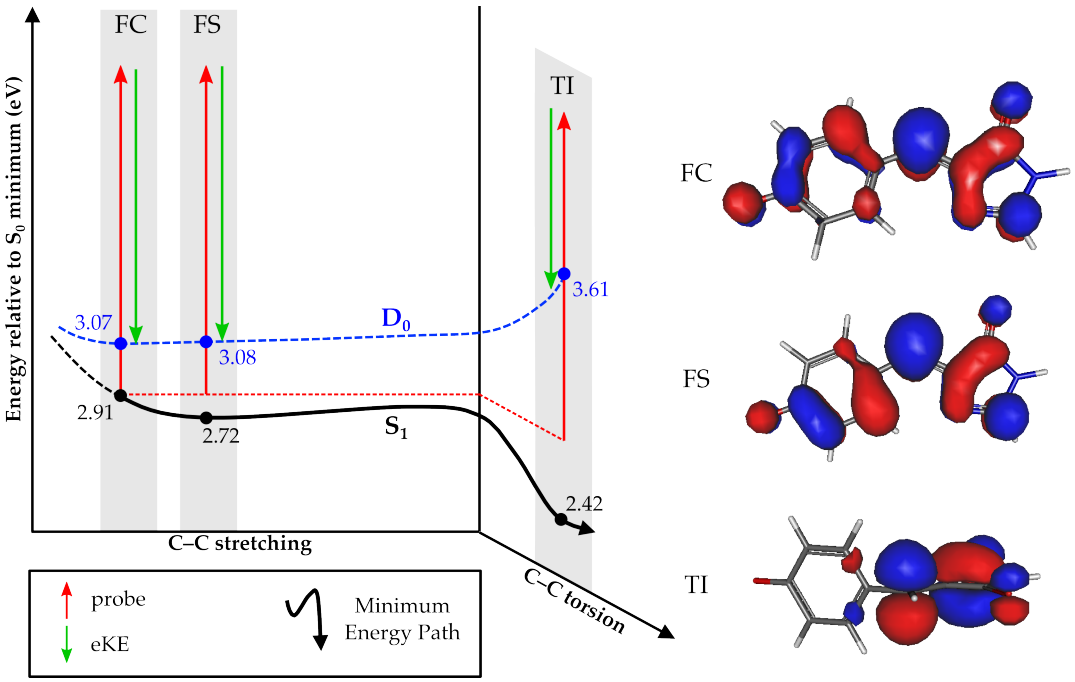

Figure 5.10: Schematic potential energy curves and calculated CASPT2 single-point energies along the reaction path FC → FS → TI. Also shown are the relevant state-averaged S_1 CASSCF molecular orbitals. The increase in energy of the D_0 relative to the anion states leads to a shift to lower *eKE*s when population has reached the TI. From here the most likely decay path is internal conversion back to the anion ground state.

to possess a small barrier in the gas-phase, thereby favouring the formation of the ϕ-rotated TI geometry.[26]

Following excitation to the FC geometry, the FS can be reached primarily via a stretching of the allyl C−C bonds. This is likely to be very fast, occurring on a timescale of 10s of femtoseconds and the calculated potential energy surface is rather flat between the FC and FS geometries.[26] The calculated D_0 neutral energies (figure 5.10) indicate only a small shift in energy for the D_0 surface between the FC and FS geometries, suggesting that the photoelectron spectrum originating from both states should be very similar. Following formation of the FS geometry, a negligible barrier (0.02 eV) connects this to the TI state. This motion involves a significant change in reaction coordinate, as bond stretching of the allyl group is replaced by a rotation around the weakened bonds (ϕ). The motion along the potential energy surface, FC → FS → TI is associated with a significant stabilisation of the S_1 energy by 0.49 eV, in qualitative agreement with the original calculations by Olivucci *et al*[26] and in quantitative agreement with more recent studies.[42] During this motion along the S_1 potential energy surface, the corresponding D_0 energy increases by 0.54 eV, as shown in figure 5.10. Once population in the S_1 has reached the TI minimum, it most likely decays to the anion ground state via internal conversion, given the reduced S_0-S_1 energy gap at this geometry and the significantly higher D_0 energy.

5.3.3 Discussion

Detailed *ab initio* calculations confirm the initial assignment and interpretation of the photoelectron data and offer an insight into the underlying structural dynamics. Following excitation into the FC geometry, the excited state evolves within tens of femtoseconds to form the FS. This motion will occur within the cross-correlation of the laser pulses (130 fs) and will thus not be distinguishable with the current time resolution of the experiment. Furthermore the photoelectron spectra arising from the FC and FS state are likely to be very similar, given the very small change in D_0 energy associated with FC $\rightarrow$ FS motion. Therefore the photoelectron spectrum arising from the fast decaying component c_1 (red trace in figure 5.8(b)) corresponds to the photoelectron spectrum from a combination of FC and FS population. Following formation of the FS, the system will evolve towards the TI geometry. Given the large geometric rearrangement, this motion is expected to take significantly longer than the formation of the FS from the FC geometry. Furthermore, the energy of the D_0 state is calculated to increase by 0.54 eV along this coordinate, while the S_1 excited state is stabilised by 0.49 eV with respect to the FC energy. This is in excellent agreement with experimental data; after the decay of the initial S_1 geometry a feature emerges that is substantially red-shifted ($\sim$0.5 eV) and broadened (figure 5.9). The spectral shift is due to the higher energy of the D_0 state, leading to emission of electrons with lower *eKE* as indicated in figure 5.10. The additional width is due to the divergence of the S_1 and D_0 surfaces, leading to a significantly wider Franck-Condon window for photodetachment.

The conceptual picture of the dynamics then is as follows; following excitation of the FC geometry in the S_1 state, the system evolves to form the FS geometry within the time resolution of our experiment (sub-100 fs). From this it undergoes a rotation around the ϕ torsional angle on a timescale of 330 fs, forming the TI geometry. The TI undergoes no further geometric rearrangement, but decays on a single exponential 1.4 ps timescale, most likely via internal conversion to the anion ground state. This does not appear to be associated with any spectral changes, the overall mechanism is shown schematically in figure 5.11.

The observed dynamics and associated lifetimes (330 fs and 1.4 ps) are remarkably similar to those observed in solution phase studies of HBDI, where fluorescence up-conversion revealed characteristic lifetimes of 340 fs and 1.1 ps for $HBDI^-$ in methanol.[43–45] These dynamics were interpreted as an initial motion along an S_1 vibrational coordinate, followed by a redistribution of the vibrational energy and decay from the formed intermediate. This is consistent with our interpretation of the dynamics in isolated $HBDI^-$, where we have identified the second step as the rotational motion around ϕ using quantum chemistry calcu-

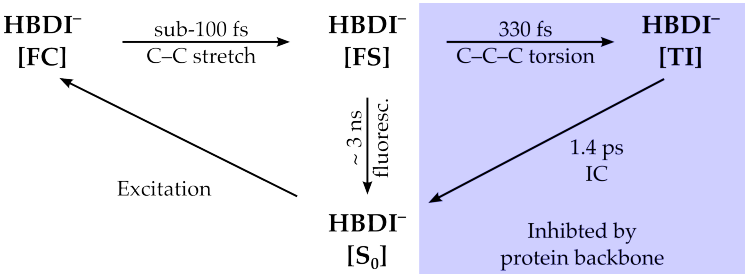

Figure 5.11: Decay pathways of the $HBDI^-$ chromophore. Following excitation into the Franck-Condon (FC) geometry, the system undergoes a stretch along the allyl C-C bridge to form the fluorescent state (FS). In the natural protein environment, fluorescence occurs from this state on a nanosecond timescale. In the gas-phase or solution however, an alternative decay pathway is accessible via rotation around the C-C-C bridge (ϕ), forming the twisted intermediate (TI) geometry, which can subsequently internally convert (IC) to the anion ground state on a picosecond timescale.

lations. The outstanding similarity between the dynamics in solution and in the gas-phase furthermore highlights the very minor role autodetachment from the S_1 state plays in the gas-phase,[22,36] a pathway that is indisputably inaccessible in solution. The time-resolved photoelectron spectra furthermore show no evidence for any dynamics in the indirect emission feature ($eKE < 0.1$ eV).

Earlier theoretical studies suggested different decay pathways for the solvated and isolated GFP chromophores. This was based primarily on the observation that in solution rotation about both the C7−C8 and the C4−C7 bonds is barrierless, whilst in the gas-phase a barrier is inhibiting C7−C8 rotation, leading to preferential relaxation via rotation about C4−C7 (ϕ).[26] Depending on the axis of rotation, the encountered energy separation of the S_0 and S_1 states evolves differently, thereby influencing the rate of internal conversion between the two. In solution the energy separation is significantly larger following C4−C7 rotation than rotation about C7−C8, and hence it was concluded that the latter must be the major decay channel leading to internal conversion; whereas rotation about C4−C7 would lead to a trapping of population and a bottleneck in the dynamics.[26] The observation of remarkably similar decay dynamics and timescales in both media suggests that similar decay pathways are operational in both environments. Although we cannot definitively assign the rotation to a specific bond, the presence of a potential barrier for rotation about C7−C8 makes this the less likely pathway in the gas-phase.

The observed insensitivity of the excited state dynamics to the environment are surprising given the very different absorption spectra recorded in the two media. Whereas the gas-phase absorption is very similar to that observed for the chromophore in the natural protein environment,[12,13] $HBDI^-$ in water shows a spectral shift of ∼0.3 eV in comparison with natural GFP.[10] This suggests that either the FC geometries are different between the two environments, or that sol-

vation stabilises or destabilises electronic states of the chromophore to different extends. Either of these effects is expected to have a bearing on the underlying excited state dynamics. However, it should be noted that the similarity of the absorption spectra *in vacuo* and in the protein could be coincidence and the result of a cancellation of red-shifting and blue-shifting interactions in the protein. The observed dynamics are furthermore unexpected because in the natural protein environment dynamics slow down by 3 orders of magnitude (compared with the isolated chromophore) and proceed on a nanosecond timescale. This suggests that the β-barrel of the protein is neither solution like, nor gas-phase like as has been previously suggested.[12,14,15]

Given the observed dynamics, and assignment of the decay pathway, one can begin to understand the function of the protein backbone within GFP. In natural wild-type GFP the TI geometry is almost never reached and population trapped in the FS geometry, whereas in solution or in the gas-phase the FS is only an intermediate with lifetimes on the order of 330 fs. Therefore the protein backbone affects the excited state potential energy surfaces of the chromophore, such that the formation of the TI geometry is inhibited. As the TI is formed by rotation around torsional angle ϕ, the protein barrel appears to dramatically restrict this rotation. This is consistent with observed dynamics in extremely viscous solvents, where this rotation is equally restricted and the dynamics slow down considerably.[47] Considering the chromophore inside the protein, it is covalently bound to the protein on the imidazole site, while the hydroxy-anion is restricted by hydrogen bonds.[2,53,54] However, comparison of the dynamics of the chromophore in water and of the isolated chromophore indicates that the presence of hydrogen bonding alone does not significantly influence the observed dynamics. Similarly, the addition of bulky groups to the chromophore appears to slow down the dynamics by less than an order of magnitude.[55] Therefore it must be the combined action of the protein barrel on both sides of the chromophore that prevents the torsional motion around ϕ, thereby trapping excited state population in the fluorescent geometry and leading to the outstanding versatility of GFP as a marker and probe in molecular biology and the life sciences.

5.4 Conclusion

A comprehensive study of the intrinsic electronic properties and excited state dynamics of a model chromophore of GFP was presented. Using photoelectron spectroscopy and time-resolved photoelectron spectroscopy, isolated $HBDI^-$ was studied in the gas-phase and results interpreted using quantum chemical calculations.

Single-colour photoelectron spectroscopy revealed that the vertical detachment energy of $HBDI^-$ is 2.8 ± 0.1 eV. This is significantly higher than the maximum of the $S_1 \leftarrow S_0$ transition, and hence the S_1 excited state is bound with respect to electron loss in the Franck-Condon region, despite earlier theoretical studies suggesting otherwise. Following resonant excitation of the S_1 state, thermionic emission of electrons was observed, indicating that internal conversion back to the S_0 anion ground state is an active decay pathway from the S_1 state. UV photoelectron spectroscopy at 6.15 eV photon energy revealed the presence of several electronic excited states in neutral HBDI. These were assigned with the aid of TD-DFT calculations and formed excited states corresponding to the removal of an electron from successively more bound molecular orbitals in the parent anion. All observed excited states could be uniquely assigned, providing important benchmark information for future theoretical studies of the GFP chromophore.

Following the observation that the S_1 state of $HBDI^-$ is bound in the gas-phase, and internal conversion an operative decay mechanism, the intrinsic electronic dynamics of this state were investigated, in collaboration with the Fielding group (UCL) who provided *ab initio* calculations. Time-resolved photoelectron spectroscopy was used to first resonantly excite the $S_1 \leftarrow S_0$ transition, and subsequently probe the system through photodetachment. A bi-exponential decay was observed, with two distinct components corresponding to different lifetimes and photoelectron peak shapes. These data were interpreted and the underlying molecular dynamics identified using *ab initio* calculations. Following excitation of the S_1 this state rapidly (sub-100 fs) stretches along the allyl bond centre, forming the fluorescent state geometry. This subsequently evolves via a twisting of the bridging $C-C-C$ bond to form a twisted intermediate configuration. This deformation has a characteristic lifetime of 330 fs and can clearly be distinguished in the photoelectron spectra. Once population has reached the TI geometry it undergoes internal conversion to the anion ground state with a lifetime of 1.4 ps. This available ultrafast non-radiative decay is very similar to that observed in solution and highlights the function of the protein barrel around the chromophore in GFP. In the protein the chromophore is fixed in space through covalent bonds on one side and through hydrogen bonding on the other end, thereby preventing the rotation around the $C-C-C$ axis, such that population never reaches the TI geometry and remains trapped in the FS geometry, from where strong fluorescence is observed on a nanosecond timescale.

Further studies on fluorescent chromophores aim to elucidate the non-radiative relaxation pathway in more detail and establish the minimum protein scaffold needed to maintain fluorescence. Studies are currently under way in our laboratory that make use of a fluorinated version of the HBDI chromophore. The addi-

tion of fluorine atoms increases the electron affinity of the system, while leaving the excited state energetics and dynamics unchanged. This should eliminate any autodetachment from the excited state, which is now significantly more bound than in ordinary $HBDI^-$. If the dynamics observed in this case are identical to those in ordinary HBDI, this is final proof of the bound nature of the S_1 excited state, which is still disputed in theoretical studies.

The major aim of future studies is to understand in detail the motion on the excited state and how natural GFP maintains its fluorescence. A first step is to introduce bulky substituents around the benzene moiety, thereby severely restricting the rotation about the C−C−C bridge, similar to solution phase studies.[55] This should lead to a significant decrease in the rate of torsional motion, thereby increasing the measured 330 fs lifetime. The internal conversion timescale, once the TI geometry is reached, should be unaffected. The next step is then the incremental introduction of the protein scaffold around the chromophore, in the gas-phase. The aim is to recover the fluorescent properties and understand in detail the interactions between the chromophore and protein needed to inhibit radiationless decay. This work can furthermore be extended to other families of fluorescent proteins as a basic understanding of the underlying photophysics and photochemistry is needed for the development of new fluorescent probes, opening up yet more applications across the life sciences.

References

[1] O. Shimomura, F. H. Johnson, Y. Saiga, *J. Cell. Comp. Physiol.* **59**, 223 (1962).

[2] R. Y. Tsien, *Annu. Rev. Biochem.* **67**, 509 (1998).

[3] M. Zimmer, *Chem. Rev.* **102**, 759 (2002).

[4] S. R. Meech, *Chem. Soc. Rev.* **38**, 2922 (2009).

[5] V. Sample, R. H. Newman, J. Zhang, *Chem. Soc. Rev.* **38**, 2852 (2009).

[6] R. Heim, D. C. Prasher, R. Y. Tsien, *Proc. Natl. Acad. Sci. USA* **91**, 12501 (1994).

[7] M. Chattoraj, B. A. King, G. U. Bublitz, S. G. Boxer, *Proc. Natl. Acad. Sci. USA* **93**, 8362 (1996).

[8] G. H. Patterson, S. M. Knobel, W. D. Sharif, S. R. Kain, D. W. Piston, *Biophys. J.* **73**, 2782 (1997).

[9] G. Bublitz, B. A. King, S. G. Boxer, *J. Am. Chem. Soc.* **120**, 9370 (1998).

[10] H. Niwa, *et al.*, *Proc. Natl. Acad. Sci. USA* **93**, 13617 (1996).

[11] N. M. Webber, K. L. Litvinenko, S. R. Meech, *J. Phys. Chem. B* **105**, 8036 (2001).

[12] S. B. Nielsen, *et al.*, *Phys. Rev. Lett.* **87**, 228102 (2001).

[13] L. H. Andersen, *et al.*, *Eur. Phys. J. D* **20**, 597 (2002).

[14] M. W. Forbes, R. A. Jockusch, *J. Am. Chem. Soc.* **131**, 17038 (2009).

[15] M. W. Forbes, A. M. Nagy, R. A. Jockusch, *Int. J. Mass. Spec.* **308**, 155 (2011).

[16] E. Epifanovsky, I. Polyakov, B. Grigorenko, A. Nemukhin, A. I. Krylov, *J. Chem. Theory Comput.* **5**, 1895 (2009).

[17] E. Epifanovsky, I. Polyakov, B. Grigorenko, A. Nemukhin, A. I. Krylov, *J. Chem. Phys.* **132**, 115104 (2010).

[18] S. Kojima, *et al.*, *Tetrahedron Lett.* **39**, 5239 (1998).

[19] V. Voliani, *et al.*, *J. Phys. Chem. B* **112**, 10714 (2008).

[20] D. A. Horke, A. S. Chatterley, J. R. R. Verlet, *J. Phys. Chem. Lett.* **3**, 834 (2012).

[21] C. R. S. Mooney, *et al.*, *J. Phys. Chem. A* **116**, 7943 (2012).

[22] Y. Toker, D. B. Rahbek, B. Klrke, A. V. Bochenkova, L. H. Andersen, *Phys. Rev. Lett.* **109**, 128101 (2012).

[23] A. Nemukhin, B. Grigorenkoa, A. Savitskya, *Acta Natur.* **2**, 33 (2009).

[24] T. Yanai, D. P. Tew, N. C. Handy, *Chem. Phys. Lett.* **393**, 51 (2004).

[25] M. J. Frisch, *et al.*, *Gaussian09* revision a.02 (2009).

[26] M. E. Martin, F. Negri, M. Olivucci, *J. Am. Chem. Soc.* **126**, 5452 (2004).

[27] I. V. Polyakov, B. L. Grigorenko, E. M. Epifanovsky, A. I. Krylov, A. V. Nemukhin, *J. Chem. Theory Comput.* **6**, 2377 (2010).

[28] E. P. Wigner, *Phys. Rev.* **73**, 1002 (1948).

[29] A. Sanov, R. Mabbs, *Int. Rev. Phys. Chem.* **27**, 53 (2008).

[30] B. Baguenard, J. C. Pinar, C. Bordas, M. Broyer, *Phys. Rev. Acta Natur.* **63**, 023204 (2001).

[31] B. Baguenard, J. C. Pinar, F. Lpine, C. Bordas, M. Broyer, *Chem. Phys. Lett.* **352**, 147 (2002).

[32] K. Hansen, K. Hoffmann, E. E. B. Campbell, *J. Chem. Phys.* **119**, 2513 (2003).

[33] M. Kjellberg, *et al.*, *Phys. Rev. A* **81**, 023202 (2010).

[34] C. E. Klots, *Z. Phys. D* **20**, 105 (1991).

[35] T. F. O'Malley, *Phys. Rev.* **137**, A1668 (1965).

[36] D. A. Horke, J. R. R. Verlet, *Phys. Chem. Chem. Phys.* **14**, 8511 (2012).

[37] A. A. Voityuk, M.-E. Michel-Beyerle, N. Rsch, *Chem. Phys. Lett.* **296**, 269 (1998).

[38] W. Weber, V. Helms, J. A. McCammon, P. W. Langhoff, *Proc. Natl. Acad. Sci. USA* **96**, 6177 (1999).

[39] A. A. Voityuk, A. D. Kummer, M.-E. Michel-Beyerle, N. Rsch, *Chem. Phys.* **269**, 83 (2001).

[40] T. Laino, R. Nifos, V. Tozzini, *Chem. Phys.* **298**, 17 (2004).

[41] A. Toniolo, S. Olsen, L. Manohar, T. J. Martinez, *Farad. Discuss.* **127**, 149 (2004).

[42] C. Filippi, M. Zaccheddu, F. Buda, *J. Chem. Theory Comput.* **5**, 2074 (2009).

[43] D. Mandal, T. Tahara, N. M. Webber, S. R. Meech, *Chem. Phys. Lett.* **358**, 495 (2002).

[44] K. L. Litvinenko, N. M. Webber, S. R. Meech, *J. Phys. Chem. A* **107**, 2616 (2003).

[45] D. Mandal, T. Tahara, S. R. Meech, *J. Phys. Chem. B* **108**, 1102 (2004).

[46] A. D. Kummer, *et al.*, *J. Phys. Chem. B* **106**, 7554 (2002).

[47] R. Gepshtein, D. Huppert, N. Agmon, *J. Phys. Chem. B* **110**, 4434 (2006).

[48] P. Altoe, F. Bernardi, M. Garavelli, G. Orlandi, F. Negri, *J. Am. Chem. Soc.* **127**, 3952 (2005).

[49] H.-J. Werner, *et al.*, *MOLPRO* 2010.1, a package of ab initio programs (2010).

[50] G. Karlström, *et al.*, *Computat. Mater. Sci.* **28**, 222 (2003).

[51] V. Veryazov, P.-O. Widmark, L. Serrano-Andrs, R. Lindh, B. O. Roos, *Int. J. Quantum Chem.* **100**, 626 (2004).

[52] F. Aquilante, *et al.*, *J. Comput. Chem.* **31**, 224 (2010).

[53] M. Orm, *et al.*, *Science* **273**, 1392 (1996).

[54] F. Yang, L. G. Moss, G. N. Phillips, *Nat. Biotech.* **14**, 1246 (1996).

[55] J. Conyard, *et al.*, *J. Phys. Chem. B* **115**, 1571 (2011).

Chapter 6

Conclusion

Any intelligent fool can make things bigger, more complex and more violent. It takes a touch of genious - and a lot of courage - to move in the opposite direction.

E.F. Schumacher

This chapter concludes this thesis. It starts with a summary of the preceding chapters, highlighting the areas investigated and any conclusions drawn. Following on from this will be a section suggesting improvements to the current experimental setup. Some of these are still in the planning stages, while others have already been designed and build, but are yet to be implemented. This is followed by a section on suggested future research projects for the anion photoelectron imaging spectrometer. While each of the current projects (covered in chapters 3 to 5) has suggestions for further study included, this separate section proposes a few completely new directions that have not been previously explored. Finally, this chapter and thesis will be completed with a few concluding remarks.

6.1 Recapitulation of Previous Chapters

The first chapter of this thesis provides a general introduction into the area of femtochemistry and time-resolved photoelectron spectroscopy in particular. The basic theoretical concepts are introduced and their application to intramolecular relaxation processes shown. A broad overview of the current literature in the field of anion photoelectron spectroscopy and time-resolved photoelectron spectroscopy is given.

The experimental setup of our anion beam machine, photoelectron imaging setup and femtosecond laser system is presented in chapter 2. The use of an electrospray ionisation source allows the production of large molecular anions and polyanions in the gas-phase. These are subsequently trapped in a cylindrical electrode ion trap and mass selected by a Wiley-McLaren time-of-flight mass spectrometer. Target ions are intersected by femtosecond laser pulses in the centre of a novel velocity-map imaging setup, utilising a resistive glass tube for the creation of a smooth electric field gradient. Collected photoelectron images are analysed using the polar-onion peeling algorithm, yielding photoelectron spectra and angular distributions.

Chapter 3 outlines in detail our research on electron acceptor radical anions and their excited state dynamics. We investigated several common electron acceptors based on the quinone moiety, which exhibits electron transfer rates in excess of those predicted by Marcus theory. Our results show that the quinones posses several electronic excited states which couple very strongly to the anionic ground state and could partake in an electron transfer process. All investigated systems exhibited the same behaviour, showing that it really is the quinone electronic backbone that is responsible for the efficient electron acceptance. In the case of *p*-Benzoquinone, the simplest of the quinoid systems, we observed two ex-

cited state resonances above the detachment threshold that can accept an excess electron and stabilise the charge in the anion ground state in sub-100 fs. This alternative pathway appears to be operative in all quinoids studied and explains the abundance of these systems in biological and technological electron acceptors.

Our recent results on the dynamics of polyanions are presented in chapter 4. We are particularly interested in the nature and properties of the repulsive Coulomb barrier (RCB). By studying dianions of fluorescein and pyrromethene-556 we showed that (i) every ro-vibrational state of a system has its own RCB associated with it and that the inner RCB increases with increasing internal energy; (ii) tunnelling through the RCB is a highly adiabatic process; (iii) if an excited state bound solely by the RCB has a competing non-radiative decay channel this can have dramatic effects on the observed photoelectron spectra collected with nanosecond laser pulses due to photon cycling; (iv) The RCB has a large effect on the trajectories of outgoing photoelectrons and this can be used to probe structural dynamics in polyanions. We demonstrate this by following the rotational dephasing dynamics of an aligned sample of dianions in real time through the photoelectron angular distributions.

Chapter 5 outlines recent results from the study of the chromophore of the green fluorescent protein (GFP). The first photoelectron spectrum of the isolated chromophore anion in the gas-phase was presented, providing much needed benchmarks for future theoretical studies. We demonstrated that the S_1 excited state of the chromophore is bound with respect to electron loss in the gas-phase. Using time-resolved photoelectron spectroscopy we discovered that the primary decay pathway of the chromophore in vacuum is similar to that in solution and involves a fast (sub-100 fs) bond stretching motion, followed by a twist about the C−C−C bond in 330 fs. The system subsequently relaxes via internal conversion to the ground state. In the natural protein the fast twisting motion is prevented by the protein backbone, leading to a trapping of population in an excited state well, from where fluorescence is the major decay pathway.

6.2 Suggested Experimental Improvements

In the first years of operation of the anion photoelectron imaging spectrometer a few areas of the experimental apparatus have been identified that can be improved upon. Currently the major restriction for the sensitivity of the spectrometer is the number of ions produced per ion packet. We estimate a population of less than 500 ions per packet, increasing the time requirements for a full time-resolved study and limiting the applications of the spectrometer to sys-

tems with large absorption and detachment cross-sections or systems where a large observable change occurs in the photoelectron spectra. To overcome these limitations requires a redesign of the interface between the electrospray source and the time-of-flight mass spectrometer. Specifically, the transmission into the ion trap needs to be improved and the trap itself needs to confine a larger volume. The current trap only contains a volume of $\sim$1 mm^3, which limits it to holding approximately 10^3 charges due to the space charge limit.[1,2] A further limitation of the current design is the minimal degree of control over the internal (rotational) temperature of the ions, which cannot be cooled below room temperature. This is a further problem that can be overcome with a complete overhaul of the current ion trap design, which should incorporate the ability to cool parts of the trap and the buffer gas used inside the trap.

As the studies on *p*-Benzoquinone have shown (chapter 3) the time resolution achieved with our laser setup is sometimes insufficient for the observation of very fast non-radiative processes, especially those involving motion through conical intersections. This can be significantly improved by the incorporation of a second pulse compressor, such that the compression of pump and probe pulses can be adjusted separately. We furthermore consider the idea of utilising a gas cell for the production of a white light continuum, which can subsequently be compressed to very short (sub-10 fs) pulses.

6.2.1 Revised electrospray interface and ion trap

To address the shortcomings of the current setup and produce a higher ion current with more control over the ions internal temperature, the electrospray-vacuum interface as well as the ion trap have been redesigned. These parts have been manufactured already, but are yet to be implemented and tested.

In order to produce a colder beam of ions, one would ideally use a supersonic expansion, as is commonly done in molecular beam sources. This typically requires a pressure differential of about 5 orders of magnitude between two adjacent vacuum regions, unattainable in our current setup.[3] To increase the pressure differential between regions 1 and 2 we will replace the current pinhole (1 mm orifice) with a new skimmer with a 0.5 mm aperture, thereby severely reducing the conductance between the regions.[4] Furthermore, the installation of a liquid nitrogen cryo-pump in region 2 will lower the pressure further by trapping condensibles, a primary source of background gas due to the large amount of solvent ejected from the electrospray source. We estimate an achievable pressure of 10^{-4} Torr in region 2, corresponding to a pressure gradient between the first two regions of approximately 4 orders of magnitude. Given the significantly lower pressures in the second region, one can now use electrostatic Einzel lenses

for the simple and effective focussing of the ion beam after the skimmer.[5] This will ensure the maximum transmission into the new ion trap design.

The current ring electrode trap offers too small a trapping volume and does not lend itself to cooling, due to the lack of sufficiently large surfaces in the trapping region. Thus a different trapping geometry was considered, with the most common choice for charged particles being a Paul trap.[6,7] This consists of a central ring electrode and two endcap electrodes, with the trapping volume made up of hyperbolic surfaces sharing common asymptotes.[8] Using a combination of radio-frequency (RF) fields on the central ring electrode for radial confinement and direct current (DC) on the endcap electrodes for axial confinement leads to the desired trapping effect. Moreover, the large surfaces of the trap can be effectively cooled and, in combination with cold buffer gas in the trap, be used to eject cold ions from the trap. However, the manufacture of Paul traps is non-trivial, due to the hyperbolic surfaces of the electrodes. Instead a simplified design was chosen, known as a cylindrical ion trap (CIT).[9] Like a classic Paul trap, this consists of a central ring electrode and two endcaps, however these are made up of flat surfaces, significantly easing manufacture. A CIT then appears to be ideally suited to the experimental needs, it is easy to manufacture; can be cooled effectively due to the large surfaces and leaking in of cooled helium buffer gas, and offers a large trapping volume.[10]

The finished design for the new interface and trap are shown in figure 6.1(a). Ions enter region 2 through a beam skimmer (labelled A) with inner diameter (ID) 500 μm and cone angle of 50°.[3,11] Placed 5 mm downstream from the edge of the skimmer is an Einzel lens electrode (B) with ID 8 mm and a length of 6 mm. A further 5 mm downstream the CIT is located, it consists of two endcap electrodes, 3 mm thick in the centre and placed 10 mm apart. The central ring electrode (D) has an ID of 21 mm and is 12 mm long, such that it overlaps with the endcaps by 1 mm, as indicated in the drawings. The entrance electrode (C) has a 3 mm orifice in the centre through which the trap is loaded. The exit endcap electrode is split into two pieces (E1 and E2) for more efficient unloading of the trap, which is crucial for successful operation of the CIT. A conventional quadrupole trap is unloaded by applying a repulsive DC voltage to the central ring electrode, thereby forcing ions into the centre of the trap, and subsequently pushing ions out by applying the required DC voltages to the endcaps. However, this mechanism requires switching of the RF voltage on the ring electrode, which is non-trivial given the high voltages needed ($\sim$1 kV) and the desired repetition rate of 1 kHz. Instead we opted to modify the exit endcap electrode such that this provides an electrostatic force pulling ions into the centre of the trap, as well as towards and through the endcap. This is achieved by splitting the electrode into two pieces that fit inside each other and that can have different voltages

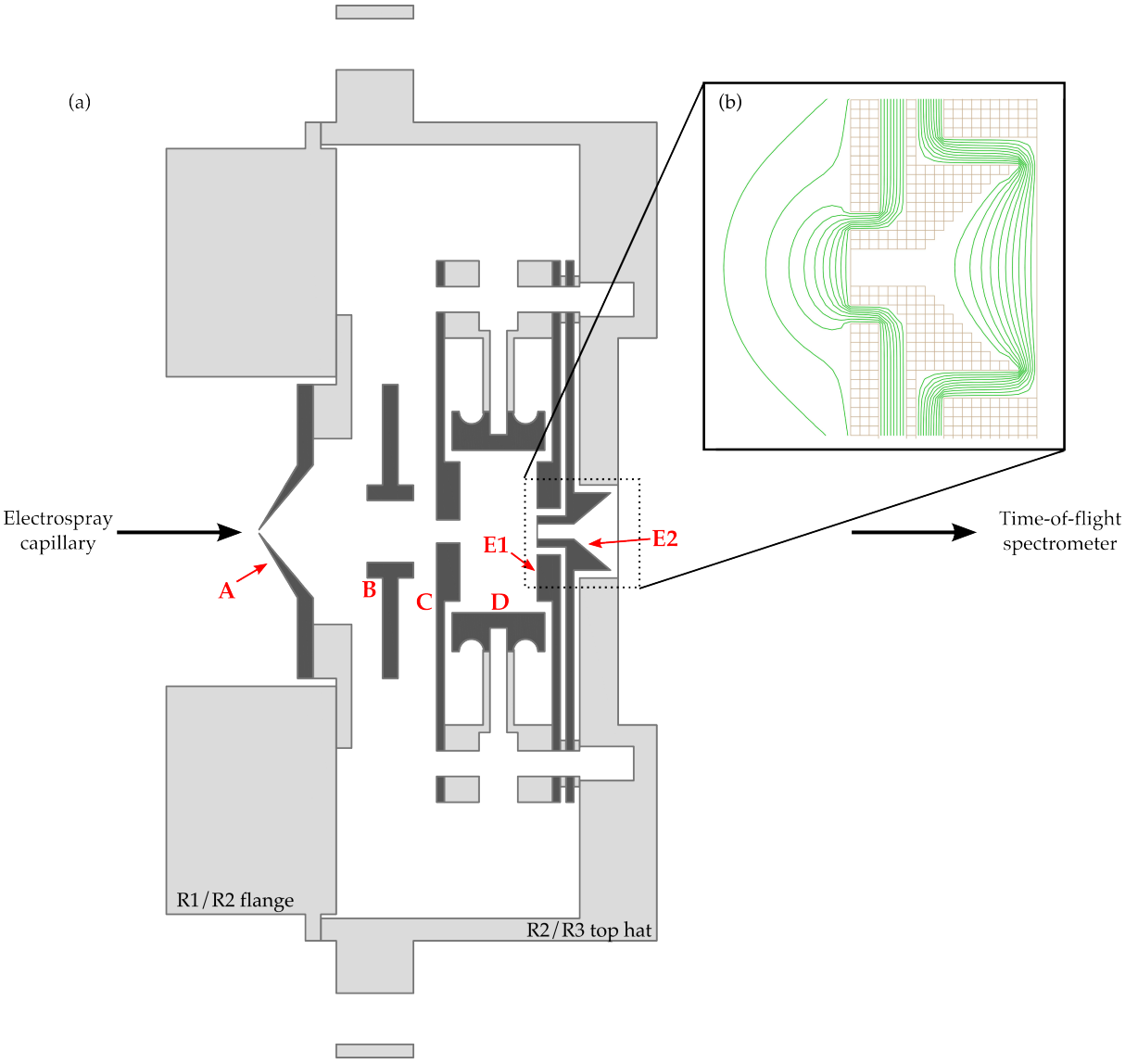

Figure 6.1: New design for regions 1 and 2 of the spectrometer (see text for details and dimensions). (a) Ions enter region 2 through a beam skimmer (A) and get focussed by an Einzel lens (B) into a cylindrical ion trap, consisting of a front endcap (C), a ring electrode (D) and an exit endcap split into two pieces (E1 and E2) to allow efficient extraction of ions from the trap. (b) Field lines around the exit endcap electrode during ion ejection from the trap.

applied. Figure 6.1(a) shows the designed geometry; the exit endcap plate (E1) has a large orifice of 6 mm into which the inner electrode (E2) is fitted. This inner electrode has an OD of 4 mm and an ID of 2 mm. During the extraction of ions an attractive potential is applied to the inner piece (E2), thereby forcing ions towards the centre of the trap. By applying a large repulsive potential to the entrance end cap, ions are pushed out through the 2 mm orifice. In order to avoid any unwanted focussing effect, the extraction orifice is covered with high-transmission stainless steel mesh. The inner piece (E2) has a conical opening on the non-trap side, this acts to radially collimate the produced beam of anions. Stainless steel mesh is placed over the orifice itself to avoid unwanted focussing effects. The simulated field lines (using SimIon 8.0[12]) during ion extraction are

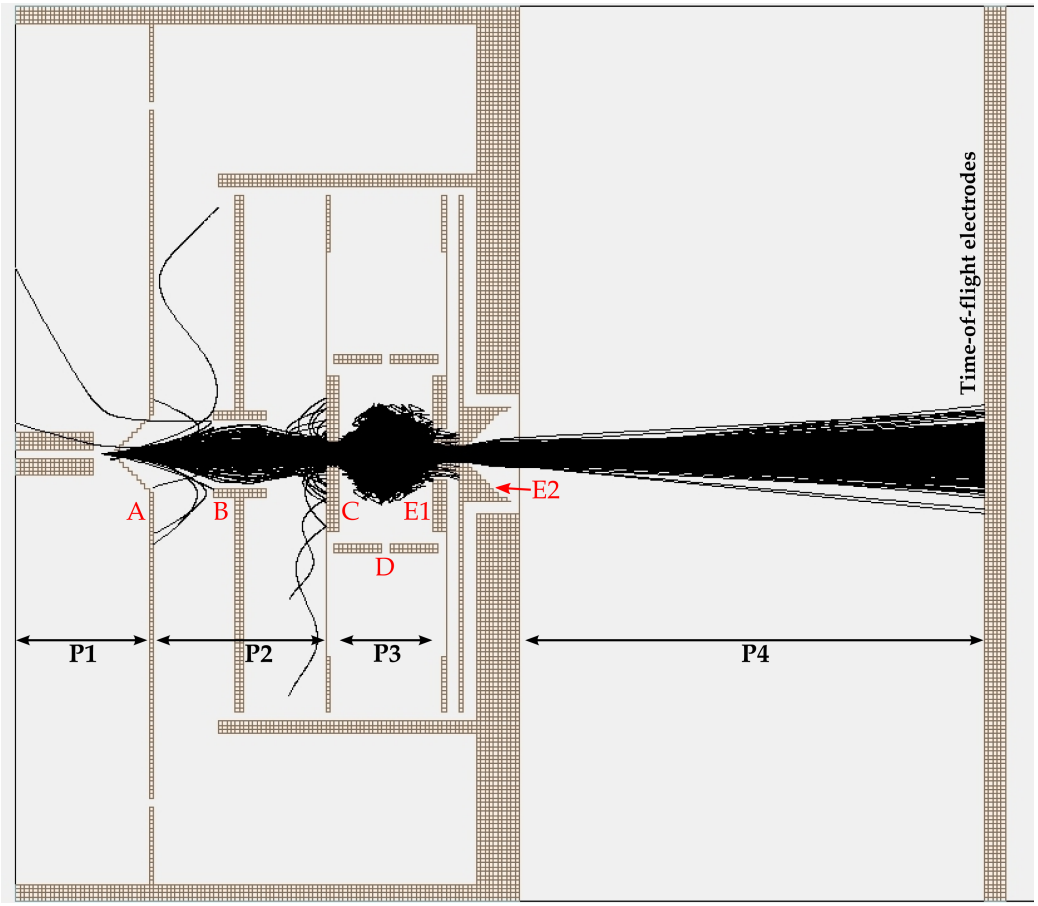

Figure 6.2: SimIon simulation of the new trap design, with parts labelled as in figure 6.1 and P1 - P4 indicating different pressure regions simulated, corresponding to 3 Torr, 10^{-4} Torr, 10^{-3} Torr and 10^{-5} Torr, respectively. Simulated were 1800 ion trajectories (m/z = 200 Da), 46% of ions are successfully trapped and ejected and impact on the time-of-flight electrodes.

shown in figure 6.1(b).

The central ring electrode in this design can furthermore be used to cool the ion population and buffer gas in the trap. For this purpose it is manufactured from copper and has two grooves machined around the outside diameter, as shown in figure 6.1(a), which are of 1/8" diameter, such that cooper piping carrying liquid nitrogen (or another refrigerant) can be circulated around the electrode. Additionally, the ring electrode has as small 1 mm diameter hole drilled through radially, in the centre of the electrode. This allows cold buffer gas to be leaked into the centre of the trap.

The design of the entire interface was optimised using trajectory simulations in SimIon 8.0, and a simulation of the finalised design is shown in figure 6.2.[12] To accurately simulate the experimental conditions and trapping, a simple hard-sphere collisions model was used to simulate the different pressure regions. A background gas mass of 28 amu and temperature of 300 K was assumed. The different pressure regions are indicated by the labels P1-P4 and these were set

to 3 Torr, 10^{-4} Torr, 10^{-3} Torr and 10^{-5} Torr, respectively. The figure shows a simulation of 1800 ions of mass-to-charge ratio 200 Da, created at the exit point of the capillary. Simulations show that 46% of ions impact on the time-of-flight (TOF) electrodes, having been successfully trapped and ejected. By considering the impact positions, times and energies of these ions we can estimate the overall efficiency of the interface. We find that 88% were successfully collimated to within a 5 mm diameter, the size of the orifice on the TOF electrode. 82% of ions possess a kinetic energy between 120 eV and 180 eV on impact, a range that can be brought into focus by our TOF geometry. Furthermore 76% of ions arrive within a 2 μs window, which corresponds (at an average kinetic energy of 140 eV) to a spatial spread of $\sim$2 cm. The distance between the TOF electrodes is 3 cm, and simulations show that this initial spatial spread can be brought into focus at the interaction region with our design. Finally, taking into account losses at the two stainless steel meshes used (90% transmission each), we estimate that approximately 20% of ions initially generated successfully enter the TOF region and can be focussed and mass selected. Considering that the ion current through the skimmer is around 10 pA, this corresponds to 2×10^4 charges per ion packet at a repetition rate of 1 kHz, an improvement of 2 orders of magnitudes compared to the current setup.

6.2.2 Improving time resolution

Recent experiments looking at internal conversion dynamics through conical intersections have shown that a better time resolution is highly desirable, and in some cases necessary, to study these dynamics in detail. The time resolution in pump-probe experiments is limited by the cross-correlation between the two pulses and for our laser setup this is currently on the order of 130 fs if pulses in the visible are used. The limiting factor at present is the use of only a single pulse compressor following amplification of the laser pulses in the regenerative amplifier (see chapter 2 for details). As the compressor is located before the frequency conversion stages (either harmonic generation or optical parametric amplification, OPA), it also serves to pre-compensate the pulse for the group-velocity dispersion (GVD) experienced during frequency conversion. However, the use of a single compressor means both pump and probe pulse have the same GVD. This is a problem especially when the output from the OPA is used in conjunction with a fundamental beam. The OPA introduces severe GVD due to the number of transmissive optics along the beam path, whereas the fundamental beam does not need to pass through any additional optical elements. With only a single compressor for both pulses, a compromise has to be reached and the overall time-resolution is limited. This problem can be overcome with the introduction of a second pulse compressor to allow individual GVD compensation and therefore temporal compression of the pump and probe pulses individually.

Introduction of a simple prism or grating pair compressor should allow the production of transform-limited pump and probe pulses simultaneously and yield time resolutions of sub-50 fs.[13,14]

We are furthermore considering the production of even shorter duration laser pulses. A simple and economical approach to achieve this and maintain tunability is to focus high power ultrashort pulses into a gas cell, leading to extreme spectral broadening and (ideally) the production of a white-light continuum.[15–17] This continuum can subsequently by temporally compressed by a grating, prism or chirped-mirror compressor, yielding broadband few-cycle laser pulses. Alternatively, one can first select a spectral slice out of the continuum with dichroic mirrors before pulse compression, giving tunability across the entirety of the continuum. By focussing 30 fs pulses (at 800 nm) into a SF_6 filled gas-cell an ocatave-spanning continuum can be formed.[18] Using dichroic optics a spectral slice centred at 550 nm was separated from a broadband continuum and compressed (using a pair of chirped-mirrors) to 11.5 fs pulse durations (full-width at half maximum). In a similar fashion a spectral slice around 800 nm could be compressed to yield 9 fs pulses.[18] This method promises to be a simple and affordable way of producing few-cycle laser pulses with tunability across the visible (depending on the available dichroics) and preparations are under way in our laboratory to explore this as a source for pump and probe pulses in photoelectron spectroscopy.

6.3 Future Research Directions

Each of the preceding sections outlining current experimental progress in our laboratory (chapters 3 to 5) contained a section of future directions within that project. For the study of electron acceptor radical anions the next major aim is to observe the entirety of an electron transfer process in the gas-phase, probably by studying electron transfer in mixed valence systems, either based on transition metals or small organic molecules. Our investigations of polyanions showed that the repulsive Coulomb barrier can be used as a probe for large amplitude structural dynamics. We hope to exploit this in the near future to observe the *cis-trans* isomerisation of a large system, such as a diazo-benzene or a stilbene, in the gas-phase in real time. Finally, the next logical step in our project on the green fluorescent protein is the stepwise addition of the protein backbone to the chromophore, in the gas-phase, to study the effect this has on the fluorescent properties and establish the minimum framework needed for fluorescence.

In addition to these ongoing projects, the scope and applicability of our anion photoelectron imaging spectrometer is extremely large and a few completely

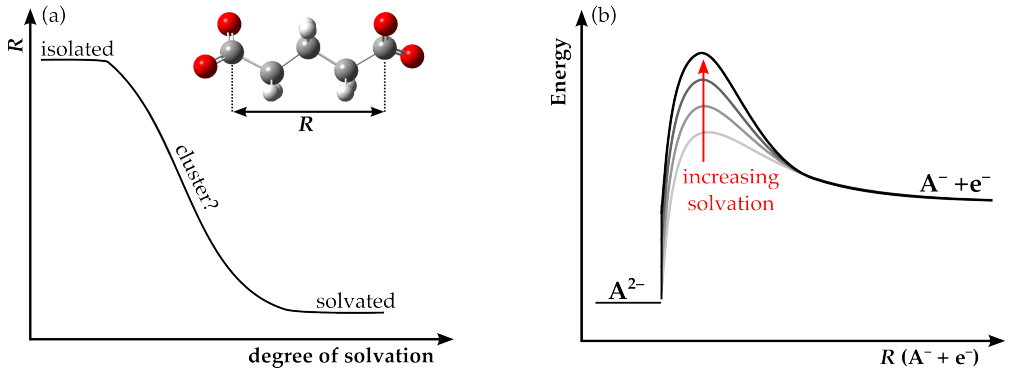

Figure 6.3: Effect of solvation on isolated polyanions. (a) Introducing solvent molecules around an anion should lead to a shielding of the excess charges, leading to a decrease in bond length in linear polyanions, for example dicarboxylates. (b) The effect of shielding should furthermore increase the repulsive Coulomb barrier experienced during photodetachment from a polyanion due to the stronger short-range interactions.

new research directions are proposed below.

6.3.1 Studies of solvation

The study of solvation effects using clusters of molecules in a gas-phase environment is a very active field of research. It tries to bridge the gap between the solution phase, the environment most chemistry in nature and technology happens in, and the gas-phase, a highly controllable environment that enables precision measurements.[19] However, many chemical properties and reactions are highly dependent on the presence of solvent, or are mediated by it. The use of molecular clusters tries to bring these two together by introducing solvent in a controllable manner around a molecule, which can still be studied in detail using gas-phase techniques. This methodology is especially applicable to anion systems, as solvent has a profound effect on their stability and reactivity, but also for experimental reasons; charged clusters can easily be separated in a mass spectrometer and the effect of solvation studied in a systematic manner by the sequential addition of single solvent molecules. While the study of anionic clusters using molecular beam sources is a well established field of research,[19–21] using electrospray ionisation to study the dynamics of clusters containing complex anions or even polyanions has received comparatively little attention.[22,23] With small experimental modifications it should be possible to study these system using our current experimental setup, opening up a whole new field with several potential projects.

Studying the effect of solvation on polyanions is one potential new area. The central questions here are how does solvation stabilise the polyanion and how many solvent molecules are required for an effective screening of the excess

charges? This charge screening should furthermore affect the nuclear geometry of the polyanion; a reduced repulsion between the charge centres should lead to a measurable contraction of the entire polyanion, especially in linear systems with terminal charge centres such as dicarboxylates, as indicated in figure 6.3(a). This will furthermore affect the repulsive Coulomb barrier (RCB) of the polyanion, which is highly dependent on the distribution of excess charge. How will the RCB change with solvation, is a single solvent molecule sufficient to significantly raise the RCB threshold (figure 6.3(b)), or does it require the presence of several solvent molecules to observe noticeably stronger short-range interactions? The use of polyanions also allows the study of solvation dynamics themselves and the arrangement of solvent following a change in the charge distribution of a molecule. Starting with a solvated polyanion, detachment of one excess charge will alter the charge distribution and the solvent molecules will rearrange to accommodate the new environment. This will affect the spectroscopy of the remaining negative charges in the system, which can be probed in real time using photoelectron imaging.

6.3.2 Molecular-frame photoelectron angular distributions

Molecular alignment (and orientation), that is the fixing of a molecule in space in one, two or three dimensions, is a growing field of research and several methodologies have been developed for this purpose.[24–26] However so far the vast majority of studies have applied these techniques to neutral systems. Very few examples in the literature (one of them being from our group) report the alignment of anions in the gas-phase, and these studies relied on a resonant electronic excitation for the creation of a 1D aligned population.[27,28] In principle, however, it is possible to apply the techniques of strong-field alignment, both field-free and not, to anionic systems. Singly charged anions often have a large dipole moment (and polarisability) due to the excess charge, making them ideal candidates for alignment experiments. Alignment (and ideally orientation) allows the extraction of molecular frame information, avoiding the orientational averaging inherent to studies of randomly distributed molecules. Of particular interest in recent years has been the study of molecular frame photoelectron angular distributions, with a special edition of *Journal of Physics B: Atomic, Molecular and Optical Physics* devoted entirely to the subject (Volume 45, Issue 19, October 2012).[29]

The study of aligned systems in the gas-phase has numerous applications and allows the extraction of information that would not be observable from randomly distributed samples. Photoelectron angular distributions (PADs) arise from the interference of the outgoing partial photoelectron waves following photodetachment, and are subject to symmetry constraints (see section 1.3.2).[30,31] The ob-

servation of laboratory frame PADs carries information about the underlying molecular orbital from which the electron was detached, and when studied in a time-resolved manner dynamic information about the orbital, and any changes in orbital structure, can be extracted. This was recently demonstrated (theoretically) for the isomerisation of acetylene to form the vinylidene structure.[32] A theoretical study by the Seideman group has furthermore shown that molecular frame PADs allow the extraction of electronic dipole matrix elements for the bound-to-free electron transition, as well as rotational probability distributions, carrying information about rotational coherences.[33]

We have demonstrated in chapter 4 how the observed PADs in polyanions are dominated by the presence of the repulsive Coulomb barrier (RCB) and how the RCB, if it is adequately probed, carries information about the underlying molecular structure.[28] This technique relies on an initially aligned sample of polyanions to allow the observation of the shape of the RCB in the laboratory frame. While this has been demonstrated using a resonant electronic transition to create an ensemble of aligned excited molecules, combining this technique with molecular alignment methodologies would make it universally applicable. This would provide a new way of obtaining structural dynamics of polyanions in the gas-phase, with femtosecond resolution and is entirely laboratory based without the need for large scale facilities such as synchrotrons or free-electron lasers.

6.4 Concluding Remarks

This thesis has described several applications of our new femtosecond photoelectron imaging spectrometer, offering the unique capability of studying complex and multiply-charged anions in the gas-phase with ultrafast time resolution. Our studies focus on the excited state dynamics in these systems and specifically how anions or polyanions react to excess electronic energy and through which pathways they relax. We follow these dynamics using time-resolved photoelectron spectroscopy and photoelectron angular distributions, the latter was first applied in our group to the study of anion dynamics. The projects outlined in this work include the study of (i) electron acceptors, and determining why quinone based electron acceptors have these outstanding capabilities and are ubiquitous in nature; (ii) isolated polyanions, where we have demonstrated a new methodology to extract structural dynamics and (iii) the green fluorescent protein (GFP) chromophore and we have demonstrated its properties in the gas-phase and determined the action of the protein backbone that enables the functioning of GFP. The capabilities of our spectrometer are all but exhausted and several exciting projects are currently under way or being planned, aiming

to further our understanding of the electronic structure and dynamics of anions that are so crucial to many of their properties and functions in nature, technology and science in general.

References

[1] E. Fischer, *Z. Phys.* **156**, 1 (1959).

[2] S. Guan, A. G. Marshall, *J. Am. Soc. Mass Spectrom.* **5**, 64 (1994).

[3] R. Campargue, *J. Phys. Chem.* **88**, 4466 (1984).

[4] J. H. Moore, C. C. Davis, M. A. Coplan, *Building Scientific Apparatus* (Perseus Books, Cambridge, 2003).

[5] R. E. Imhof, F. H. Read, *J. Phys. E: Sci. Instr.* **1**, 859 (1968).

[6] W. Paul, H. Steinwedel, *Z. Naturforsch. A* **8**, 448 (1953).

[7] W. Paul, *Angew. Chem. Int. Ed.* **29**, 739 (1990).

[8] R. E. March, *Mass Spectrom. Rev.* **28**, 961 (2009).

[9] D. B. Langmuir, R. V. Langmuir, S. Haywood, R. F. Wuerker, Containment device (1962).

[10] D. Gerlich, *Adv. Chem. Phys.* **82**, 1 (1992).

[11] R. Campargue, *Rev. Sci. Instrum.* **35**, 111 (1964).

[12] *SimIon 8.0* scientific instrument services inc.

[13] W. T. Silfvast, *Laser Fundamentals* (Cambridge University Press, Cambridge, 2004), second edn.

[14] C. Rulliere, *Femtosecond Laser Pulses* (Spinger, New York, 2005), second edn.

[15] G. Stibenz, N. Zhavoronkov, G. Steinmeyer, *Opt. Lett.* **31**, 274 (2006).

[16] B. E. Schmidt, *et al.*, *Opt. Express* **16**, 18910 (2008).

[17] N. Zhavoronkov, *J. Opt. A* **11**, 125201 (2009).

[18] N. Zhavoronkov, *Opt. Lett.* **36**, 529 (2011).

[19] J. R. R. Verlet, *Chem. Soc. Rev.* **37**, 505 (2008).

[20] A. Sanov, W. Carl Lineberger, *Phys. Chem. Chem. Phys.* **6**, 2018 (2004).

[21] X. Chen, S. E. Bradforth, *Annu. Rev. Phys. Chem.* **59**, 203 (2008).

[22] X.-B. Wang, X. Yang, J. B. Nicholas, L.-S. Wang, *Science* **294**, 1322 (2001).

[23] X.-B. Wang, X. Yang, L.-S. Wang, *Int. Rev. Phys. Chem.* **21**, 473 (2002).

[24] K. F. Lee, D. M. Villeneuve, P. B. Corkum, A. Stolow, J. G. Underwood, *Phys. Rev. Lett.* **97**, 173001 (2006).

[25] H. Stapelfeldt, T. Seideman, *Rev. Mod. Phys.* **75**, 543 (2003).

[26] L. Holmegaard, *et al.*, *Nat. Phys.* **6**, 428 (2010).

[27] Z. Lu, R. E. Continetti, *Phys. Rev. Lett.* **99**, 113005 (2007).

[28] D. A. Horke, A. S. Chatterley, J. R. R. Verlet, *J. Phys. Chem. Lett.* **3**, 834 (2012).

[29] R. R. Lucchese, A. Stolow, *J. Phys. B: At. Mol. Opt. Phys.* **45**, 190201 (2012).

[30] R. Mabbs, E. R. Grumbling, K. Pichugin, A. Sanov, *Chem. Soc. Rev.* **38**, 2169 (2009).

[31] G. Wu, P. Hockett, A. Stolow, *Phys. Chem. Chem. Phys.* **13**, 18447 (2011).

[32] T. N. Rescigno, D. Nicolas, A. E. Orel, *J. Phys. B: At. Mol. Opt. Phys.* **45**, 194001 (2012).

[33] S. Ramakrishna, S. Tamar, *J. Phys. B: At. Mol. Opt. Phys.* **45**, 194012 (2012).